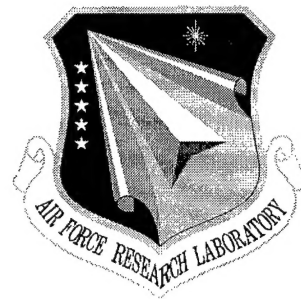


AFRL-SN-RS-TR-1998-143
Final Technical Report
July 1998



PROCEEDINGS OF THE 1997 ANTENNA APPLICATIONS SYMPOSIUM

University of Massachusetts

Daniel H. Schaubert, et al

DTIC QUALITY INSPECTED 2

APPROVED FOR PUBLIC RELEASE; DISTRIBUTION UNLIMITED.

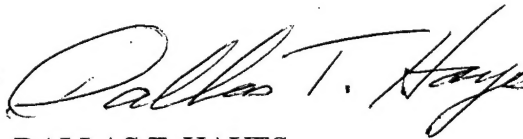
19981027 029

AIR FORCE RESEARCH LABORATORY
SENSORS DIRECTORATE
ROME RESEARCH SITE
ROME, NEW YORK

This report has been reviewed by the Air Force Research Laboratory, Information Directorate, Public Affairs Office (IFOIPA) and is releasable to the National Technical Information Service (NTIS). At NTIS it will be releasable to the general public, including foreign nations.

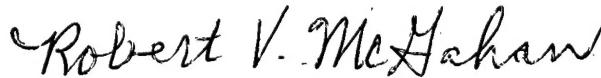
AFRL-IF-RS-TR-1998-143 has been reviewed and is approved for publication.

APPROVED:



DALLAS T. HAYES
Project Engineer

FOR THE DIRECTOR:



ROBERT V. MCGAHAN, Technical Director
Electromagnetics Technology Division
Sensors Directorate

If your address has changed or if you wish to be removed from the Air Force Research Laboratory Rome Research Site mailing list, or if the addressee is no longer employed by your organization, please notify AFRL/SNHA, 31 Grenier St., Hanscom AFB, MA 01731-3010. This will assist us in maintaining a current mailing list.

Do not return copies of this report unless contractual obligations or notices on a specific document require that it be returned.

REPORT DOCUMENTATION PAGE			Form Approved OMB No. 0704-0188	
<small>Public reporting burden for this collection of information is estimated to average 1 hour per response, including the time for reviewing instructions, searching existing data sources, gathering and maintaining the data needed, and completing and reviewing the collection of information. Send comments regarding this burden estimate or any other aspect of this collection of information, including suggestions for reducing this burden, to Washington Headquarters Services, Directorate for Information Operations and Reports, 1215 Jefferson Davis Highway, Suite 1204, Arlington, VA 22202-4302, and to the Office of Management and Budget, Paperwork Reduction Project (0704-0188), Washington, DC 20503.</small>				
1. AGENCY USE ONLY (Leave blank)	2. REPORT DATE Jul 98	3. REPORT TYPE AND DATES COVERED Final Sep 97		
4. TITLE AND SUBTITLE PROCEEDINGS OF THE 1997 ANTENNA APPLICATIONS SYMPOSIUM		5. FUNDING NUMBERS C - F30602-97-C-0334 PE - 62702F PR - 4600 TA - 14 WU - PP		
6. AUTHOR(S) Daniel H. Schaubert, et al				
7. PERFORMING ORGANIZATION NAME(S) AND ADDRESS(ES) University of Massachusetts Department of Electrical & Computer Engineering Amherst, MA 01003		8. PERFORMING ORGANIZATION REPORT NUMBER		
9. SPONSORING/MONITORING AGENCY NAME(S) AND ADDRESS(ES) AFRL/SNHA 31 Grenier St. Hanscom AFB, MA 01731-3010		10. SPONSORING/MONITORING AGENCY REPORT NUMBER AFRL-SN-RS-TR-1998-143		
11. SUPPLEMENTARY NOTES AFRL Project Engineer: Zachary O. White, SNHA, (781) 377-3191				
12a. DISTRIBUTION AVAILABILITY STATEMENT Approved for public release; distribution unlimited.		12b. DISTRIBUTION CODE		
13. ABSTRACT (Maximum 200 words) The Proceedings of the 1997 Antenna Applications Symposium is a collection of state-of-the-art papers relating to phased array antennas, multibeam antennas, satellite antennas, microstrip antennas, reflector antennas, HF, VHF, UHF and various other antennas.				
14. SUBJECT TERMS Antennas, Microstrip, Multibeam Antenna, Satellite Antennas, Broadband Antennas, Reflector, HF, VHF, UHF, Array Antennas		15. NUMBER OF PAGES 324		
		16. PRICE CODE		
17. SECURITY CLASSIFICATION OF REPORT UNCLASSIFIED	18. SECURITY CLASSIFICATION OF THIS PAGE UNCLASSIFIED	19. SECURITY CLASSIFICATION OF ABSTRACT UNCLASSIFIED	20. LIMITATION OF ABSTRACT UL	

**PROGRAM FOR
1997 ANTENNA APPLICATIONS SYMPOSIUM**

WEDNESDAY, SEPTEMBER 17, 1997

I. ANTENNA SYSTEMS

	page #
1. Keynote Address The Iridium Main Mission Antenna and Other Advanced Phased Array Concepts <i>J. Schuss</i> , Raytheon Andover, MA	*
2. Airborne DBS Receive System <i>P. Halsema, B. Anderson, and J. Frisco.</i> , Harris Corporation Melbourne, FL	1
3. A Comparison of Waveguide & Multilayer Microstrip Arrays for Airborne EHF SATCOM <i>J. S. Herd</i> , Rome Laboratory Hanscom AFB, MA	19
4. A Photonics-Steered, Wideband Phased Array for Shipboard Application <i>D. C. Collier, D. Bobowicz and J. Wojtowicz</i> , Northrup Grumman Corporation Norwalk, CT	35
5. Development of a Fiber-Optic Beamformer Network for True Time-Delay Control of an Array Transmitter <i>M. Y. Frankel, P. J. Matthews and R. D. Esman</i> , Naval Research Laboratory Washington, DC	45
6. Light-Weight, Efficient, High-Gain Phased Array <i>K. Tripp, G. D. Hopkins, A. E. Nelson and W. P. Cook</i> Georgia Tech Research Smyrna, GA	63

* Not included in this volume.

II. PATTERN SYNTHESIS AND CONTROL

- | | | |
|-----|---|-----|
| 7. | Array Antenna Beam Pointing Error Due to Random Errors
<i>J. B. Yon and D. Davis</i>
Northrop Grumman Corporation
Baltimore, MD | 93 |
| 8. | Analysis of Antenna Pattern Aperture Efficiency and Sidelobe Characteristics Using Array Factor Woodward Sample Point Information
<i>K. G. Ramsey and B. R. Myers</i>
Northrop Grumman Corporation
Baltimore, MD | 107 |
| 9. | A Comparison of Resistive and Reactive Corporate Power Divider Networks for Phased Array Antennas
<i>K. Ommodi</i>
Raytheon TI Systems
McKinney, TX | 119 |
| 10. | Constrained Feed for Lightweight, Overlapped, Subarray Antennas
<i>P. R. Franchi, M. Champion, H. Southall and Lt. D. Linafelter</i>
Rome Laboratory
Hanscom AFB, MA | 141 |
| 11. | Laser Induced Pulsed Picosecond Electromagnetic Sources (LIPPES) for 2- and 3-Dimensional Phased Array Antennas
<i>J. R. Reid, E. E. Crisman and J. S. Derov</i>
Rome Laboratory
Hanscom AFB, MA | 157 |
| 12. | Development of Microwave and MMW Integrated Phased Arrays with Simple Control
<i>J. S. Khodorkovsky, E. F. Zaitsev, A. G. Gouskov, A. S. Cherepanov, G. A. Yufit and M. R. Beltran</i>
Beltran, Inc.
Brooklyn, NY | 171 |
| 13. | CEM Code Validation Using Infrared Imaging Techniques
<i>M. Seifert</i>
Rome Laboratory, Rome, NY
<i>J. Norgard</i>
University of Colorado, Colorado Springs, CO | 193 |

THURSDAY, SEPTEMBER 18, 1997

III. Antennas and Elements

		page #
14.	Lightweight Phased Array Antennas <i>L. Diaz and P. K. Kelly</i> Ball Aerospace & Technology Corporation Broomfield, CO	209
15.	Miniature UHF SATCOM Antenna for Airborne Platforms <i>W. McKinzie</i> Atlantic Aerospace Electronics Corporation Greenbelt, MD	225
16.	Twist Polarizer Design <i>L. Diaz, P. K. Kelly and A. Shroyer</i> Ball Aerospace & Technology Corporation Broomfield, CO	235
17.	A Characterization of the Sinuous Antenna Implemented in a Polarimeter <i>T. Holzheimer</i> Raytheon E-Systems Greenville, TX	253
18.	Optimized Design Methodology of Cavity-Backed Microstrip Antennas with Dielectric Overlays <i>D. J. Hermes and P. J. Collins</i> Air Force Institute of Technology Wright-Patterson AFB, OH	283
19.	A Genetic Antenna Design for Improved Radiation Over Earth <i>B. S. Sandlin and A. J. Terzuoli</i> Air Force Institute of Technology Dayton, OH	301

Identifiers for Proceedings of Symposia
The USAF Antenna Research and Development Program

Year	Symp. No.	Identifier
1951	First	
1952	Second	C054 520
1953	Third	AD63794
1954	Fourth	AD63139
1955	Fifth	AD90397
1956	Sixth	AD114702
1957	Seventh	AD138500
1958	Eighth	AD301151
1959	Ninth	AD314721
1960	Tenth	AD244388 (Vol. 1)
		AD319613 (Vol. 2)
1961	Eleventh	AD669109 (Vol. 1)
		AD326549 (Vol. 2)
1962	Twelfth	AD287185 (Vol. 1)
		AD334484 (Vol. 2)
1963	Thirteenth	AD421483
1964	Fourteenth	AD609104
1965	Fifteenth	AD474238L
1966	Sixteenth	AD800524L
1967	Seventeenth	AD822894L
1968	Eighteenth	AD846427L
1969	Nineteenth	AD860812L
1970	Twentieth	AD875973L
1971	Twenty-First	AD888641L
1972	Twenty-Second	AD904360L
1973	Twenty-Third	AD914238L

Antenna Applications Symposium

		RADC TR#	ADA#
1977	First	None	955413
1978	Second	None	955416
1979	Third		077167
1980	Fourth		205907
1981	Fifth		205816
1982	Sixth		129356
1983	Seventh		142003; 142754
1984	Eighth	85-14	153257; 153258
1985	Ninth	85-242	166754; 165535
1986	Tenth	87-10	181537; 181536
1987	Eleventh	88-160	206705; 206704
1988	Twelfth	89-121	213815; 211396
1989	Thirteenth	90-42	226022; 226021
1990	Fourteenth	91-156	237056; 237057
1991	Fifteenth	92-42	253681; 253682
1992	Sixteenth	93-119	268167; 266916
1993	Seventeenth	94-20	277202; 277203
1994	Eighteenth	95-47	293258; 293259
1995	Nineteenth	96-100	309715; 309723

AIRBORNE DBS RECEIVE SYSTEM

Paul Halsema, Brian Anderson, and Jeff Frisco
Harris Corporation, Government Aerospace Systems Division
PO Box 94000
Melbourne, FL 32902

In selecting antenna systems for airborne satcom reception, a wide variety of trades need to be closely examined. Normal antenna design parameters and their associated trades are easily usurped by commercial considerations, such as life cycle cost, maintenance costs, operational costs and installation time. A DBS reception and distribution system has been developed which optimizes these trades for commercial avionics. This paper presents the architecture trades associated with the development of the antenna subsystem for this application. The impact of design options ranging from 2D electronically scanned phased arrays to simple mechanically scanned apertures are considered. The final design of the antenna subsystem, including the aerodynamic radome, waveguide aperture, and pointing and tracking electronics is discussed.

1. Introduction

This paper discusses the tradeoffs considered while developing an antenna for airborne DBS satellite reception. Much of the trade space is outside the antenna engineer's normally comfortable regime of gain, sidelobes, and beamwidth. We first provide a summary of the technical requirements and then discuss the driving non-technical requirement of life cycle cost. The advantages and disadvantages of several candidate antenna architectures are discussed in Section 4 and a summary of the design of the selected architecture is presented in Section 5.

2. Technical Requirements

There are a variety of assumptions that feed into the generation of requirements for the antenna system. In the commercial arena these assumptions are often tied back to the business strategy of the product being introduced and will result in different technical requirements for different business approaches. In this example, considerations such as ground based operation, percentage link closure, geographic coverage area (international, continental United States (CONUS), a percentage of CONUS, etc.), and aircraft flight regime (takeoff, landing, cruise, range of banking, etc.) all affect the specifications chosen and therefore the specifics of the design. Widely divergent business strategies will result in vastly different antenna systems that provide "DBS reception", however the details of when, where, and how much will also vary. For this trade, requirements were derived which provide adequate link margin when operated with a DBS satellite at cruise altitude anywhere within the continental United States. As part of these requirements special considerations were included to receive simultaneous dual polarization and continue to operate when all DBS orbital slots are filled. In addition to these technical requirements are the commercial considerations of cost (ultimately life cycle cost) and customer acceptance. The key technical requirements for the antenna system are summarized in Table 1.

Table 1. Antenna Technical Requirements.

G/T: 9.7 dBi/K
Sidelobes: 20 dB or lower at 8° to 10° from main beam and at 9° intervals
Scan Range (includes aircraft motion): 17° – 67° Elevation, 360° Azimuth
Automatically acquire and track
Operate to 35,000 ft.
Meet requirements of DO160C (environmental, structural, EMI, etc.)
Design for variety of commercial aircraft (B737 "class" and up)
Simultaneous RHCP and LHCP
Axial Ratio less than 1.5 dB

3. Life Cycle Cost Considerations

It is becoming commonplace to make system procurement and deployment decisions based on Life Cycle Cost (LCC). This is especially true in the commercial marketplace where the customer's profit is eroded by hidden costs. In many cases the organization developing the system is completely separate from the organization or company that will operate the system. Each company may have different objectives for the system (ultimately leading to an improvement in their company's profit). The entire system can effectively be evaluated from a perspective of net payback or profit. Every expense associated with the system throughout its life (that is, the life cycle cost) can be weighed against the payback anticipated from the system. While it is extremely difficult to generate a quantitative evaluation of such a set of variables, considering the system in this

manner leads to a mind set that makes the evaluation of tradeoffs and alternatives much more effective. This mind set helps to clarify the importance of various factors when developing the design.

Although there are a variety of interrelated and at times tenuous factors that affect a system's LCC, the major drivers can be grouped into the initial costs, the maintenance costs, and the ongoing operating costs. While these factors are normally considered equally important, in actual practice one or another tends to dominate the decision making process. Accurate information is seldom available for every factor, resulting in the need to make assumptions and/or extrapolations from prior experience. A simple approach of minimizing each LCC driver independently while optimizing technical performance is doomed to frustration and failure since each of these goals will tend to drive the design in different directions. A truly optimum design is achieved when adequate performance is provided while balancing the different components of the LCC to provide adequate short term and long term payback. The following paragraphs will briefly look at each of the LCC terms.

3.1 Initial Costs

This includes not only the unit production costs but also amortized development costs, investment expense, installation costs, and the costs due to lost

opportunity. Lost opportunity costs accrue when the aircraft is out of service for system installation. For most commercial airlines this is a sizable cost requiring installation time to be tightly controlled. Short term budget constraints must also be included when considering acceptable level of initial costs.

3.2 Maintenance Costs

Maintenance costs are the periodic costs required to maintain and repair the equipment as necessary. As with any cost item less is always better, however, some cost is certainly acceptable and manageable. Aircraft maintenance crews regularly inspect and maintain a variety of aircraft systems. Design attention to keep the interval reasonable (such as annual or biannual) and the required effort low (less than a few hours) allows any required maintenance effort to be simply included in the standard annual aircraft checks.

3.3 Ongoing Operating Costs

Ongoing operating costs can directly affect the long term operational viability of the system. These costs tap directly into the life blood of the operation and, if allowed to grow too large, can result in a system never entering production or once produced never being used. On the other hand, over emphasis of operational costs or considering these costs from a purely qualitative perspective (e.g., must be minimized) can lead to a distortion of the system design resulting

in explosive initial costs. For the system to be truly viable the designers must struggle to balance these various cost factors with some reasonable injection of quantitative data while considering the qualitative objectives.

The largest contributor to the operational cost of an antenna system comes from the increase in drag caused by the antenna and its mounting structure on the aircraft. This reduces the airframe's efficiency resulting in greater fuel consumption, one of the largest line items associated with operating an aircraft. The quantitative relationship between drag and fuel consumption is complex and is affected by the specific flight characteristic (attitude, wind speed, air speed, thrust, weight, etc.). Conceptually fuel consumption can be considered proportional to drag. Clearly then, the antenna's drag must be kept small — typically this leads to a requirement for the antenna's height above the airframe to be very small. It does not take long for an antenna engineer working with aircraft to become exposed to the terms “conformal” and “low profile”. Unfortunately, these terms are regularly used to refer to widely divergent implementations in an effort to convey the best possible image to all audiences. This contributes to confusion in an area already suffering from poor definition and lack of hard data.

Rather than use ambiguous terms, or set arbitrary height constraints, we should focus directly on the parameter of interest — drag. Many items need to be considered in evaluating aircraft drag in a meaningful manner. While height

above the airframe is important, it is not the only or even the predominant factor. When looked at as a fluid dynamics problem it becomes evident that the detailed shape exposed to the airstream is important. A well-designed structure (which may or may not include a radome) can have significantly less drag than a shorter, yet poorly designed, structure. Early in the development of this antenna, parametric analyses were carried out to bound the effects of different structures on drag. For the purposes of these analyses, the antenna was assumed to be covered with a radome having a continuous, smooth outer surface. Figure 1 shows a portion of the results. Over the range shown, the change in drag is roughly directly proportional to changes in radome height and diameter. While lower drag is always preferred, it can be seen from the figure that outer dimensions as large as 6" by 40" have minimal effect.

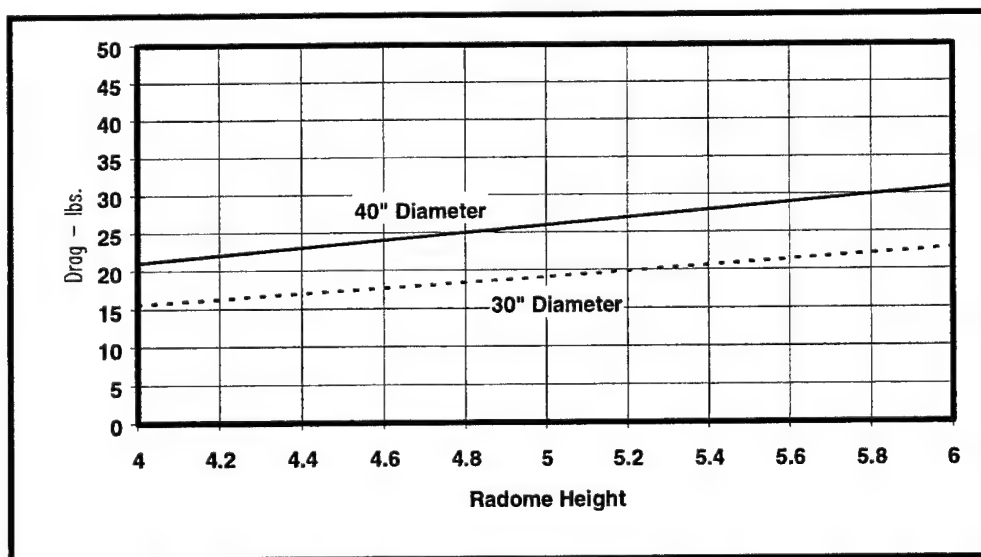


Figure 1. Added Drag as a Function of Radome Height and Diameter.

4. Assessment of antenna architecture options

Several options exist for an antenna to satisfy the requirements outlined above. To meet the G/T requirement the antenna must provide reasonably high gain. This leads to array and reflector designs. The class of array antennas can be further broken down into full two-dimensional electronically steered phased arrays, hybrid electronically and mechanically steered phased arrays, and mechanically steered fixed-beam arrays. Let us begin by assuming that each antenna option is designed to meet the above requirements as closely as possible. Certainly there still will be performance differences to be considered, but in truth the greatest differences fall outside the antenna engineer's design space. These non-electromagnetic considerations ultimately drive the selection of the antenna architecture.

4.1 Two Dimensional Electronically Scanned Array

A two-dimensional electronically scanned phased array (2D-ESA) offers the lowest profile aperture and could be designed to be truly conformal to the aircraft's skin. A truly conformal design would have excessive installation costs for this application. A non-conformal, but still low profile, design would require at least 3500 radiating elements and would be about three feet wide by four feet long. The antenna would extend about 2" above the aircraft at the center line. To maintain the low profile, the top surface of the antenna would include an integral

flat plate radome. Fairings along the periphery provide a smooth transition to the airframe.

4.1.1 Advantages

The 2D-ESA is capable of high beam slew rates that can allow it to maintain satellite track under a wide variety of aircraft dynamics. Additionally, from a maintenance cost perspective, the absence of moving parts increases reliability and essentially eliminates the risk of mechanical failure. This can result in the lowest maintenance antenna design. Some design care must be taken to ensure that the large number of active components and interconnects does not adversely effect overall reliability. Since the array is sized to meet the requirements over its entire scan range, it will provide excess G/T everywhere but at maximum scan. This increase in G/T (as much as 5–6 dB) increases the system's robustness and provides additional fade margin for operation on the ground.

4.1.2 Disadvantages

The benefits of a phased array antenna are dramatically offset by its initial cost. The cost of this approach is at least an order of magnitude greater than other choices with equivalent performance. This is true even when using extremely optimistic estimates for unit production costs. This large price differential stems from the electronics required to electrically steer a beam in two dimensions;

effectively this translates to an amplifier and phase shifter behind each of the 3500 radiating elements. In practice the improvements in reliability and drag for the commercial aviation market has only marginal value. This is best seen by comparing the antenna choices for INMARSAT. This mature market has shown that the conformal approaches have similar market share even when demanding only a marginal increase in price.

Another concern is the relationship between the array's performance and the maximum scan angle. Figure 2 dramatically demonstrates the reduction in G/T due to scan loss as measured on a similar array. This is compensated for in the array design by increasing the number of elements an amount equal to the expected loss at the scan limit. It can be seen from this figure that scans beyond

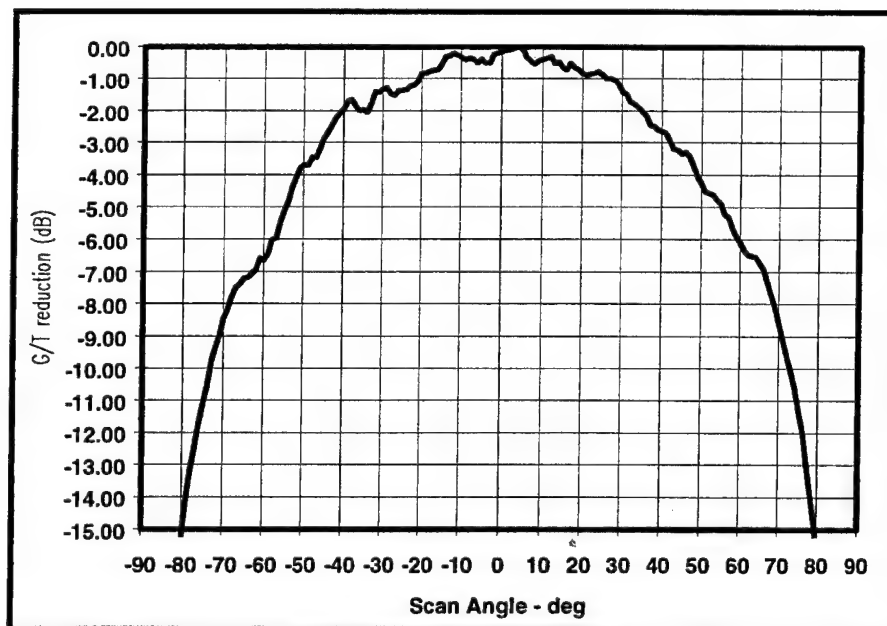


Figure 2. Measured Reduction in Array G/T Due to Scan Loss.

60° incur a large penalty, while more than 70° requires a prohibitive number of elements. As the scan loss increases so does the polarization mismatch. A very high quality, state of the art array design might achieve 3 - 4 dB axial ratio at 60°. Again this degrades rapidly with increased scan. These effects translate into design risk and an increase in development costs. With the large number of elements the designer wants to stay as high up the scan loss curve as possible while still ensuring system operation. The scan effects of this design also put firm limits on the range of satellite and aircraft geometries that can be accommodated. While this may be appropriate for some business strategies (e.g., southern US coverage only), it could be a severe constraint for others (e.g., any strategy that includes Maine or any satellite not located close to the center of CONUS).

4.2 Hybrid Mechanically/Electronically Scanned Array

A hybrid mechanically/electronically scanned array, often referred to as a 1D-ESA, can take advantage of some of the features of the 2D-ESA while mitigating the large cost impact. This antenna system, as the name implies, combines electronic beam steering in one dimension (elevation) with mechanical steering in another (azimuth). This can be thought of as a one dimensional phased array mounted on an azimuth turntable. This reduces the number of control elements (amplifiers and phase shifters) by the square root of the number required for the 2D-ESA. Sizing estimates put this array at 35" diameter and 3" high. The

azimuth mechanism is located at the edges of the array where the curvature of the fuselage results in additional packaging volume.

4.2.1 Advantages

The large reduction in control elements results in a roughly proportional reduction in initial cost for the antenna. This is the major benefit of the 1D-ESA and the primary reason for considering it an option. In addition, the overall array design and packaging are significantly simpler providing a further cost savings.

4.2.2 Disadvantages

The 1D-ESA suffers from the same disadvantages as the 2D-ESA except for the initial cost. Again, these issues translate into development cost and risk. In addition to these disadvantages, the 1D-ESA has some additional maintenance and operating costs. The maintenance costs are due to the moving mechanisms which are subject to normal wear. This results in a need for periodic inspections and possibly scheduled maintenance actions. As discussed above, this consideration is not as dramatic as it may seem. Aircraft have extremely reliable mechanical linkages on many of the control systems with periodic inspections and maintenance requirements. The use of proven avionics mechanisms with inspections scheduled such that they coincide with other aircraft inspections translates this from a concern into a normal operating procedure. A final

disadvantage is the impact on operating cost as a result of the increased height and therefore increased drag of this design. As seen earlier, however, this change (1" to 3" height) is so small that it is negligible.

4.3 Mechanically Steered Array

One step further along the trade circle is the fully mechanically steered fixed-beam array. This antenna consists of a planar array mounted on an elevation over azimuth pedestal. While a square or circular aperture design would have a significant height above the fuselage (about 13 inches), a rectangular aperture will minimize that effect. A rectangular aperture of about 5" in the elevation plane by 32" in the azimuth plane provides the required performance while minimizing height. Total height above the fuselage is about 6", including an aerodynamically shaped radome.

4.3.1 Advantages

The overwhelming advantage to this approach is the low initial cost. By eliminating the need for a large number of expensive modules to phase shift and amplify the signals, a major portion of the hardware cost is eliminated. Only a few amplifiers are required to buffer the loss of the combining network. This results in a cost that is at least an order of magnitude less than the 2D-ESA and perhaps a factor of 3 less than the 1D-ESA. The aperture is also physically much

smaller than either of the electronically scanned designs since the mechanically steered array has no scan loss effects to compensate for. In general, the array design and packaging is much simpler than the other options, but careful attention must be paid to minimizing losses in front of the low noise amplifier.

4.3.2 Disadvantages

Although the initial hardware cost is low and the design is less complex than the full phased array approach, there are some drawbacks to this particular approach. The largest perceived drawback is the total height of the antenna system. However, as discussed above an appropriate radome design allows the drag impact to be minimized for a given height. This is not meant to say that any arbitrary height is acceptable. Drag increases non-linearly with antenna height. The effects of the boundary layer, fuselage diameter, and even the area available for radome shaping all become increasingly dominant as the height is increased. There are other aerodynamic concerns as well, such as slip stream and air flow over the control surfaces that must be taken into account. Referring to Figure 1 we can see that a 6" design only has 20 to 30 pounds of drag.

The mechanically steered array will incur additional maintenance costs, just as was the case with the 1D-ESA. The drive mechanisms for this antenna are somewhat simpler than the 1D-ESA since they can be located just behind the

aperture. Again, using reliable avionics design approaches with inspections synchronized with other aircraft maintenance actions keeps this cost low.

4.4 Reflector

The simplest antenna for this application from an antenna designer's perspective is a reflector or dish antenna. Commonly these antennas are used in ground-based communications and have become familiar to the consumer through satellite TV and DBS TV services. A traditional design approach would require a dish diameter of at least 15". At this height, significant drag effects would occur. Lower profile approaches (such as a line source fed cylindrical dish) exist with added complexity. The net result of such approaches is an antenna that is more complex, higher, and has degraded beam performance (mainly sidelobe level and polarization purity) when compared to the mechanically steered array.

5. Selected Design Implementation

For our set of commercial objectives the design chosen was the mechanically steered array. This approach was deemed the best value choice when weighing the technical merits and life cycle cost of the product. The disadvantages of this approach, drag and maintenance, were mitigated by focusing on a low drag radome design and ensuring the design used avionics quality motors and mechanisms. The design consists of four main components: the aperture,

pedestal, antenna controller, and radome. Figure 3 shows the first three of these components (and the GPS antenna) which were designed and built in conjunction with EMS Technologies, Inc. (photo courtesy of EMS Technologies, Inc.).

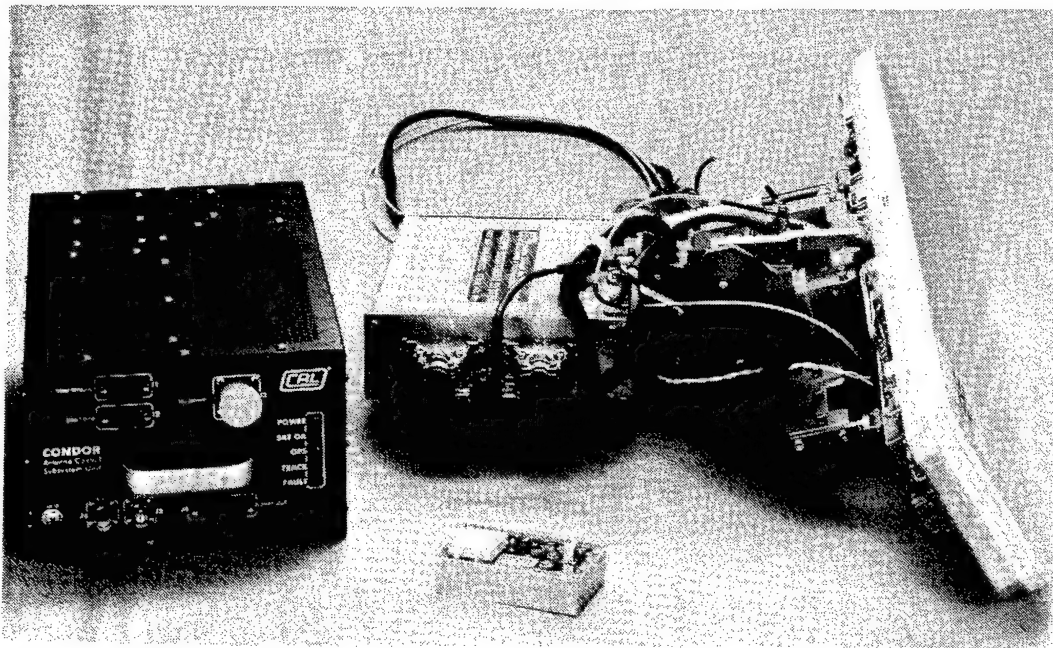


Figure 3. Operational Aperture, Pedestal, Controller, and GPS Antenna.

The antenna aperture is a dual circularly polarized design. Left and right hand received polarizations are transformed into dual linear using a 3 layer meander line polarizer. Next the signal is coupled into a dual nested waveguide combiner using waveguide slot elements. Both the row and column combiners use a resonant mode structure. Finally the signal is amplified in a Low Noise Amplifier.

The pedestal has separate mechanisms for azimuth and elevation control. The azimuth steering uses a direct drive motor centered on the azimuth pointing axis to reduce back lash and to provide high precision pointing in the axis with a

narrow beamwidth. The elevation steering is accomplished using a motor driving a drive screw mechanism.

The antenna controller provides the “smarts” necessary to autonomously acquire and track the satellite. The antenna controller uses a combination of open loop sensor based, GPS, and closed loop conical scan based signals for satellite tracking. Acquisition is accomplished primarily using GPS data with a GPS antenna and receiver as an integral part of the antenna system.

The radome shape was optimized using a Computational Fluid Dynamics model of the aircraft. Considerations included drag, lift, slip plane turbulence and the elimination of turbulence at aircraft control surfaces. The final analysis indicated 32 pounds of drag. A photograph of the flight radome is shown in Figure 4.



Figure 4. Photograph of Low Drag, Aerodynamic Radome

The electrical design of the radome was performed in a parametric fashion. Various designs were investigated and their effects on antenna performance determined. The true system effect is a little more difficult to determine, since the radome performance parameters (ohmic loss, reflective loss, and depolarization) contribute to different terms in the system link budget. Gain, system noise temperature, and cross polarization interference are all affected by the radome. To make the evaluation more straightforward, we combined the various radome effects with an equation that represented the net effect on system link margin. A representative contour plot for a C-Sandwich radome is shown in Figure 5.

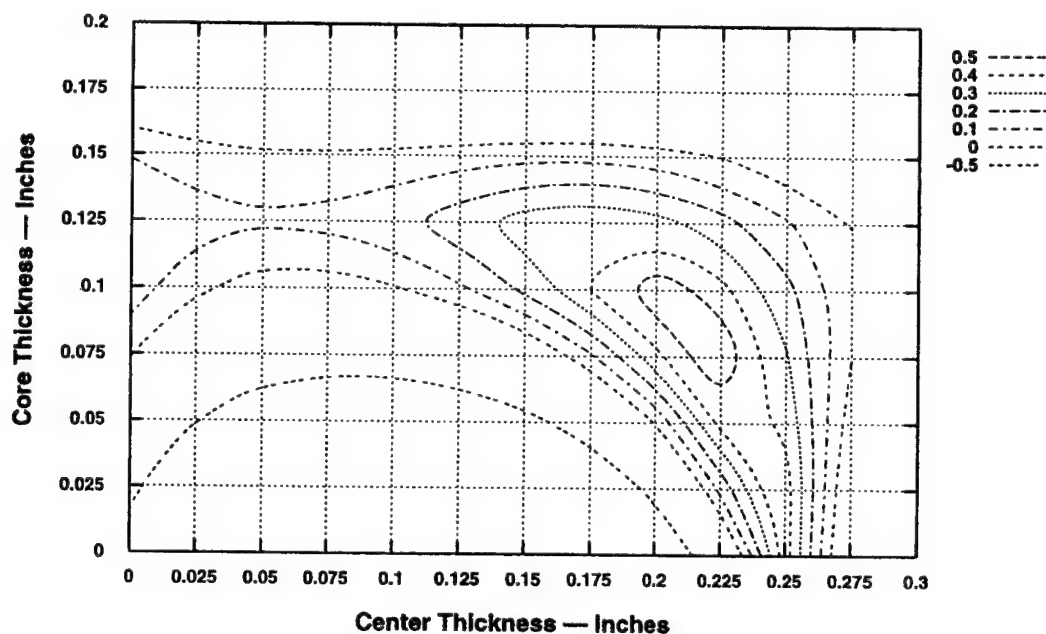


Figure 5. System Margin Contours for Various Radome Dimensions.

A COMPARISON OF WAVEGUIDE AND MULTILAYER MICROSTRIP ARRAYS FOR AIRBORNE EHF SATCOM

**Jeffrey S. Herd
Sensors Directorate
Air Force Research Laboratory
31 Grenier St.
Hanscom AFB, MA 01731-3010**

Abstract:

Future airborne SATCOM systems will require thin, low cost phased arrays. Wide angle scanning bandwidth and low axial ratio specifications present unique technology challenges. A primary cost driver is the number of GaAs MMICs, and it is therefore desirable to minimize the number of elements needed to maintain link budget over the scan volume. This paper compares two recently developed EHF array architectures, a circular waveguide array with WAIM, and a stacked patch microstrip array with balanced feeds. The G/T and EIRP for each array will be discussed, along with other factors such as cooling and packaging.

1. Introduction

Airborne EHF SATCOM systems can benefit substantially from the use of thin phased array antennas. Conformal phased array apertures offer lower aerodynamic drag and radar cross section than conventional dish antennas with protruding radomes, and have no moving parts to degrade reliability and increase maintenance costs.

The key performance requirements of airborne EHF SATCOM antenna arrays are summarized in Table 1. In particular, the need for wide angle scanning ($\pm 70^\circ$) has a significant influence on array size. A primary cost driver is the number of elements needed to maintain the link budget over the scan volume.

This paper compares two recently developed EHF array architectures; a

BANDWIDTH	20.2-21.2 GHz on Receive 43.5-45.5 GHz on Transmit
GAIN VARIATION WITH SCAN ANGLE	6 dB MAX (1.34 dB mismatch at maximum scan)
G/T (receive array). EIRP (transmit array)	+5 dB/K 46 dBw
AXIAL RATIO (RHCP)	10 dB max
SCAN COVERAGE	$\pm 70^\circ$

Table 1. Key Performance Requirements of EHF SATCOM Arrays.

circular waveguide array with WAIM, and a stacked patch microstrip array with balanced feeds. Of particular interest is the relative performance of the two element types in terms of scanning bandwidth, mismatch loss, active element pattern, and axial ratio. Additional factors such as array manufacture, packaging, and cooling will also be discussed.

2. Baseline EHF Array Architectures

Figure 1 shows an exploded view of the 20 GHz receive array developed by Boeing in the EHF Low Cost Active Phased Array (ELCAPA) Program [1]. This array has a circular waveguide aperture covered by a Wide Angle Impedance

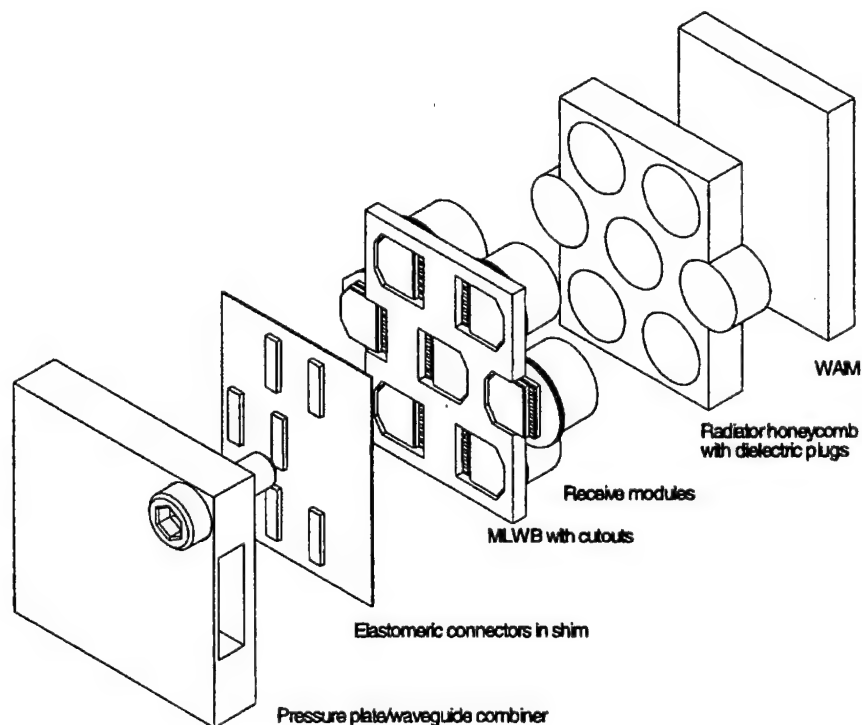


Figure 1. Boeing 20 GHz ELCAPA Receive Array Architecture [1].

Matching (WAIM) layer. The active circuitry with LNA and phase shifter resides on a multilayer wiring board (MLWB), feeding into a waveguide power combining network. The overall thickness of the array is less than 1". A similar architecture is currently under development for the 44 GHz transmit array.

The active immittances of the waveguide arrays are matched by a multilayer WAIM sheet, such that the active reflection loss is less than 1.25 dB and the axial ratio is less than 4.0 dB over the entire scan volume. An example of the scanning reflection loss of the receive array at 21.2 GHz is shown in figure 2.

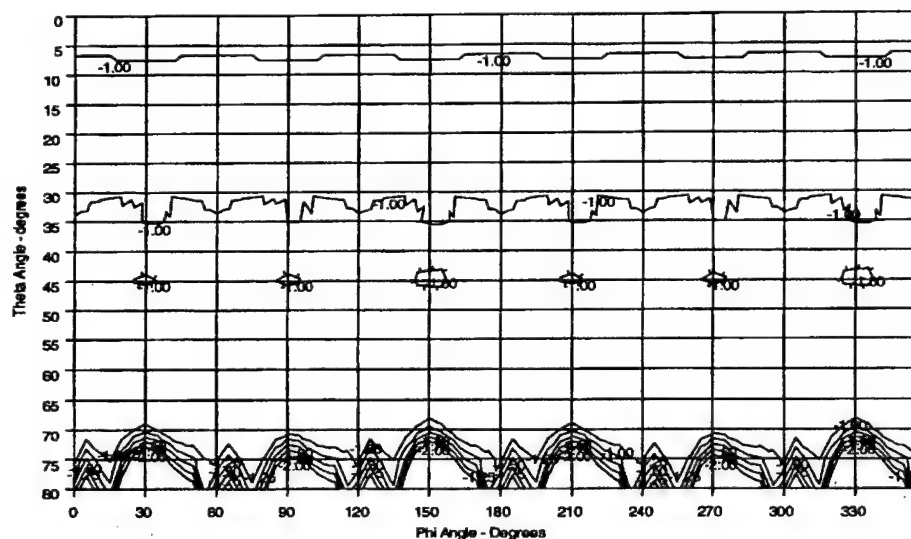


Figure 2. Calculated Infinite Array Reflection Loss of Boeing ELCAPA Array at 21.2 GHz [1].

Figure 3 shows the tile array concept used by Texas Instruments for the Advanced Low-cost PHased Array (ALPHA) Program. In this architecture, the radiating elements are stacked microstrip patch antennas. The rf power combining network, polarizing circuitry, and digital logic circuitry are integrated on a multilayer board [2]. The multilayer board is interfaced electrically to the MMIC circuits underneath via a special z-axis material [3]. The forced air cooling system is located directly beneath the MMIC quad tiles. In order to obtain the desired scanning reflection coefficient and axial ratio performance, it was necessary to use four balanced feed probes for each element. The phasing of the feed probes requires three hybrids and one delay section, and, as the polarizing network is before the LNA, the insertion loss of these components has a direct impact on the system noise temperature.

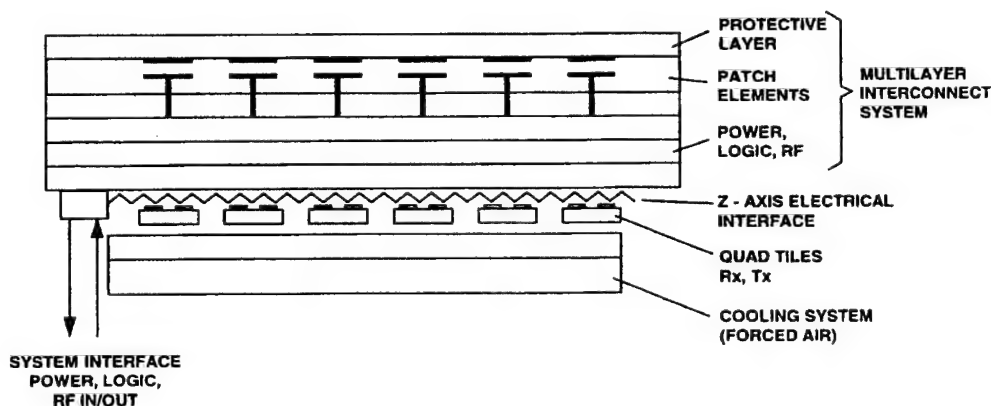


Figure 3. Texas Instruments ALPHA Tile Array Architecture [2].

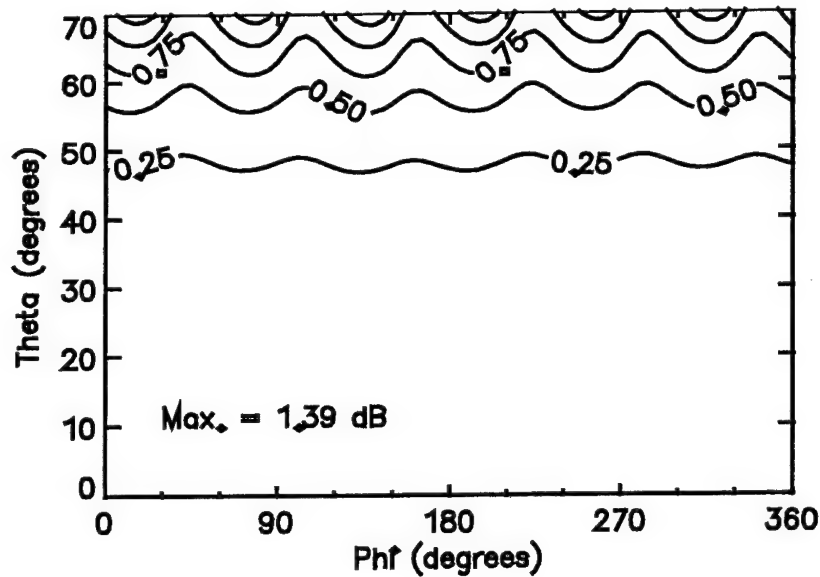


Figure 4. Calculated Scanning Mismatch Loss of TI ALPHA Receive Array at 20.7 GHz [2].

The overall thickness of the array is less than 1", with the cooling system comprising the greatest portion.

The stacked microstrip patch elements of the TI arrays were designed using an infinite array analysis code for multilayer microstrip arrays [4]. An optimizer was used to find the element and feed network geometries which meet the desired performance specifications of the arrays. An example of the calculated scanning reflection loss of the array at 20.7 GHz is shown in figure 4. The maximum mismatch loss over the scan volume is 1.39 dB. The maximum calculated value of axial ratio over the scan volume is 4.34 dB.

3. Array G/T and EIRP Calculations

The differences between the two array element types can be quantified in terms of the number of elements needed to achieve the desired gain to noise temperature ratio (G/T) for the receive array, and the effective isotropic radiated power (EIRP) for the transmit array over the scan volume and frequency range. Although there are other important metrics by which the two can be compared, this metric is an important one, since the number of elements in the array, and hence the number of GaAs MMICs, is by far the primary cost driver in active phased arrays.

FREQUENCY	21.2 GHz on receive 44.0 GHz on transmit
SCAN ANGLE	70°
ANTENNA NOISE TEMPERATURE	43.7° K
LNA NOISE FIGURE	1.5 dB
PHASE AND AMPLITUDE ERRORS	
3 BIT PHASE SHIFTER	0.37 dB
4 BIT PHASE SHIFTER	0.22 dB
FAILED ELEMENTS (6%)	0.27 dB on receive 0.54 dB on transmit
TRACKING, SQUINT, AND ANGLE ESTIMATION ERRORS	0.46 dB

Table 2. Assumptions for G/T and EIRP Calculations.

To implement the comparison, a spreadsheet analysis was developed to calculate the number of elements needed to achieve the system specifications for each array type. Standard formulas for array G/T and EIRP were applied [5]. Some of the input parameters are common to both arrays, and they are listed in Table 2. Many other scenarios are of course also possible, but it is felt that this set provides representative values for the sake of comparison. The rest of the input

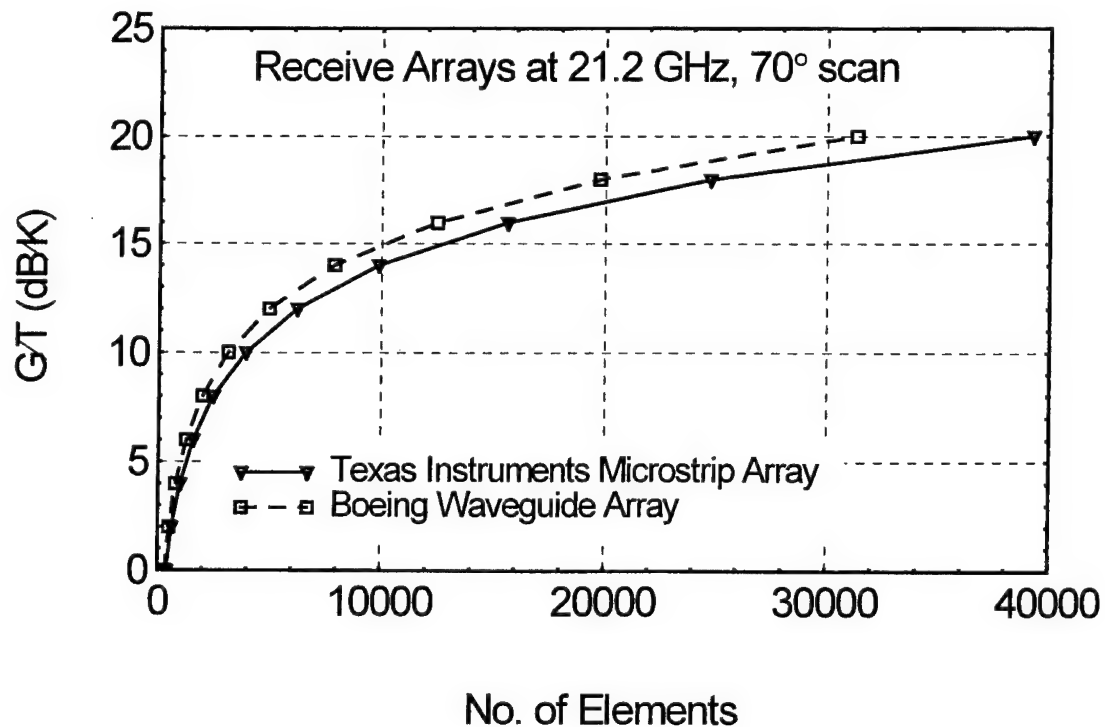


Figure 5. Calculated G/T vs. Number of Elements for Receive Arrays at 21.2 GHz, 70° scan.

parameters are unique to each array, and sample spreadsheets for the receive and transmit arrays are given in figures 7,8,9, and 10. Note that the choice of the output power of the elemental amplifiers in the transmit arrays has been left to the array designer, since this quantity is partly dictated by the amount of cooling capacity for each architecture. Results of the array sizing calculations are shown in figures 5 and 6. Figure 5 shows the calculated G/T versus number of elements for the receive arrays at 21.2 GHz and 70° scan. The Boeing waveguide array requires about 20% fewer elements. As can be seen in the sample G/T calculations in figures 7 and 8, the TI microstrip array has slightly larger impedance mismatch and axial ratio losses at the maximum scan angle. In addition, the hybrid network required for the balanced feeds introduces losses which increase the cascaded noise temperature.

Figure 6 shows the calculated EIRP versus number of elements for the transmit arrays at 44 GHz and 70 ° scan angle. Approximately 70% more elements are required by the Boeing array versus the Texas Instruments array. This factor comes directly from the difference in the output power amplifiers. The Texas Instruments array uses a 350 mW power amplifier, whereas the Boeing array uses a 100 mW power amplifier. The difference in selected power is partly dictated by the ability to cool the amplifiers. The Boeing transmit array has a waveguide power distribution network beneath the MMIC modules. The tile array

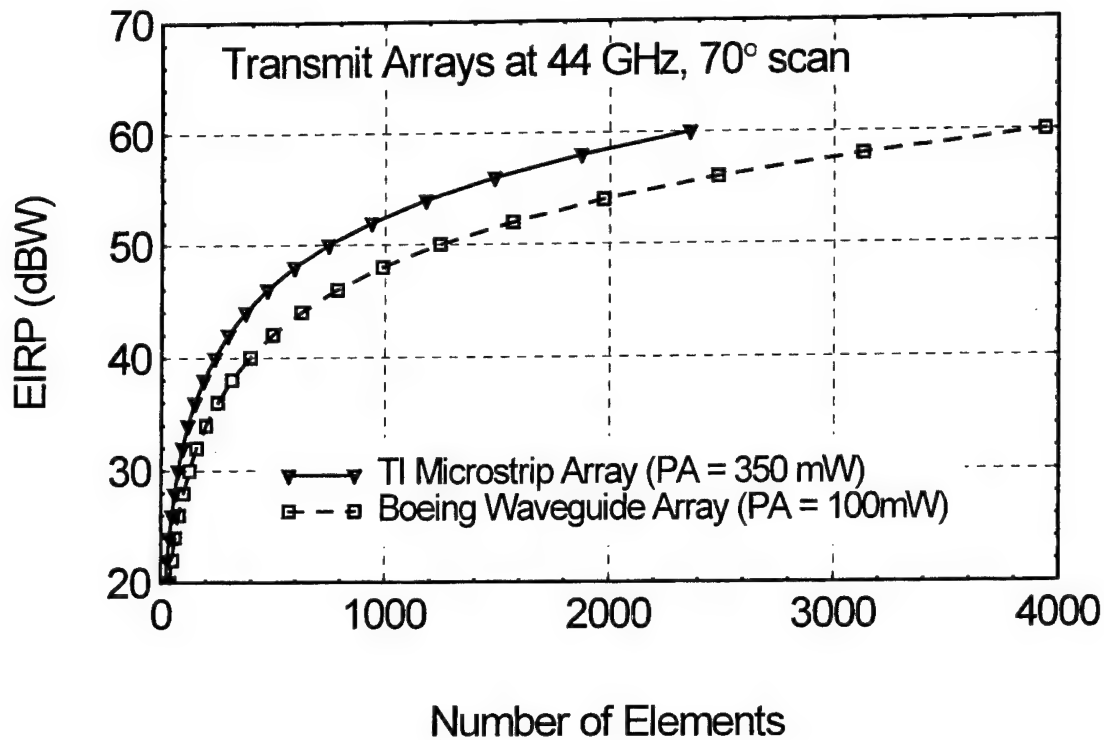


Figure 6. Calculated EIRP vs. Number of Elements for Transmit Arrays at 44 GHz, 70° scan.

architecture of the Texas Instruments array has the cooling layer directly beneath the MMIC chips, as can be seen in figure 3.

4. Summary

Two EHF SATCOM array types have been compared; a circular waveguide array with a WAIM sheet, and a stacked microstrip patch array with balanced probe feeds. Both types of arrays offer low cost, lightweight geometries

which are less than 1" in thickness. The waveguide array has slightly better scanning impedance match and axial ratio at the maximum scan angle, as can be seen in the sample G/T and EIRP spreadsheets. The stacked microstrip array requires four balanced probe feeds to achieve the wide angle scan performance, and the additional hybrid circuitry needed for the probe phasing introduces a 0.6 dB loss in front of the LNA. As a result of these factors, the stacked microstrip array is about 20% larger than the waveguide array for the same G/T.

For the transmit case, the microstrip array utilizes a higher power amplifier. The tile array architecture has a very efficient cooling scheme, whereby the MMIC power amplifiers and phase shifters are located directly adjacent to the cooling system. As a result, the waveguide transmit array is about 70% larger than the tiled microstrip array for the same EIRP.

Additional factors in the comparison of the two arrays are the manufacture, assembly, and maintenance costs of the two array types. The tiled array architecture requires no bondwires, and this will ultimately lead to higher yield, greater reliability, and lower cost. However, technology required for the design and manufacture of the multilayer rf and digital networks with vertical interconnects is still at an early stage. While the tile array technology is evolving, the waveguide array technology continues to offer a reliable and cost effective alternative which meets the current requirements of EHF SATCOM.

Acknowledgments

The author gratefully acknowledges useful discussions on this subject with Robert Mailloux and John Turtle of the Air Force Research Laboratory, with Gary Miller of Boeing Space and Defense Group, and with Kevin Ommodt and Chris Hemmi of Texas Instruments.

References

- [1] J. Freeman, "EHF Low Cost Active Phased Array (ELCAPA)", Interim Report, Air Force Contract No. F30602-95-C-0051, Boeing Defense and Space Group, April 1996.
- [2] T. Jones, "Advanced EHF Airborne Arrays", Quarterly Review, Air Force Contract No. F30602-95-C-0055, Texas Instruments, Inc., June 1997.
- [3] K. Ommodt, "Vertical Interconnects for Phased Array Packaging," IEEE AP-S Symposium Digest, pp. 1334-1337, July 1996.
- [4] J. Herd, "Full Wave Analysis of Proximity Coupled Rectangular Microstrip Antenna Arrays," Electromagnetics, pp. 21-46, January 1991.
- [5] R. Mailloux, *Phased Array Antenna Handbook*, Artech House, pp. 40-50, 1994.

Boeing G/T Spreadsheet	
Calculated by J. Herd 3/6/97	
Evaluation Frequency (GHz)	21.2
Wavelength (meters)	0.01415
Dx (meters)	0.00691
Dy (meters)	0.00797
Area (sq meters)	5.5E-05
Do Directivity of Element (linear)	3.45682
Desired G/T in dB/K	5
Desired G/T in 1/K	3.16228
Noise Temperatures (in deg. K)	
Sky Temp	43.7
WAIM Losses	3.2
Module Input Losses	21
1st LNA Noise Figure Contrib	129.7
2nd LNA/Phase Shifter Contrib	12.1
Module Output Losses	0.2
Subarray Combiner Losses	2.3
Array Combiner	4
Cascaded Noise Temp (K) Tc	216.2
Required G linear = (G/T)*Tc	683.684
System Losses	
Phase & Amp Errors (dB)	0.22
Tracking+Squint+Estimation (dB)	0.46
Element Failure (6%) (dB)	0.27
System Losses in dB	0.95
System Losses linear	1.24451
ϵ_1 Sys Efficiency	0.80353
Element Losses	
Projected Area Loss (dB)	4.66
Scanning Mismatch Loss (dB)	1.04
Polarization Mismatch Loss (dB)	0.22
Element Losses in dB	5.92
Element Losses linear	3.90841
ϵ_2 Element Efficiency	0.25586
Number of Elements $N=G/(\epsilon_1*\epsilon_2*Do)$	962

Figure 7. G/T Spreadsheet for Boeing Receive Array.

Texas Instruments G/T Spreadsheet	
Calculated by J. Herd 3/6/97	
Evaluation Frequency (GHz)	21.2
Wavelength (meters)	0.014151
Dx (meters)	0.00805
Dy (meters)	0.00699
Area (sq meters)	5.63E-05
Do Directivity of Element (linear)	3.531125
Desired G/T in dB/K	5
Desired G/T in 1/K	3.162278
Noise Temperatures (in deg. K)	
Sky Temp	43.7
Element and Hybrid Losses	42.96
1st LNA Noise Figure Contrib	137.4
Phase Shifter Losses	1.54
Combining Manifold Losses	8.66
2nd LNA Noise Figure Contrib.	0.423
Cascaded Noise Temp (K) Tc	234.683
Required G linear = (G/T)*Tc	742.1328
System Losses	
Phase & Amp Errors (dB)	0.22
Tracking+Squint+Estimation (dB)	0.46
Element Failure (6%) (dB)	0.27
System Losses in dB	0.95
System Losses linear	1.244515
ε1 Sys Efficiency	0.803526
Element Losses	
Projected Area Loss (dB)	4.66
Scanning Mismatch Loss (dB)	1.85
Polarization Mismatch Loss (dB)	0.254
Element Losses in dB	6.764
Element Losses linear	4.74679
ε2 Element Efficiency	0.210669
Number of Elements N=G/(ε1*ε2*Do)	1241

Figure 8. G/T Spreadsheet for Texas Instruments Receive Array.

Boeing EIRP Spreadsheet	
Calculated by J. Herd, 3/6/97	
Element Directivity Calculation	
Evaluation Frequency (GHz)	44
Wavelength (meters)	0.006814
Dx (meters)	0.00372
Dy (meters)	0.00322
Area (sq meters)	1.2E-05
Desired EIRP in dBW	45
Desired EIRP in Watts	31622.78
Do Directivity of element	3.242289
Element Efficiency Calculation	
Scan Loss at 70 deg. in dB	4.66
Ohmic Losses in dB	0.8
Polarization Mismatch in dB	0.22
Reflection Mismatch in dB	0.58
Array Phase and Amplitude Errors in dB (4 bit phase shifter)	0.22
Failed Elements in dB	0.54
Total efficiency Eff	0.198609
Available Element Output Power W (Pa)	0.1
Number of Elements $N = \sqrt{EIRP / (Eff * Do * Pa)}$	700

Figure 9. EIRP Spreadsheet for Boeing Transmit Array.

Texas Instruments EIRP Spreadsheet	
Calculated by J. Herd, 3/6/97	
Element Directivity Calculation	
Evaluation Frequency (GHz)	43.5
Wavelength (meters)	0.006892
Dx (meters)	0.00381
Dy (meters)	0.0033
Area (sq meters)	1.26E-05
Desired EIRP in dBW	45
Desired EIRP in Watts	31622.78
Do Directivity of element	3.326328
Element Efficiency Calculation	
Scan Loss at 70 deg. in dB	4.66
Ohmic Losses in dB	0.6
Polarization Mismatch in dB	0.254
Reflection Mismatch in dB	1.85
Array Phase and Amplitude Errors in dB	0.22
Failed Elements in dB	0.54
Total efficiency Eff	0.154028
Available Element Output Power in Watts (Pa)	0.35
Number of Elements $N = \sqrt{EIRP / (Eff * Do * Pa)}$	419

Figure 10. EIRP Spreadsheet for Texas Instruments Transmit Array.

**Antenna Applications Symposium
University of Illinois
September 17-19, 1997**

A Photonics-Steered, Wideband Phased Array for Shipboard Application

by

Dan Bobowicz, Don Collier and John Wojtowicz

**Northrop Grumman Corp.
P.O. Box 746- MS 55
Baltimore, MD 21203**

Abstract:

In a joint venture with the Naval Research Laboratory, engineers from Northrop Grumman have designed and are fabricating a wideband, time delay, phased array transmitting antenna to meet the Navy's shipboard ECM needs into the 21st Century. This Advanced Technology Demonstration antenna is now in the fabrication phase; the electrical design was completed in December, 1996. Range testing is scheduled to begin in the first quarter of 1998.

Unique features of this 2-D scanned array include time delay beam steering using a photonics feed manifold that limits frequency dispersion losses and undesirable time delay grating lobes. The utilization of a photonic feed also permits remotely locating the beam steering computer and RF transmitter anywhere on the ship, as much as two hundred meters removed from the antenna. This represents an important cost savings, because the operating environment below decks is much less severe for this equipment. By limiting the frequency dispersion, a wide instantaneous bandwidth can be achieved.

The rectangular transmit array consists of 480 radiating elements, 240 horizontally oriented, 240 vertically oriented. Each element is a stepped notch radiator design patented by Northrop Grumman, which features a stable beamwidth with good impedance match over a frequency bandwidth in excess of 1.5 octaves.

Background

The Advanced Technology Demonstration (ATD) antenna described in this paper is an active, 2D-scanned ECM array designed to provide fleet protection over a wide frequency bandwidth. It forms an integral part of a system designed and built jointly by Northrop

Grumman Corp. and the Naval Research Laboratory (NRL) in Washington, DC. Work commenced on the project in January, 1996 and will culminate in dynamic testing at the NRL's Chesapeake Bay Detachment in Maryland during the summer of 1998.

ECM Transmitter Block Diagram

As depicted in Figure 1, the ECM Transmitter is partitioned into outboard and inboard subsystems in order to install the signal formation and control section at a convenient location within the ship, while the antenna portion is mounted at an optimum site on the ship structure for proper angular coverage.

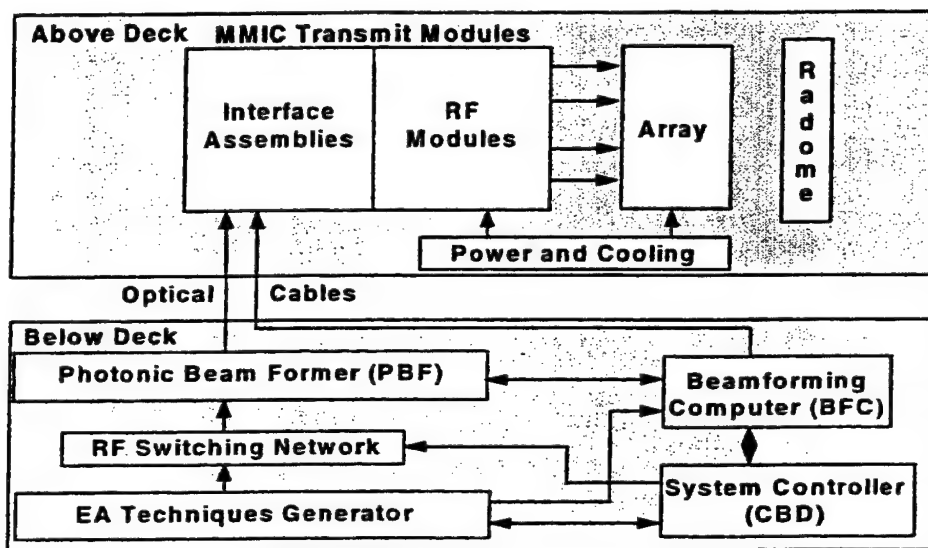


Figure 1 - ECM Transmitter Functional Block Diagram

With the exception of the Beamforming Computer (BFC), NRL engineers designed and built all the below decks equipment, and Northrop Grumman engineers designed and built all the above decks equipment. This paper describes the outboard array and subassemblies, while a companion paper presented by NRL outlines the photonics assemblies and associated subsystems located below decks.

The planar array in the outboard section of the ECM Transmitter is an active aperture design (a power amplifier and phase shifter for each radiating element) which permits a modular, platform-adaptable approach. The array consists of radio frequency (RF) photo-detectors, power amplification and phase shift modules, a planar aperture of radiating elements and a wideband radome. The inboard section is made up of a fiber-optic

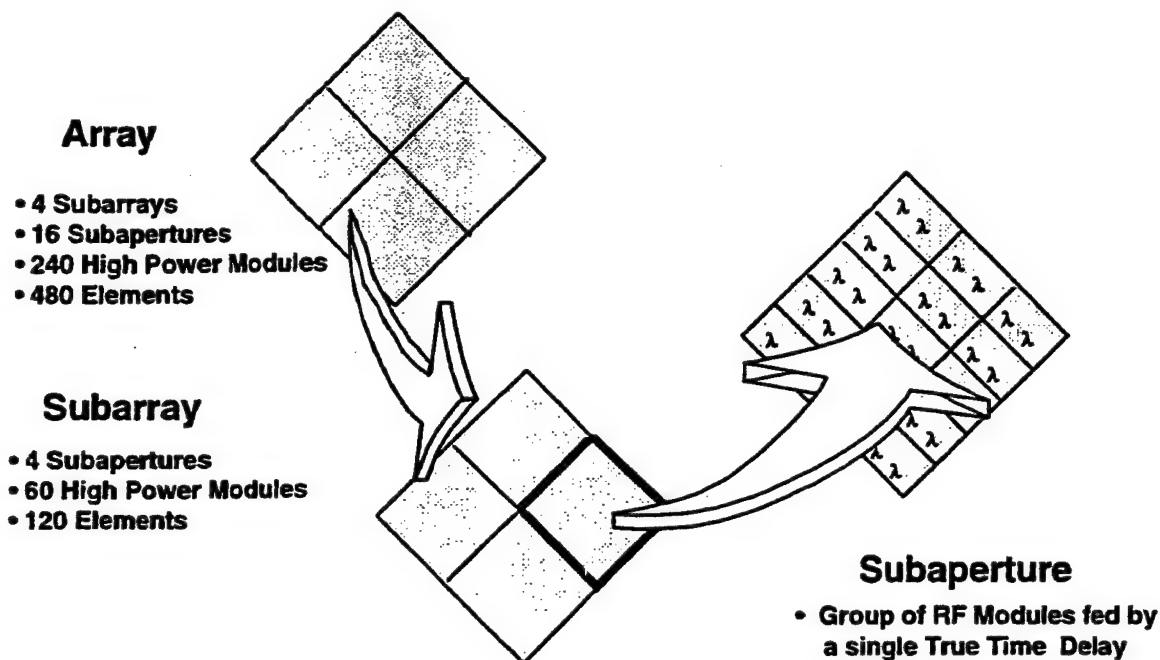


Figure 3. Array Nomenclature

The Photo Detectors recover the RF and convey it to one of 16 Interface Amplifiers, where array gain control is performed in cases where a non-uniform amplitude distribution is desired. The RF then passes through a 1-to-15 power divider manifold to the power modules, where final phase shift and amplification are performed. The active aperture planar array has sufficient radiating elements and associated Microwave Monolithic Integrated Circuit (MMIC) power amplifiers to achieve required effective radiated power (ERP). A wideband radome provides antenna protection from the environment with minimal impact on antenna performance.

Design Tradeoffs

When designing a phased array antenna, cost is a prime consideration. The array designer can achieve the required ERP (array gain times radiated power) by providing a large radiating aperture, which requires the installation of many costly radiating elements and transmit modules. A more cost-effective method is the approach adopted in the current design, i.e., optimization of a limited number of efficient wideband, state-of-the-art, high power RF amplifiers. Since such MMIC devices are currently limited to 2 to 3 Watts output power, losses in the transition from output amplifier to free space must be kept to a minimum in order to make the design practical.

The following chart in Table I lists the predicted losses in dB from the RF power amplifier to free space at three frequencies, with 60° beam scan.

	Loss in dB		
	f(low)	f(mid)	f(high)
Module Interconnect	0.10	0.10	0.10
Isolator	1.00	1.00	1.00
Isolator Line	0.44	0.66	0.84
90 Deg. Hybrid	0.13	0.24	0.20
Spreader Line	0.18	0.29	0.34
Radiator	0.30	0.30	0.84
Radome	0.50	0.60	0.20
Scan Loss	3.61	3.28	7.21
Aperture Efficiency	0.00	0.00	0.00
Power Loss	0.00	0.00	0.00
Total Loss in dB	6.26	6.47	10.77

Table I. Predicted Array Loss Budget at Maximum Scan Angle

Another cost-performance tradeoff led to the decision to minimize the number of modules by increasing the spacing between radiating elements. The wider spacing caused the formation of grating lobes under certain ship conditions at the upper end of the operating frequency band, and the consequent loss of up to 3 dB in ERP. This additional loss is reflected in the loss budgets of Table I at f(high), and also in the graph of Figure 4. During the tradeoff study, it was found that grating lobes would appear when the transmitter was tuned to the high end of the operating band *and* the ship was pitching and rolling at an extreme angle, *and* the array beam was scanned to 45° or more. Since this condition occurs less than 5% of the time, it was considered a fair trade which saved many thousands of dollars.

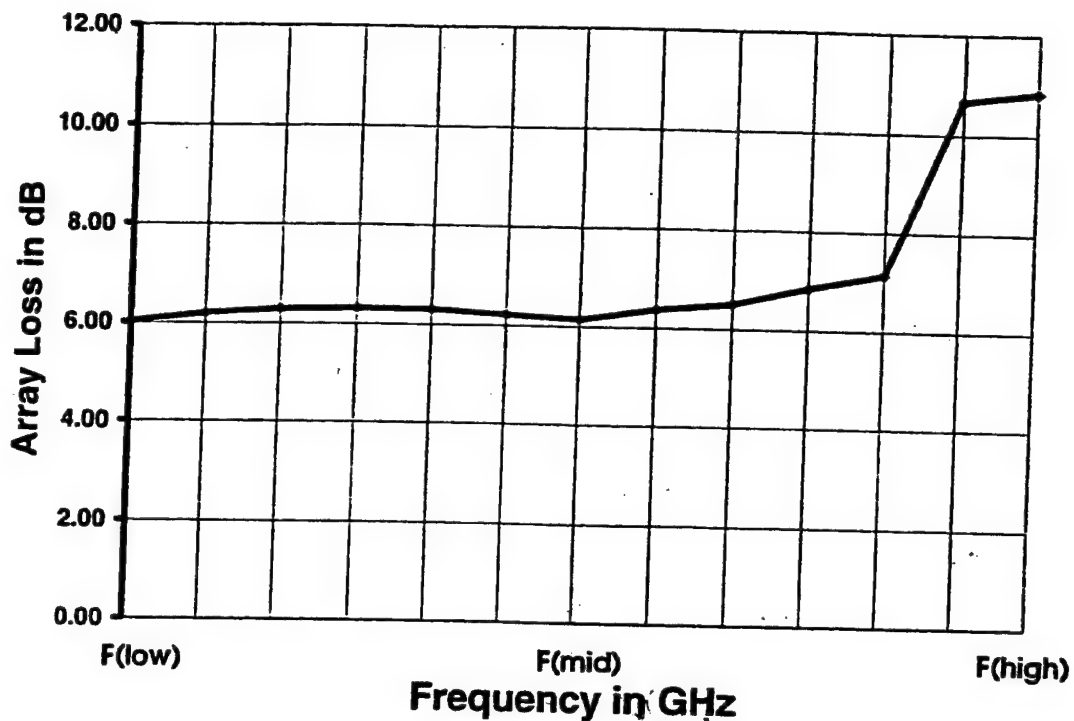


Figure 4. Predicted Array Loss Budget vs Frequency

Array Mechanical Layout

Figure 5 illustrates the mechanical layout of the transmit array.

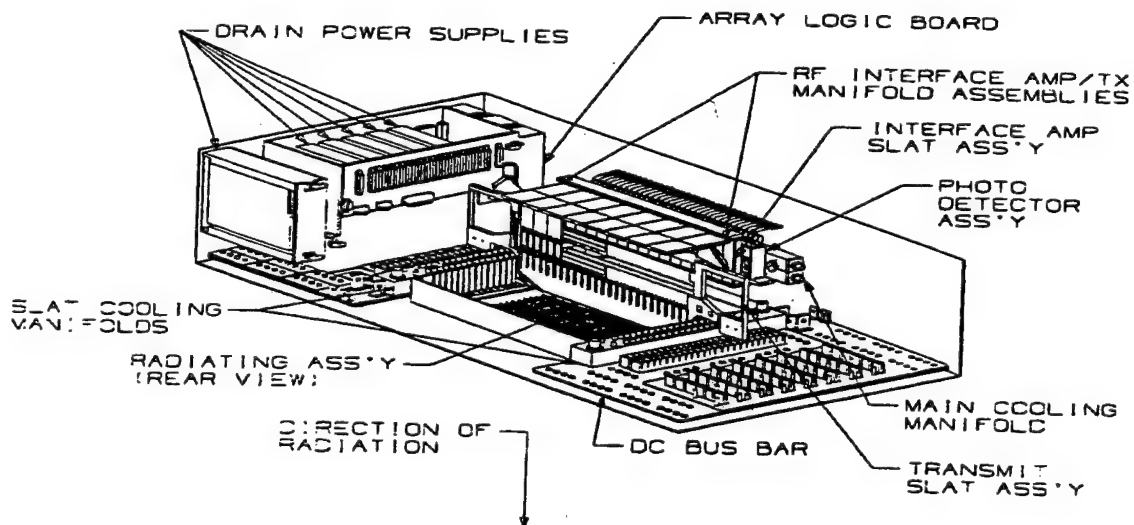


Figure 5. Array Mechanical Layout

The modular building blocks consist of the power supply assemblies, of which there are 4, the 11 cold plates or slat assemblies where the power amplifiers and phase shifters are mounted, and the 20 stripline transition boards which connect the power amplifiers to the radiating elements. Emphasis was placed on the ability of the array to survive component failures. Thus, if one or two power supplies were to go out, the array could continue to operate. Likewise, as many as 10% of the RF power modules could fail, without seriously degrading system performance. Coolant liquid, connected to the external heat exchanger unit, flows through the slat assembly cold plates underneath the RF power amplifiers and keeps the MMIC junction temperatures within prescribed limits. A single slat assembly is shown in Figure 6.

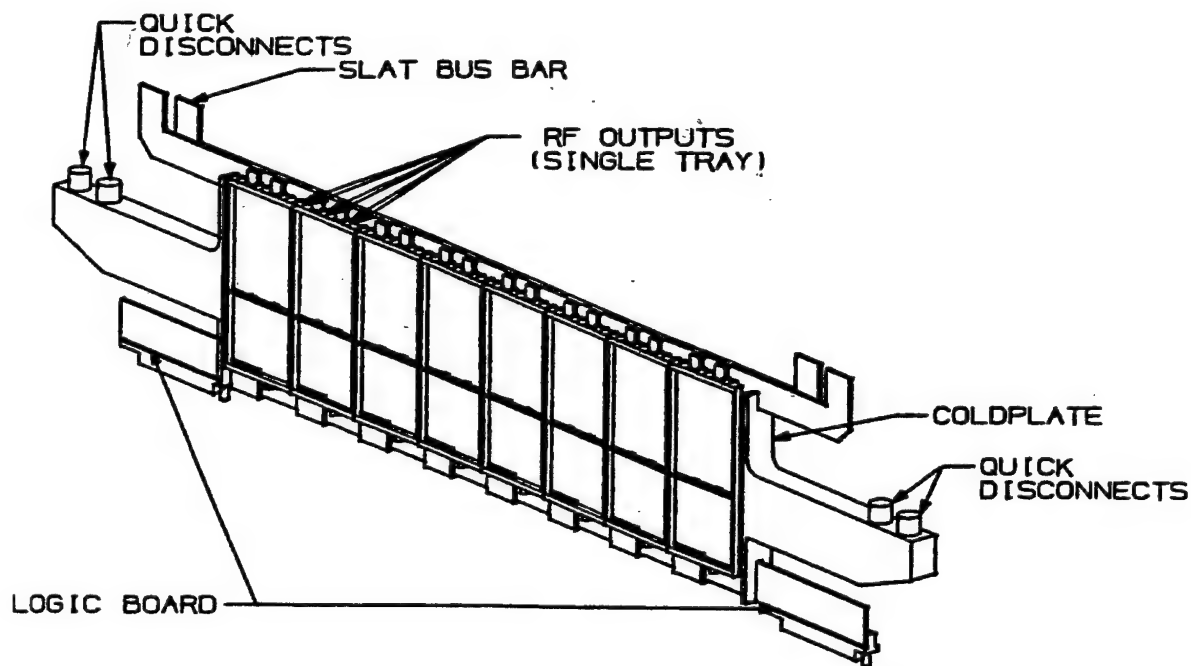


Figure 6. Slat Assembly Layout

Array Aperture

The array aperture consists of 240 pairs of wideband, stepped notch radiating elements aligned vertically and horizontally. Several radiator designs were considered, including the stripline exponential notch, but investigation by computer simulation showed that over the required frequency bandwidth, the stepped notch performed best. The limited

interelement spacing imposed by the need to minimize grating lobes at extreme scan angles was an important factor.

The notch radiators transition from coaxial push-on connectors to stripline to slot-line to free space. Impedance matching at each stage is achieved using Northrop Grumman-developed optimization routines. The stepped notch design itself is described in two Northrop Grumman patents. A drawing of a notch radiating pair, along with a Smith Chart predicting impedance performance over the frequency band is shown in Figure 7.

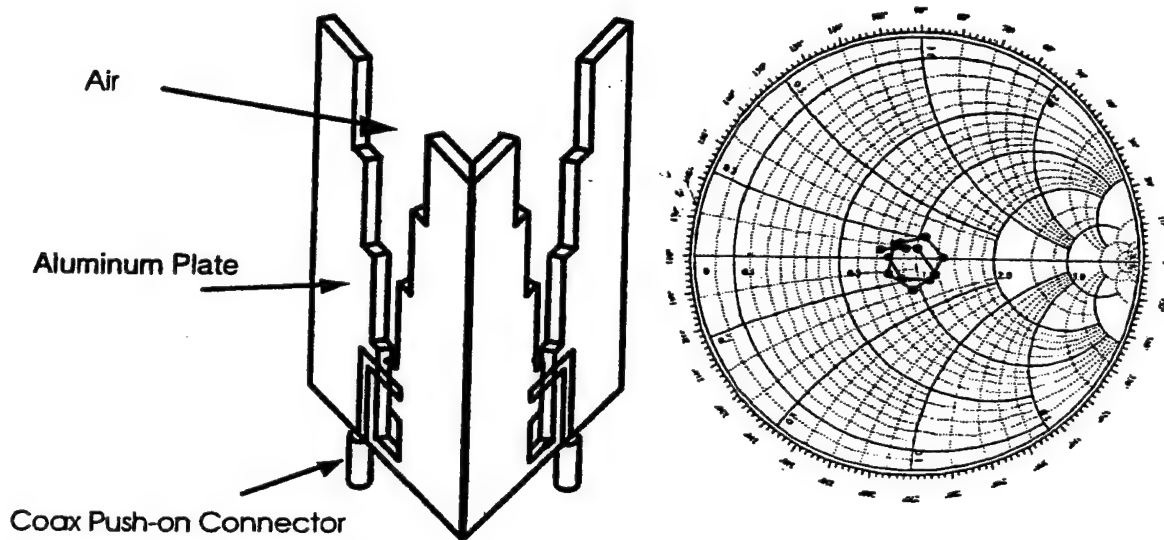


Figure 7. A Stepped Notch Radiator Pair

The transmit array will be mounted aboard ship in a diamond configuration, as shown in Figure 3. This orientation has the advantage of providing low sidelobes at the ship's horizon without sacrificing ERP, as would be the case for either a Taylor or Bayliss amplitude distribution. An unscanned and scanned azimuth pattern simulation is seen in Figure 8 .

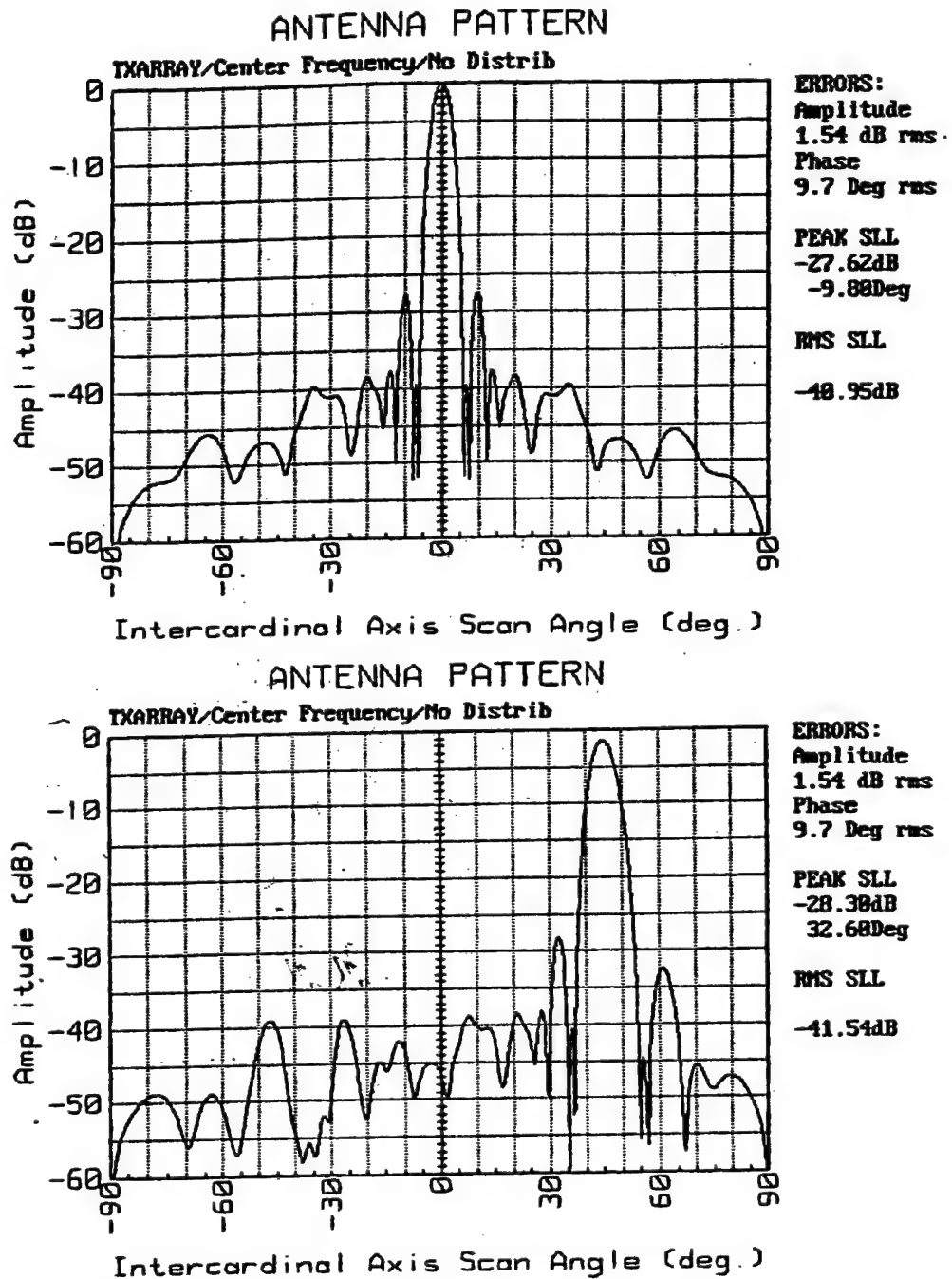


Figure 8. Unscanned and Scanned Azimuth Pattern Simulations

The absence of high sidelobes along the horizon is further illustrated in the topographical pattern prediction of Figure 9. The vertical axis is elevation and the horizontal axis is

DEVELOPMENT OF A FIBER-OPTIC BEAMFORMER NETWORK FOR TRUE TIME-DELAY CONTROL OF AN ARRAY TRANSMITTER

Michael Y. Frankel, Paul J. Matthews, and Ronald D. Esman
CODE 5672, Optical Sciences Division
Naval Research Laboratory
Washington, DC 20375-5338

Abstract: We report the development and demonstration of a fiber-optic beamformer for true time-delay steering of a two-dimensional Northrop-Grumman transmitter array. The beamformer is designed as a cost-effective method for distributing microwave signals, and for providing a true time-delay function, to antenna sub-arrays. The architecture overcomes limitations typical of photonic time-delay networks by operating from C through Ku bands, and by being stable, low-cost, and based on all commercial components. The beamformer is based on a simple optical dispersive prism delay approach, with separate azimuth and elevation control stages. The azimuth dispersive prism includes an amount of dispersion in each link proportional to the corresponding column position in the array. The microwave signals, properly time-delayed for azimuth steering, are amplified and serve as inputs to identical dispersive prisms feeding the elements in each column. The elevation dispersive prisms include an amount of dispersion in each link proportional to the corresponding row position in the array. Each time-delayed microwave signal feeds a single flared-notch element in a 4 x 4 array. Two-dimensional array pattern measurements in an anechoic chamber demonstrated independent $\pm 30^\circ$ azimuth and $\pm 30^\circ$ elevation steering. There is no observed squint over C through Ku frequencies limited by the microwave components.

1. Introduction

Phased-array antennas are finding increasing applications in modern commercial and military Radar and communication systems. The individual element control that is possible with array antennas permits the implementation of such functions

as dynamic beam steering and shaping. The distribution of microwave signals over fiber-optics is advantageous to metal waveguides in the areas of routing pliability, system size and weight, signal loss and bandwidth, and susceptibility to electro-magnetic interference. Furthermore, fiber-optic systems also make possible signal processing functions such true time-delay, which is required for precise angle steering over wide instantaneous bandwidths.

The Northrop-Grumman array transmitter requires operation of C through Ku bands with a wide instantaneous bandwidth coverage. The instantaneous bandwidth requirement necessitated a beamformer partitioning into a true time-delay portion for sub-array control, and a phase-only portion at the array element level. Considering the frequency requirements, the true time-delay portion of the beamformer could not be implemented via all-electronic techniques, and a photonic solution was deemed appropriate.

The desire for a true time-delay capability has driven the development of a variety of photonic techniques. Some of the more prominent include electronically-selected optical delay lines [1], switched optical delay lines [2, 3, 4], optimized schemes combining both optical and electronic time-delay switching [5], schemes based on optically-coherent control of arrays [6], acousto-optically based delay lines [7], fiber Bragg grating-based delay lines [8, 9], and schemes based on fiber-

optic dispersive delay lines [10, 11]. Unfortunately, most of these techniques have not progressed beyond conceptual laboratory demonstrations, as they are hampered by the demands for precisely matched optical elements, excessive power losses, instability, or specialized component development. The exceptions have been the switched delay line techniques described in [1] and [5] for MHz through 3 GHz frequency ranges, and a dispersive delay line technique developed by ourselves for under 2 to over 18 GHz frequency ranges [11].

After performing extensive trade-off analysis of the various photonic techniques in terms of development risk, implementation costs and performance, the dispersive-fiber based approach was selected as an optimal one. While meeting the performance requirements, the technique mitigates development risks and costs by relying on all commercially available components that are leveraged off the high-volume production of the telecommunications industry.

Here, we describe a prototype system that was developed and built to validate the basic concepts of the dispersive fiber based beamformer for complete two-dimensional true time-delay control of an ultrawideband transmitter array. The demonstrated beamformer exhibits an unprecedented combination of independent $\pm 30^\circ$ azimuth and $\pm 30^\circ$ elevation steering over a microwave component-limited bandwidth of 6 to 18 GHz. Thus, the technique has overcome the problems

discussed above and shows the capability to be transitioned to real-world ultrawideband array transmitters.

2. System Configuration

The dispersive fiber based beamformer is shown schematically in Fig. 1. The optical sources for both azimuth and elevation steering control are single polarization fiber-optic lasers with output wavelength tunable over a range of >50 nm around 1540 nm [12]. The beamformer functionality is described as follows. The system microwave input signal drives an electro-optic Mach-Zehnder modulator (MZM) in the azimuth control fiber-optic stage. The MZM modulates the amplified laser output and the modulated optical carrier is then fed to a 4-channel fiber-optic dispersive prism. Each channel includes dispersion-shifted (DS) and high-dispersion (HD) fiber segments to provides overall dispersion proportional to the position of a corresponding column of antenna elements within the array. Thus, the signal propagation velocity depends on the optical carrier wavelength. Tuning the wavelength of the laser (λ_{az}) changes the delay of the microwave signals demodulated by the individual link p-i-n photodiodes (PD) and produces azimuth true time-delay steering.

The microwave signals, appropriately time-delayed for azimuth control, are in amplified by a set of matched amplifiers and used as inputs to a set of nominally-identical MZMs. The optical carrier from another Iota laser is corporately distributed to the MZMs and fed to a set of nominally-identical fiber-optic dispersive prisms providing dispersion in each link proportional to the position of the corresponding row of antenna elements within the array. Thus, tuning the wavelength of the second laser (λ_{el}) imparts additional delays onto the microwave signals and effects elevation steering.

Each fiber-optic link also included a fiber-optic attenuator (FOA) for microwave frequency-independent interchannel gain equalization and a microwave trombone for small time-delay error trimming during the system calibration procedure. Furthermore, microwave isolators were used after all photodiodes to reduce the system response rf ripple due to their high output impedance.

A nominal unit length of $\mathcal{L}_{hd} = 200$ m of HD fiber from Corning ($D_{hd} \sim 88$ ps/nm·km) was used in the azimuth-controlling prism. Thus, the consecutive links had 0, 200, 400, and 600 m of HD fiber respectively. The overall link lengths were equalized with DS fiber to produce equal interlink delay at $\lambda_{az}=1540$ nm. A nominal unit length of $\mathcal{L}_{hd} = 50$ m of HD fiber was used in the four identical elevation-controlling prisms, with the overall delays equalized with DS

fiber at $\lambda_{el}=1540.5$ nm. The required precision of HD and DS fiber lengths are ~ 1 m and ~ 1 cm respectively, and does not pose a significant problem [11].

The laser wavelength detuning $\Delta\lambda$ for a desired microwave beam steering angle can be computed as

$$\Delta\lambda = \frac{d_e}{c \cdot D_{hd} \cdot l_{hd}} \cdot \sin(\Theta_o), \quad (1)$$

where d_e is the element spacing, c is the speed of light in air, and Θ_o is the required steering angle.

3. Laboratory Beamformer Characteristics

The assembled fiber-optic beamformer was calibrated and characterized in the laboratory before antenna chamber tests. First, the HD fiber dispersion was verified to be uniform along the length of the source spool to within the measurement resolution of ± 1 ps/nm•km.

Second, the four fiber-optic link responses of the azimuth prism were measured as shown in Figure 2. These were verified to be consistent with the MZM half-wave voltage (V_π) of ~ 15 V, the average PD photocurrent of ~ 0.6 mA, and the microwave losses associated with additional microwave components (bias Tee, trombone, isolator, connectors, etc.). Furthermore, ~ 39 dB gain, ~ 3 dB noise figure microwave amplifiers were incorporated into each azimuth prism fiber-

optic link to amplify the signals for the elevation stages. The amplifiers were matched to ± 1 dB in gain and $\pm 10^\circ$ in phase across the complete 6 to 18 GHz frequency band. The amplifier variation defined the interlink gain and phase tracking inaccuracies at this stage of the beamformer, and the amplifier bandwidth specifically limited the beamformer to the 6-18 GHz frequency range. The pronounced roll-off in the link gain with increasing frequency (see Fig. 2) is due to the combined effect of the MZM and PD responses. The response resonances observed at 11.5 GHz, 16 GHz, and 16.8 GHz were traced to the MZM. The MZMs used in this system were pre-production devices, and these resonances are eliminated in the improved production versions.

The noise floor at the input to the elevation stages was verified to be determined by the thermal noise at the input of the microwave amplifiers, with the contribution of laser and Er amplifier noise being negligible. The system dynamic range was limited by the saturation of the azimuth stage MZM, since all PDs and microwave amplifiers were operated well below their saturation points.

The amplitude and phase tracking of the microwave signals feeding the sixteen antenna elements were measured to validate the complete beamformer. For maximum bandwidth, the signals feeding individual antenna elements must track in both amplitude and phase across the complete 6 to 18 GHz frequency range

simultaneously. Figure 3(a) shows the amplitude tracking of the 16 microwave signals feeding the individual antenna radiating elements across the 6 to 18 GHz frequency range. Figure 3(b) shows the phase tracking of the same 16 signals normalized to one to remove the large phase slope due to the signal propagation delay through the beamformer. The observed RMS variation of ± 1 dB and $\pm 5^\circ$ at low and intermediate frequencies is due to the individual microwave component variation from link to link. The increased RMS variation of ± 2.5 dB and $\pm 10^\circ$ at high frequencies is determined by the differences among the microwave amplifiers and the MZMs used to drive each elevation prism, with these errors being common to all elements in a single column.

The array is optically steered by tuning the wavelength of the azimuth and elevation laser sources. Thus, there are additional wavelength-dependent errors that may come into play. In our system, the wavelength dependence of the characteristics of the optical fibers, MZMs and PDs was small. The dominant error factor was the wavelength dependence of the fiber-optic couplers, which were standard types specified to ± 0.3 dB coupling ratio tolerance. Figure 4 shows the measured wavelength dependence of a 10 GHz microwave signal amplitude of the four azimuth prism channels referenced to the first one. The observed wavelength dependence is less than ± 0.4 dB over the 1525 to 1548 nm range, but

increases considerably above 1550 nm. We have therefore selected a wavelength of 1540 nm for the azimuth prism and 1540.5 nm for the elevation prisms as the center wavelength to maintain high optical power while minimizing the signal wavelength dependence during optical array steering. The real array will incorporate electronic attenuators making it possible to dynamically compensate for the residual wavelength dependence during array steering.

4. Antenna Chamber Characterization

The fiber-optic beamformer was connected to an antenna array and tested in a compact radar range. A network analyzer was used to drive the system and to detect the received signal. The azimuth and elevation control lasers and the beamformer input MZM were placed in the operator control room. The remaining components of the fiber-optic beamformer were mounted inside an aluminum enclosure and were positioned immediately behind the antenna. The beamformer was controlled solely through one single-mode fiber feeding the azimuth dispersive prism and one polarization-maintaining fiber feeding the four elevation dispersive prisms.

The 8 x 32 array antenna elements were flared-notch elements suitable for operation over the 6 to 18 GHz band, and were arranged on a rectangular grid

[13]. The 4 x 4 actively-driven elements were separated by 3.7 cm in azimuth and 0.93 cm in elevation. The passive elements were terminated into 50 Ω .

The microwave insertion loss of the elevation fiber-optic stage was sufficiently high such that the microwave signal leakage from the amplifiers feeding the elevation MZMs was picked up by the receiver. This background radiation introduced a ripple on the antenna patterns and corrupted the measurement of the pattern nulls. Fortunately, this background radiation preceded the signal in time by the propagation delay through the elevation stage. Therefore, we used the network analyzer time windowing facility to numerically remove this signal component from the measurements. An improved system design would increase amplifier shielding and add microwave amplifiers to feed the radiating elements.

Figure 5 shows an intensity plot and the cardinal azimuth and elevation axis cuts for the single element patterns at 12.2 GHz. The element patterns indicate how well the array is expected to perform over a wide range of steering angles and frequencies. The element patterns at lower frequencies were fairly well behaved over the complete covered range of angles. However, deep nulls (>15 dB) in the element patterns are observed at the four corners along intercardinal cuts for the tested array. The angular position of the nulls converged to broadside with

increasing frequency. An different array design that does not have this problem is being explored for the final system implementation.

Figure 6 shows the array pattern intensity plots as a function of mechanical angle and frequency with the laser wavelengths adjusted for broadside microwave beam radiation ($\lambda_{az}=1540$ nm, $\lambda_{el}=1540.5$ nm). The measured array patterns were normalized by a measured single-element pattern. The elevation patterns were measured point-by-point with a fairly large 15° angle increment to keep the measurement time within a reasonable range. Still, they show the expected broad main lobe, which narrows with increasing frequency but stays steered to broadside. The position of the main lobe is shifted to $+5^\circ$ in elevation due to a mechanical boresight misalignment.

The azimuth pattern shows the expected performance with the main lobe steered to broadside and narrowing with increasing frequency. The narrow main lobe and the observed grating lobes are due to the chosen large separation between the actively fed element columns.

Broadband squint-free array steering is demonstrated by detuning the laser wavelengths from the nominal center wavelength to $\lambda_{az}=1536.4$ nm, $\lambda_{el}=1536.9$ nm, without any other adjustments. From (1), the array is expected to be steered to -30° in azimuth and -30° in elevation. Figure 7 shows the measured array

pattern intensity plots normalized by a single-element pattern as a function of mechanical angle and frequency. The elevation pattern is not well defined due to its large measurement angle increment. However, a broad main lobe can be observed at -25° in elevation, with position being frequency independent within measurement resolution. Again, the main lobe is shifted from the expected angle by $+5^\circ$ due to the boresight misalignment.

The azimuth pattern angular resolution is much better and clearly shows the main beam lobe steered to -30° . Its position is observed to be independent of frequency within the measurement resolution, as expected for true time-delay steering. The grating lobes and two sidelobes are also clearly seen, and show the expected frequency-dependent behavior.

Measurements at other azimuth and elevation steering angles are consistent with the results expected for a wideband array transmitter with independent azimuth and elevation time-delay steering over 6-18 GHz.

5. Conclusions

We developed a novel fiber-optic true time-delay beamforming technique for broadband steering of two-dimensional array antennas. The technique is based on

simple dispersive prism optical delay lines, with cascaded prism stages for independent azimuth and elevation steering control. The fiber-optic beamformer was extensively characterized for microwave signal losses, dynamic range, and signal amplitude and phase tracking errors. The performance was consistent with theoretical calculations based on the individual system component characteristics. The fiber-optic beamformer was then used to drive a 4x4 flared-notch transmitter array, and antenna patterns were measured in an anechoic chamber. The measurements show squint-free array steering across a $\pm 30^\circ$ azimuth and $\pm 30^\circ$ elevation range over a 6 to 18 GHz frequency range. We believe this to be a first-ever demonstration of such wideband array steering capabilities in two dimensions.

6. Acknowledgment

We would like to thank M. Parent and J. Valenzi for help with array pattern measurements and Office of Naval Research for financial support.

REFERENCES:

- [1] J.J. Lee, R.Y. Loo, S. Livingston, V.I. Jones, J.B. Lewis, H.W. Yen, G.L. Tangonan, and M. Wechsberg, "Photonic wideband array antennas," IEEE Trans. Ant. Prop., vol. 43, pp. 966-982, Sept. 1995.

- [2] E. Ackerman, S. Wanuga, D. Kasemset, W. Minford, N. Thorsten, and J. Watson, "Integrated 6-bit photonic true-time-delay unit for lightweight 3-6 Ghz Radar beamformer," 1992 IEEE MTT-S Digest, pp. 681-684, 1992.
- [3] N.A. Riza and N. Madamopoulos, "High signal-to-noise ratio birefringence-compensated optical delay line based on a noise-reduction scheme," *Opt. Lett.*, vol. 20, pp. 2351-2353, Nov. 1995.
- [4] L. Pang, J. Leonard, T.-H. Lin, G.A. Magel, S. Eshelman, "Silica-based optical delay lines and switches for phased array radar control," *Proc. SPIE*, vol. 2489, pp. 65-71, 1995.
- [5] A. Goutzoulis, K. Davies, J. Zomp, P. Hrycak, and A. Johnson, "A hardware-compressive fiber-optic true time delay steering system for phased-array antennas," *Micr. J.*, pp. 126-140, Sept. 1994.
- [6] L. Xu, R. Taylor, S.R. Forrest, "The use of optically coherent detection techniques for true-time delay phased array and systems," *J. Lightwave Techn.*, vol. 13, pp. 1663-1678, Aug. 1995.
- [7] E.N. Toughlian, H. Zmuda, and P. Kornreich, "A deformable mirror-based optical beamforming system for phased array antennas," *IEEE Photon. Techn. Lett.*, vol. 2, pp. 444-446, June 1990.
- [8] G.A. Ball, W.H. Glenn, and W.W. Morey, "Programmable fiber optic delay line," *IEEE Photon. Techn. Lett.*, vol. 6, pp. 741-743, June 1994.
- [9] J.E. Roman, M.Y. Frankel, P.J. Matthews, and R.D. Esman, "Time-steered array with a chirped grating beamformer," *Electron. Lett.*, **33**, 652-653, Apr. 1997.
- [10] S.T. Johns, D.A. Norton, C.W. Keefer, R. Erdmann, and R.A. Soref, "Variable time delay of microwave signals using high dispersion fiber," *Electron. Lett.*, vol. 29, pp. 555-556, March 1993.
- [11] M.Y. Frankel and R.D. Esman, "True time-delay fiber-optic control of an ultrawideband array transmitter/receiver with multibeam capability," *IEEE Trans. Microwave Theory Techn.*, vol. 43, pp. 2387-2394, Sept. 1995.

[12] D.G. Cooper, J.L. Dexter, and R.D. Esman, "Widely tunable polarization-stable fiber lasers," IEEE J. Selected Top. Quant. Electron., vol. 1, pp. 14-21, Apr. 1995.

[13] Hughes Ground Systems Group, El Segundo, CA.

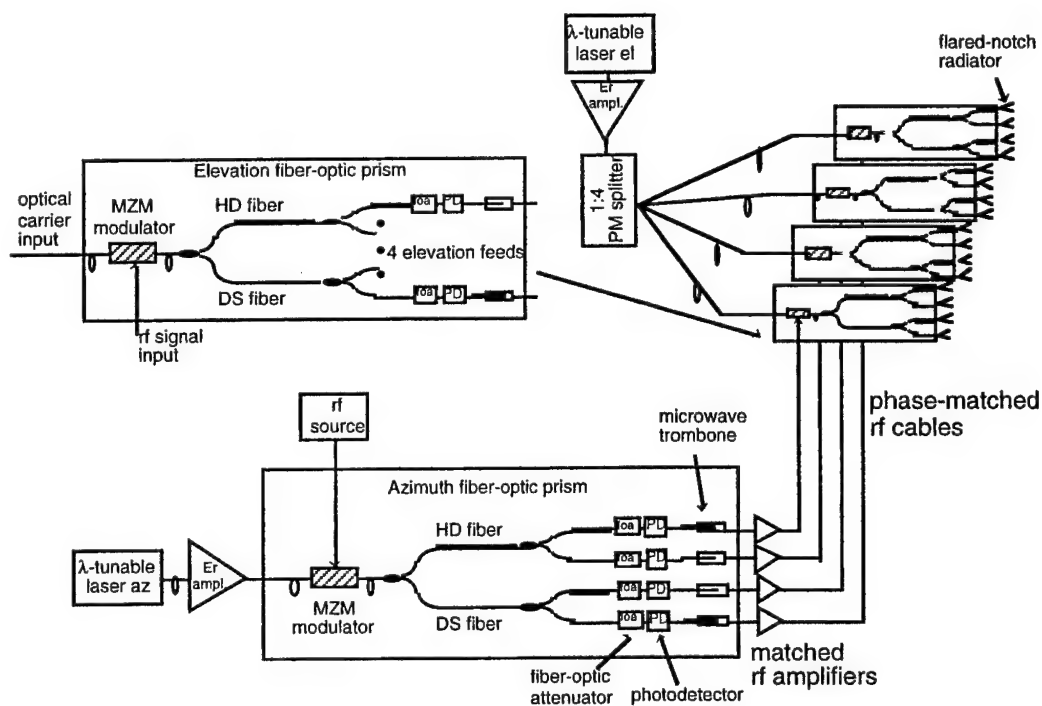


Figure 1. Dispersive fiber based beamformer schematic diagram.

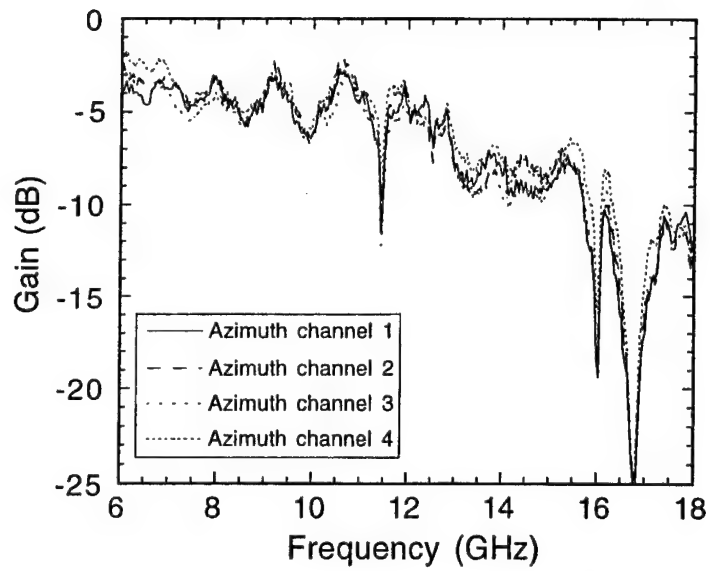


Figure 2. Azimuth channel gain response and tracking characteristics.

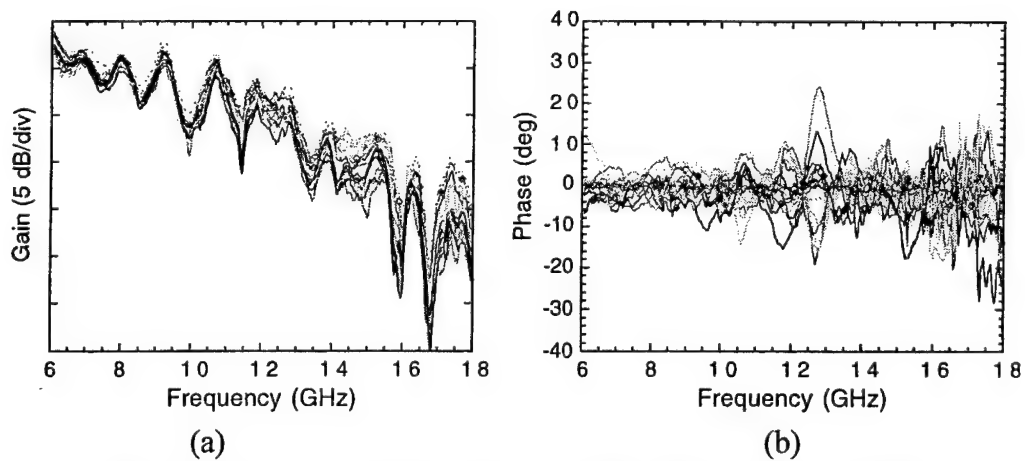


Figure 3. Beamformer output signal tracking (a) gain, (b) phase.

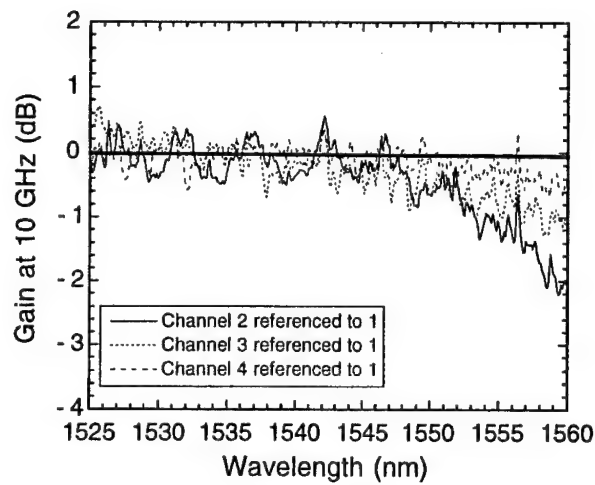


Figure 4. Amplitude response of the azimuth channels at 10 GHz as a function of wavelength.

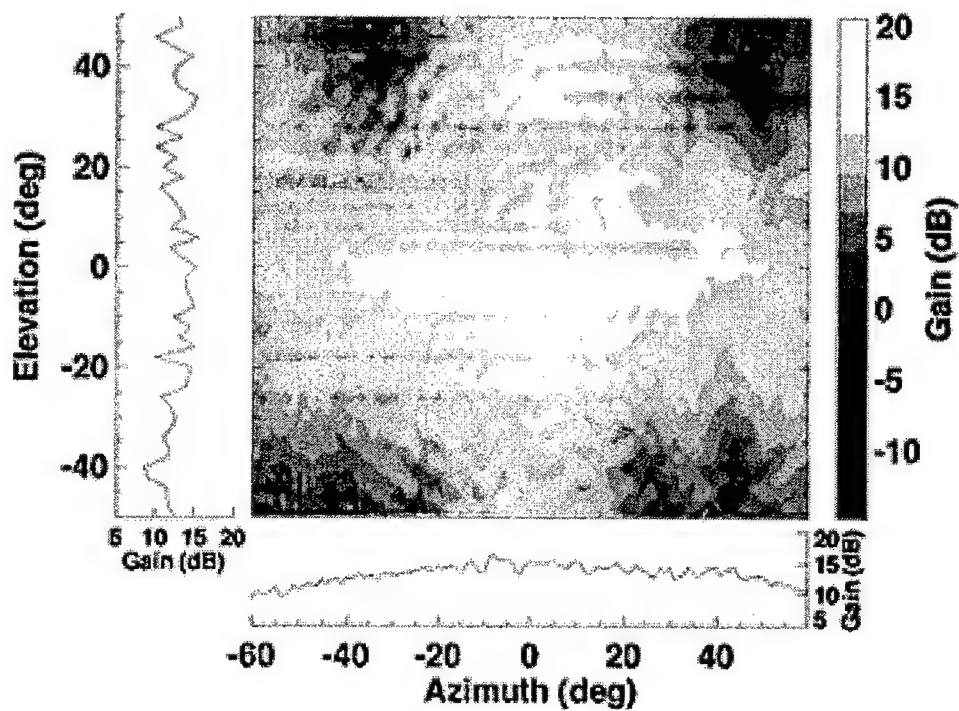


Figure 5. Intensity plot of a single element pattern at 12.2 GHz, including cardinal plane cuts.

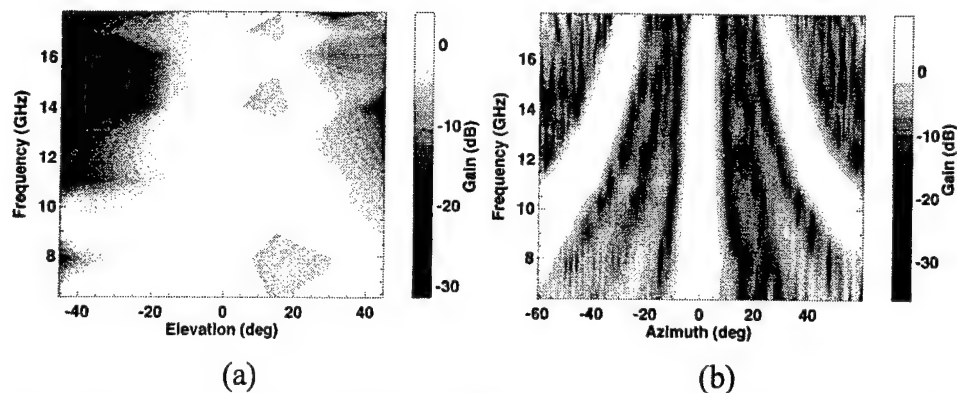


Figure 6. Intensity plots of array patterns as a function of frequency and mechanical angle for beam optically steered to broadside (a) azimuth angles, (b) elevation angles

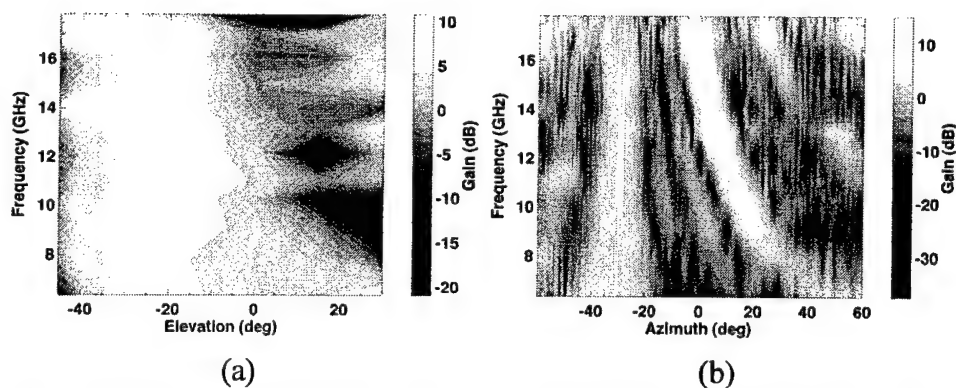


Figure 7. Intensity plots of array patterns as a function of frequency and mechanical angle for beam optically steered to -30° azimuth and -30° elevation (a) azimuth angles, (b) elevation angles

LIGHT-WEIGHT, EFFICIENT, HIGH-GAIN PHASED ARRAY

Victor K. Tripp
Glenn D. Hopkins
Archer E. Nelson
William P. Cooke

Sensors and Electromagnetic Applications Laboratory
Georgia Tech Research Institute
7220 Richardson Rd.
Smyrna, Georgia 30080

Abstract: A novel design is presented for a phased-array radar of 10,000 square wavelengths that radiates 2 KW at X-Band and scans in two dimensions. The primary specification constraints are that the weight must be less than 1,500 lbs. and that it must consume less than 15 KW of prime power. A space-fed lens architecture was chosen with diode branch-line phase-shifters. Two novel aspects of the design are that the shifter resolution is only 2 bits and grating lobes are allowed in the elevation principal plane.

1.0 INTRODUCTION

The most common constraints on antenna design normally are size and cost. For the design effort discussed in this paper, the size is not an issue at all, and the cost is secondary to weight and efficiency. The required antenna is a high-performance fire-control radar antenna to be carried by an aerostat. The Georgia Tech Research Institute (GTRI) is presently performing a two-part conceptual design and feasibility demonstration for the Antenna Technology Branch of Rome Laboratory in conjunction with DARPA and US Army Missile Command. The objective of the first phase was to determine the feasibility of such a lightweight phased-array antenna (LAPA) by demonstrating the critical technology areas and their sensitivity to weight and budget. The second phase will demonstrate a small subarray in sufficient detail to accurately determine the full array cost and power consumption.

The antenna architecture is a 3.2-meter circular space-fed lens array with a passive aperture and a 3-channel monopulse horn feed mounted 3.2 meters in front of the aperture center. The aperture consists of vertically oriented PC boards with edges presented to the feed. The boards are etched with flared notch antennas on both edges with 2-bit PIN diode phase shifters in between and with a 3-way combiner connecting each shifter to a triplet of notch radiators. Each such shifter and radiator triplet is one of about 14,720 array elements. A

microprocessor on each board will receive frequency and elevation and azimuth beam positions from the beam steering computer and, using its location, compute the phase shift for each of the 16 elements on its board. The transmitter will use 8 TWT amplifiers summed by waveguide combiner. Figure 1 illustrates the geometry of the antenna system.

2.0 REQUIREMENTS

The weight and power-consumption limits apply to all components of the antenna system that are airborne. The antenna is suspended from a stabilization platform, and all components below the platform are part of the antenna. It is enclosed in an opaque windscreen that nearly eliminates wind loading and temperature gradients on the antenna. Figure 2 shows a block diagram of the antenna and radar system, which identifies components that will be airborne and part of the weight and power budgets. The primary mechanical requirement is that all airborne components must weigh less than 1,500 lb.

Table 1 presents the electrical requirements of the antenna system defined in Figure 2. The size is noteworthy, 9800 square wavelengths provides nearly 50 dBi directivity which translates to over 45 dBi gain in this case. The prime power consumption is one of the primary requirements since all power must be transmitted through the tether of the aerostat. The antenna must be efficient because 2 KW of the 15 KW limit must be radiated from the aperture. The remaining 13 KW includes all the heat generated by the transmitters, the phase shifters, the power supplies, and the circuitry to operate everything, including the cooling system. A novelty of this design is that grating lobes are allowed to appear in the elevation plane, but they are not be directed toward the ground because of the potential for "hot clutter." Allowing grating lobes decreases the number of elements from about 22,000 to 14,720. The primary savings are cost and the prime power needed to operate the shifters. There is only a small reduction in weight.

3.0 ARCHITECTURE TRADEOFFS

The basic architecture selected is a space-fed lens array with passive elements containing phase shifters controlled to scan in both dimensions. Angular resolution is obtained using azimuth and elevation difference patterns generated by a 3-channel monopulse feedhorn

cluster. There are also six low-gain guard channels for sidelobe blanking and other functions, as shown in Figure 2. A series of tradeoffs are described next.

Table 1. Electrical Requirements On Broadside

Parameter	Value	Comment
Aperture Size	8 sq. m.	Very large, $9,800 \lambda^2$
Prime Power	15 KVA	Firm requirement
Avg. Radiated Power	2 KW	ERP may take precedence
Peak Radiated Power	20 KW to 10 KW	Depends on duty cycle
Duty Cycle	10% to 20%	
Dwell Mode	20 msec	Desired at average power
Operation Frequency Band	9.5 - 10.5	(10 %)
Instantaneous Bandwidth	50 MHz	(0.5%)
Electronic Scan	± 60 Az ± 7.5 El	Allows limited-scan techniques
Polarization	Vertical	Cross-pol. TBD
Sidelobes, RMS	-50 dB Az	0 dBi may take precedence
Near Sidelobe Level	-30 dB	Affects clutter rejection
Grating Lobe Level	-10 dB	At 13° (none below horizon)
Gain	45.6 dBi	
Effective Radiated Power (ERP)	80 dBW	Expected ERP
Beamwidth	$0.6 \times 0.6^\circ$	Can be elliptical up to 2:1, El to Az
Beam-Pointing Error	<0.1 mrad	
Number of targets	32	Plus missile tracking
Beam update time	80 msec ?	Steering and frequency
Auxiliary channels	6	Cover SL in scan volume

3.1 Feed Approaches

One of the first architecture decisions to be made is whether the RF feed will be constrained or unconstrained, that is, a manifold network or a space feed. In general, the space feed saves weight, cost, and RF efficiency, especially for arrays of such large numbers of elements as this one. The primary reason to use a constrained feed is to gain aperture illumination control, for instance, for high-performance sidelobe levels or row-column steering. In the present case, the primary sidelobe requirement is an RMS one, which can readily be achieved with the space-feed architecture. The gain and peak sidelobe level (SLL)

requirements are more benign. Row-column steering is not an option with a space feed (unless its bandwidth is very small) because the shifters are required to focus the beam in addition to steering it. Focusing cannot be divided into row and column functions.

A closely related decision is whether the array should reflect the space-fed signal or transmit it like a lens. The obvious advantage to the reflect array is that it is simpler because the backside can be occupied by the support structure, whereas the support of a lens must form a ring allowing radiation from both the front and back of the lens. However, the most determining factor is that the aperture stiffness of the reflect array is required to be far higher than that of the lens. Figure 3 illustrates the effect on radiation of first and second order aperture deformation for the three fundamental approaches: constrained feed, space-fed reflector, and space-fed lens. Figure 4 quantifies the difference in tolerance of aperture deformation by comparing the levels that would cause a 0.2 dB gain reduction. Clearly, the lens configuration is far more forgiving of aperture deformation and therefore would require much less weight in structural support.

3.2 Scanning Approaches

A lens array that scans in both elevation and azimuth is considered to be the baseline architecture. The lens is a "bootlace" lens, which means that the electrical distance through the lens is determined not by physical thickness, but by properly adjusted delay lines or phase shifters connecting each pair of radiators. This system allows a rather simple 3-port feed, as shown in Figure 5. However, it requires complex hardware for steering the beam. In particular, every element must be steered independently, and must, therefore, have its own phase-shifter driver. The drivers can be addressed by rows and columns if the bootlace is a time-delay type or if the bandwidth is small enough (about 1%). Otherwise, each driver will have to be separately addressable.

Clearly, it is desirable to reduce this level of complexity since higher complexity usually engenders higher cost and lower reliability. To significantly reduce the complexity of the lens, its scanning requirement must be reduced to one dimension, either azimuth or elevation. Then the other dimension of steering must be accomplished by the feed.

This separation could be accomplished by a linear scanning feed of the kind illustrated in Figure 6. Here the lens, or bootlace, may be singly curved, and must scan in azimuth only. Unfortunately, the reduction in complexity does not yield a reduction in weight for this case. The weight saving is that only one driver is needed per column, rather than per element. On the contrary, there is a net weight increase due to a larger lens array and a much larger feed system.

Another possible scheme is the multiple-beam lens approach shown in Figure 7. One could obtain nearly perfect focusing of the beam by contouring the lens surface according to the theory of Rotman [1, 2], but it is not really necessary for a scan range of only $\pm 7.5^\circ$. If the lens were shaped to have a 2:1 width to height ratio, then only about 20 feeds would be needed to fill the elevation scan range. Thus, there are fewer feeds, but each must handle at least half the total power on transmit. Furthermore, there are now 20 high-power circulators, as well as 40 copies of the receive components. The conclusion is that reduced complexity may reduce cost, but it does not reduce weight.

3.3 Element Lattice

An array architecture must be determined for optimum compatibility with the system requirements for low weight and high efficiency, along with the scan requirements for $\pm 7.5^\circ$ elevation and $\pm 60^\circ$ azimuth coverage. A straightforward phased-array design with a triangular lattice and no grating lobes would require approximately 22,000 elements. For weight and cost considerations, it would be desirable to reduce the number of elements. Due to the limited field of view (LFOV) required in elevation, it is possible to cover the scan region with a substantially fewer number of elements since grating lobes are allowed outside the scan volume.

To avoid grating lobes within the scan region, the size of the element is approximately 2.5 wavelengths in the vertical dimension and slightly larger than one-half wavelength in the horizontal dimension. However, grating lobes also cannot be tolerated below the main beam due to "hot clutter" susceptibility. Therefore, the elevation spacing can only be allowed to increase to about 1.4 wavelength, which reduces the required number of elements to less than 15,000, and further methods were sought to mitigate the lower grating lobe.

Figures 8 and 9 illustrate the grating lobe analysis in "cosine space." The region inside the unit circle is real space, and the region enclosed by dotted lines is the specified scan volume. The x's represent grating lobe positions for the present rectangular grid design. Only two grating-lobe positions fall within the visible region. The +'s are the near grating lobe positions for the triangular grid obtained by simply shifting every other column of elements by one-half of the vertical element spacing. With the main beam at broadside, all of these grating lobes are in imaginary space. The solid lines connect the broadside main beam to a scanned position or a grating lobe to its scanned position. In each case, only the movement of the grating lobe of interest is shown, though they all move on parallel paths.

The case marked with ⊗ in Figures 8 and 9 is the worst case for the rectangular grid because the grating lobe is highest relative to the main beam. The relative grating-lobe height is the worst for the triangular grid when the beam is scanned to the ⊗ position, but its azimuth position is far from the target position.

An attractive method of trading grating lobe levels for aperture performance over a specified scan volume (as well as element count) is to tilt the antenna mechanically. By tilting the antenna broadside axis upward by 22° , the lower grating lobe is moved out of real space far enough so that, even when the array is scanned to the maximum specified elevation angle in the vertical major plane, the grating lobe remains in imaginary space, shown in Figure 9. Note that the specified scan volume is now a curved sector entirely below the x-z plane. Thus the element pattern must scan downward to compensate for the upward tilt of the aperture. An estimate for the increased in worst case gain loss due to tilting the antenna is about 0.7 dB.

The combination of the triangular lattice and upward tilting was examined; however, in that case, a lower grating lobes enters real space when the beam is scanned to the upper corner of the scan region, as shown in Figure 9. Thus, mechanically tilting the rectangular lattice antenna was the approach selected to minimize the effects of grating lobes.

3.4 RF Amplification

The next major architecture decision is whether to amplify the RF signal at the antenna ports or at the elements. This issue applies to both the transmitting power amplifiers and the low-noise receive amplifiers (see Figure 2). Here the cost differential is dramatically in favor

of single-point amplification, but weight and efficiency must be considered. The trend in the modern phased-array art is toward distributed amplification because higher transmit power and lower receive noise can be achieved. This is especially true where space feeding is not an option. In the present case, the transmit power can be readily achieved by summing the output from several TWT amplifiers.

The TWT RF efficiency has already been demonstrated at greater than 35% over a broad band, whereas that of the solid-state amplifiers will probably be at most 25%. However, when all required power supplies are included, the total prime power that the solid state approach requires is estimated at 11.1 KW, which is essentially the same as that calculated for the TWT approach (see Section 6).

The efficiency requirement is a significant constraint in itself, but lower efficiency increases weight because it increases the required cooling capacity. If the distributed solid state amplifiers require liquid cooling, the weight impact would be prohibitive. Liquid cooling of the TWTs is unlikely. Also TWTs can operate at a much higher temperature (85° C) than typical solid state amplifiers can. Without considering liquid cooling in either case, the total weight estimate for all amplifiers plus power supplies was over 400 lb for the solid state approach and 350 lb for the TWTs. Table 2 summarizes the tradeoffs including the possibility of a single TWT or Chystron amplifier tube.

Table 2. Relative Ratings of the Three Candidate Architectures

Requirement	Single Tube	Multiple Tubes	Solid-State
Weight	2	1	3
Cost	1	2	3
Reliability/Graceful Degradation	3	2	1
Radar Sensitivity for Given Prime Power	2	3	1

4.0 LENS ELEMENT

4.1 Radiators

Several candidate radiators are suitable for this application. Primary consideration is that they be amenable to etching on a PC board with radiation tangent to the board. Dipoles

have been used in similar configurations, but they require a balun and probably a groundplane. Flared notch radiators are popular for phased arrays, especially where a large bandwidth is needed [3, 4]. Their bandwidth exceeds the bandwidth for LAPA, but they are directive and would be very easy to feed with a microstrip-to-slotline coupler.

One such notch could be connected to either end of each shifter, but they would take up more room than necessary, and on the side toward the feed, the element pattern would be too narrow to properly illuminate the feed. Therefore, at least two such notch radiators must be coupled to either side of the shifter. Then the element pattern can be steered toward the feed by phasing the two radiators of each element appropriately. Unfortunately, these radiators exhibit some antiresonance behavior at about the size it would take to fit a pair into the spacing of one element. Since our bandwidth is not large for these elements and the scan range is not large in the affected plane, it is probable that design parameters could be adjusted to overcome this phenomenon. However, the safest approach is to simply use three radiators for each element on either side of the lens.

A coupler then must be designed to connect the three radiators. Unisolated couplers would be the easier and less costly to fabricate and cause less RF loss than isolated couplers. However, such a configuration becomes a retrodirective array for any incoming signal from a direction other than that of the main beam. Since there is no scattering requirement for this antenna, there is no problem on the front side of the lens, but the elements on the rear must be steered toward the feed or they will reflect their power back the feed. A preliminary unisolated 3-way coupler is shown in Figure 10. Notice that the slotline is fed by the microstrip a quarter of a slotline wavelength from the center between the two outer feeds. This technique cancels the 180° phase difference that would appear on the notch radiators if they were fed symmetrically. Figure 11 shows a contour map of the active element pattern obtained from coupling measurements on a small array.

4.2 Phase-Shifter Resolution

The most important decision is probably the number of phase shifter bits needed to meet the sidelobe and pointing-accuracy requirements. For a PIN diode shifter, it is important to minimize the number of bits for prime power consumption and cost, as well as RF loss. To

determine how many bits were needed, the SLL and beam-pointing error were calculated for various numbers of bits.

For these calculations, the edge taper of lens illumination was reduced until the peak SLL was about -35 dB. This taper reduced the directivity to nearly 1 dB below the optimum. Also, the phase errors were randomized so that the quantization error was not correlated to position. Without the randomization, the bootlace phase mitigates this correlation but does not eliminate it. Even at this low level, these near sidelobes are not much affected by the number of bits.

The average sidelobe level, however, is greatly affected by the number of bits. The bit quantization errors cost nearly a dB of gain, and that energy removed from the main beam is spread somewhat evenly over the hemisphere, raising the average sidelobe level. Here we are concerned only with the average over the azimuth principal plane. Table 3 shows that 2 bits will marginally achieve the average SLL of 0 dBi. However, when losses are included, all SLLs (and peak levels) will be nearly 2.3 dB lower. (Without randomizing quantization errors, this level is over 4 dB higher.) Also, in the table, directivity includes aperture taper and spillover loss.

Table 3. Effect of Phase Quantization on SLL

Number of Bits	Directivity (dBi)	Mean SLL (dB)	Relative SLL (dB)	RMS SLL (dBi)	Relative ASLL (dB)
2	47.6	15.1	-32.5	-0.2	-47.82
3	48.3	15.3	-33.0	-4.4	-52.71
4	48.4	15.15	-33.25	-7.7	-56.11
∞	48.5	15.0	-33.5	-9.2	-57.71

The beam-pointing error is also not much degraded by bit quantization; we calculated a standard deviation of 0.011 mrad in azimuth and 0.018 mrad in elevation for 2-bit shifters. The statistical distributions for the azimuth calculations are shown in Figure 12 for 1000 difference patterns. The patterns do include many scan positions, and the standard deviation must be scaled by the cosine of the scan position; for instance, it would be 0.022 for an azimuth scan of 60°. The actual pointing position was determined by calculating the difference pattern level at the desired position of the beam. This level was divided by the slope through

an ideal null to determine the actual location of the null. Since there was some filling in of the null, this method seldom indicated zero error; thus, it may be slightly pessimistic. In any case, the error is clearly far below the allowed error.

4.3 Shifter Approach

The phase shifter type is important because, for the diode shifter, more bits means more prime power consumption, RF loss, and cost; but these effects are not significant for ferrite shifters. Table 4 compares the baseline diode shifter with one of the best commercially available ferrite shifters mounted in a microstrip configuration. Since the ferrite is non-reciprocal it must be reset between transmission and reception. The reset time establishes minimum target distance. If sufficient reset time is not available, a reciprocal model must be used, which (for this application) is two ferrites with circulators. The ferrites are latching, so that their power consumption depends on the number of switches per second. For the non-reciprocal case, there must be two switches for every transmit-receive (T/R) cycle, but for the reciprocal case, there is only one switch per new beam direction. We estimate that the beam update rate is about 80 μ sec, which means that this shifter will require 1.1 W of power. For 15,000 elements, such shifters would consume the whole power budget. Thus, 2-bit diode shifters offer the best performance for this application.

Table 4. Phase-Shifter Comparison

	PIN Diode	Ferrite (non-reciprocal)	Ferrite (reciprocal)
Weight	15 lb	26 lb	60 lb
Power Consumption	60 μ W/bit	50 μ J/switch	100 μ J/switch
Insertion Loss	0.5 dB/bit	0.7 dB	1.2 dB
RF Power Capacity	3 W	100 W	100 W
Size (in)	1.4 x 0.5 x 0.02	1.7 x 0.2 x 0.1	2.5 x 0.4 x 0.1
T/R Switch Time	N/A	5 μ sec	N/A

Diode-based phase shifters can be designed in a wide range of architectures, including: loaded line, hybrid coupled, PIN switched line length, and varactor tuned reactance forms. Each of the architectures offers different RF performance, flexibility, dc supply power and

control requirements. The requirements of low weight and passive cooling indicate that the phase shifter should be fabricated using a single substrate, that is, in either slotline or microstrip form.

The branchline hybrid coupler with switched reflective terminations was selected as the microstrip architecture for each of the two bits. Glance [5, 6] demonstrated the RF performance and low power consumption of a hybrid coupled phase bit. This bit configuration can provide any phase shift and uses the fewest diodes per bit. The series diode and open circuit reflection configuration was selected over the shunt diode and short circuit version because of the additional modeling that would have been required to fully characterize the multiple plated-hole short circuits.

4.4 Shifter Design

A suitable selection of the substrate material on which to design the microstrip shifters and radiators is very important. For light weight, it should be thin, but since it is structural as well as an RF dielectric, it must be rigid enough to resist bending and since the mechanical design calls for it to be under modest tension, it cannot be too soft. For these reasons, the high-performance teflon-based boards were rejected in favor of the new low-loss fiberglass-based boards. Also, these new boards cost significantly less and allow normal fiberglass processing like the standard PC board laminate. The Rogers 4003 is such a board and was selected in 20-mil thickness as a good compromise between loss and weight. Its dielectric constant is 3.38, and its loss tangent is 0.002.

Since the control circuitry will be carried on standard PC boards bonded to the back of the Rogers RF board, the coefficients of thermal expansion (CTE) must match closely in the directions tangent to the board. Also, they must be close enough to copper in the normal direction that the plated through holes can stretch without breaking. Table 5 shows that the relevant CTE values are in excellent agreement.

The phase shifter was designed based on a 70-ohm microstrip and modeled using Libra by HP/EEsof. Figure 13 presents the phase shifter circuit trace layout. The circuit size shown is approximately 1.75" x 0.625". The actual size required will be approximately 2.0" x

Table 5. Coefficients of Thermal Expansion

MATERIAL	X ($\times 10^{-6}$)	Y ($\times 10^{-6}$)	Z ($\times 10^{-6}$)
Rogers 4003	11	14	46
FR-4	10	15	65
Copper *	10	10	10
Aluminum	6.5	6.5	6.5

* 30% stretching is allowed

0.75". The three bias pads are each 100 mils square and may be relocated and resized as needed with the integration of the driver circuitry. The thinnest line is 12 mils and the widest is 65 mils. The diode selected was MP 5232, case style M2.

Each bit requires two diodes. Each diode will be forward biased at 40 mA with a series resistance of 1.6 ohms, resulting in a forward bias power of approximately 2.6 mW per diode. The maximum forward bias power required for the two-bit phase shifter with four diodes will be 10.4 mW. Each diode will be reversed biased at -50 VDC with a current of approximately 10 μ A, resulting in a reverse bias power of approximately 0.2 mW per diode. The maximum forward bias power required for the two-bit phase shifter with four diodes will be 2.0 mW. The average power required for the diodes will be 6.2 mW per shifter.

4.5 RF Performance Analysis

The phase shifter design was optimized to minimize the transmission loss through the device and maximize the phase accuracy for each state over the frequency band of 9.5 to 10.5 GHz. All of the following data are based on simulation. The performance estimates will be confirmed through the fabrication and testing of prototype components. Figure 14 shows predicted phase accuracy for each of the four phase states, 0°, 90°, 180°, and 270° as a function of frequency. Figure 15 presents the S-parameter transmission and reflection performance of the two-bit shifter for each of the four phase states as a function of frequency. At the center frequency of 10.0 GHz, the reflection coefficient was below -20 dB, and the transmission coefficient greater than -1 dB. Notice the performance degrades at frequency band edges.

5.0 STRUCTURE AND CONTROL ELECTRONICS

The truss structure supporting the lens and feed, as shown in Figure 1, must be analyzed in the future with a finite-elements program to minimize the weight while maintaining the required lens firmness in the motion environment defined by measurements of a 71 m tethered aerostat in a 50 knot mean wind with a 10 f/s RMS Dryden gust. Analysis will first be done with no stabilization, as a worst case; then if the structure is too heavy, the stabilization will be taken into account. Weight estimates so far have been for aluminum, but the structure could easily be made of composite material.

5.1 Lens Structure

As discussed below, the lens has significant rigidity, but it will also be held in modest tension by the circular frame around it, which will add to the rigidity.

Given the vertical array element spacing of 1.45", the board size was chosen to be small enough to accommodate most photoplotting and etching facilities and to maintain sufficient mechanical rigidity. The upper limit for these considerations was about 24", so a 16-element board was selected yielding a 23.2-inch length. This is also a fortuitous number for digital control considerations. The basic board layout is presented in Figure 16, showing the radiating elements and the integrated-circuit components.

Given the horizontal spacing of 0.582", the required area of 8 square meters can be obtained with 920 such boards, some cut to half height to form an approximately circular aperture. There are 5 rows of such boards making an aperture 116" high.

The present method of supplying power and controls to the individual elements uses a mother board running across the top of the array. The mother board will follow the peripheral steps by using a flexible ribbon from one level to the next. At each column, a flexible leader or ribbon cable will branch off the mother board. This ribbon cable will be soldered to an adapter card, which will serve as a connector to mate with the top aperture PC board in each column. A mounting bracket will support the column at the top and clamp the adapter card to the top board. A termination card and mounting bracket will also mate with the last card of each column, though there is no electrical connection.

Power and signal connections between adjoining boards are integrated into the fabrication of each board. The top end of each board has a region that is recessed through some of the laminations to expose the circuit contact pads. The other end of each board has a corresponding recess on the opposite side of the board with a mating set of contact pads. When a pair of boards is connected, the cover plate and nut plate sandwich and press the electrical contact pads together to complete the electrical path from one board onto the next.

Each column will be made up of the appropriate number of PC boards fastened together, as shown in Figure 17. To maintain board spacing between adjacent boards, a set of spacer ribs will extend horizontally across the front and back of the lens at the board joint positions. The spacer ribs will be notched so as to mesh with the nut and cover plates of each board connection. The spacer ribs will assist in holding the boards at equal spacing and help the array to act as a flat uniform sheet by restricting the movement of any single column in relation to the columns on each side of it.

RF leakage between aperture PC boards will be minimized by placing a ground wire between columns. This ground wire will be supported by a foam strip attached to each board, as shown in Figure 17. The foam strip will aid in stiffening the board and act as a horizontal spacer between the boards to prevent bending between the board ends. The foam strip will have to be notched to clear RF traces on the board (for cooling), connection plates, and the spacer ribs.

5.2 Control Circuitry

The array switch consists of: (1) one array interface processor (AIP), (2) 920 phase shift processors (PSP) (one on each aperture PC board), (3) bus decoding and logic driver circuits, and (4) 29,440 phase shift driver circuits (32 per board). The antenna control circuit is responsible for controlling the phase shifters by calculating the frequency dependent phase shift values and reporting any faults detected by the built-in-test (BIT) features.

The PSP controls the phase shift driver circuits. The PSP calculates the phase shift values for each of the 16 phase shifters on its board and outputs the value to the phase shift drivers. The PSP also runs continuous BIT and reports problems to the AIP. The input on

which the PSP bases its phase-shift calculation is three data words, elevation scan angle, azimuth scan angle and frequency. The shifters must focus the beam as well as scan it.

Each aperture PC board has: (1) one PSP, (2) 32 PIN drivers, (3) 16 two bit phase shifters, (4) 16 receive/transmit antenna element pairs, (5) one +3.3 volt DC switching voltage regulator, and (6) one +1 volt DC switching voltage regulator. The receive/transmit antenna elements and the phase shifters are on one side of the board; the digital circuits, power supplies, and PIN diode drivers are on the other side of the board, as shown in Figure 16. A block diagram is shown in Figure 18.

6.0 PREDICTED RESULTS

6.1 Performance

A typical azimuth directivity pattern is shown in Figure 19 calculated for a particular randomization of 2-bit phase shifters. Figure 20 shows the elevation patterns for minimum and maximum scan positions of $\pm 7.5^\circ$, to illustrate the dynamics of the grating lobes. The elevation patterns do not include phase-shifter errors, but they have essentially the same effect on sidelobes in elevation as in azimuth. All these patterns are calculated at approximately the highest frequency, 10.5 GHz.

The gain is calculated using the parameters and values in Table 6. The part of the efficiency that must be added to the patterns just presented is calculated in the column labeled "Loss, Rel. Directivity," which relates the gain to the input of the feed.

6.2 Weight Budget

A budget of estimated weights is presented in Table 7. The structure depends on mechanical finite-element optimization and, therefore, is not very firm since the analysis has not yet been done. However, it is believed to be conservative.

6.3 Prime-Power Budget

The prime power budget is presented in Table 8.

Table 6. Gain And Loss Budgets

Item	Ohmic Loss	Non-Ohmic Loss	Loss, Rel. Directivity
Cos (broadside)		-0.0	
Aperture Taper		-1.8	
Circulator	-0.2	-0.05	
Feed	-0.2	-0.05	-0.2
Spillover		-0.25	
Rear Radiators	-0.2	-0.1	-0.3
Shifter (2-bit)	-0.9	-0.1	-1.0
Front Radiators	-0.1	-0.1	-0.2
Phase Quantization		-0.9	
Radom Errors		-0.1	-0.1
Array Surface Warp		-0.2	-0.2
Windscreen	-0.05	-0.0	-0.05
TOTAL	-1.65	-3.65	-2.05

Table 7. Weight Budget

Item	Weight (lb)
TWT Power Supplies	240
TWTs and Combiner	110
Circulator and Feed	30
Aperture PC Boards (920)	185
PC Board Clamps (3676)	100
LNAs and T/R Switches (10)	30
Receivers and Exciter	100
Power Supply for Receiving	60
Shifters and Drivers (14,720)	20
Shifter Processors (920)	2
Interface Board and Cables	5
Structure	450
Cooling	42
TOTAL	1374

Table 8. Prime Power Budget

Item	Efficiency / Loss	Power in (W)	Power Spent @
RF Generation & Radiation			11730
TWT Power Supplies	82%	11730	
TWTs and Combiner	35%	9617	
Circulator and Feed	-0.50 dB	3366	
Spillover	-0.25 dB	3000	
Lens (Radiators and Shifters)	-1.50 dB	2825	
Radiated Power		2000	
LNAs and T/R Switches (10)			50
Receivers and Exciter			450
Power Supply for Receiving			90
Shifter Drive Power (14,720)			1175
Shifter Processors (920)			84
Interface Board and Cables			3
Cooling			250
TOTAL			14432

7.0 CONCLUSION

A large, high-performance phased-array has been designed that will be efficient, light-weight, and relatively inexpensive. This design is a case where the latest technology does not best satisfy the requirements. It is a new application of relatively mature technology, which minimizes development risk and should offer high operational reliability. Further conclusions will be drawn from the results of the demonstration currently in progress.

8.0 ACKNOWLEDGEMENTS

All work reported in this paper was sponsored by Rome Laboratories (RL), Electromagnetics and Reliability (ER) Directorate, Antenna Technology Branch, Hansom AFB under contract F19628-97-C-0008. Support is also acknowledged from DARPA and US Army Missile Command. The authors are grateful for the guidance provided by Lt. Dale Linafelter, the sponsor technical monitor.

9.0 REFERENCES

1. W. Rotman and R.F. Turner, "Wide Angle Lens for Line Source Applications," *IEEE Trans. Ant. Prop.* Vol. AP-11, pp 623-632, November 1963.
2. W. Rotman and P. Franchi, "Cylindrical Microwave Lens Antenna for Wideband Scanning Applications," *IEEE Symposium on Antennas and Propagation, Digest*, pp. 564-567, June 1980.
3. D.H. Schaubert, "Wide-Band Phased-Arrays of Vivaldi Notch Antennas," *Tenth International Conf. on Antennas and Propagation*, Vol. 1, pp. 6-12, April 1997.
4. D.H. Schaubert, J. Shin, and G. Wansch, "Characteristics of Single-Polarized Phased-Array of Tapered Slot Antennas," *1996 IEEE Symposium on Phased Array Systems*, pp. 102-106, October 1996.
5. B. Glance, "A Fast Low-Loss Microstrip PIN Phase Shifter," *EE Transactions on Microwave Theory and Techniques*, Vol. MTT-27, No. 1, pp. 14-16, January 1979.
6. B. Glance, "A Fast Low-Loss Low-Drive 14-GHz Microstrip PIN Phase Shifter," *IEEE Transactions on Microwave Theory and Techniques*, Vol. MTT-28, No. 6, pp. 669-671, June 1980.

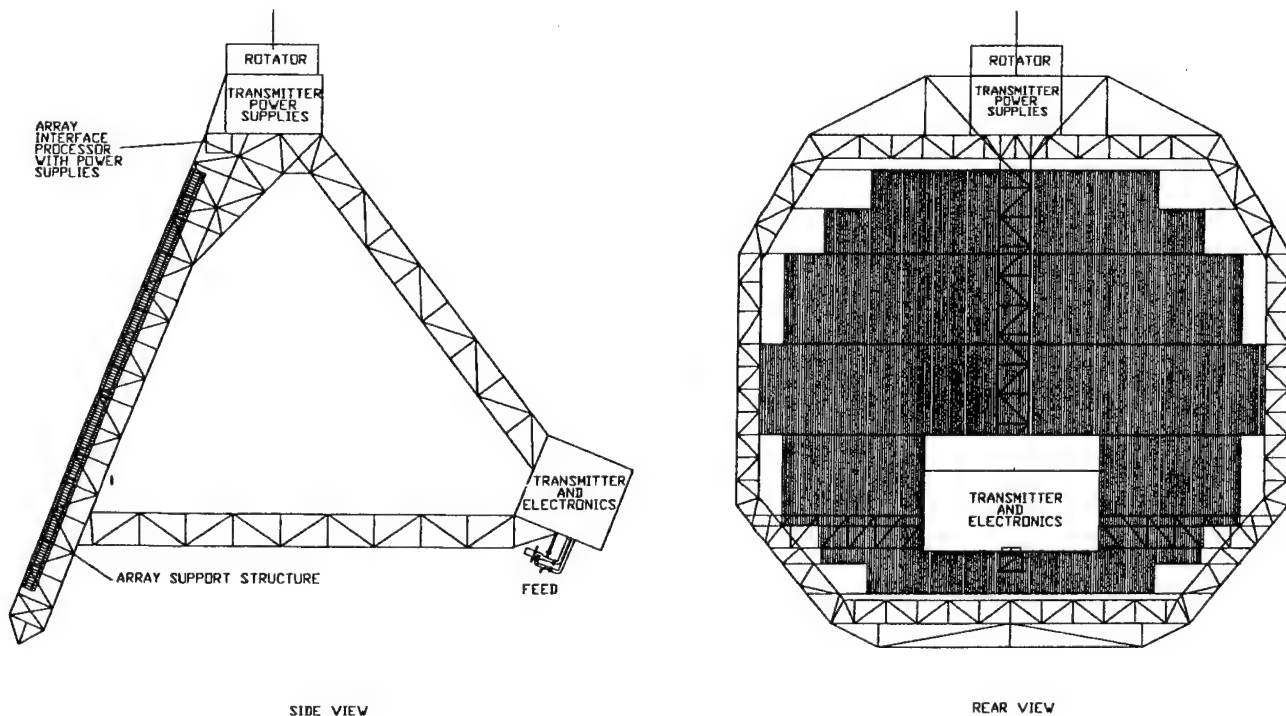


Figure 1. Mechanical Layout of Complete Antenna

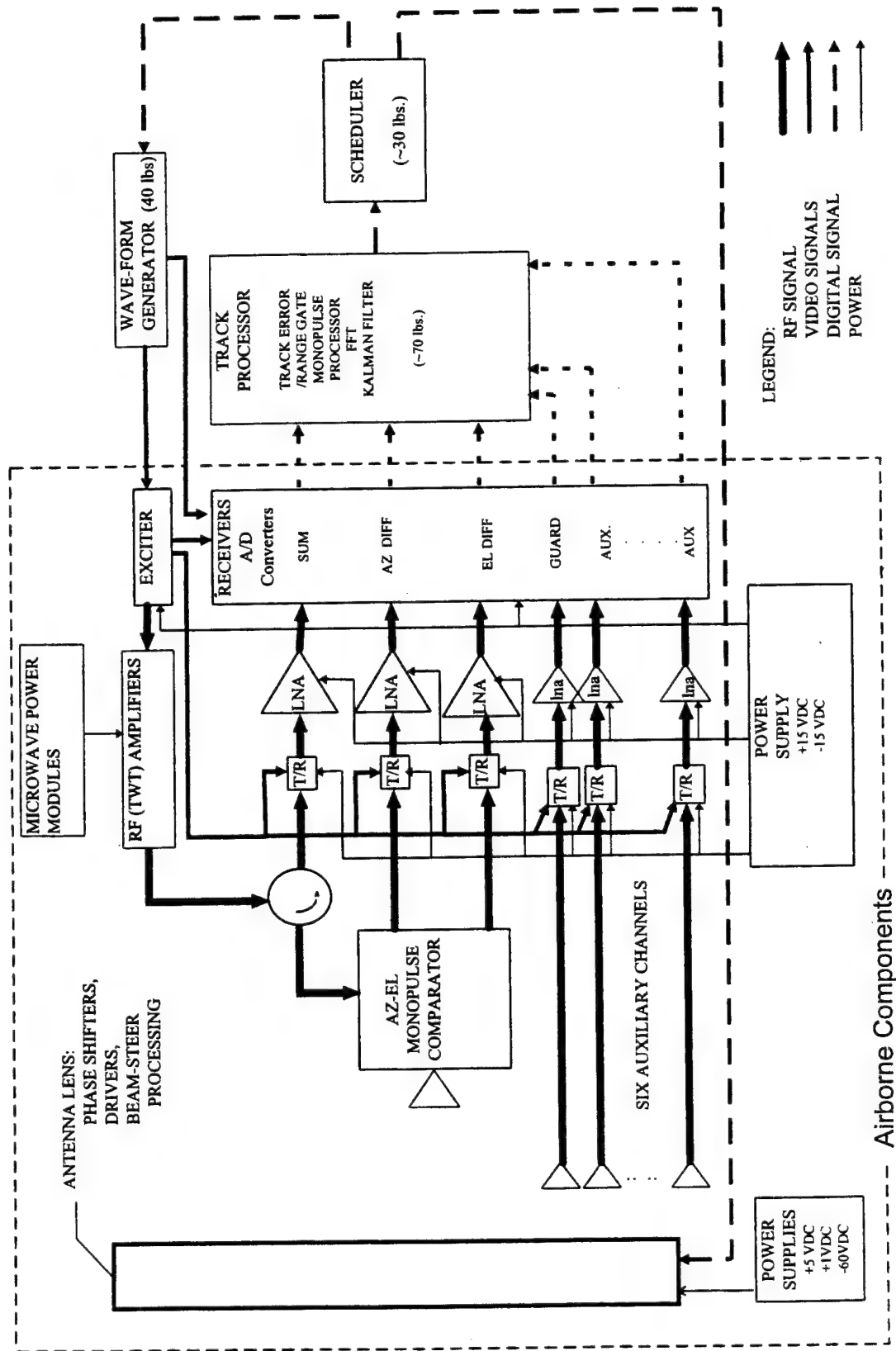


Figure 2. Block Diagram of the Complete Antenna System

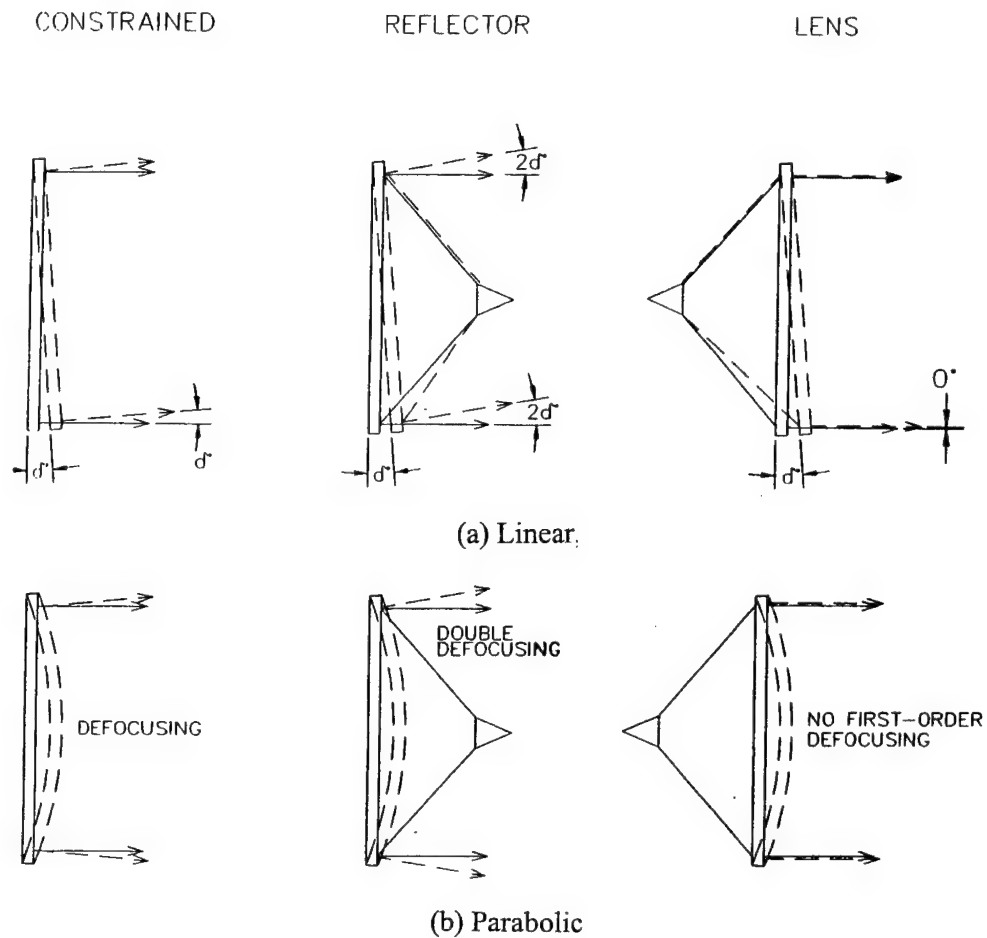


Figure 3. Conceptual Effects of Aperture Surface Deformations: (a) Linear, (b) Parabolic

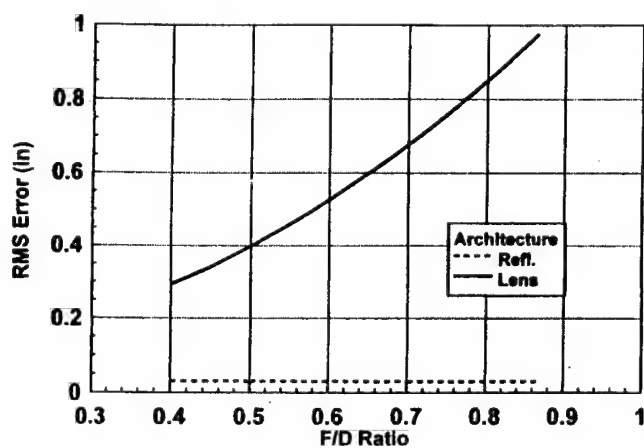


Figure 4. Surface Deformation That Causes 0.2 dB Gain Loss

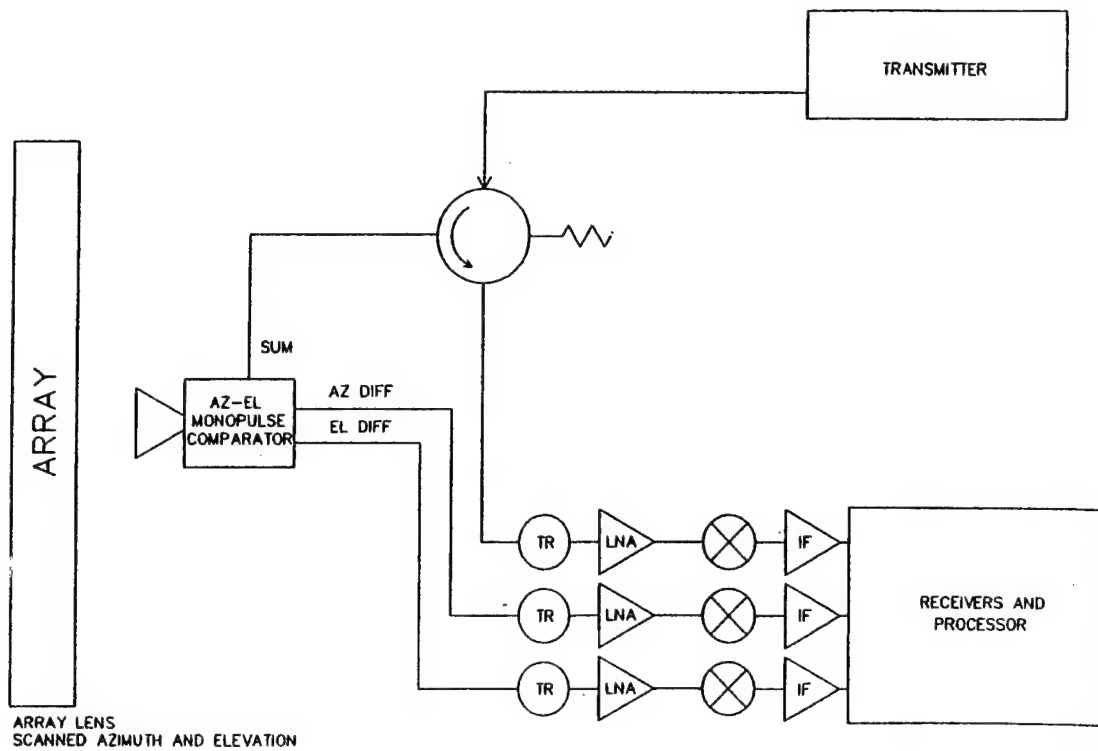


Figure 5. Simple Feed Architecture for Space-Fed Lens

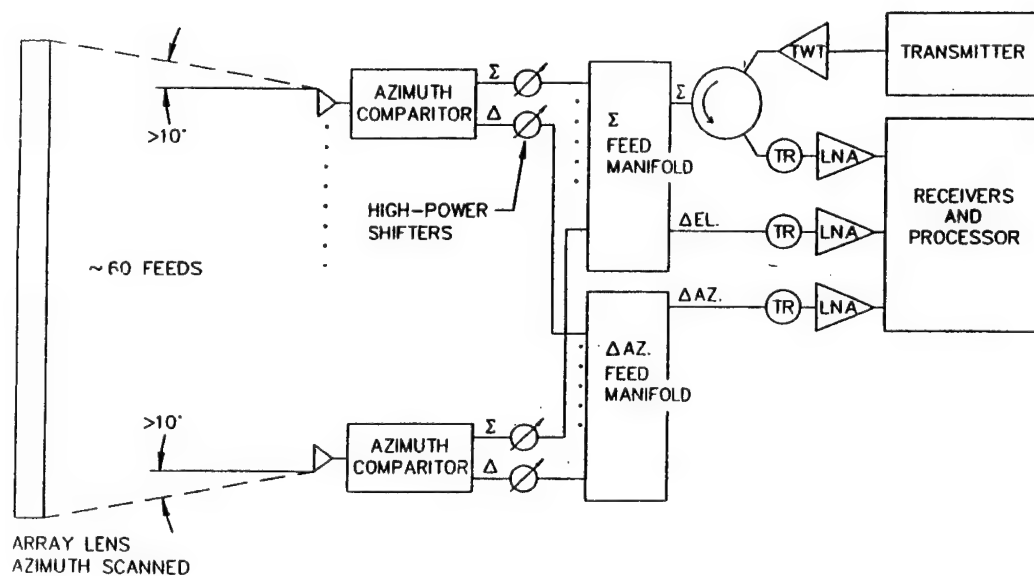


Figure 6. Elevation-Scanned Space-Feed Architecture

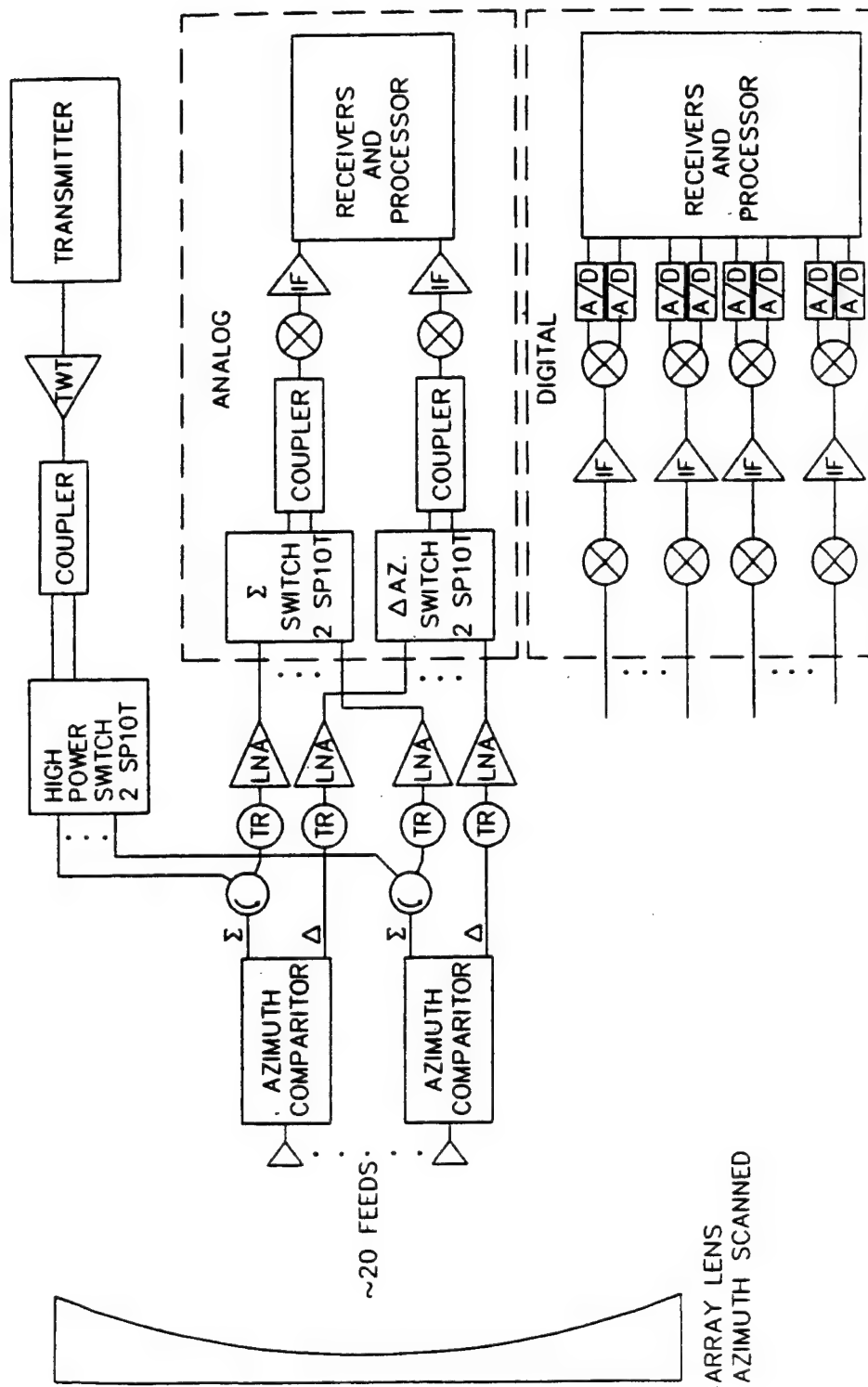


Figure 7. Multiple-Beam Space-Feed Architecture

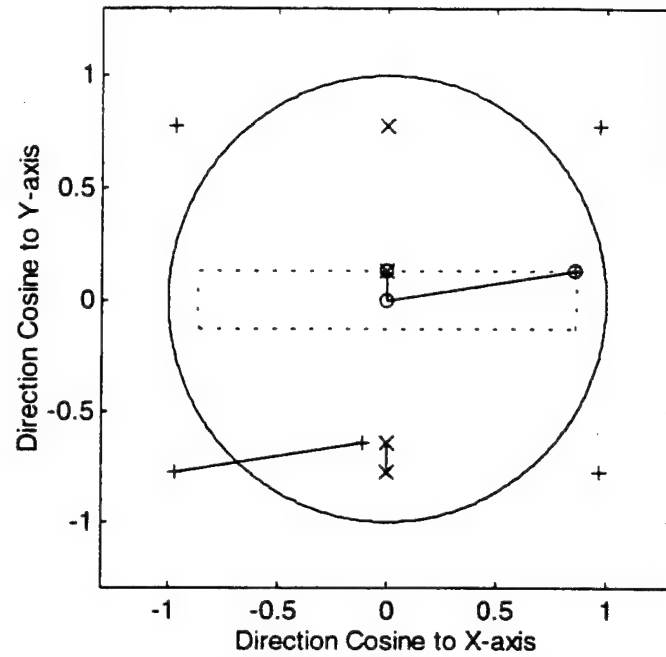


Figure 8. Grating-Lobe Locations for Rectangular and Triangular Element Grids

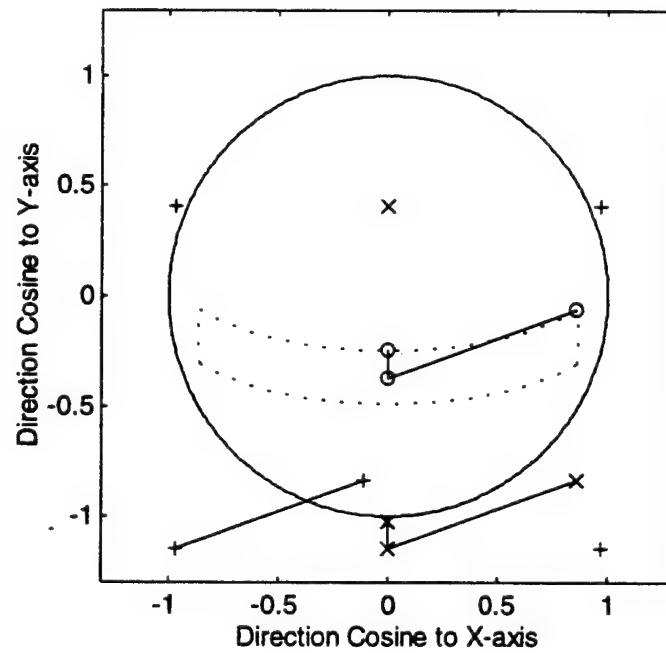


Figure 9. Grating-Lobe Locations with Aperture Tilted 22°

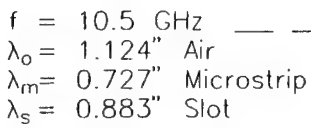


Figure 10. Preliminary Lay-Out of Radiator

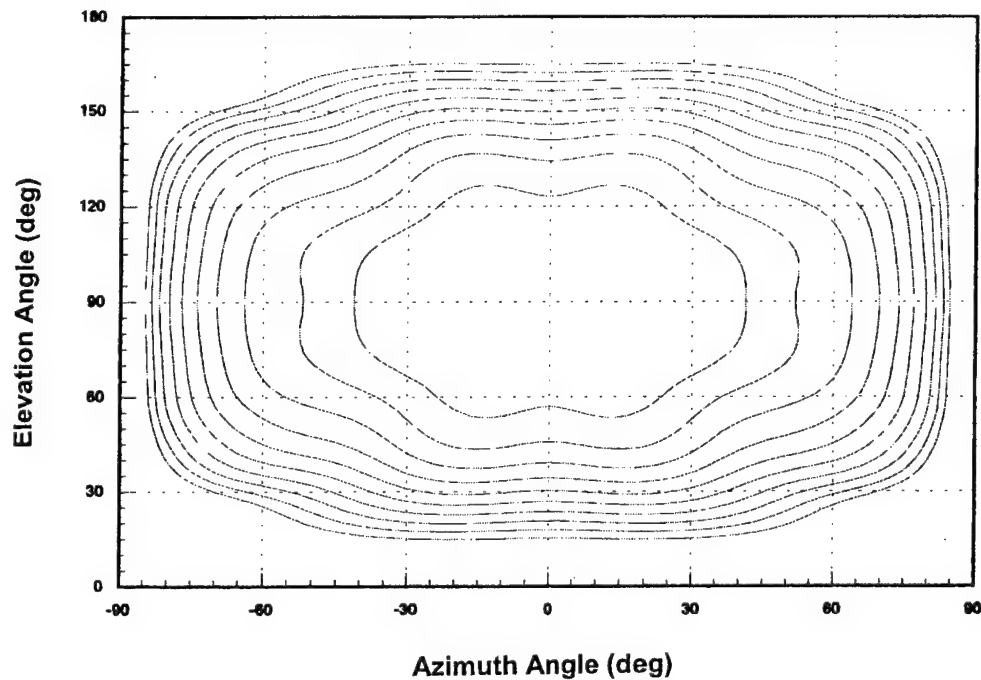


Figure 11. Active Element Pattern Contours at 1 dB Increments

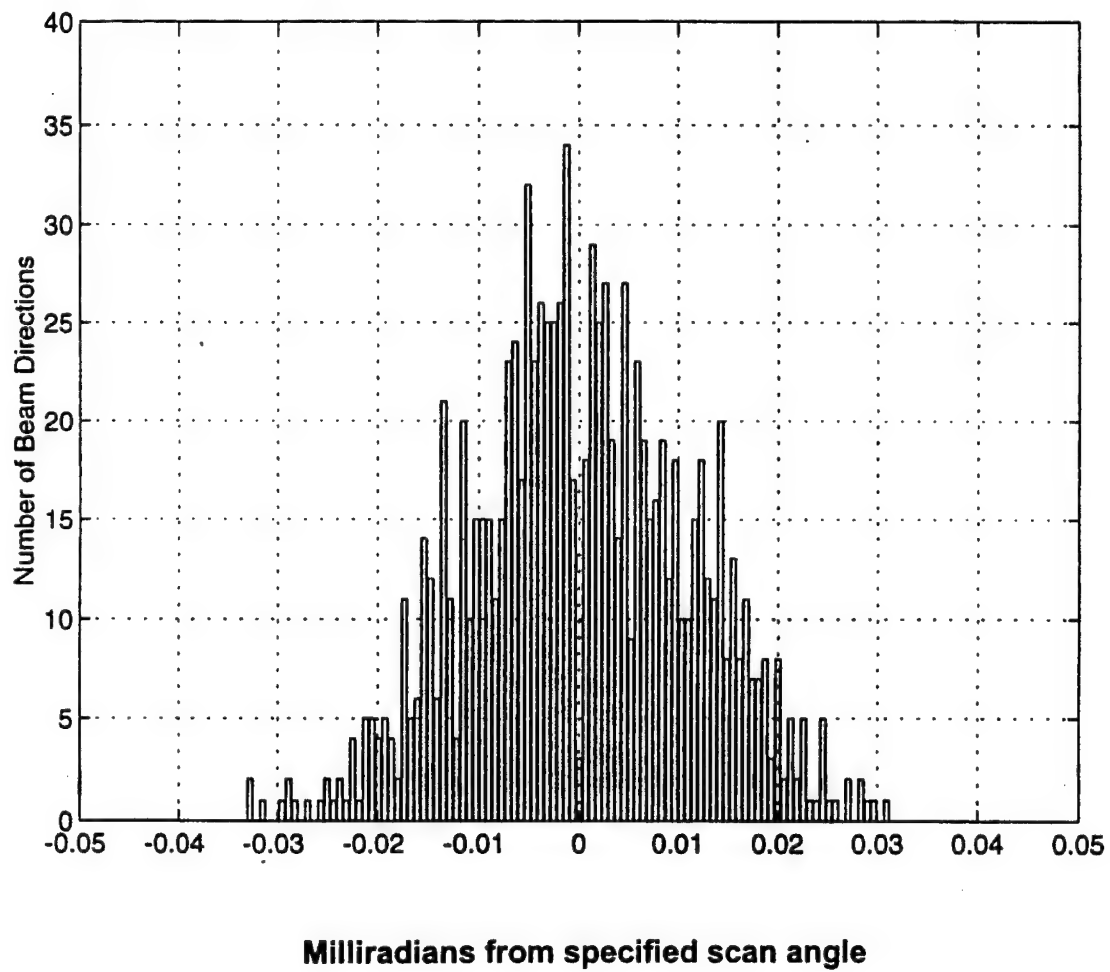


Figure 12. Azimuth Beam-Pointing Statistics

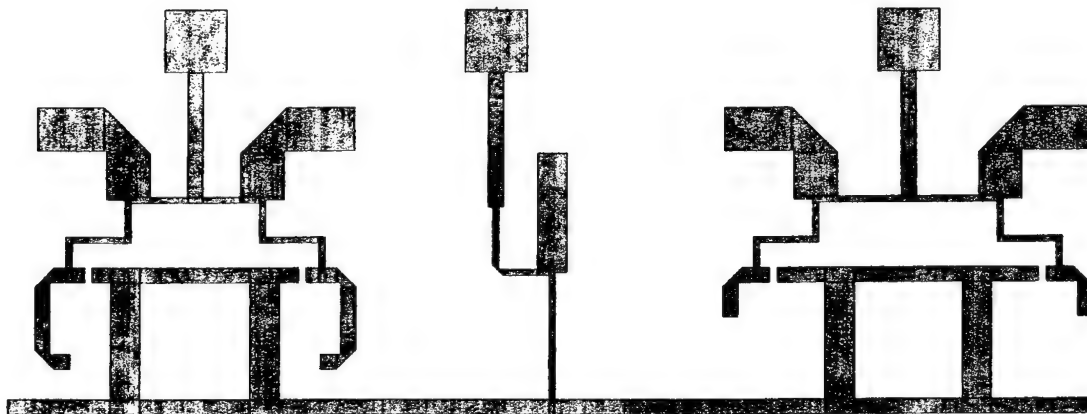


Figure 13. Artwork for 2-Bit Diode Microstrip Phase Shifter

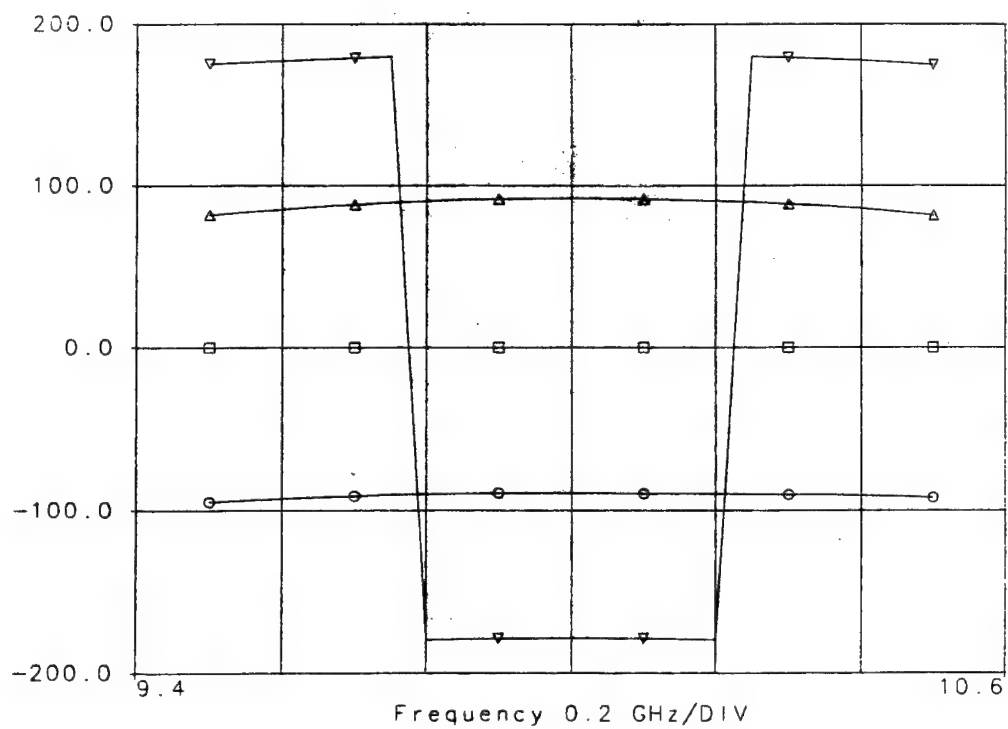
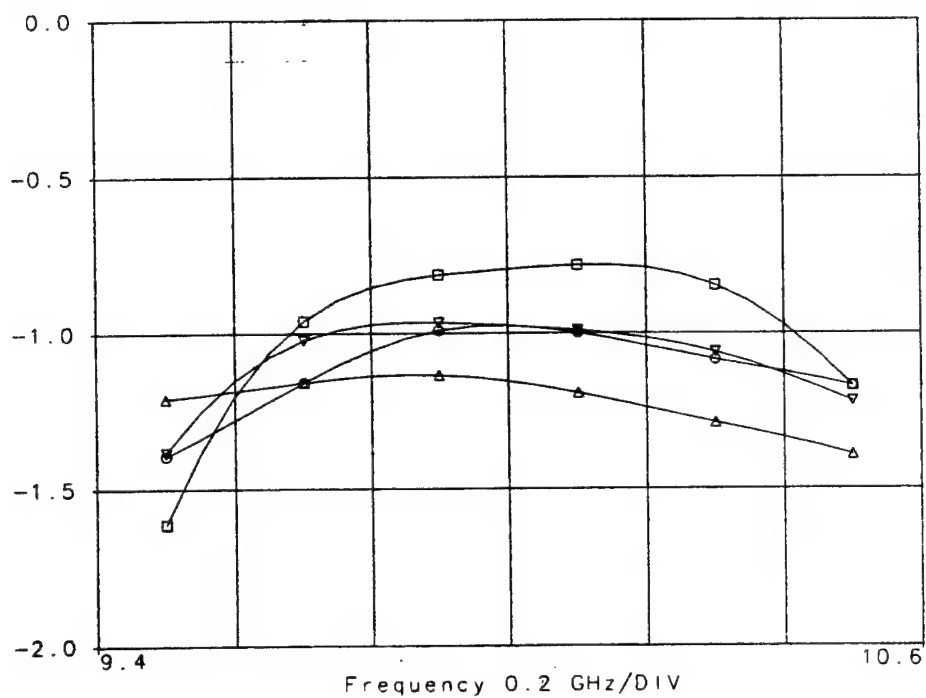
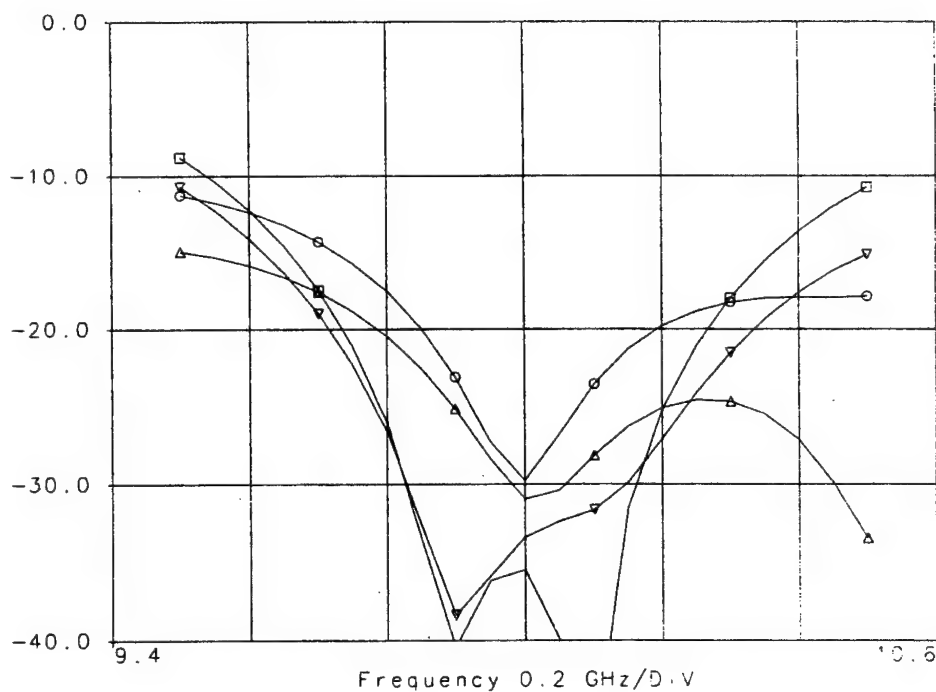


Figure 14. Calculated Phase Shift for Four States of Phase Shifter



(a) Transmission



(b) Reflection

Figure 15. S-Parameter Calculations for Four States of Phase Shifter: (a) Transmission (b) Reflection

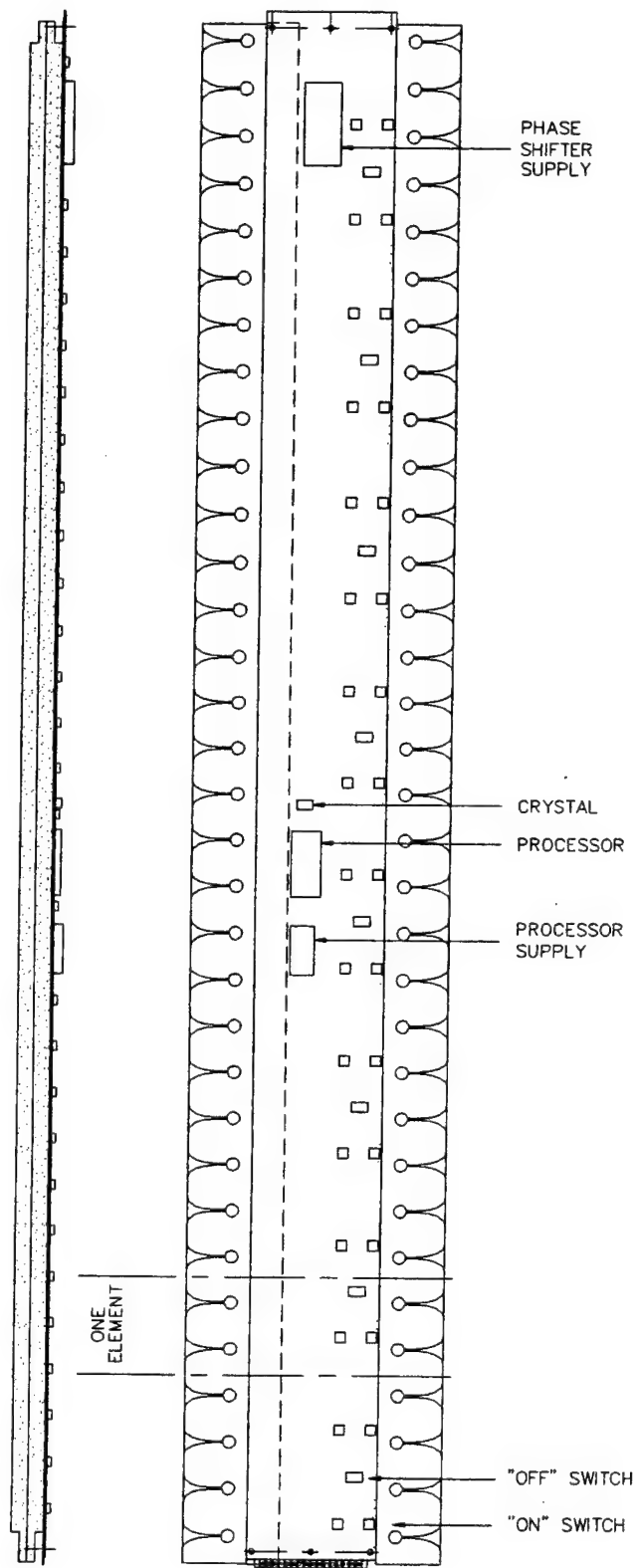


Figure 16. Mechanical Layout of One 23.2" Aperture PC Board (back view)

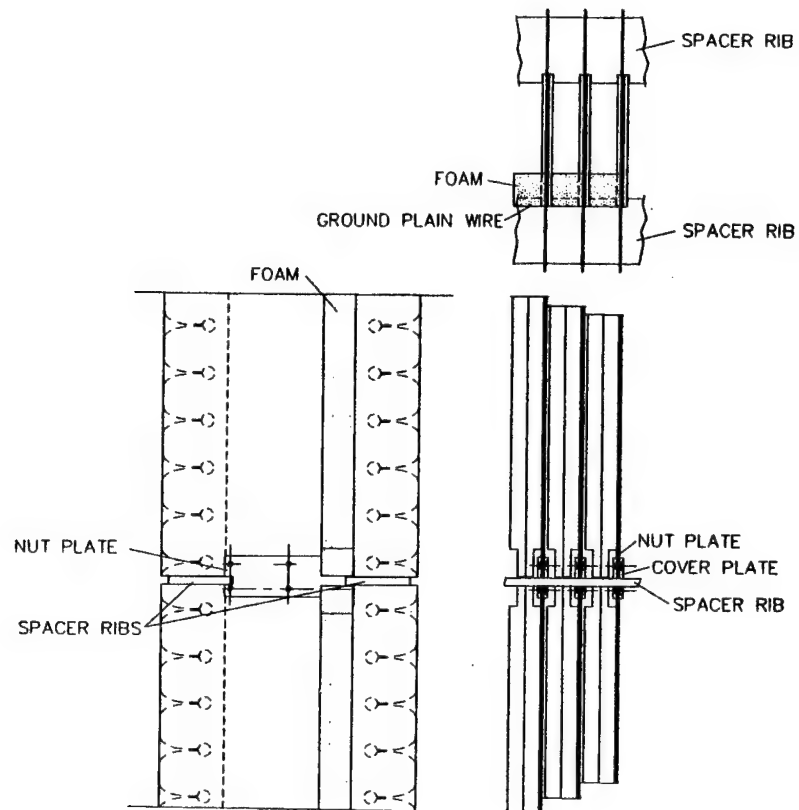


Figure 17. Mechanical Details of Horizontal Spacer Ribs

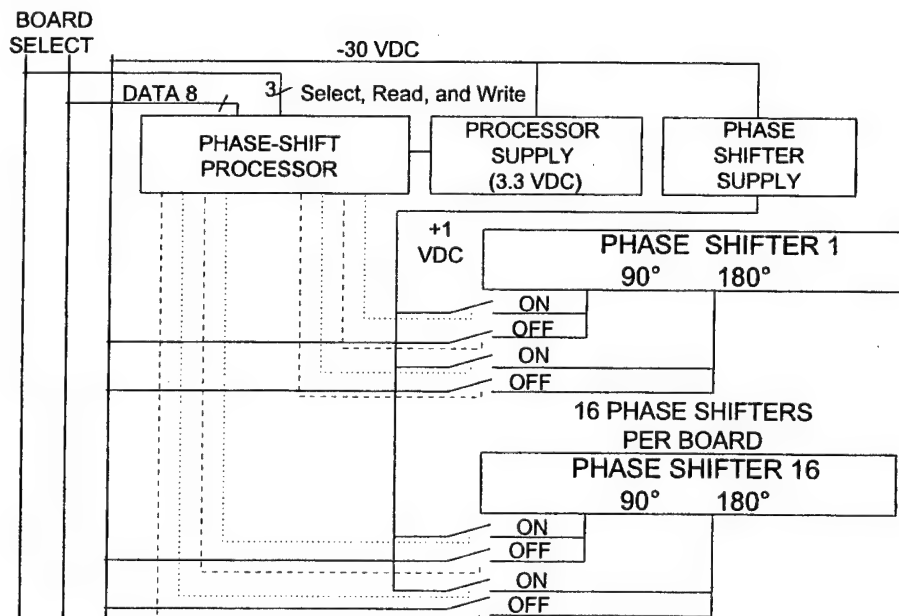


Figure 18. Aperture PC Board Block Diagram

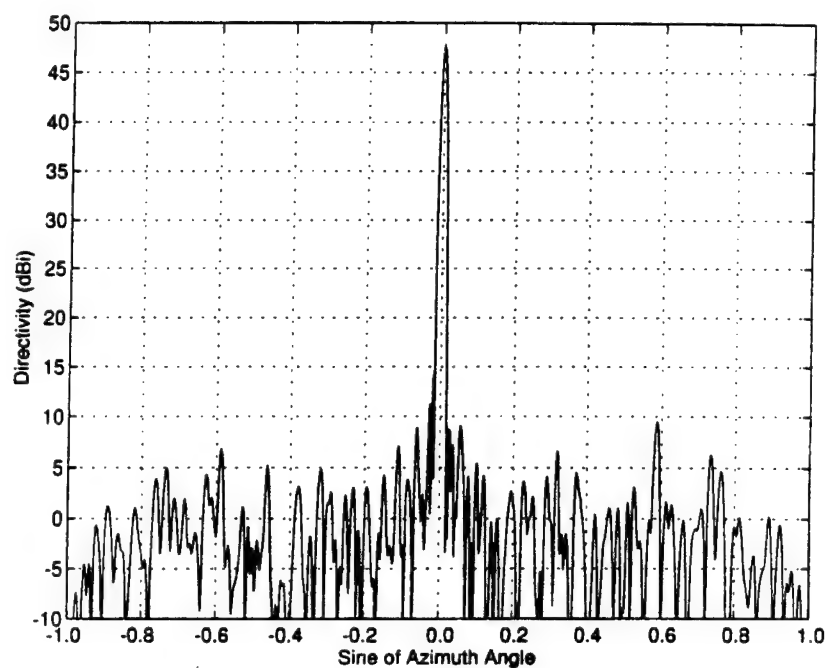


Figure 19. Calculated Azimuth Directivity Pattern Including 2-Bit Quantization Error

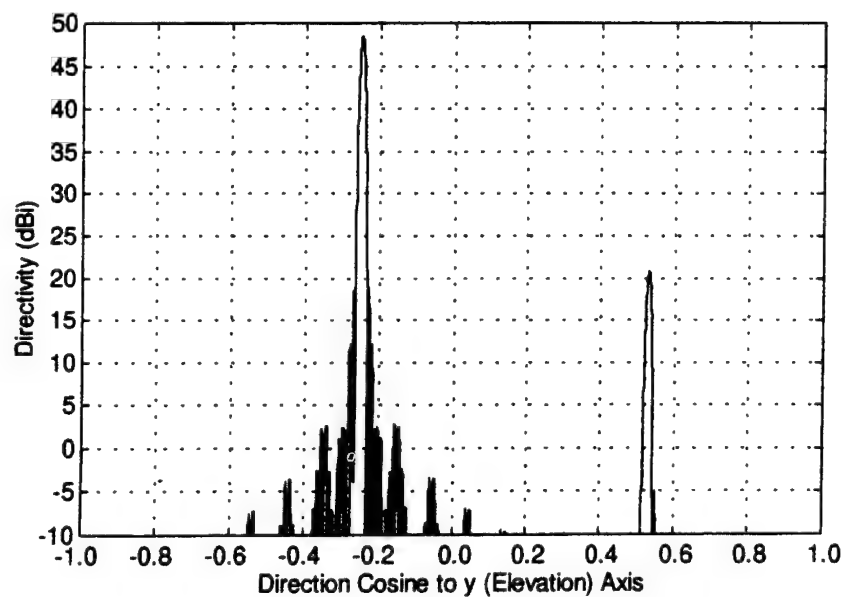


Figure 20. Calculated Elevation Directivity Pattern for 7.5° Elevation Scan, With Respect to Tilted Aperture

Array Antenna Beam Pointing Error Due To Random Errors

James B. Yon and Daniel Davis
Northrop Grumman Corporation
ESSD Divison
Baltimore, MD 21203

Abstract: A wide variety of system applications use large array antennas to meet high angular resolution requirements. An important function in their design stage is allocating mechanical/electrical modular tolerances which will meet beam pointing accuracy requirements. Ultimately, errors affecting beam pointing can be viewed as phase error in the radiated distribution which is subdivided into random and systematic errors. A description, and example, of the relationship between random distribution phase errors and its effect on beam pointing error (BPE) is described. The random errors may apply to individual elements, groups of elements, or a combinations of both as would be the case in large array antennas due to their modular construction. BPE effects are discussed for both one-way and two-way transmit/receive patterns to accommodate system requirements found in a broad range of applications.

Simple expressions are demonstrated to provide accurate predictions of BPE. The discussion includes a wide variety of concepts:

- relationship between BPE and individual module levels
- relationship between BPE and combined module levels
- relating errors to one-way and two-way BPE
- converting between RMS and CEP BPE

These concepts are vital to relating component tolerances to BPE system requirements. Of importance is the generality of the developed relationships which makes them applicable to many systems.

1. Introduction

A wide variety of system applications use large array antennas to meet high angular resolution requirements. An important function in their design stage is allocating mechanical/electrical module tolerances which will meet beam pointing accuracy requirements. Ultimately, errors affecting beam pointing can be viewed as phase error in the radiated distribution which is subdivided into random and systematic. The following discussion provides a description, and an example, of the relationship between random distribution phase errors and its effect on beam pointing error (BPE). The random errors may apply to individual elements, groups of elements (modules), or a combination of both as would be the case in large array antennas by nature of their modular construction. Furthermore, BPE effects will be discussed for both one-way and two-way transmit/receive patterns to accommodate system requirements found in a broad range of applications.

2. Background

Figure 1 shows a generic modular constructed array antenna having three levels; 36 M1 Modules in the antenna, 16 M2 Sub-Modules per M1, and 4 Radiating Elements (REL) per M2. The production of such an antenna will introduce errors

at each level based on the achievable tolerances of the individual components. Standard design practice ensures accountability of these errors by maintaining an error budget. Sub-allocation of system level requirements provides the necessary acceptance criteria of this error budget. The following discussion is key to this sub-allocation process, specifically in regards to beam pointing error resulting from random errors at each of the module levels.

BPE requirements may come in a variety of forms but more commonly in terms of either an RMS error associated with the principal plane axes or a Circular Error Probability (CEP) such as a 95% CEP. Both representations are illustrated in Figure 2. Either form is equally acceptable where the conversion from one to the other is explained in detail as follows.

The two dimensional BPE can be described by a joint Gaussian distribution whereby the azimuth and elevation axes are scaled, without loss of generality, thus allowing the standard deviation to be represented by a single RMS BPE value. The joint Gaussian distribution can then be rewritten in terms of a CEP as:

$$\text{CEP}(\theta \leq \chi) = 1 - e^{-1/2 \left(\chi / \text{BPE}_{\text{rms}} \right)^2} \quad (1)$$

Solving for χ , such that $CEP(\theta \leq \chi) = .95$ as given by the above example, gives

$$\begin{aligned}\chi(95\% \text{ CEP}) &= \sqrt{-2 \cdot \ln(1 - 0.95)} \cdot BPE_{rms} \\ &= 2.448 \cdot BPE_{rms}\end{aligned}\quad (2)$$

It is shown that the BPE_{rms} is related to the 95% CEP by a scale factor of 2.448.

Other scale factors can be derived for different CEP percentages using equation (2).

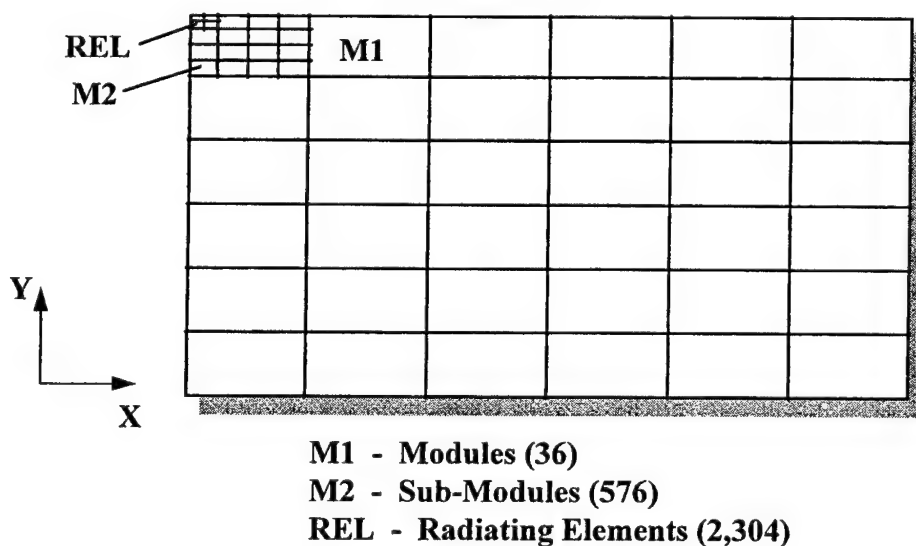


Figure 1 Modular Array Antenna Configuration of Three Levels

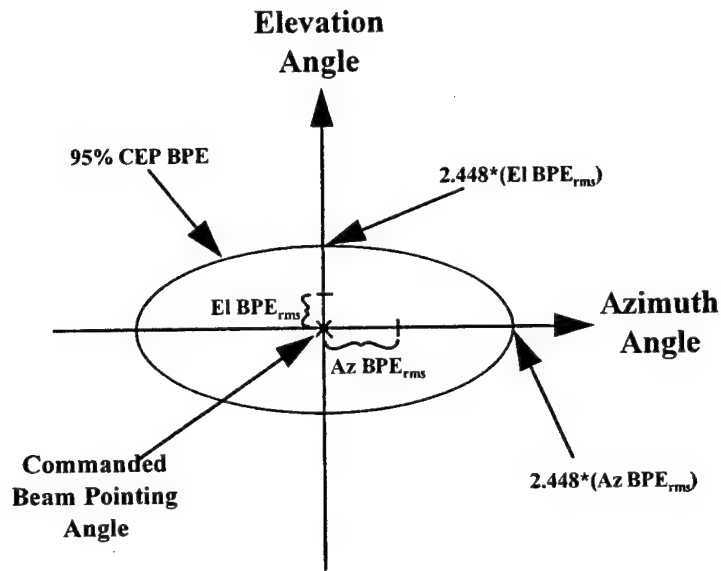


Figure 2 Illustration of RMS and 95% CEP BPE

3. Discussion

A well known fact is that aperture phase errors induce beam pointing error, unlike amplitude errors. Simple expressions have been derived to relate the RMS BPE of one-way and two-way patterns due to random phase errors on various module levels. The two-way BPE relation assumes that transmit and receive errors are independent. Equations (3) and (4) were empirically derived with the aid of computer modeling. Individual transmit and receive BPEs are determined from equation (3) and the two-way BPE is related to the one-way BPEs as expressed in

equation (4). The results exhibit the proper behavior based on open literature of similar, but not identical situations.^[1] A common finding is the relationship being proportional to the RMS phase error and inversely proportional to the square root of the number of elements.

$$\text{One - Way (Tx / Rx) BPE}_{\text{rms}} = \frac{\phi_{\text{rms}} \cdot \Omega_{3\text{dB}}}{91 \cdot \sqrt{N_x \cdot N_y}} \quad (3)$$

$$\text{Two - Way BPE}_{\text{rms}} = \frac{\sqrt{(\text{Tx BPE}_{\text{rms}})^2 + (\text{Rx BPE}_{\text{rms}})^2}}{2} \quad (4)$$

where,

BPE_{rms} = RMS beam pointing error

ϕ_{rms} = RMS phase error for a given module size

$\Omega_{3\text{dB}}$ = one-way beamwidth in azimuth or elevation

(BPE_{rms} , ϕ_{rms} , and $\Omega_{3\text{dB}}$ are in units of degrees)

N_x = number of modules/elements in the horizontal plane

N_y = number of modules/elements in the vertical plane

Equations (3) and (4) determine BPE due to individual module levels (i.e. M1, M2, or REL as in Figure 1), thus providing a BPE contributor due to each level. The total BPE due to all random errors can be shown from random error theory as the RSS of the individual BPE contributors under the condition that the errors from one module level are independent from the other levels. Applying RSS to the right side of equation (3) and moving constants to the outside of the summation results in equation (5). The total two-way BPE is determined from equation (6).

$$\text{One - Way (Tx / Rx) BPE}_{\text{rms total}} = \frac{\Omega_{3\text{dB}}}{91} \sqrt{\sum_i \left[\frac{\Phi_{\text{rms}_i}^2}{N_{x_i} \cdot N_{y_i}} \right]} \quad (5)$$

$$\text{Two - Way BPE}_{\text{rms total}} = \frac{\sqrt{\left(\text{Tx BPE}_{\text{rms total}} \right)^2 + \left(\text{Rx BPE}_{\text{rms total}} \right)^2}}{2} \quad (6)$$

where the subscript “i” denotes the various module levels in the modular constructed array antenna (i.e. M1, M2, and REL as in Figure 1).

Equations (3) through (6) can be related to a CEP BPE simply by multiplying by the appropriate scale factor as discussed earlier.

By way of example, the above theory is demonstrated by comparing results to those generated from computer simulation. Table 1 shows a fictitious set of random errors for an array antenna comprised of three module levels similar to that shown in Figure 1. The antenna consists of 4 RELs per M1 and 16 M1s per M2. To illustrate a family of curves, the overall antenna size consists of 4 M2s wide with a height ranging from 2 to 10 M2s high.

Module Type	Tx ϕ_{rms}	Rx ϕ_{rms}	N_x	N_y
REL	20°	16°	32	16 - 80
M1	10°	8°	16	8 - 40
M2	2.5°	2°	4	2 - 10

Table 1 Error Budget Example for a Three Module Level Antenna

Furthermore, the antenna assumes uniform illumination on transmit and cosine weighting in both planes on receive. The weighted receive provides a beam

broadening factor of 1.34 in each plane. This results in a beam broadening factor of 1.13 for the -6 dB point of the two-way pattern. The comparison of calculated versus simulated individual BPE contributors is shown in Figures 3, 4, and 5 for REL, M1, and M2 errors, respectively, where BPE is expressed in terms of the one-way or two-way percent beamwidth. Figure 6 shows a comparison of the total BPE over the given range of antenna heights. Statistical results of the simulated BPEs were obtained from a sample of 1000 patterns which proved adequate for deriving RMS results.

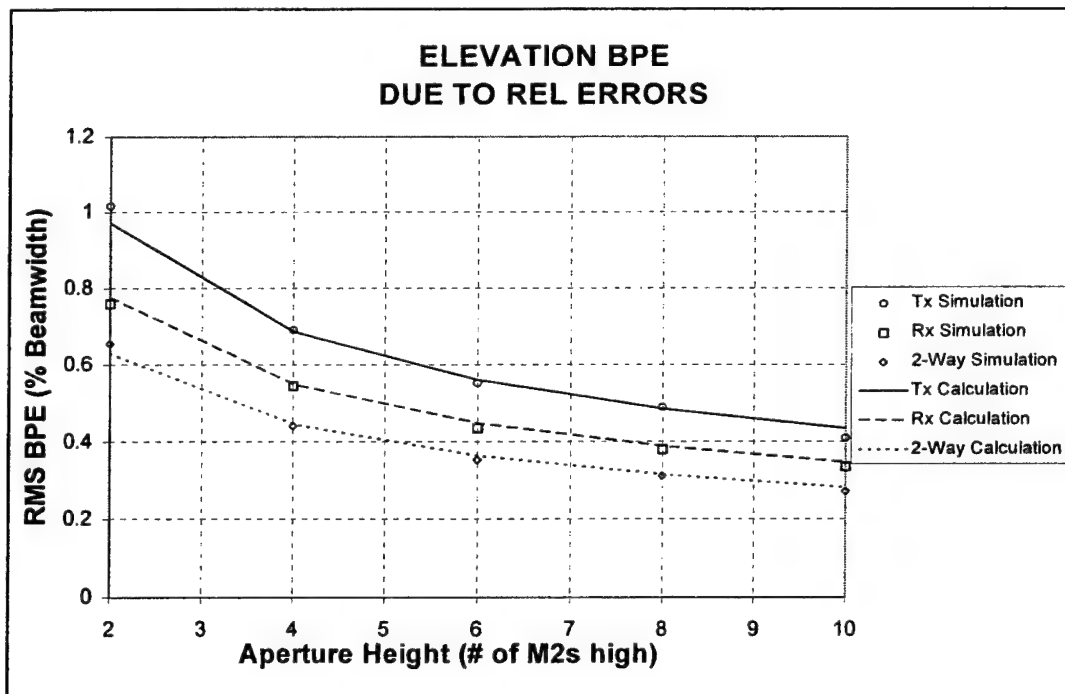
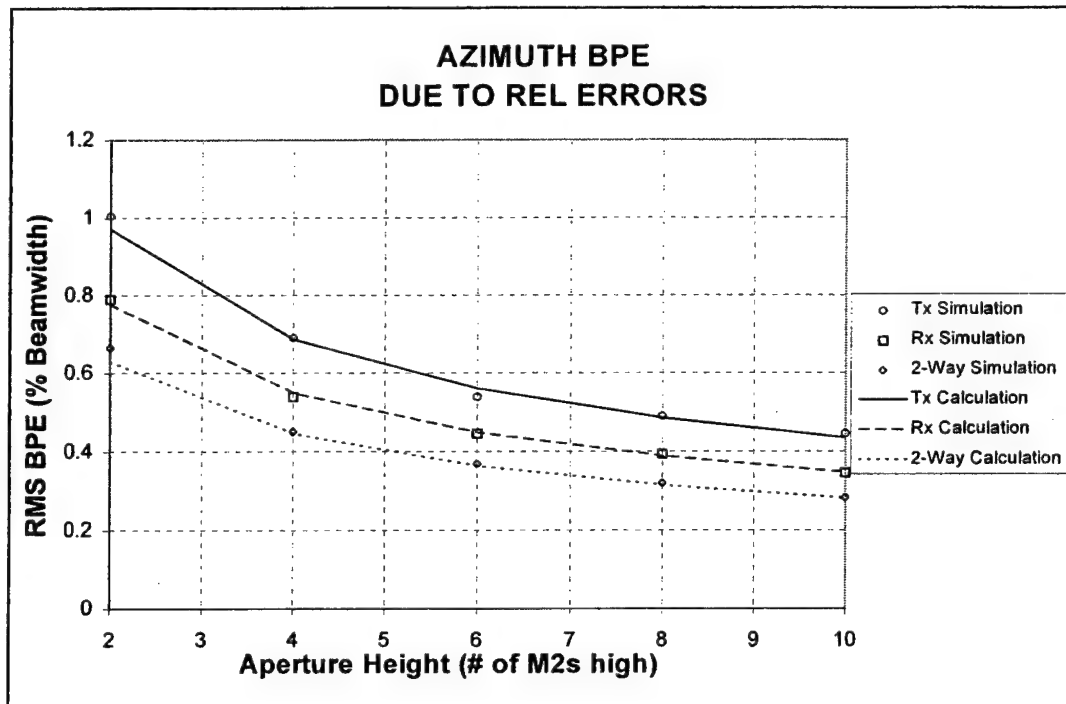


Figure 3 Comparison of Calculated Versus Simulated REL Induced BPE

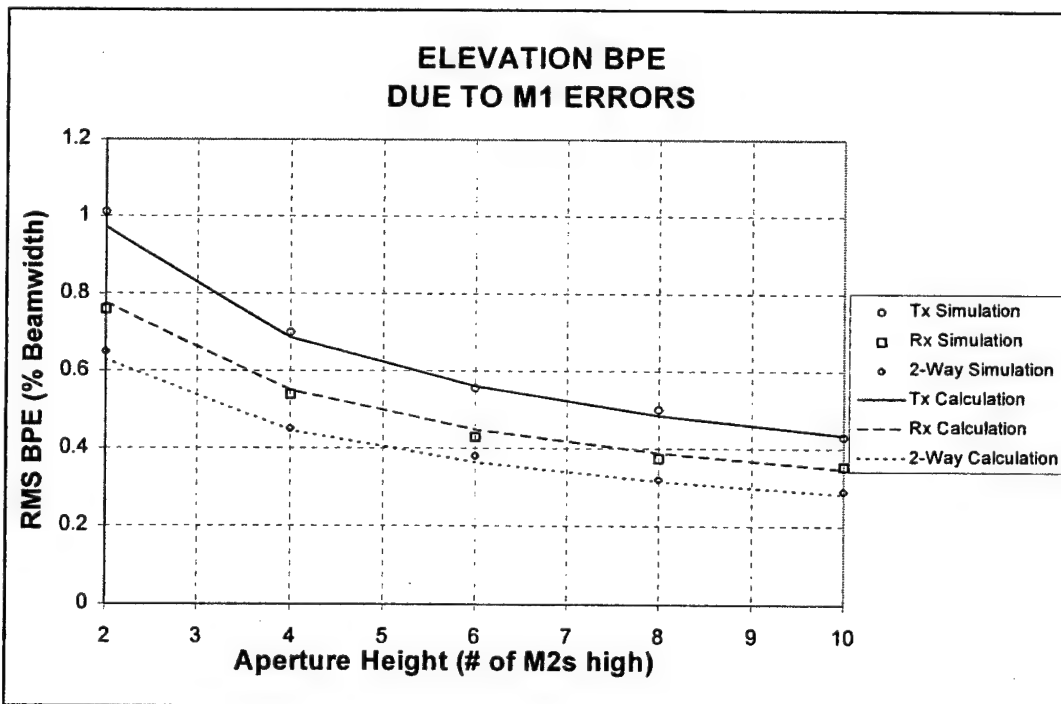
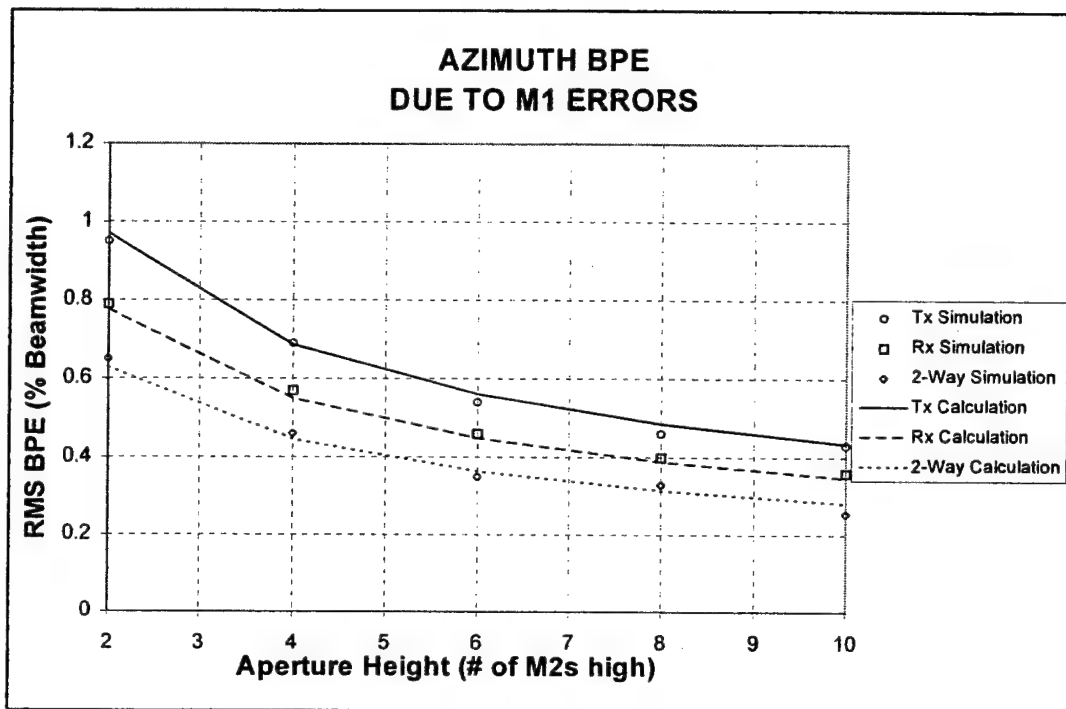


Figure 4 Comparison of Calculated Versus Simulated M1 Induced BPE

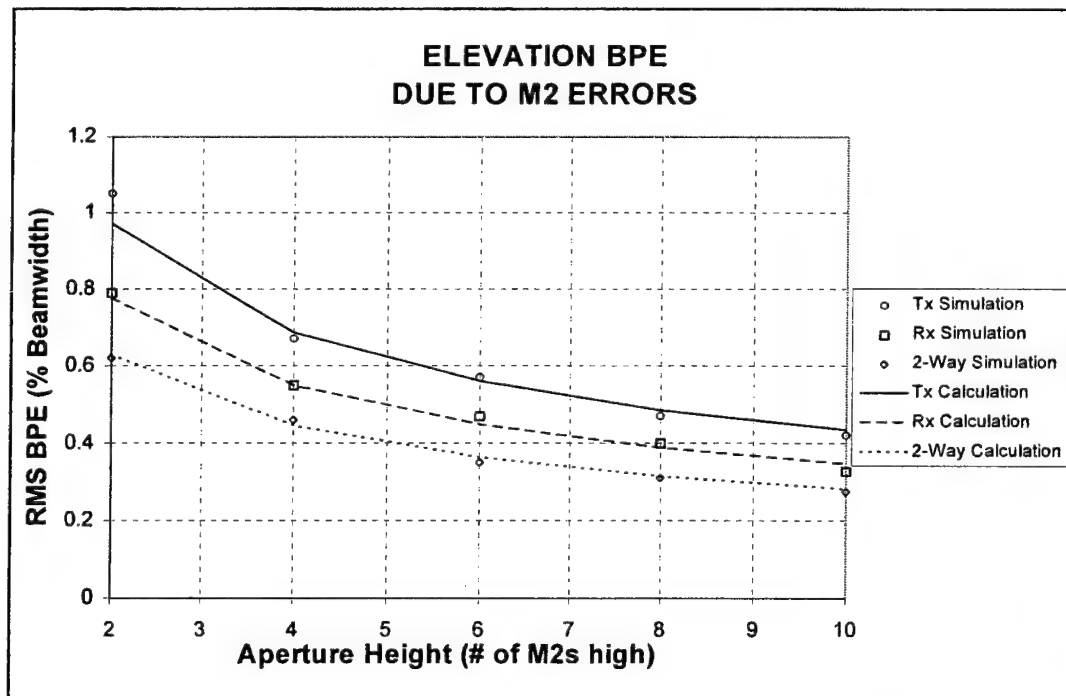
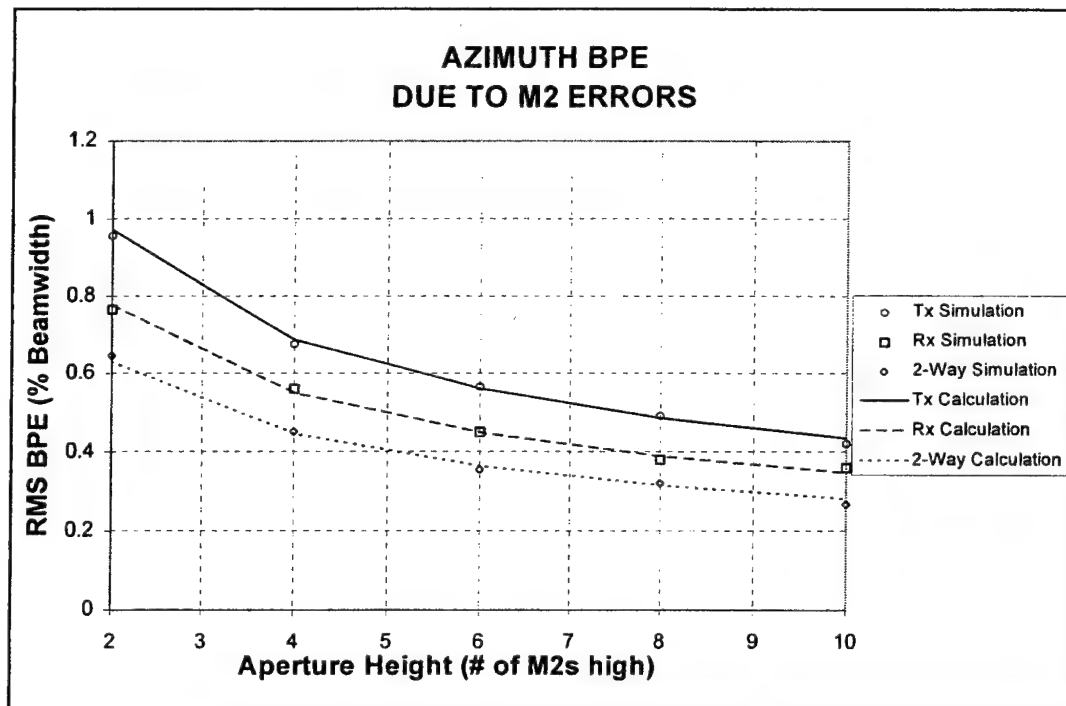


Figure 5 Comparison of Calculated Versus Simulated M2 Induced BPE

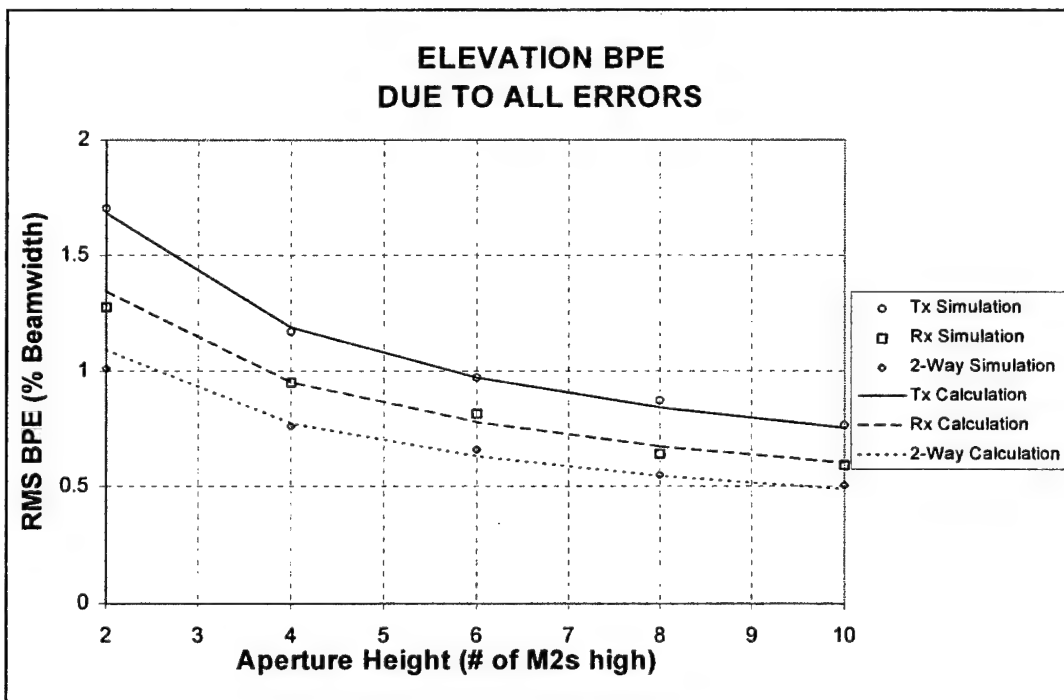
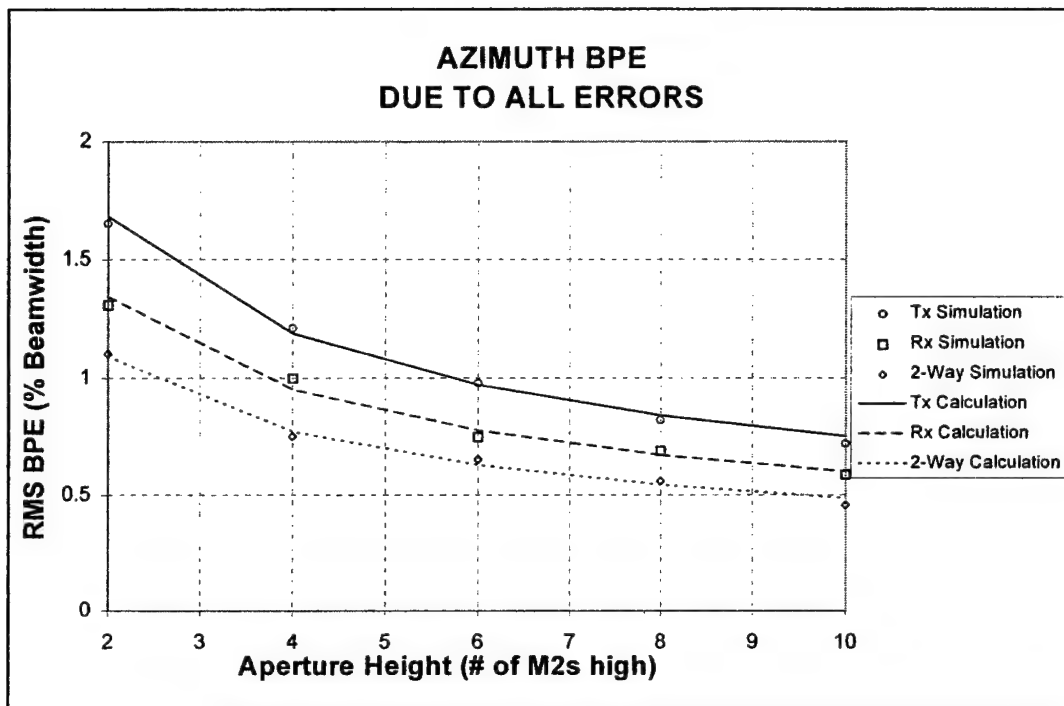


Figure 6 Comparison of Calculated Versus Simulated Total BPE

4. Summary

Simple expressions have been demonstrated to provide accurate predictions of BPE resulting from random phase errors across an array antenna constructed of modular sections. The discussion includes a detailed understanding of a wide variety of concepts such as:

- relationship between BPE and individual module levels
- relationship between BPE and combined module levels
- relating errors to one-way and two-way BPE
- converting between RMS and CEP BPE

The importance of these concepts is vital to integrating expected component tolerances to meet the required system level BPE specifications. Of equal importance is the generality of the developed relationships which makes them applicable to many systems.

^[1] Skolnik, M. I.: Introduction to Radar Systems (2nd ed.), McGraw-Hill Publishing Co., New York, pp. 318-322, 1980.

Analysis of Antenna Pattern Aperture Efficiency and Sidelobe Characteristics Using Array Factor Woodward Sample Point Information

Benjamin R. Myers

Kurt G. Ramsey

**Northrop Grumman
Electronic Sensors and Systems Division
Baltimore, MD**

September 17, 1997

Abstract

The use of the Woodward¹ synthesis procedure for effecting the realization of antenna patterns with special beam shapes has been used extensively; both in determining theoretical complex aperture distributions and in realizing them with a variety of array aperture feed networks. This paper examines the antenna pattern information available at the Woodward sample points of an array pattern and makes use of it to compute the aperture efficiency of the linear array pattern and the magnitude of the complex pattern voltages which can be used as inputs to a special feed network such as a Butler Matrix or a Blass feed network in order to realize the pattern in question.

Introduction

It is well known that the synthesis of linear array antenna patterns can be accomplished by the use of $\sin(Nx)/\sin(x)$ beams of the appropriate amplitude at the Woodward sample points associated with the array aperture element spacing and number of elements. Upon further examination, it is found that by sampling, e.g., a theoretical 60 dB Tchebyscheff pattern at its Woodward sample points that the voltage values obtained there can be used to compute the pattern aperture efficiency and are the weighting values of

the $\sin(Nx)/\sin(x)$ beams that, if placed at the corresponding Woodward sample points, can be used to realize the pattern in question, exactly, using an N port Butler Matrix or an N layer Blass feed network.

Technical Discussion

Referring to Figures 1 and 2, and noting that the Woodward sample points for an N element array are located in sine space, at the values:

$$-\lambda/2s + (k-1)(\lambda/Ns) \quad k=1, 2, 3, \dots, N \quad (1)$$

where:

λ = the free space wavelength at the operating frequency of the array

we define the geometry of the subject analysis.

This paper demonstrates that by sampling the theoretical linear array pattern at the Woodward sample points, defined in Figures 1 and 2, the information obtained can be used, in a very simple fashion, to determine the aperture efficiency of the linear array pattern and also provides the amplitude of the N composing beams that can be used to synthesize the beam using an N port Butler Matrix; the composing beams being of the form:

$$E(\theta) = W_k/N(\sin(N\pi s(\sin(\theta)+\sin(\phi_k))/\lambda))/\sin(\pi s(\sin(\theta)+\sin(\phi_k))/\lambda) \quad (2)$$

where:

$$\sin(\phi_k) = -\lambda/2s + (k-1)(\lambda/Ns) \quad k = 1, 2, 3, \dots, N$$

W_k = the voltage value of the pattern being analyzed at the kth Woodward sample point of that pattern

s = the array radiating element spacing

θ = the array angle space variable

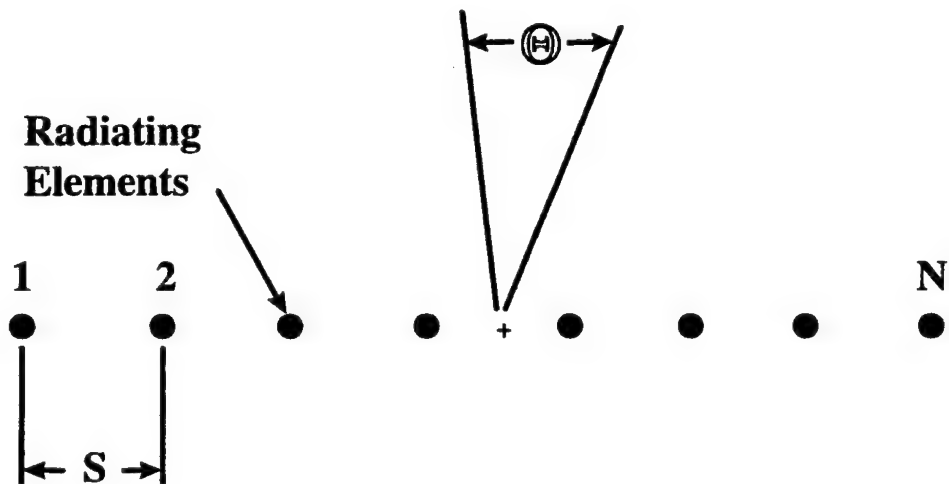
$E(\theta)$ can be recognized as the pattern of a uniformly illuminated linear array

scanned to a generalized Woodward sample point with a voltage multiplier of W_k .

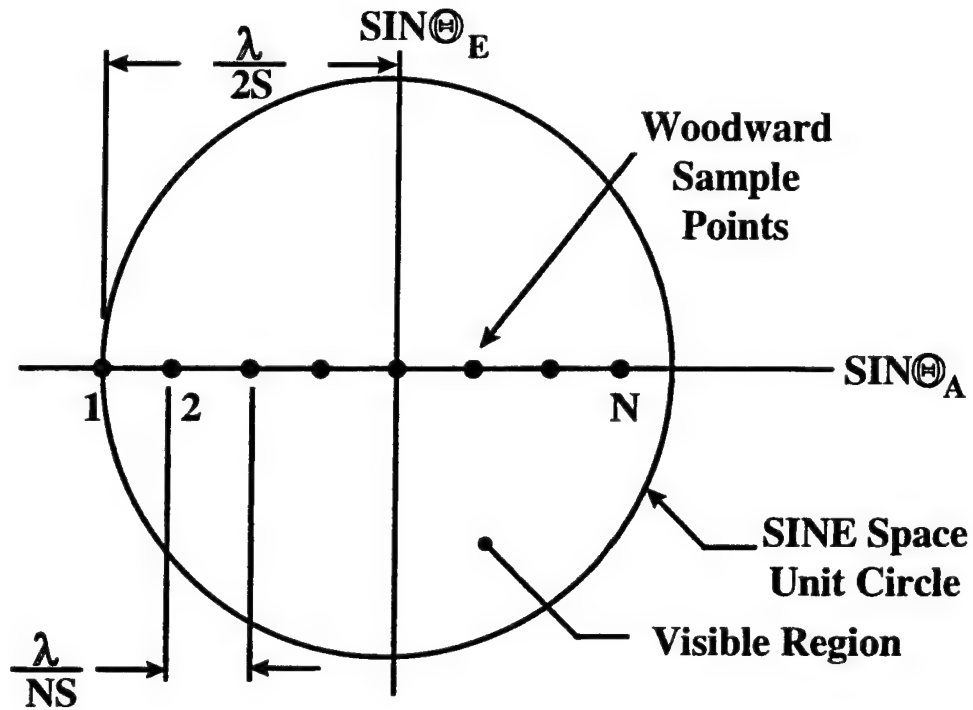
If we let $s = \lambda/2$:

$$\sin(\phi_k) = -1 + (k-1)(2/N)$$

and we will employ $s = \lambda/2$ for most of the discussions below.



Linear Array Geometry
Figure 1



Linear Array Woodward Sample Points
Figure 2

Using a 32 element array, with various Tchebyscheff linear array patterns, we can compute the aperture efficiency of the patterns using both of the following formulas (see Figure 3):

$$\eta = 10 \log_{10} \left(\frac{(\sum A_k)^2}{(N \sum A_k^2)} \right) \quad k = 1, 2, \dots, N \quad (3)$$

where:

A_k = the voltage at the k th radiating element in the aperture

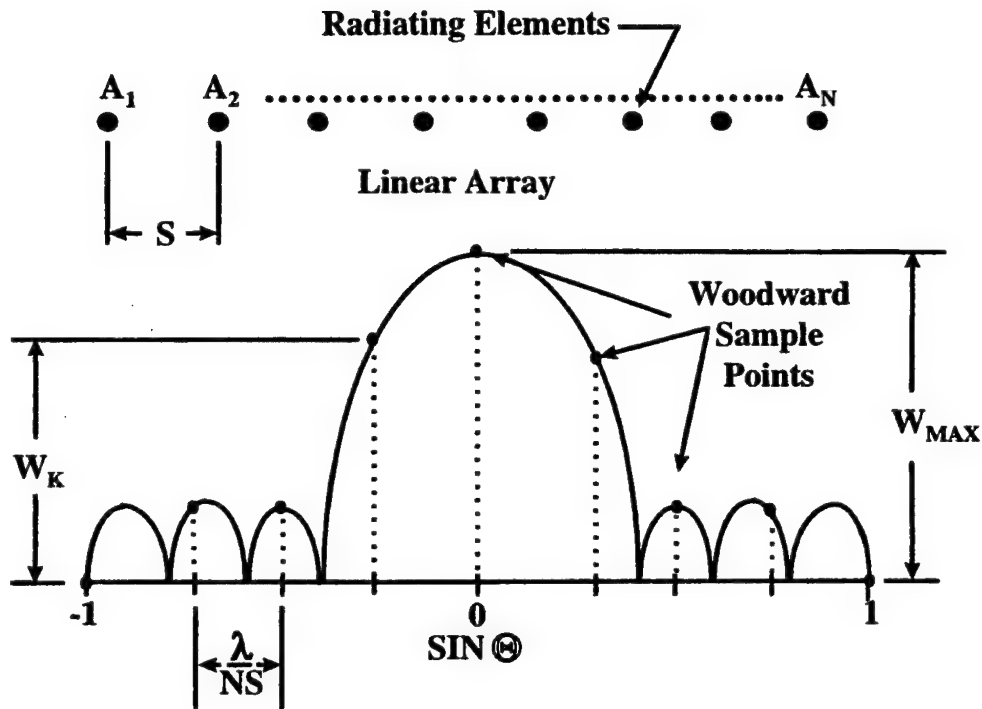
or:

$$\eta = 10 \log_{10} \left(\frac{(W_{MAX})^2}{(\sum W_k^2)} \right) \quad k = 1, 2, \dots, N \quad (4)$$

where:

W_{MAX} = the Woodward sample point voltage value at the pattern maximum (shown at 0 degrees in Figure 3)

W_k = the values of the voltages at the N Woodward sample points of the pattern of Figure 3



Woodward Sample Point/Pattern Geometry Definition
Figure 3

Table 1 shows a comparison of computed efficiency values (in dB) using formulas (3) and (4) for Tchebyscheff patterns having sidelobe levels of -20, -40 and -60 dB.

Table 1

Tchebyscheff Pattern Efficiency Comparison

Efficiency η

<u>Sidelobe Level</u>	<u>Formula (3)</u>	<u>Formula (4)</u>
-20 dB	-.3916 dB	-.3916 dB
-40 dB	-1.095 dB	-1.095 dB
-60 dB	-1.903 dB	-1.903 dB

The values in the table above agree exactly, (actually to six significant figures).

Figure 4 shows a 60 dB Tchebyscheff linear array pattern, one of several Tchebyscheff patterns being analyzed. The number of radiating elements is chosen to be 32; a convenient power of 2 and a number compatible with Butler Matrix beamformer configurations.

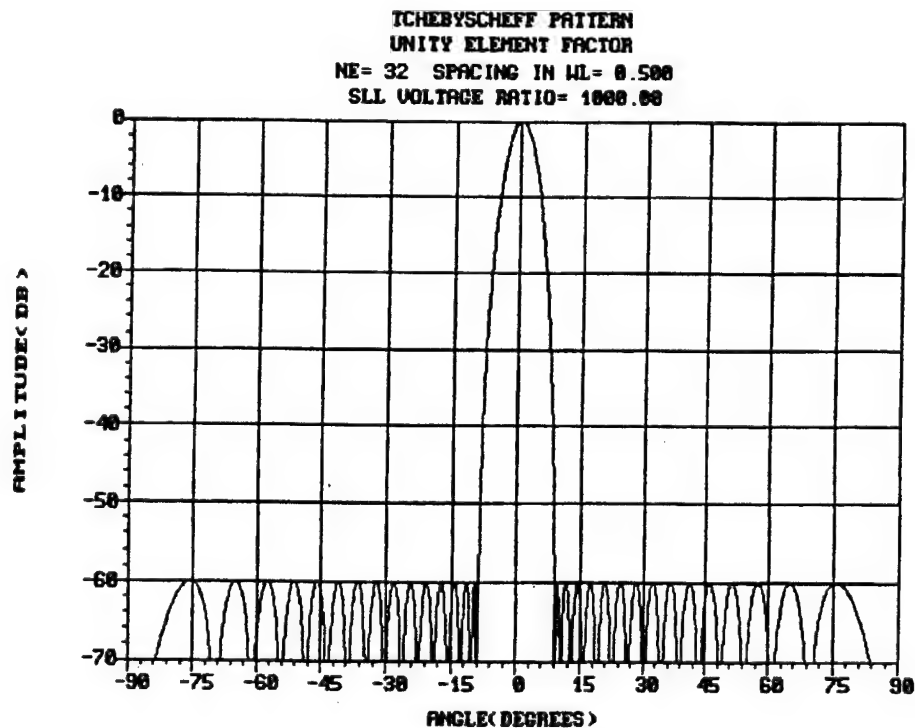


Figure 4

The linear array pattern of Figure 4 is computed using a standard DFT routine to transform from the aperture domain to the pattern domain. This pattern is then sampled at its N Woodward sample points to obtain the voltages W_k there. These values of W_k are the voltage values that are applied to an N port Butler Matrix in order to realize the pattern of Figure 5.

The values of W_k are used to generate the Tchebyscheff pattern of Figure 5 via the following relationship:

$$T(\theta) = \sum W_k / N (\sin(N\pi s(\sin(\theta) + \sin(\phi_k)) / \lambda)) / \sin(\pi s(\sin(\theta) + \sin(\phi_k)) / \lambda) \quad k=1,2,\dots,n \quad (5)$$

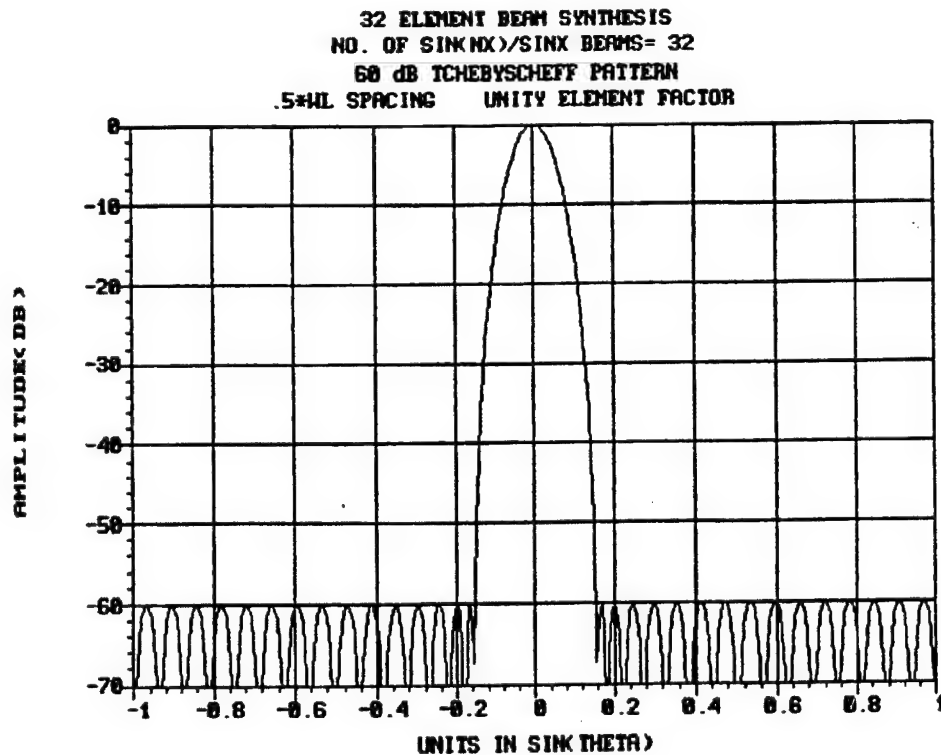


Figure 5

$T(\theta)$ is the sum of N uniformly illuminated linear array patterns, each one having its main beam centered at one of the N Woodward sample points of the pattern of Figure 4. The reconstructed pattern, using equation (5), is shown in Figure 5 and demonstrates that the Woodward sample point information obtained from the pattern of Figure 4 can be used to exactly form this same pattern (see Figure 5) using an N port Butler Matrix or equivalent feed network.

Figures 6 and 7 show that the same relationships, as discussed above, hold for a 40 dB Tchebyscheff pattern. Figures 8 and 9 demonstrate the same for a 20 dB Tchebyscheff pattern.

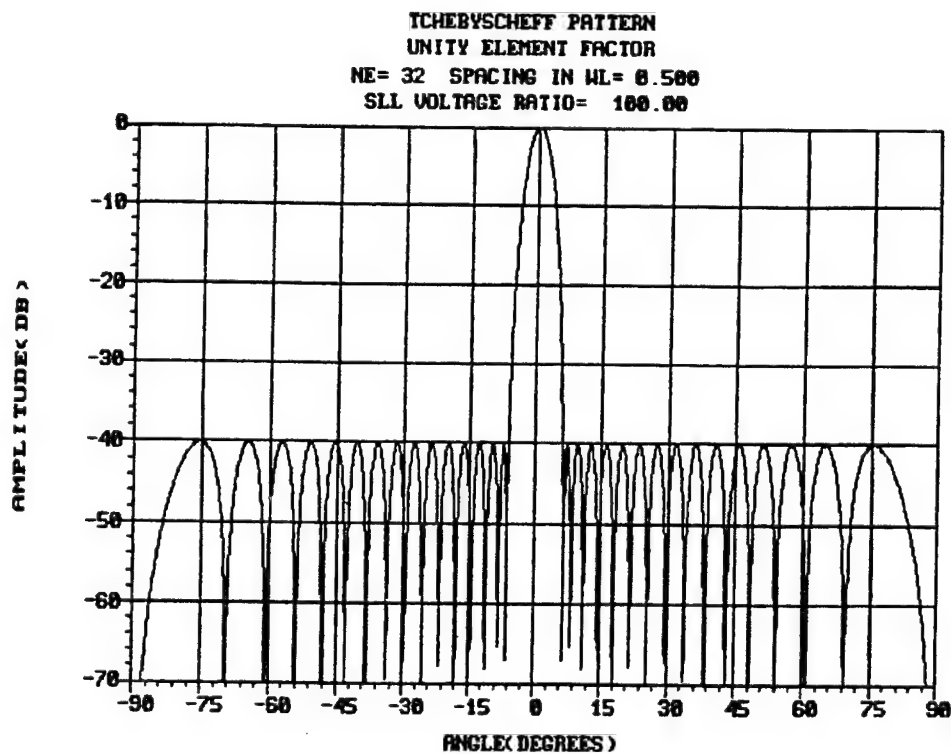


Figure 6

32 ELEMENT BEAM SYNTHESIS
NO. OF SIN(NX)/SINX BEAMS= 32
40 dB TCHEBYSCHIEFF PATTERN
UNITY ELEMENT FACTOR

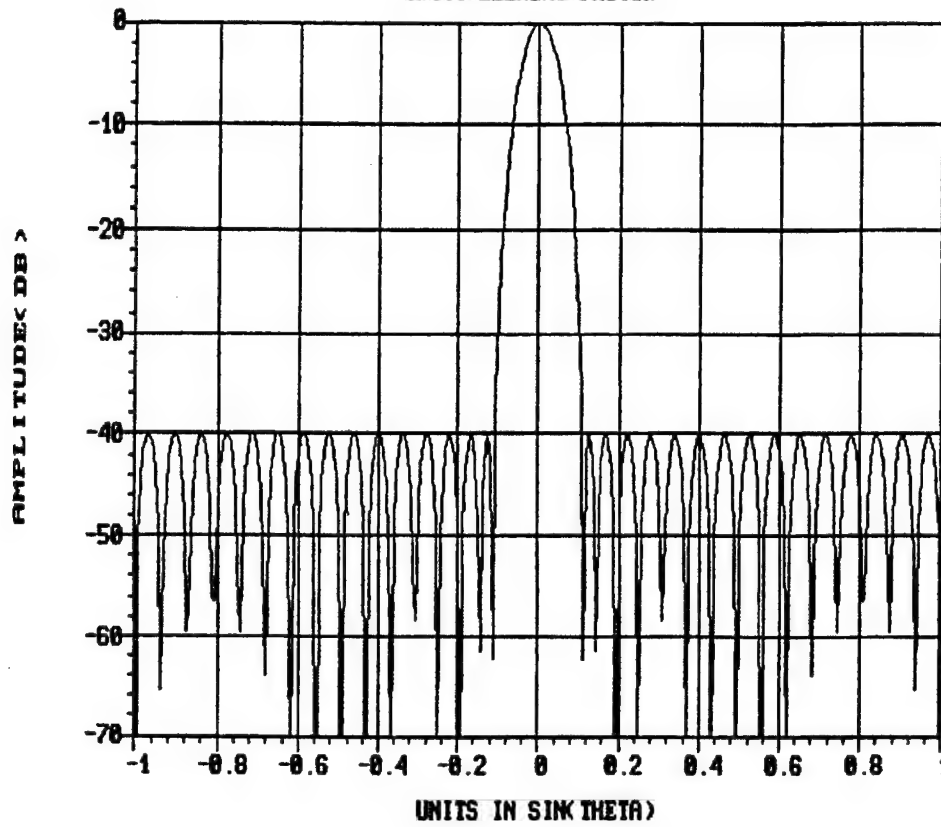


Figure 7

TCHEBYSCHOFF PATTERN
UNITY ELEMENT FACTOR
NE= 32 SPACING IN WL= 0.500
SLL VOLTAGE RATIO= 10.00

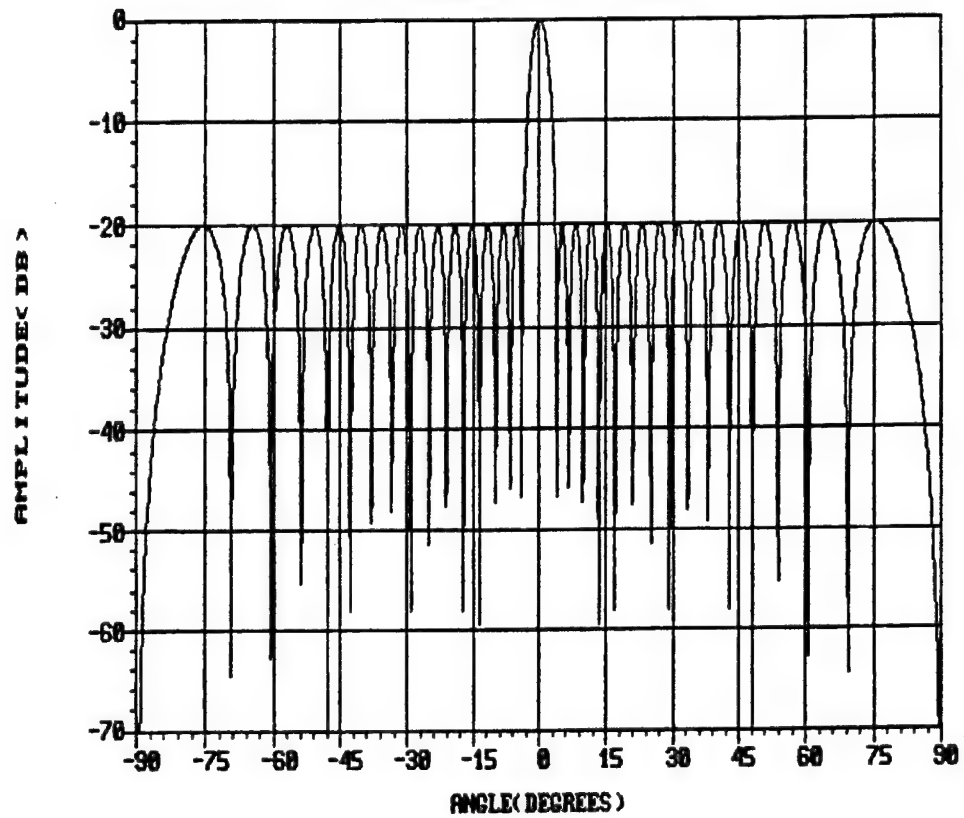


Figure 8

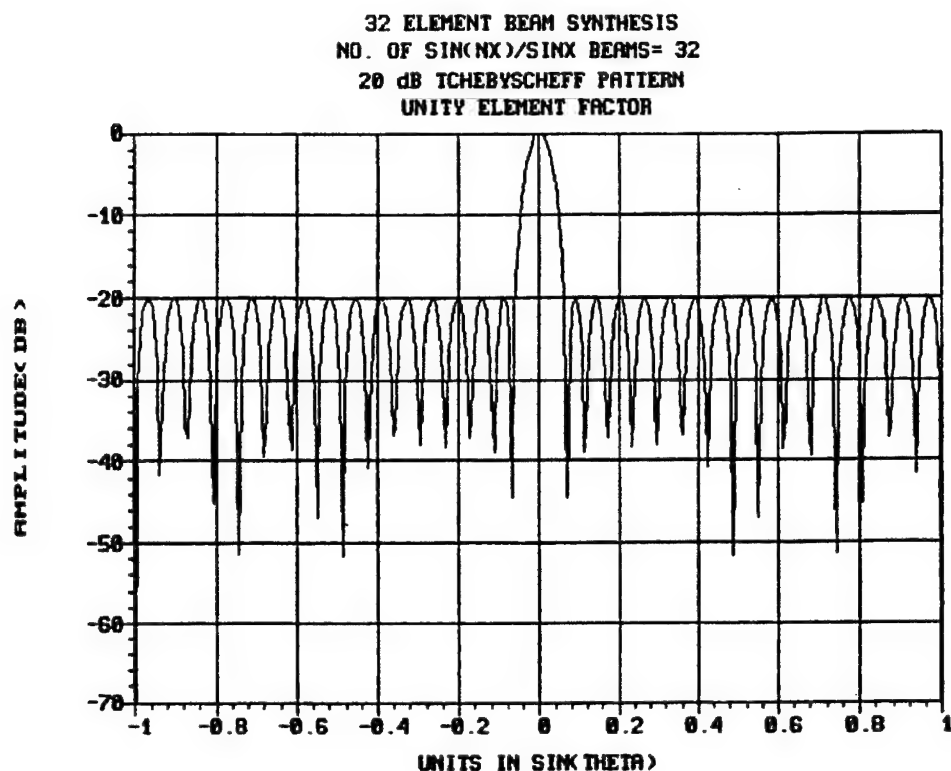


Figure 9

For spacings greater than one half wavelength, it was found that for the 60 dB Tchebyscheff pattern efficiency, the value of -1.903 dB was also obtained for both the $.5625\lambda$ and $.8\lambda$ spacing cases. This calculation took into account all "Woodward" sample points between -1 and $1 - \lambda/Ns$. The same value was obtained for these two spacings using only the normal range of 32 Woodward sample points, as well, at least to six significant figures. Pattern computations for the two element spacings just above gave similar results to those previously obtained above; i.e., excellent agreement between the DFT pattern computation method and the Woodward sample point voltage summation method.

Conclusion

The above discussion demonstrates that by sampling an arbitrary pencil beam pattern, computed from a set of predefined aperture distribution voltages, that the analysis of the Woodward sample point voltages of this pattern lead to an exact method of computing aperture efficiency and provide the values of the inputs to an N point Butler Matrix or N level Blass feed network which exactly realize the pattern in question.

Acknowledgements

The author would like to thank the late Hall Richard McComas; a brilliant and much admired colleague, for a suggestion which led to the writing of this paper.

References

- [1] Woodward, P. M. (1947). A method of calculating the field over a planar aperture required to produce a given polar diagram. *Proc. Inst. Elec. Engrs. (London)* **93**, Pt. III 1554 - 1558.
-

A COMPARISON OF RESISTIVE AND REACTIVE CORPORATE POWER DIVIDER NETWORKS FOR PHASED ARRAY ANTENNAS

Kevin W. Ommodt
Raytheon TI Systems
McKinney, TX

Abstract

Certain communication systems do not require the low sidelobe levels that are typical of radar systems. Because of this, phased array antennas for these communication systems do not need the tight control on element amplitude and phase errors that guarantee low sidelobe levels. In turn, this then calls into question the need for using resistive power dividers which help maintain low element errors. The alternative, reactive dividers, can introduce higher element errors but are smaller and less costly to implement.

This paper answers the question of whether reactive dividers can be used for large phased arrays without rigorous sidelobe requirements. The results of a theoretical analysis of a large phased array antenna with both a resistive and a reactive corporate power dividing network are presented. The effect of each of these divider networks is assessed on the overall array radiation pattern and the differences in performance are highlighted. The results indicate that reactive dividers may be used under certain conditions.

1. Introduction

There has been significant interest in using phased array antennas for a variety of communication systems in recent years. This differs from the traditional purpose for which they have been used, namely scanning radar systems. Radar systems typically require low sidelobe levels for proper operation, while certain communications systems do not require low sidelobe levels. For these communication systems, high gain is a more critical requirement. For such a communication system to maximize antenna gain, a uniform amplitude distribution is needed across the array to eliminate taper loss. This results in high sidelobes, i.e. -13 dB for a square aperture and -17 dB for a circular aperture. If an antenna by definition is going to have high sidelobes, the need for maintaining tight control of amplitude and phase errors in the array is lessened, since the primary reason for doing this is to provide low sidelobe levels.

If higher element amplitude and phase errors can be tolerated, then perhaps unconventional techniques in the corporate manifold can be considered which result in simpler fabrication. In this paper we will consider the effect of using reactive power dividers in the corporate power dividing network of a large phased array instead of the more conventional approach of using resistive power dividers.

The use of reactive dividers should result in a simpler and cheaper fabrication process.

2. Corporate Divider Networks

Corporate power dividing networks are commonly used for distributing microwave power throughout a phased array antenna system. Often Wilkinson power dividers [1] are used as the individual power splitters throughout the corporate manifold. They utilize a resistor to dissipate imbalances between the two output ports which results in good isolation over the design frequency band.

Reactive dividers are an alternative to Wilkinson dividers. They do not incorporate resistors and hence have degraded isolation between the output ports as well as degraded output port match. Figures 1 and 2 show the theoretical performance of equal power split Wilkinson and reactive power dividers, respectively. From the figures we can see that the reactive divider provides 6 dB of isolation and output port return loss while the isolation and output match of the Wilkinson divider at center frequency is perfect.

From a purely performance based point of view, the Wilkinson divider is superior. However, from a fabrication point of view, the Wilkinson divider is complicated by the need to include the isolation resistor. For example, consider a

corporate manifold implemented in stripline. The conventional method for implementing the resistors in such a circuit would be to use discrete devices which are soldered in place, often by hand. For a large array of N elements, $N-1$ resistors must be attached. This can be a painstaking and expensive process. A newer method of fabricating the resistors which is gaining acceptance is the use of etched or printed resistors which are fabricated into the stripline board. This can reduce the amount of labor required to implement the resistors, but it adds several extra processing steps to the fabrication cycle for the stripline board, which results in extra cost.

A secondary concern with the use of Wilkinson dividers is the size of the divider. Reactive dividers are in general more compact than Wilkinson dividers, and so as circuit densities continue to increase, the reactive divider may become more attractive from this standpoint as well.

3. Two Way Divider Example

The question then remains, what performance penalty exists for the use of reactive power dividers. To answer this question, we will first consider a simple two divider section of a phased array antenna as shown in Figure 3, complete with phase shifters and amplifiers. We note that for this example the phase shifter has a loss of 6 dB (we assume that solid state phase shifters which tend to have

significant loss are being used) and the amplifier has a gain of 25 dB. For now we will ignore mutual coupling between the antenna elements. If the components in each path are identical and are all matched to the system characteristic impedance, then the performance will be the same regardless of whether Wilkinson or reactive dividers are used. However, this is not a realistic case. In reality the components in the two paths will not be identical and they will not have perfect match to the system impedance.

To better understand what happens in the presence of mismatch, let us consider a mismatch at the input to the channel 1 amplifier in Figure 3. If we assume that this amplifier has a large mismatch of say -3 dB return loss, then we will certainly induce imbalance in the two channels which should show a performance difference between the Wilkinson and reactive dividers.

To give an indication of what is happening within the circuit, let us consider the first order reflected components which travel within the circuit. If we apply a 0 dB signal at the input to the circuit, we can see in Figure 4 what happens in the Wilkinson divider case. The input signal is split at the divider into two components of -3 dB each. These signals travel through the phase shifter where they are attenuated by 6 dB. The signal in channel 1 encounters the

mismatch at the amplifier while the signal in channel 2 encounters no mismatch at the amplifier and travels out to the antenna where it is radiated. The component that is reflected at the amplifier in channel 1 is of most interest to us. This reflected signal travels back through the phase shifter (where it is again attenuated by 6 dB) and then it encounters the Wilkinson divider where it is split equally with half the power going back to the input port and half being dissipated in the isolation resistor.

We can now consider the same situation for the reactive divider case as shown in Figure 5. The applied signal is the same and so a similar reflected component is generated which returns to the divider from channel 1. This time, however, the power is split three ways at the divider, with half returning to the input port (like the Wilkinson case), one quarter being reflected back into channel 1 and one quarter traveling through the divider over to channel 2. Obviously it is the last two components which cause the performance degradation in terms of element amplitude and phase error. However we note that both of these components must travel through a phase shifter two more times than the direct path, which for our example is an attenuation of 12 dB. Altogether, the reflected components are at least 21 dB down from the direct signal. From this we see that the phase shifters act in a manner similar to isolation resistors. Normally phase

shifter loss is considered to be a hindrance to the overall system performance, but for this particular issue it is beneficial in attenuating the reflected signal. Of course, if a large mismatch occurs on the divider side of the phase shifter, the loss in the phase shifter will not help in attenuating the reflected signal.

Now we haven't considered mutual coupling effects in the prior discussion, however, the isolation of the amplifier should prevent any significant power from traveling back down to the divider junction from the antenna element. Hence, mutual coupling effects should not present a problem for the reactive divider.

4. Large Array Model

In order to see if the principles discussed in the previous section hold true for a large array, we will consider extending the simple two element model of the previous section to a large array of 1024 elements. The array is 32 x 32 elements on a triangular grid with the sides of the equilateral triangle being .317" in length as shown in Figure 6. A schematic showing the network is presented in Figure 7. We will consider a receive antenna for this section as shown in Figure 7. A corporate power divider network with 1023 dividers is used. For the phase shifter an S-matrix of the form

$$\mathbf{S}_{phase} = \begin{bmatrix} -10dB \angle 0 \text{ deg} & -6dB \angle \phi_i \\ -6dB \angle \phi_i & -10dB \angle 0 \text{ deg} \end{bmatrix} \quad (1)$$

where

$$\phi_i = \text{Appropriate phase for element } i. \quad (2)$$

We note that the phase shifter loss is set at 6 dB. The phase shifter settings were set based upon theoretical values, i.e. no phase shifter quantization effects are included to avoid confusing the issue with quantization effects. An S-matrix of the form

$$\mathbf{S}_{amp} = \begin{bmatrix} -15dB \angle 0 \text{ deg} & -100dB \angle 0 \text{ deg} \\ 25dB \angle 0 \text{ deg} & -15dB \angle 0 \text{ deg} \end{bmatrix} \quad (3)$$

is used to model the amplifier.. The antenna elements are assumed to have a perfect 50 ohm match, mutual coupling effects are again ignored, and a uniform taper distribution is used across the array.

A proprietary linear network analysis program, MICRONET [2], was used to calculate the scattering matrix of the resulting 1025 port network. The amplitude and phase coefficients through the corporate divider were then summed to form an array factor which was multiplied by an element pattern of $\cos^n \theta$, where $n = 1.25$ to yield the overall array radiation pattern. This procedure was carried out for corporate networks with both Wilkinson and reactive dividers in place at a frequency of 20.7 GHz. Figure 8 shows the radiation pattern for the case of broadside scan and scan to 70 degrees in θ with $\phi = 0$. We see that the patterns for the Wilkinson and reactive dividers are essentially identical for these cases. In both of the scan cases, the peak gain of the two patterns differs by less than .01 dB.

5. Element Failure Analysis

From the analysis of the previous section we have found little difference in the overall radiated pattern when Wilkinson or reactive dividers are used. This comparison, however, assumed that all of the channels of the array were active. In an actual large operating phased array, some of the elements might be expected to fail with time and so we now shall consider the effect that element failures might have on the comparison.

From the example we considered in Section 3 we saw that a large mismatch on the antenna side of the phase shifter is attenuated by the phase shifter loss, and so this type of failure should produce minimal differences between the reactive and Wilkinson cases. A more problematic failure is that of a failure of the phase shifter itself. If a large mismatch (such as an open or short) were to be placed on the divider side of the phase shifter in Figure 3, significant imbalance between the channels will develop unattenuated by phase shifter loss. This is obviously a more severe failure mechanism than an amplifier failure in terms of producing channel imbalance. Given this fact, we will use this type of a failure to determine if the reactive dividers will provide acceptable performance with element failures in the array.

We will again use the 1024 element model from Section 4, but we now will place a short circuit on the corporate divider side of the phase shifter for 6% of the elements randomly distributed throughout the array. Rerunning the comparisons between the Wilkinson and reactive dividers, the array radiation patterns of Figures 9 and 10 result for scan angles of 0, 30, 50 and 70 degrees in θ with $\phi = 0$ degrees. Again we see that the patterns show little difference

except in the far out sidelobe structure. Only small differences in the peak gain occurs (maximum of .21 dB) for the four cases.

6. Conclusion

From a cost and size standpoint, reactive power dividers are an attractive alternative to Wilkinson power dividers for use in corporate power dividing networks for phased array antenna systems. From a performance standpoint the degraded channel to channel isolation and poor output match of reactive dividers present potential drawbacks. However, under some circumstances the effect of these negative qualities on the overall system performance is minimized. Specifically, for large phased array systems that do not require low sidelobe levels and therefore can tolerate higher element errors, reactive dividers may be an alternative. We have seen that a theoretical comparison of the radiation patterns of a large array with both Wilkinson and reactive dividers shows only minor differences in sidelobe structure when the phase shifters are relatively lossy (6 dB of loss). In this case, the phase shifters act as a pseudo isolation resistor for the corporate divider. Though the possibility of using a less costly corporate divider network may be attractive, this result should not be interpreted too broadly. The use of reactive dividers in arrays with high sidelobes is not appropriate if either

low loss phase shifters are used or phase shifters with high input/output match are used.

Acknowledgments

The author would like to acknowledge discussions with Bill Powers and Oren Kesler of Raytheon TI Systems and Jeffrey Herd of Rome Laboratory.

Portions of this work were supported by Rome Laboratory (Air Force Material Command and Space and Missile Systems Center) under contract number F30602-95-C-0055.

References

- [1] E. Wilkinson, "An N-Way Hybrid Power Divider," *IEEE Trans. Microwave Theory Tech.*, vol. 8, pp. 116-118, January 1960.
- [2] B. Powers, "MICRONET User's Guide," Texas Instruments, Inc., 1988.

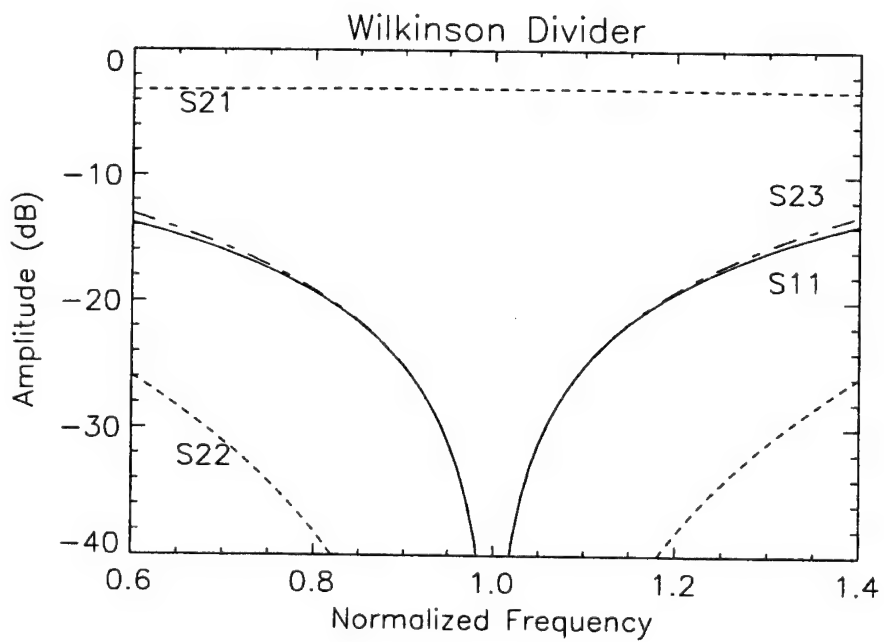
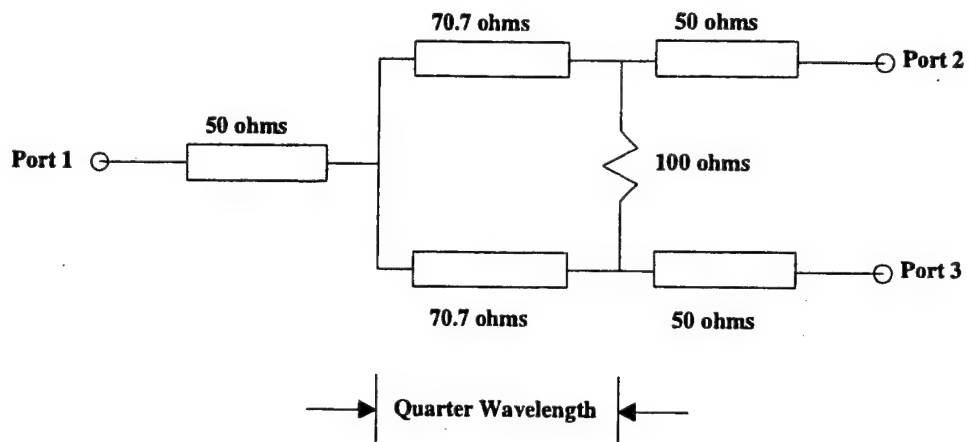


Figure 1. Theoretical Performance for Wilkinson Divider

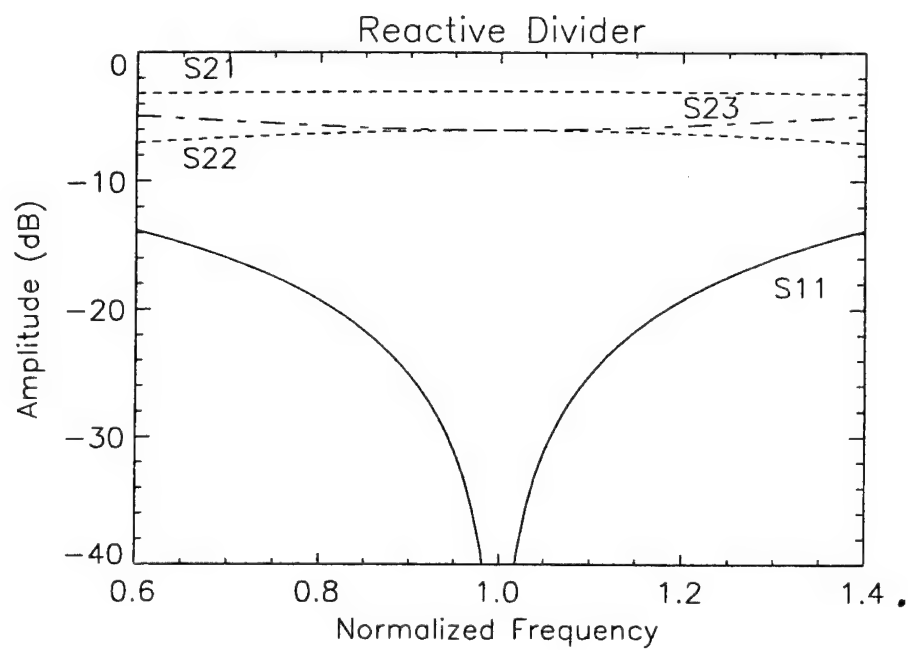
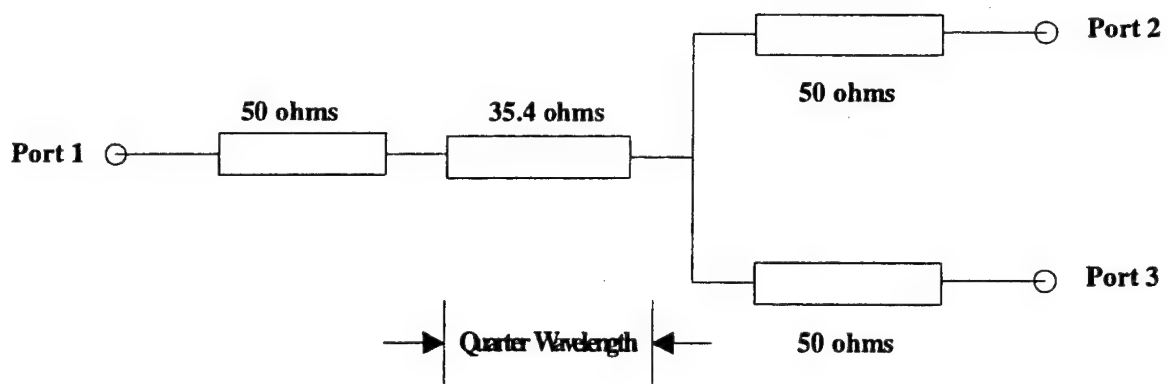


Figure 2. Theoretical Performance for Reactive Divider.

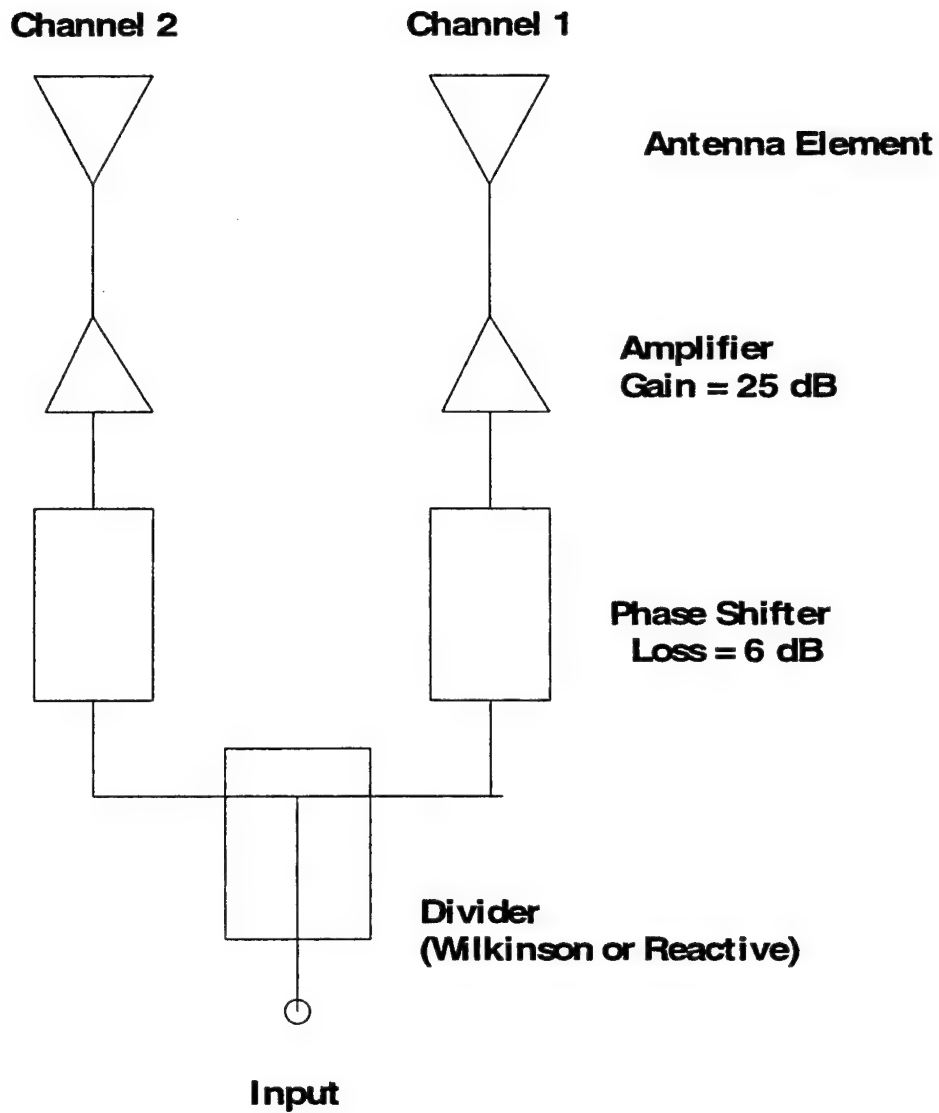


Figure 3. Two Channel Phased Array Section.

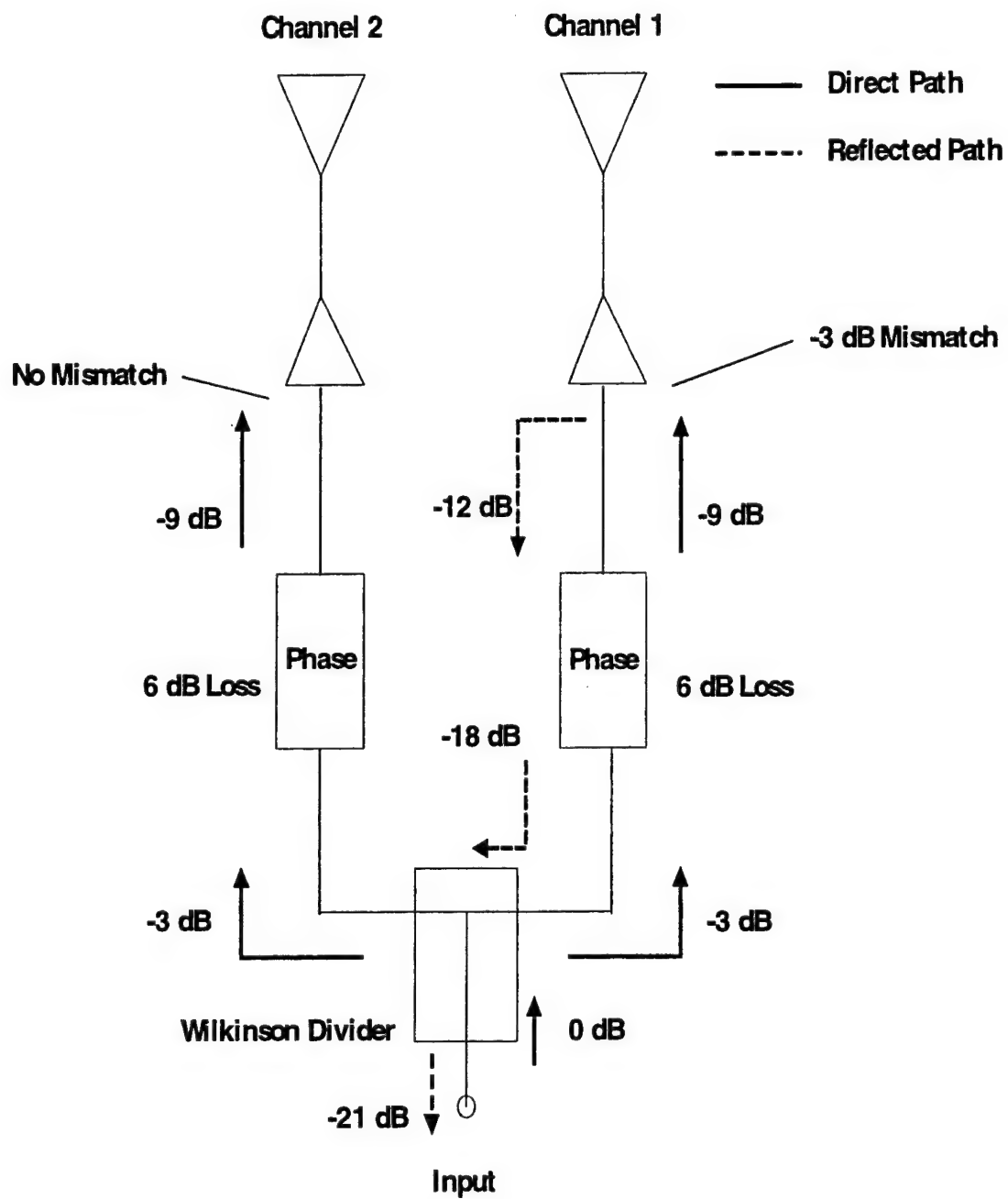


Figure 4. First Order Reflection in Two Channel Array with Wilkinson Divider.

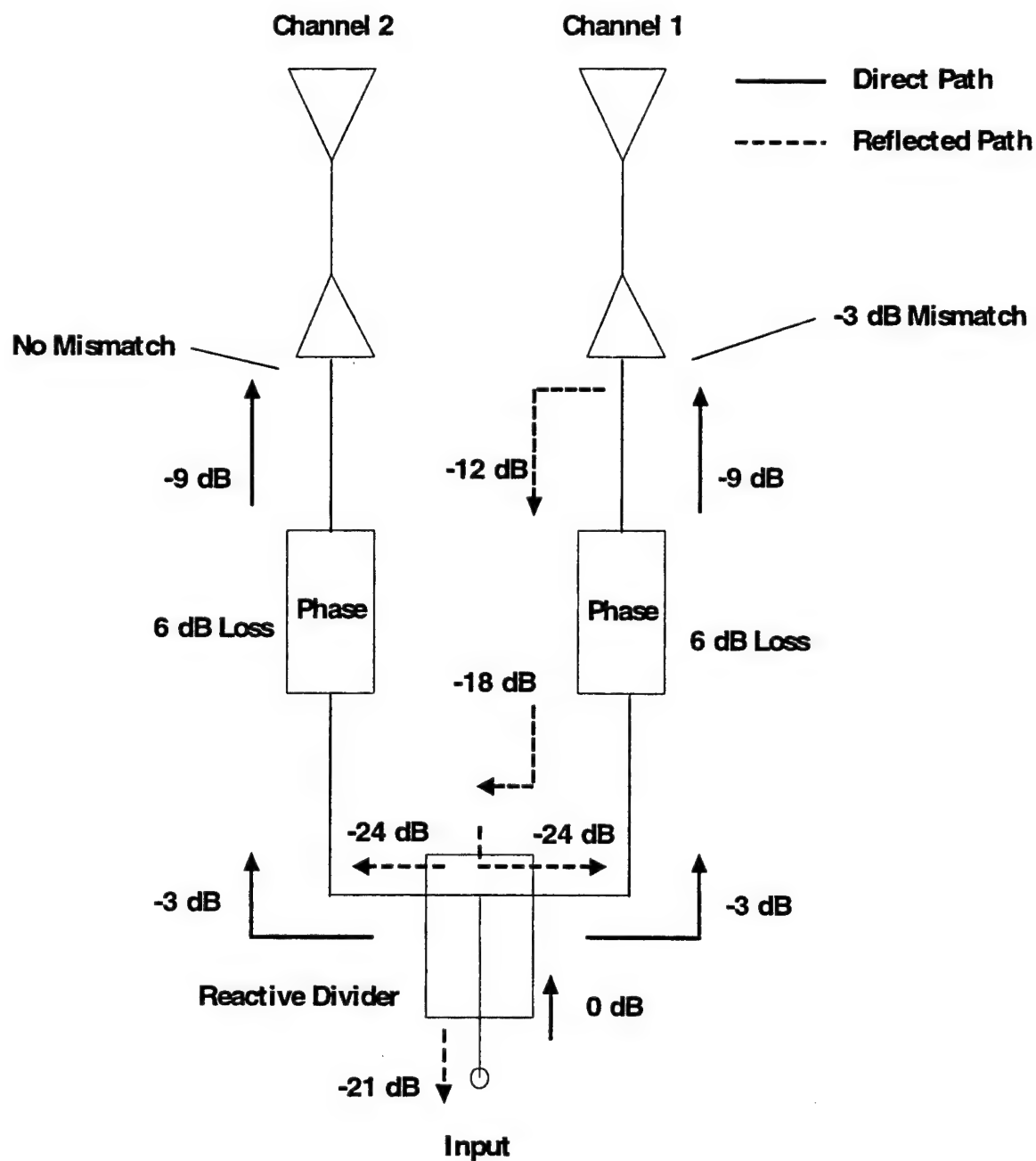


Figure 5. First Order Reflection in Two Channel Array with Reactive Divider.

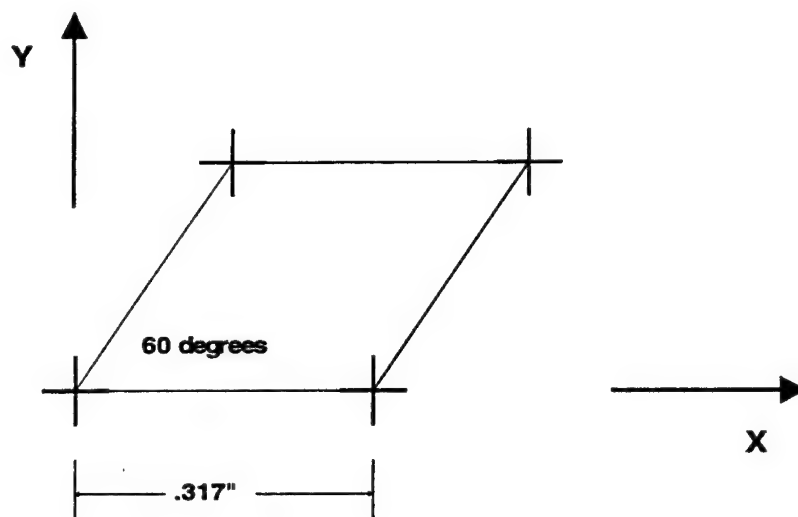


Figure 6. Array Grid Dimensions.

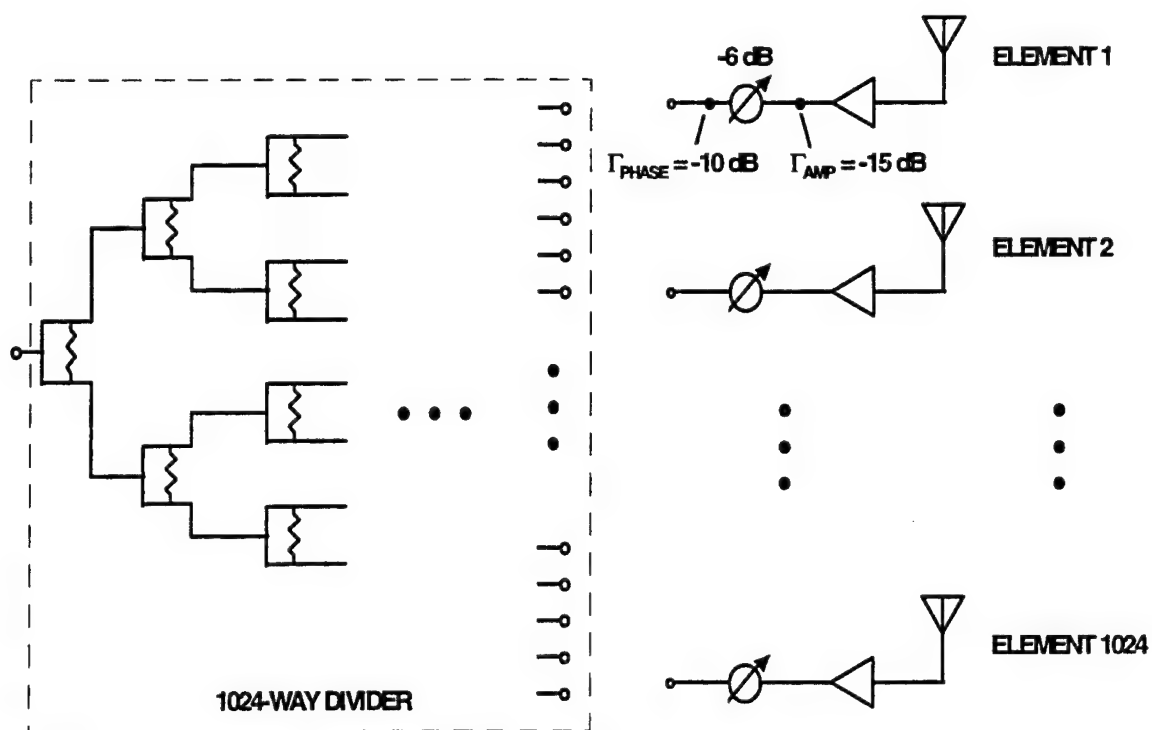


Figure 7. Large Array Model Schematic

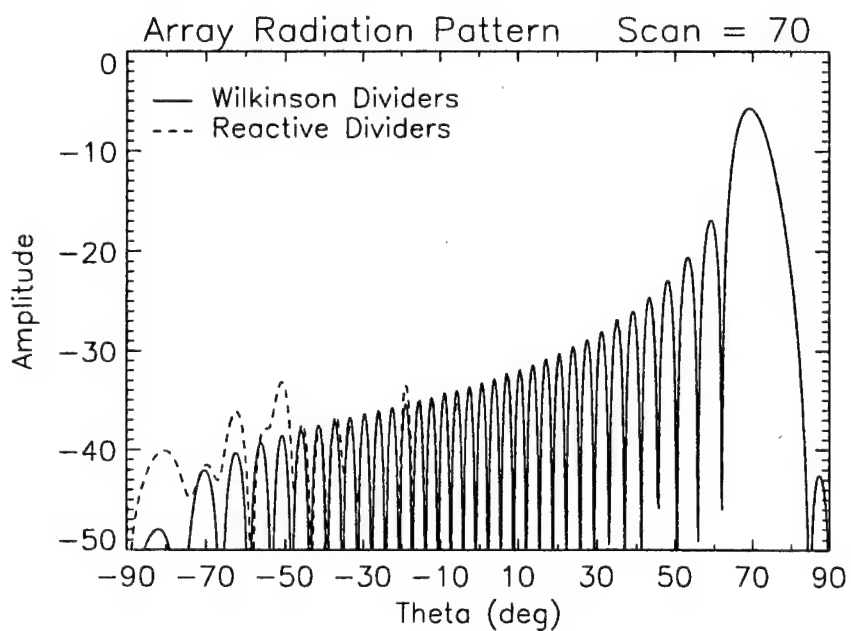
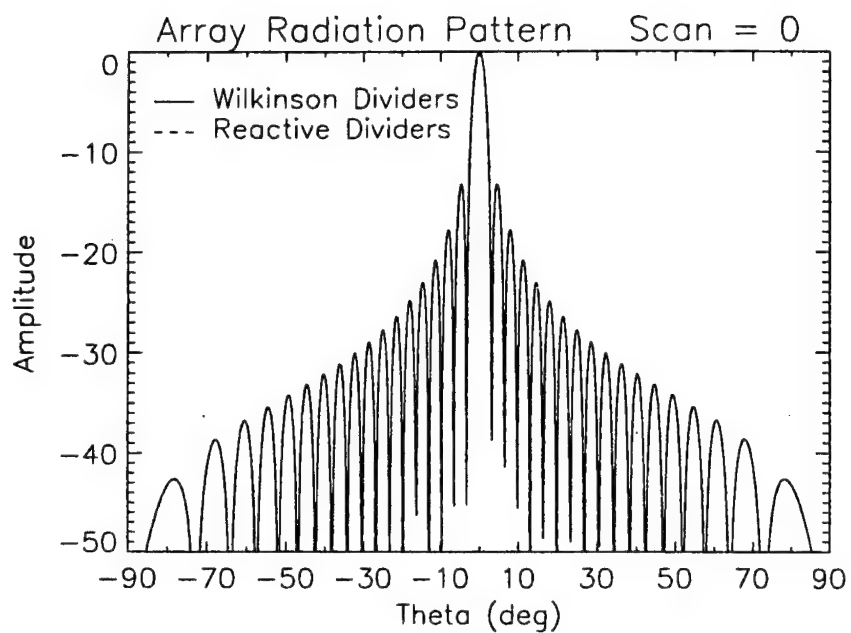


Figure 8. Array Radiation Pattern with No Element Failures and Scan Angles of 0 and 70 degrees.

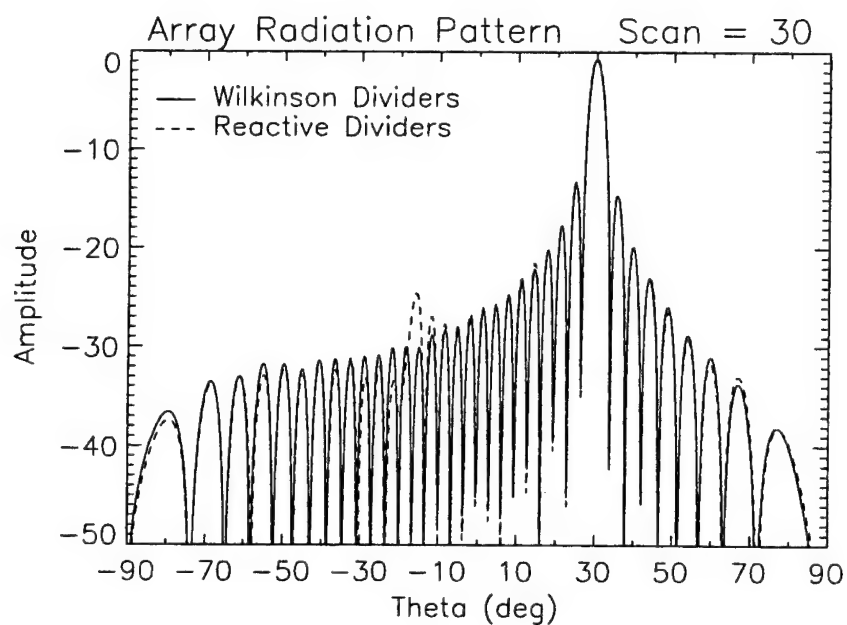
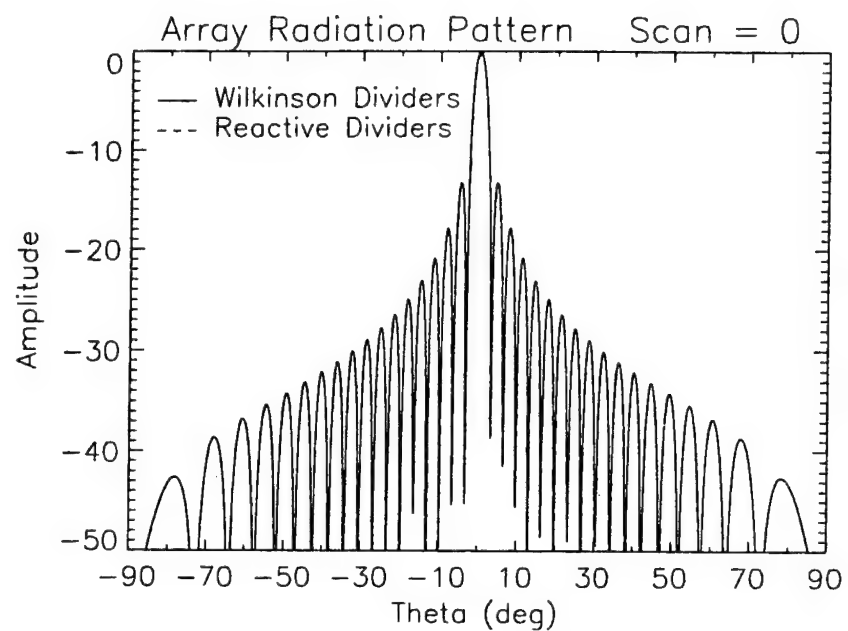


Figure 9. Array Radiation Pattern with 6% Element Failures and Scan Angles of 0 and 30 degrees.

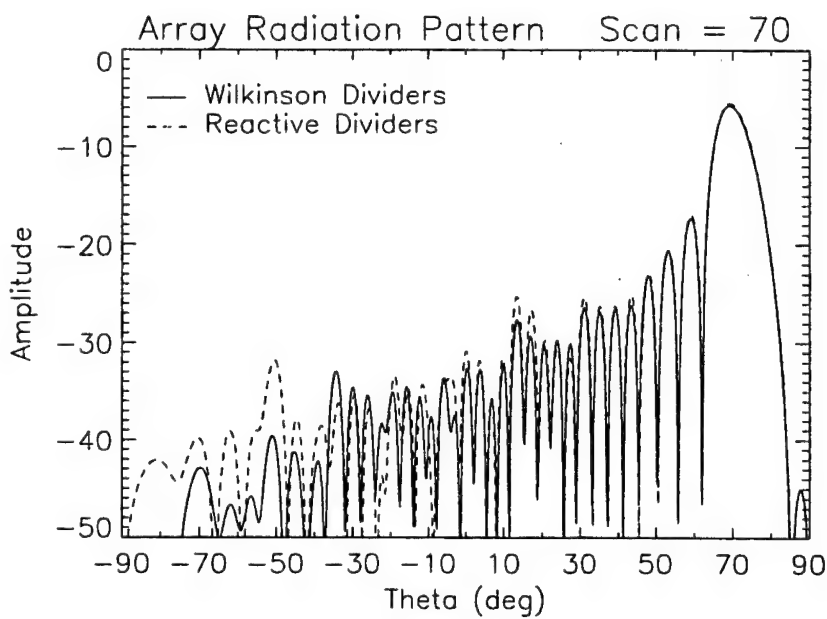
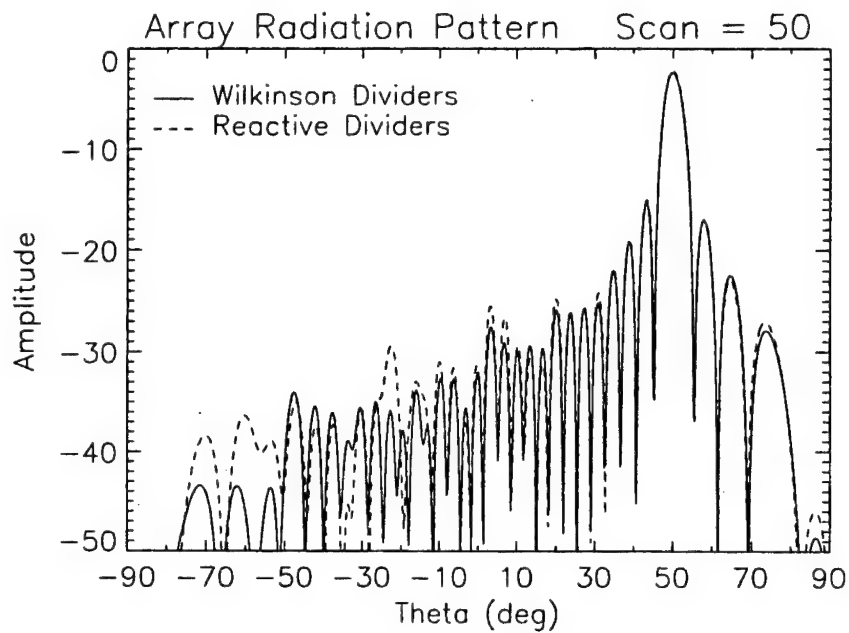


Figure 10. Array Radiation Pattern with 6% Element Failures and Scan Angles of 50 and 70 degrees.

Constrained Feed for Lightweight, Overlapped Subarray Antennas

Peter Franchi, Michelle Champion, Lt. Dale Linafelter and Hugh Southall
USAF Rome Laboratory
Electromagnetics and Reliability Directorate
RL/ERAA, 31 Grenier Street
Hanscom AFB, MA 01731-3010

Abstract

An array of overlapped subarrays using a constrained feed is shown to be a good candidate for a limited scan ($\pm 7.5^\circ$ in elevation) radar antenna application where weight is of primary concern. This approach substantially reduces the number of control elements (phase shifters and amplitude control) required in the elevation axis. We have investigated two constrained feed circuits which require the implementation of RF hybrids with unequal coupling coefficients in the cross arms. The proposed architecture is planar (or "tile") with the feed circuits located behind and parallel to the radiating face of the array. This requires multi-layer stripline with aperture coupled vertical interconnects. Both circuits result in very light weight antenna structures. In this paper, we determine optimum coupling coefficients for the RF hybrids.

1 Introduction

A phased-array antenna for an X-band tracking and fire control radar has a limited scan requirement in the elevation principal plane. The scan limits in the elevation plane are only $\theta_{max} = \pm 7.5^\circ$; however, in the azimuth plane, the scan limits are $\phi_{max} = \pm 60^\circ$. A summary of the system specifications pertinent to the antenna are shown in Table 1.

Conventional scan techniques will be used to scan the array in azimuth. To eliminate grating lobes, the element separation (in wavelengths) is constrained by

$$\frac{d_{az}}{\lambda} \leq \frac{1}{1 + |\sin \phi_{max}|}, \quad (1)$$

where ϕ_{max} is the maximum scan angle in azimuth, which is 60° , giving

$$\frac{d_{az}}{\lambda} \leq 0.536. \quad (2)$$

Aperture size	8 m ²
Aperture dimensions	$W = 150\lambda$ wide \times $L = 80\lambda$ high
Frequency	X-Band
Output power	2 KW (Avg), 10 KW (Peak)
Operating bandwidth	5 %
Instantaneous bandwidth	10 MHz
Electronic scan limits	$\pm 60^\circ AZ$, $\pm 7.5^\circ EL$
Sidelobe level (Elevation principal plane)	-35 dB RMS
Antenna weight	1500 pounds

Table 1: Phased-array antenna specifications

If we use θ_{max} in Equation 1, we get

$$\frac{d_{el}}{\lambda} \leq 0.88. \quad (3)$$

Therefore, using conventional scan techniques, phase controls can be spaced no farther than $.88\lambda$ apart. We will show that limited scan techniques allow us to place phase controls about 2λ apart resulting in a substantial savings.

Since the 8 m² aperture is assumed to be 150λ wide (azimuth) and 80λ high (elevation), and the assumed wavelength is 2.54 cm, the number of phase controls for azimuth scan is approximately 280. Associated with each active phase control are monolithic microwave integrated circuits (MMICs) such as low noise amplifiers and phase shifters as well as their associated DC and logic circuitry. In addition, a circulator is required for the radar function.

The goal is to minimize the number of phase controls, thus minimizing cost and weight. Since this is an airborne radar application, weight is a crucial parameter. For conventional beam scanning, as described above, there is little that can be done to reduce the number of phase controls; however, in the elevation plane, where the scan limits are smaller, limited scan techniques can be used to reduce the number of phase controls. Limited scan antenna systems can have many different forms, but as indicated above, the relative system cost and weight is proportional to the number of active phase controls [1].

It is instructive to first consider the minimum number of phase controls required to scan a given angular volume. Stated in various forms [1, 2, 3], the minimum number of phase controls necessary to scan an angular volume is equal to the number of antenna beams required to fill that volume. This condition is rigorous for orthogonal beams with uniform illumination [2], but has not been generalized to the cases of low sidelobe illuminations or of unequal gain (ripples) within the scan sector [1]. Since we are only considering limited scan in a single plane (elevation), we are interested in the minimum number of active phase controls required to scan in a single plane. An approximation to this minimum number of

phase controls, called the *Stangel limit*, is given by [1]

$$N_{min} = 2 \frac{\sin \theta_{max}}{\theta_3}, \quad (4)$$

for maximum elevation scan angle, θ_{max} , and half power beamwidth, θ_3 , in the elevation plane. The ratio of N , the number of phase controls actually implemented in the antenna design, to N_{min} is a measure of the economy of phase shifter usage and is called the element use factor [1]. Since the half power beamwidth in elevation is approximately $\frac{\lambda}{L}$, the element use factor can be computed from

$$\frac{N}{N_{min}} = \frac{N}{2 \frac{L}{\lambda} \sin \theta_{max}}. \quad (5)$$

The limited scan technique we propose to use is an array of overlapped subarrays [3]. Subarray phase centers are located a distance D apart, therefore, $N = \frac{L}{D}$, and the element use factor is given by

$$\frac{N}{N_{min}} = \frac{1}{2 \left[\frac{D}{\lambda} \right] \sin \theta_{max}}. \quad (6)$$

For $\theta_{max} = 7.5^\circ$, we use the minimum possible number of controls (ie $N = N_{min}$) when $\frac{D}{\lambda} \approx 3.8$. The element use factor is obviously larger than one when more than the minimum number of phase controls are used.

In Figure 1, we show the partially overlapped subarray antenna concept. The distance between subarray phase centers is D in Figure 1(a). As shown in Equation (5), D determines the element use factor. The constrained feed networks are shown notionally by the boxes in Figure 1 (a). The purpose of the feed network is to establish a suitable illumination function on the antenna aperture. Figure 1(b), shows that this illumination should approximate a sinc function. An ideal sinc function transforms into a far field pattern which is a rect function. This is the ideal subarray pattern with uniform gain over the scan region and infinitely steep skirts at the scan limits; however, this pattern cannot be realized in practice. If it could be realized, we could eliminate grating lobes as the array is scanned and still have phase controls located at relatively large spacing. There are feed circuits which allow us to approximate the desired illumination [4, 5, 6]. In the next Section, we describe two such feed circuits.

2 Constrained Feed Networks

2.1 Basic Building Block – The Quadrature Hybrid with Unequal Coupling

The basic network building block is the quadrature hybrid coupler with unequal field coupling coefficients between the crossed arms of the couplers. The representation of couplers in the DuFort circuit [4] and the Skobelev circuit [5] is slightly different, as shown in Figure 2. In Figure 2(a), the DuFort coupler is characterized by a characteristic angle ϕ . Input signals a and b are coupled to the output ports as indicated. The Skobelev coupler in Figure 2(b) is characterized by the two field coupling coefficients p and q.

2.2 Circuits of DuFort

A generalized, constrained, hybrid-coupled feed network for partially overlapped subarrays was described by DuFort [4]. The network consists of a modular arrangement of cascaded, matched quadrature hybrids. The network can be divided into two sections, referred to as type A and type B circuits. The type B circuit is a 1:M power divider constructed with M-1 hybrids, where M is the number of radiating elements per phase shifter. To provide the subarray overlap, the outputs of the type B networks are fed either directly or via crossovers to M adjacent type A circuits. The type A networks take the inputs from M adjacent type B circuits and distribute the input power to M radiating elements, producing M mutually orthogonal outputs. The type A circuits require $M(M-1)/2$ hybrids. With this architecture, excitation of a single input terminal produces an M^2 -element subarray aperture distribution. The network is passive, and, since all terminals are matched and all hybrid arms in the circuit are either interconnected, or appear at the input or output ports, the network is (theoretically) lossless. A DuFort network with $M=3$ is shown in Figure 3 for two adjacent, partially overlapping subarrays. This network has five hybrids per subarray terminal and produces a nine element subarray. The A_i , for $i = -4, -3, \dots, 0, \dots, +3, +4$ are the excitation coefficients due to the left subarray input port, while the a_i are due to the right subarray input port and, theoretically, $A_i = a_i$.

Subarray pattern control is achieved by varying the characteristic angles of the network hybrids. The number of degrees of freedom for pattern control is equal to the total number of hybrids, $M(M-1)/2 + (M-1)$. For the $M=3$ case, there are five hybrids, and thus five parameters for pattern control. However, most practical applications, including this one, require a symmetrical limited scan. This restricts the characteristic angles to those which produce a symmetrical subarray pattern, restricting the number of degrees of freedom. DuFort achieved symmetry by replacing some of the hybrids with magic-T's. For the $M=3$ case

shown in Figure 3, he replaced hybrids a, c and e with magic-T's, leaving two parameters (the characteristic angles of hybrids b and d) available for pattern control. Kachwalla [6] constructed a similar $M=3$ network using general quadrature hybrids rather than magic-T's. He achieved symmetry by imposing constraints on the outputs of the type A and type B circuits. These restrictions result in a dependency between hybrids d and e and hybrids a, b and c, and only two degrees of freedom are available for pattern control. With only two degrees of freedom, the ability to control the subarray pattern is limited, and, for some applications, a more complicated network (M larger than 3) may be needed to achieve the desired scan characteristics.

For our application, we chose to implement the network with general quadrature hybrids, rather than magic-T's. The excitation coefficients at the outputs (which feed the radiating elements) of this network are shown in Table 2 as a function of the hybrid characteristic angles. The coefficients are symmetrical about the center subarray element, and overlap the neighboring elements by three elements on either side. The radiating elements are a pair of co-phased microstrip patches separated by d_e as shown in Figure 1(a).

$A_{-4} =$	$\sin \phi_d \sin \phi_b \sin \phi_c$
$A_{-3} =$	$\sin \phi_d \sin \phi_b \cos \phi_c$
$A_{-2} =$	$-\sin \phi_d \cos \phi_b$
$A_{-1} =$	$-\cos \phi_d \cos \phi_e (\cos \phi_a \cos \phi_b \sin \phi_c + \sin \phi_a \cos \phi_c)$
$A_0 =$	$-\cos \phi_d \cos \phi_e (\cos \phi_a \cos \phi_b \cos \phi_c - \sin \phi_a \sin \phi_c)$
$A_1 =$	$-\cos \phi_d \cos \phi_e \cos \phi_a \sin \phi_b$
$A_2 =$	$-\cos \phi_d \sin \phi_e (\cos \phi_a \cos \phi_c - \sin \phi_a \cos \phi_b \sin \phi_c)$
$A_3 =$	$\cos \phi_d \sin \phi_e (\sin \phi_a \cos \phi_b \cos \phi_c + \cos \phi_a \sin \phi_c)$
$A_4 =$	$\cos \phi_d \sin \phi_e \sin \phi_a \sin \phi_b$

Table 2: DuFort Excitation Coefficients

2.3 Circuits of Skobelev

A feed network which yields subarray patterns with steeper skirts in the transition region at the scan limits was described by Skobelev [5]. It is sometimes referred to as a "chess" network due to the symmetrical pattern of the quadrature hybrid couplers as shown in Figure 4. For the case $N=1$, there are two layers of hybrids which connect to six radiating elements. Within each layer, the coupling coefficients of all the hybrids in that layer are equal. For example, in layer one, all of the p coefficients (see Figure 2) are equal to p_1 , and similarly, all the q coefficients are equal to q_1 . In layer two, all p 's are equal to p_2 and all q 's are equal to q_2 . For the case $N=2$, there are four layers of hybrids and a similar indexing of coupling coefficients holds. For $N=2$, there are ten radiating elements.

$$\begin{array}{l}
B_1 = p_1 p_2 + j p_1 q_2 \\
B_2 = j p_2 q_1 \\
B_3 = -q_1 q_2
\end{array}$$

Table 3: Skobelev N=1 Excitation Coefficients

$$\begin{array}{l}
A_1 = p_1 p_2 p_3 p_4 - p_2 p_4 q_1 q_3 - p_1 p_3 q_2 q_4 + j[p_1 p_3 p_4 q_2 + p_1 p_2 p_3 q_4 - q_1 q_3 q_4 p_2] \\
A_2 = -p_1 p_4 q_2 q_3 + j[p_1 p_2 p_4 q_3 + p_2 p_3 p_4 q_1 - p_3 q_1 q_2 q_4] \\
A_3 = -p_1 p_2 q_3 q_4 - p_2 p_3 q_1 q_4 - p_3 p_4 q_1 q_2 - j p_1 q_2 q_3 q_4 \\
A_4 = -j p_4 q_1 q_2 q_3 \\
A_5 = q_1 q_2 q_3 q_4
\end{array}$$

Table 4: Skobelev N=2 Excitation Coefficients

It is relatively simple to trace through the circuit paths to obtain the excitation coefficients at the radiating elements of the two circuits. These coefficients are shown in Tables 3 and 4. They are symmetrical about the center of the subarray aperture, therefore, $B_i = B_{-i}$, for $i=1,2,3$ and $A_i = A_{-i}$, for $i=1,2,3,4,5$ (see Figure 4). Two overlapping subarrays are shown for the N=1 and N=2 cases. The excitation coefficients for the second subarray are indicated by the lower case b_i and a_i and are equal to the respective B_i and A_i in theory. The subarrays overlap by four elements for N=1 and by eight elements for N=2.

The separation between radiating elements, d , is equal to half the separation between subarray phase centers, D . This is indicated notionally in Figure 1(a); however, D appears much larger than d in this conceptual drawing. Since D is on the order of two wavelengths, d is on the order of a wavelength, which is large enough to cause grating lobes in the (unscanned) subarray pattern. We therefore split this element into two co-phased elements (patch elements in keeping with the planar, tile architecture). In Figure 1(a), each of the radiating elements shown represents two discrete patch radiators separated by d_e . A design parameter, ϵ , is used to establish the separation which results in the best performance. The separation between the two individual patch radiators is

$$d_e = \frac{d}{2} + \epsilon. \quad (7)$$

We found that a value of $d_e = 0.585$ substantially reduces the grating lobes in the subarray pattern. For $D=2$, this means that $\epsilon = 0.085$.

In the next Section, we show subarray patterns for both DuFort and Skobelev feed circuits. The excitation coefficients used to generate these subarray patterns were obtained from an optimization process, which we also describe. We show that the excitation coefficients, when used in an array of subarrays, result in an array which can be scanned and maintain relatively low sidelobe levels.

3 Optimized Subarray Patterns

3.1 Optimization Technique

A subarray radiation pattern produced from the excitation coefficients of a subarray feed network is shown in Figure 5. For optimization, we must calculate a single number which represents the figure of merit for that subarray pattern. Then, as we vary the hybrid coupling coefficients over all possible combinations (within their valid ranges), we find the best figure of merit and select the corresponding coupling coefficients as the optimum ones. This is simply an exhaustive search procedure.

For the figure of merit, we take the weighted sum of the two areas illustrated by the vertical lines (gain loss in the scan region) and the diagonal lines (subarray pattern sidelobes above -20 dB relative to the peak subarray gain). We found that subarray sidelobes below -20 dB give good system performance. Also, we are only concerned about sidelobes up to the grating lobe location when the main beam is scanned to the scan limit. The grating lobe angle, θ_g , is indicated in the Figure 5 and is calculated from

$$\sin \theta_n = \sin \theta_0 + n \frac{\lambda}{D}, \quad (8)$$

where $n = \pm 1, \pm 2, \dots$, and θ_0 is the scan limit of 7.5° . For $D=2\lambda$, the grating lobe is at $\theta_g = \theta_{\pm 1} = \pm 21.7^\circ$. Since both areas in Figure 5 are minimum for best performance, we seek to minimize the weighted sum of both areas. We typically use equal weighting.

For the $N=2$ Skobelev circuit, we use a genetic algorithm optimization technique [7]. The cost function for the genetic algorithm is the same as the figure of merit described above.

3.2 DuFort Subarray Patterns

We vary the characteristic angles of hybrids a and d in the DuFort network and calculate a subarray pattern for each resulting aperture illumination. From these patterns, we determine the best figure of merit (calculated as described above) and the corresponding optimum characteristic angles of the hybrid couplers a and d. Characteristic angles for hybrids b, c and e are calculated from the values for a and d to give a symmetrical subarray illumination. The optimized values of the characteristic angles are shown in Table 5. These values are used with the expressions in Table 2 to calculate the subarray aperture illumination and finally, a subarray pattern. The array factor, including the subarray illumination, is combined with the two-patch radiation pattern to give the subarray pattern shown in Figure 6.

$\phi_a =$	16.2
$\phi_b =$	31.7
$\phi_c =$	16.2
$\phi_d =$	14.2
$\phi_e =$	14.7

Table 5: Hybrid Characteristic Angles, Degrees

$p_1 =$.923 (-0.70 dB)
$p_2 =$.707 (-3.00 dB)
$q_1 =$.385 (-8.29 dB)
$q_2 =$.707 (-3.00 dB)

Table 6: Optimum Coupling Coefficients for the Skobelev circuit, N=1

3.3 Skobelev Subarray Patterns

The hybrid coupling coefficients for the N=1 case are found using the exhaustive search optimization technique described in Section 3.1. The coefficients for the N=2 case are found using a genetic algorithm optimization technique [7]. The coefficients are shown in Tables 6 and 7 and the resulting subarray far field patterns are shown in Figures 7 and 8. The N=2 case has less gain loss over the scan region and steeper skirts at the scan limits.

3.4 Scan Performance

If we combine 39 of the DuFort or Skobelev (N=1) subarrays, we can obtain an estimate of the scanning performance of the array in elevation. This number of overlapped subarrays gives an aperture height of approximately 80λ . The combined subarrays are weighted using a 40 dB Taylor taper to give the desired low sidelobe, high gain main beam which will be scanned. The RMS sidelobe level in the elevation principal plane as a function of the main beam scan angle is shown in Figure 9 for both the DuFort and the Skobelev N=1 case. Although RMS sidelobe levels are low, for the larger scan angles with DuFort and for the smaller scan angles with Skobelev, the specification of -35 dB RMS is exceeded.

4 Network Implementation

One advantage of the DuFort and Skobelev networks is that they are easily realizable in a planar ("tile") architecture. Kachwalla [6] built an M=3 DuFort network in stripline for a linear array and achieved good results for a $\pm 7.5^\circ$ scan at C-band. Applying Kachwalla's design to a planar array would require one of these networks for each column in the array.

$p_1 =$.955 (-0.40 dB)
$p_2 =$.572 (-4.85 dB)
$p_3 =$.871 (-1.20 dB)
$p_4 =$.850 (-1.41 dB)
$q_1 =$.295 (-10.6 dB)
$q_2 =$.820 (-1.72 dB)
$q_3 =$.492 (-6.16 dB)
$q_4 =$.527 (-5.56 dB)

Table 7: Optimum Coupling Coefficients for the Skobelev circuit, N=2

The stripline feeds would extend normal to the back side of the array in a “brick”-type architecture.

As a starting point in our design efforts, we chose to construct a similar DuFort network in a microstrip (rather than in stripline as Kachwalla did), brick architecture at X-band to ensure that our modeling, design and manufacturing tolerances were acceptable before moving on to the more complicated tile architecture. We designed a single, M=3 feed network; however, we did not connect the output ports to radiating elements. As a first step, we will measure the excitation coefficients at the output ports using a network analyzer. A circuit layout of the brick, microstrip version is shown in Figure 10.

The ultimate goal is to construct both DuFort and Skobelev subarrays at X-band using a tile, stripline architecture. The most obvious difficulty in implementing a tile architecture is the space constraint. For an array with limited scan in one plane and conventional scan in the other plane, there is limited space for constructing the subarray feed circuits behind the array face. For our application, the space available is approximately $2\lambda \times 0.536\lambda$. For the Skobelev N=1 case, only two hybrids need to fit within this space; however, the Skobelev N=2 case requires four hybrids and the DuFort M=3 requires five hybrids plus a crossover. These more complicated networks require a multi-layer stripline configuration.

A multi-layer approach must have coupling between the isolated stripline layers. We will use the low-loss, stripline-to-stripline slot couplers proposed by Franchi [8]. We have designed couplers on several different substrates. Initial measurements have shown that low losses can be achieved with thin substrates. Unfortunately, use of thinner substrates increases line loss in the stripline feed circuit; therefore, a tradeoff is necessary between coupler loss and line loss. Additional measurements and tradeoff studies will be made before a substrate is chosen.

We provide a preliminary array weight estimate assuming a tile array architecture. The total number of transmit/receive (T/R) modules in the antenna is approximately 8600. An initial estimate of the antenna weight is about 1400 pounds, which is about 16 pounds/square foot (6 kilograms/square foot). This includes the support structure, cooling, power supplies,

radiating elements, T/R modules and cables. The estimated weight of the subarray feed network, which includes the multi-layer stripline circuits and hybrids, is about 74 pounds, or about 5 % of the antenna weight.

5 Conclusions

Two kinds of circuits were described which can be used for subarray feed networks. The coupling coefficients of the quadrature hybrids in the circuits were optimized based on a figure of merit established for the subarray pattern. Even with optimum subarray patterns, the RMS sidelobe levels for both feed circuits exceeded the design goal of -35 dB over part of the scan region, therefore, further design effort is required. In addition, an error analysis also needs to be done.

We have shown that an array of overlapped subarrays can be used to substantially reduce the number of phase controls required for a limited scan system. For our application, we were able to separate the phase controls by about 2λ , resulting in an element use factor of about 1.9, which means that we use about twice the minimum possible number of phase controls. However, we use only about 44 % of the number of phase shifters required for conventional scan in elevation.

The current experimental version is a microstrip, brick architecture, but our ultimate goal is to build stripline circuits in a planar, tile architecture to reduce antenna weight and profile. The projected weight of a full tile array is less than the 1500 pound goal.

References

- [1] R. J. Mailloux, L. Zahn, A. Martinez and G. R. Forbes. Grating Lobe Control in Limited Scan Arrays. *IEEE Transactions on Antennas and Propagation*, 27(1):79-85, January 1979.
- [2] J. J. Stangel. A Basic Theorem Concerning the Electronic Scanning Capabilities of Antennas. In *URSI Commission VI, Spring Meeting, 11 June 1974*.
- [3] R. Tang. Survey of Time-Delay Beam Steering Techniques. In *Phased-Array Antennas; Proceedings of the 1970 Phased Array Antenna Symposium*, pages 254-260. Artech House, Dedham, MA, 1972.
- [4] E. C. DuFort. Constrained Feeds for Limited Scan Arrays. *IEEE Transactions on Antennas and Propagation*, 26(3):407-413, May 1973.

- [5] S. P. Skobelev. Analysis and Synthesis of an Antenna Array with Sectoral Partial Radiation Patterns. *Radiotekhnika*, No.10:44-47, 1990.
- [6] Z. Kachwalla. A Limited-Scan Linear Array Using Overlapping Subarrays. *Journal of Electrical and Electronics Engineering, Australia - IE, Aust. and IREE, Aust.*, 3(2):126-131, June 1983.
- [7] E. E. Altshuler. Personal communication. April 1997.
- [8] P. R. Franchi and N. P. Kernweis. Electromagnetic Coupler. *Proceedings of the 1989 Antenna Applications Symposium*, RADC TR-90-42, Vol I, March 1990.

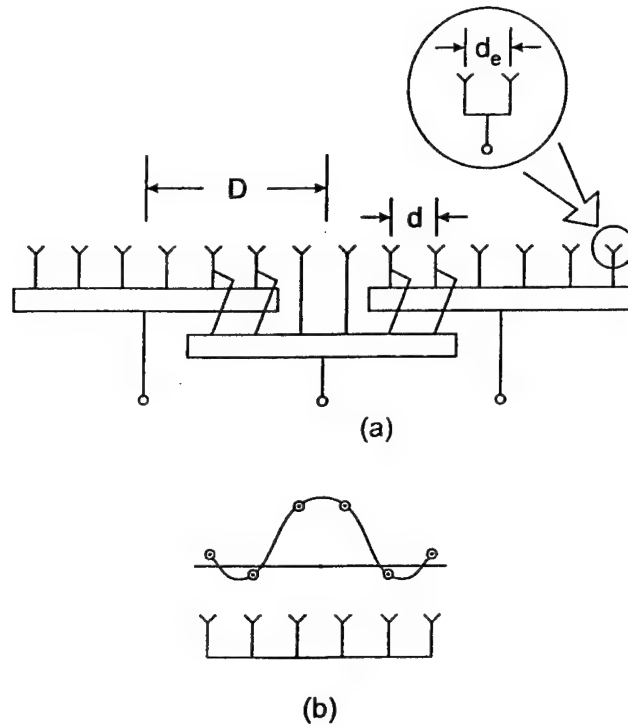


Figure 1: Partially overlapped subarray concept. (a) Architecture for three subarray example with feed networks. (b) Ideal subarray illumination.

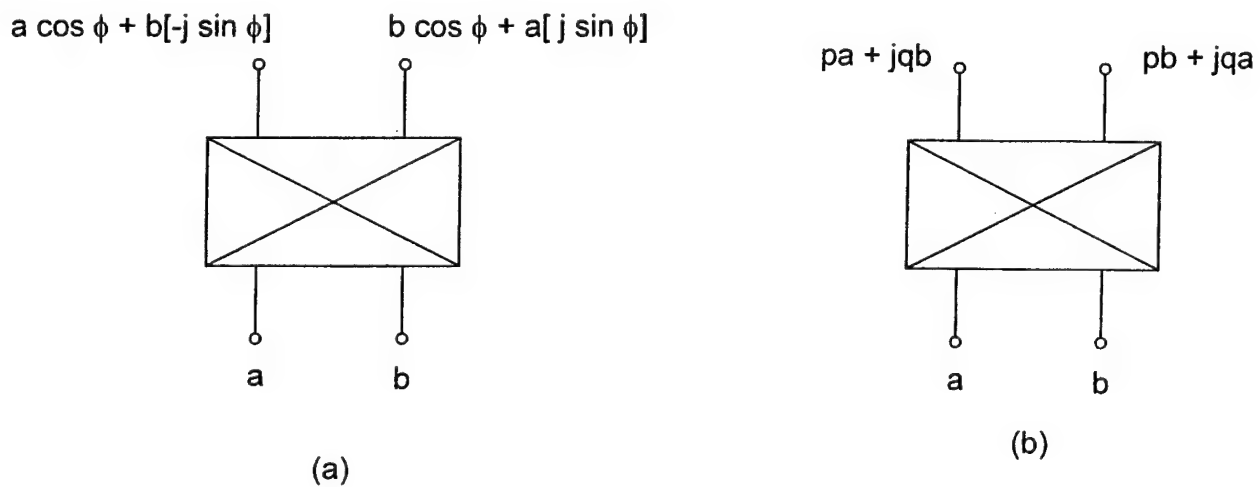


Figure 2: Quadrature hybrid coupler representation. Input signals at the two input ports are a and b . (a) DuFort with characteristic angle ϕ . (b) Skobelev with coupling coefficients p and q .

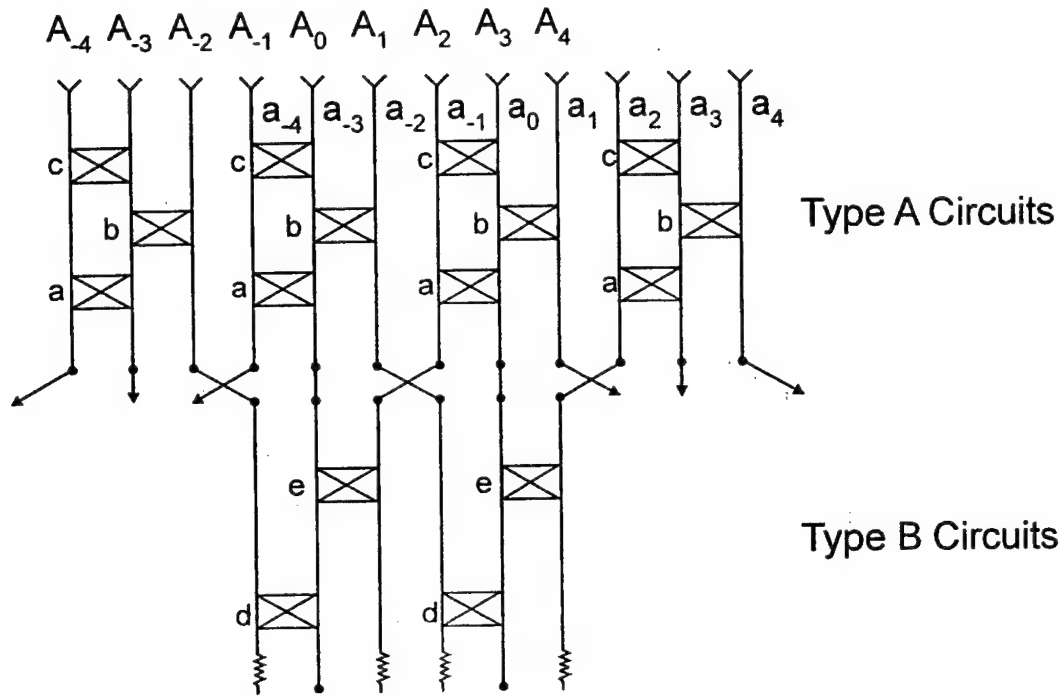


Figure 3: DuFort feed network with two adjacent subarrays shown ($M = 3$ case).

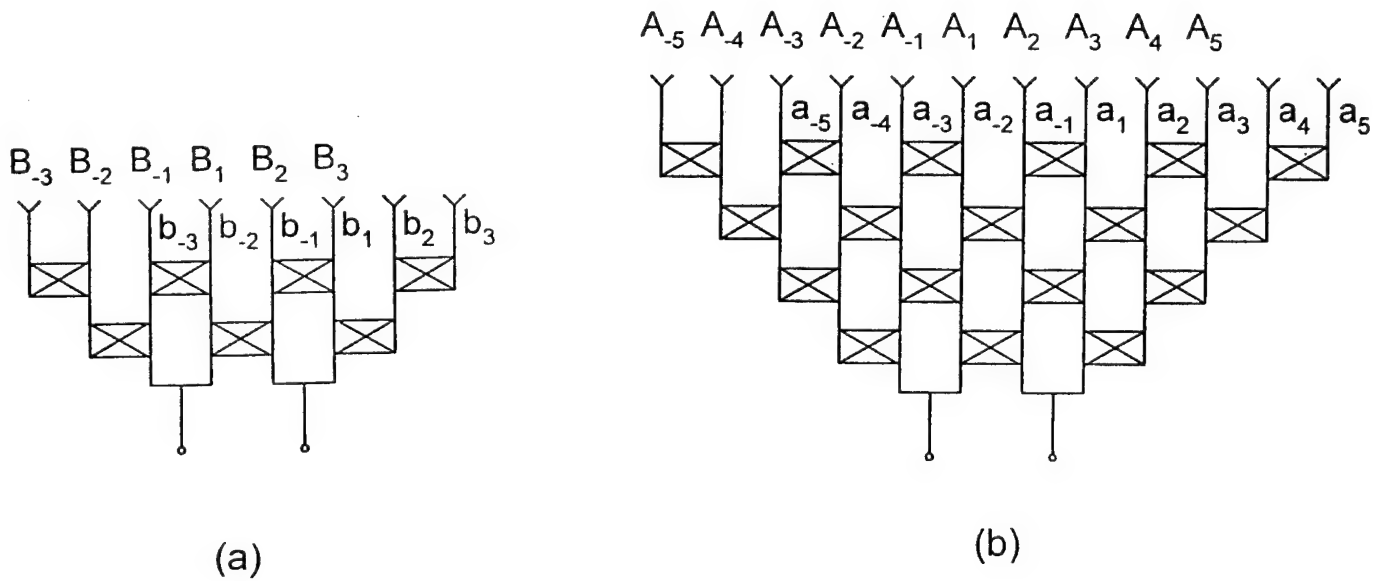


Figure 4: Skobelev (chess) feed network with two adjacent subarrays shown. (a) $N = 1$ case. (b) $N = 2$ case.

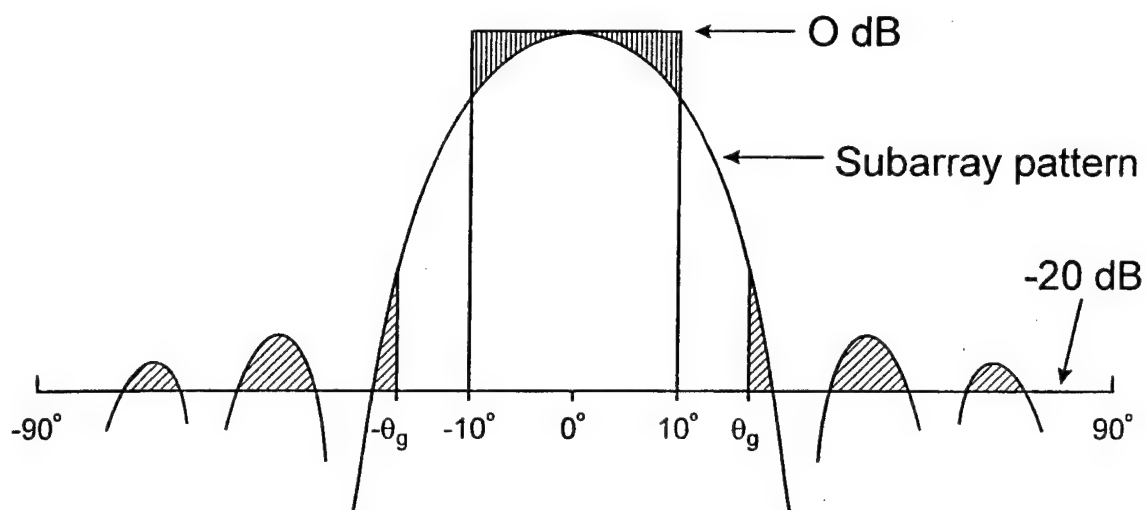


Figure 5: Typical subarray pattern illustrating the two areas used to calculate the figure of merit used for optimization. θ_g is the grating lobe location when the beam is scanned to the edge of the scan region.

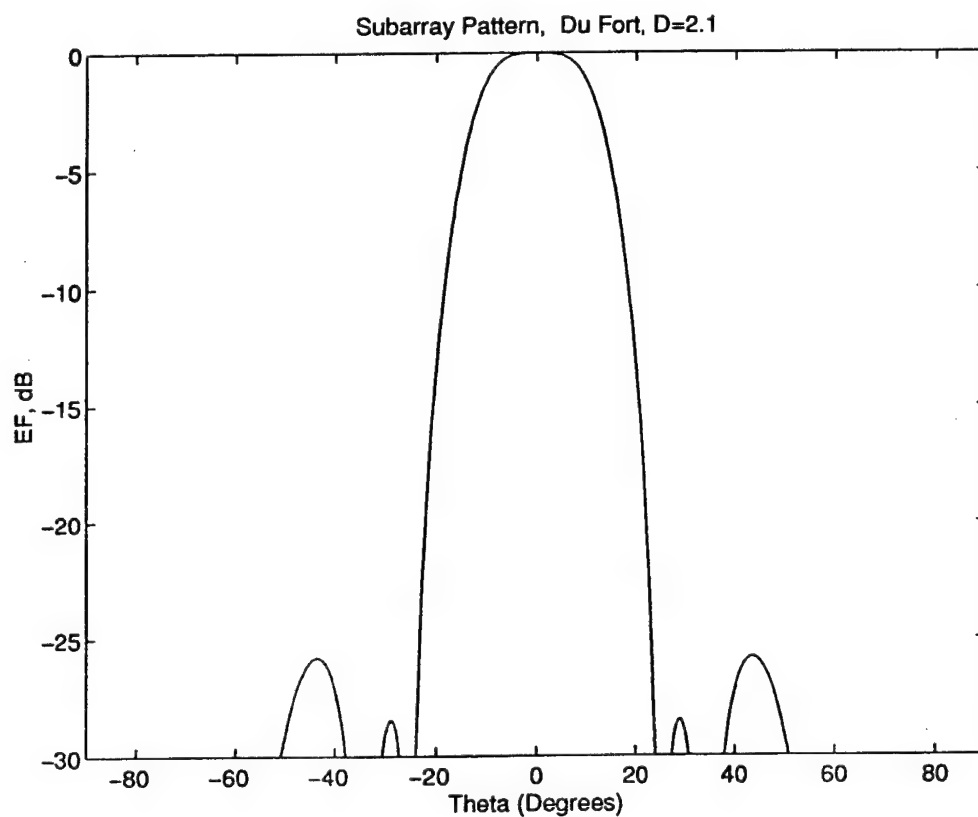


Figure 6: DuFort subarray pattern using the optimized characteristic angles.

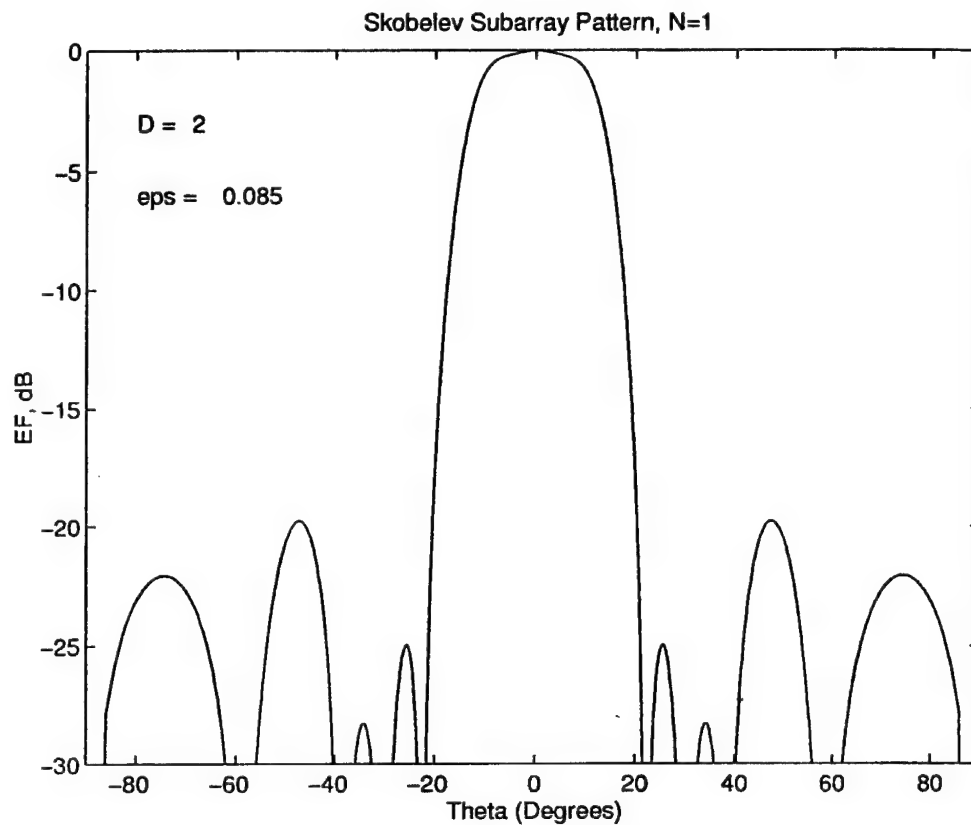


Figure 7: Skobelev ($N = 1$ case) subarray pattern using the optimized coupling coefficients.

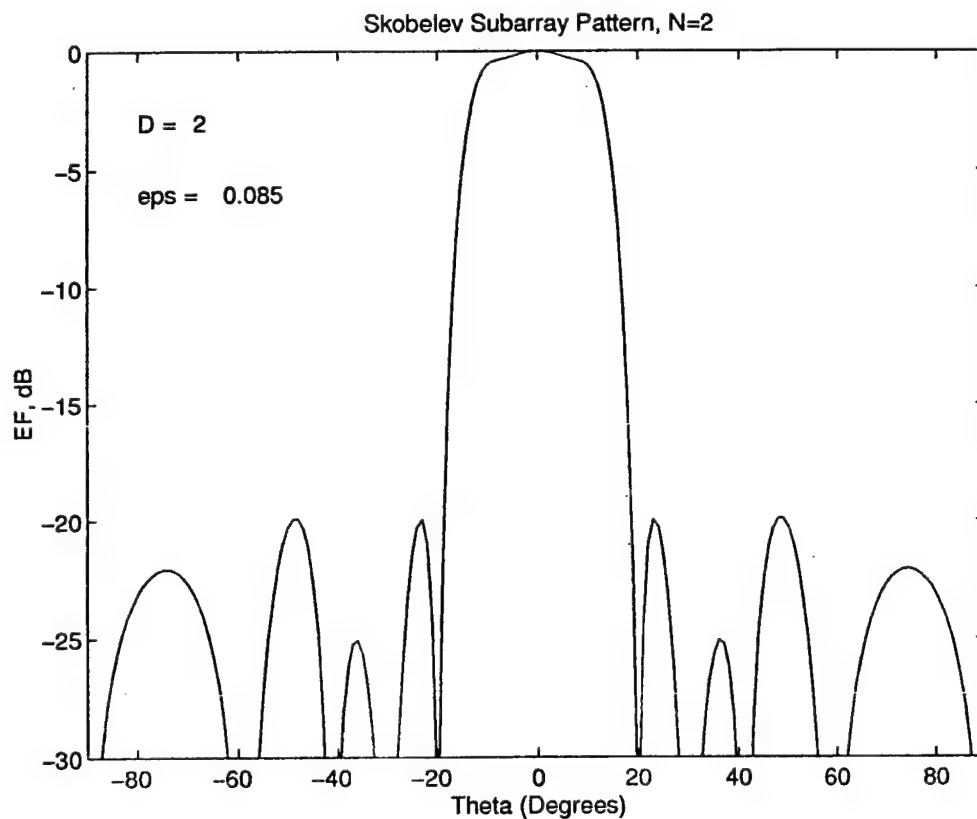


Figure 8: Skobelev ($N = 2$ case) subarray pattern using the genetic algorithm generated coupling coefficients.

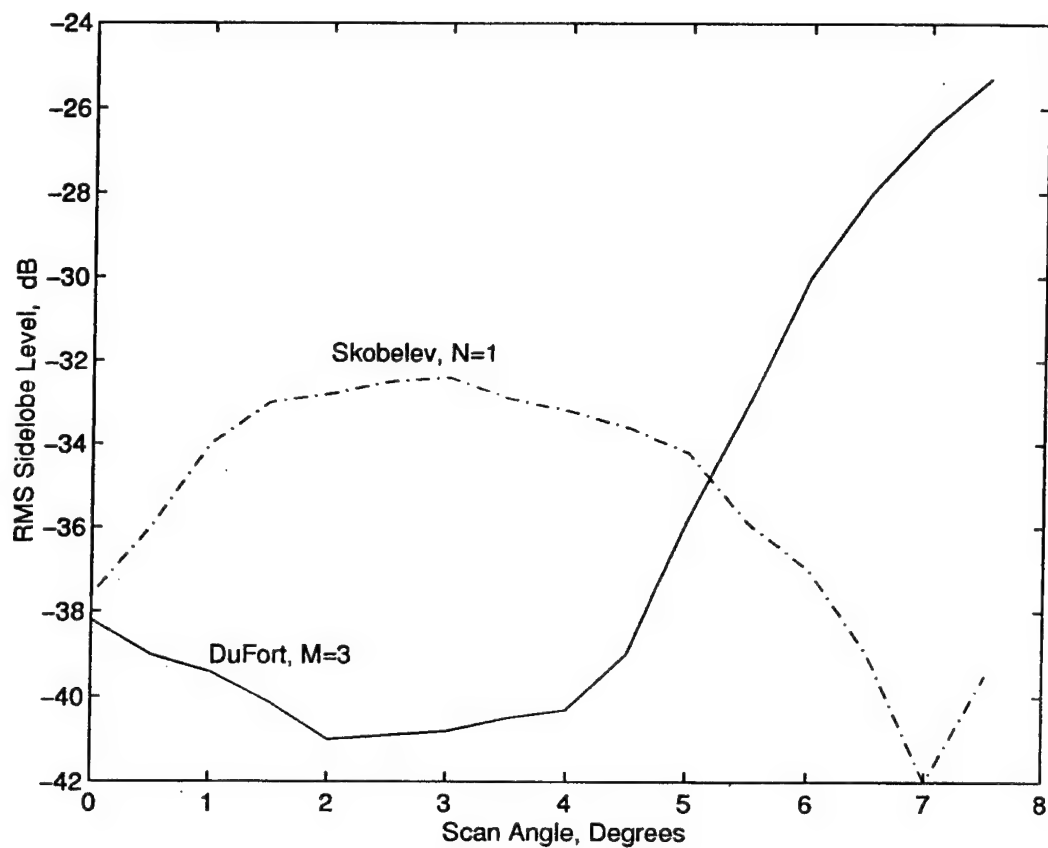


Figure 9: RMS antenna sidelobe levels for the optimum DuFort and Skobelev feed networks.

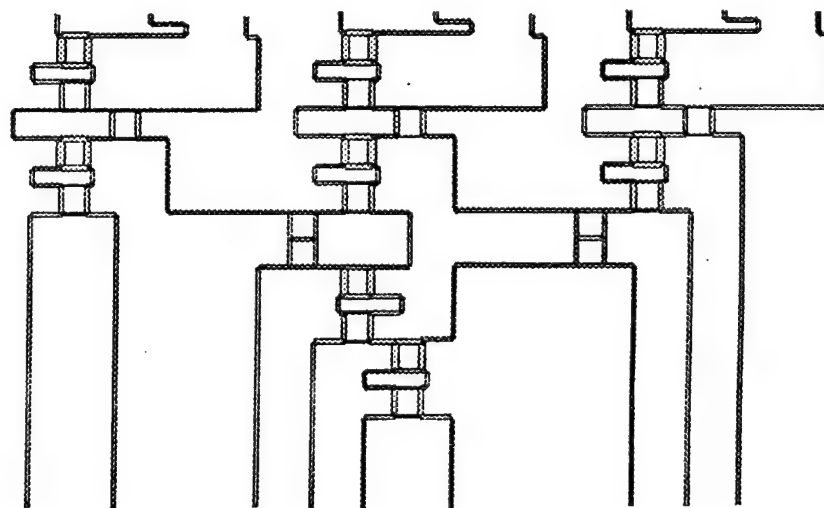


Figure 10: Circuit layout for the brick, microstrip implementation of the DuFort ($M = 3$) feed network.

LASER INDUCED PULSED PICOSECOND ELECTROMAGNETIC SOURCES (LIPPES) FOR 2- AND 3- DIMENSIONAL PHASED ARRAY ANTENNAS

J.R. Reid, E.E. Crisman and J.S. Derov
Rome Laboratory
31 Grenier St.
Hanscom AFB, MA 01731-3010

Abstract

The generation of 1-20 GHz electromagnetic (EM) pulses utilizing laser stimulation of semiconductor surfaces offers several advantages for the design of 2- and 3-dimensional phased array antennas. Electromagnetic radiation is created when optically excited carriers are accelerated in an electric field. The magnitude of the EM pulse is dependent upon the magnitude of the electric field, the fluence and wavelength of the laser, and the semiconductor material properties. The spectral energy of the EM pulse is dependent upon the length of the laser pulse. A bias voltage across two contacts provides an EM field along the wafer surface. Illuminating multiple locations on the wafer surface results in the generation of multiple laser induced pulsed picosecond EM sources (LIPPES). The ability to optically excite multiple sources utilizing only a single bias voltage makes LIPPES ideal for the construction of 2-dimensional phased arrays. Furthermore, studies of the far field radiation pattern of the antenna show that multiple elements can be combined in parallel to narrow the focus of the EM pulses. The studies also demonstrate the feasibility of 3-dimensional array construction and beam focusing. Current studies are aimed at increasing the intensity of the EM pulse by optimizing the laser wavelength and improving the beam focus by utilizing multiple elements in series.

1. BACKGROUND

The concept of generating picosecond length electromagnetic (EM) pulses using optically excited carriers, accelerated in a *dc* field was originally

demonstrated by Mourou, *et al.* [1]. Auston, *et al.*, were later able to generate and accurately measure subpicosecond EM pulses using a similar configuration [2]. Subsequent work by a number of authors [3-5] has provided insight into the generation of the pulses, and work has proceeded on steering the EM pulse by varying the bias field across the substrate [6], the incident angle of the incoming optical pulse [7,8], and the intensity pattern of the optical pulse [9].

The EM pulses generated by optically excited carriers are of particular interest to the radar community due to their ultrawideband frequency spectrum. Smith, *et al.*, have demonstrated EM pulses with frequency spectra from less than 100 GHz to over 2 THz [3]. Utilizing these ultrawideband pulses with current radar systems requires that the frequency spectra cover a range from 1 to 20 GHz. Liu, *et al.*, at Rome Laboratories, have demonstrated the generation of 50 to 80 picosecond EM pulses with the required frequency spectra [10,11].

Recent studies of the laser induced pulsed picosecond electromagnetic sources (LIPPES) at Rome Laboratory have focused on the development of 2- and 3-dimensional arrays. As will be discussed, LIPPES can readily be implemented in both a parallel configuration across the surface of a single semiconductor surface, and a series configuration utilizing multiple semiconductor surfaces, thus allowing the design of a 3 dimensional LIPPES array. Such a source permits the

outgoing EM pulse to be steered with an ultrawideband pulse propagating only in a particular direction.

2. ELECTROMAGNETIC PULSE GENERATION

The basic LIPPES setup is shown in Fig. 1. Two ohmic contacts are formed several centimeters apart on opposing ends of a semi-insulating substrate, either GaAs or InP. A large bias voltage is then placed on the electrodes. Due to the semi-insulating nature of the substrate, no current is present. A short laser pulse (50-80 ps) from by a frequency doubled YLF (526 nm) excites photocarriers in a small region of the semi-insulating substrate. The photocarriers are accelerated by the *dc* field, thus generating an electromagnetic (EM) pulse.

The frequency spectra of the EM pulse is determined by the shape and

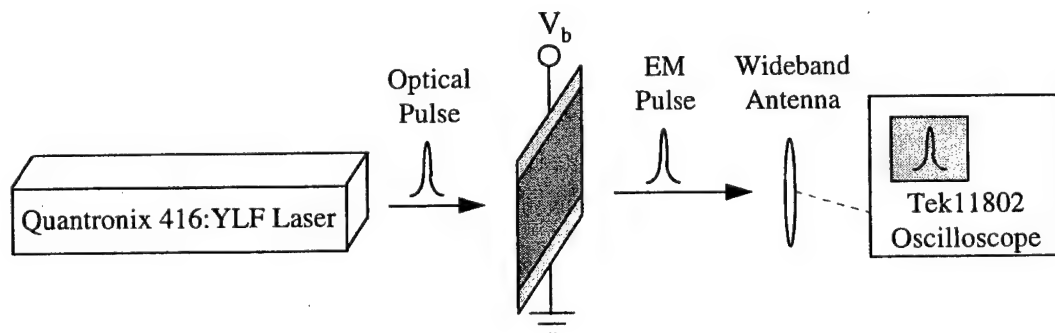


Figure 1. Basic setup of the LIPPES experiments. A short optical pulse is generated by a Quantronix 416:YLF laser. The pulse illuminates a semi-insulating substrate creating photocarriers. The carriers are accelerated by a *dc* bias resulting in an EM pulse. The electromagnetic pulse is detected by a wideband antenna and recorded on a Tek. 11802 sampling oscilloscope.

length of the optical pulse. Utilizing an 80 picosecond optical pulse results in an EM pulse with a frequency spectra over the desired 1-20 GHz range [10]. The magnitude of the pulse is dependent upon a number of factors, including the *dc* bias, the number of photocarriers generated, and the carrier mobility of the substrate. Several papers have covered the influence of these factors on the magnitude of the EM pulse [10-13]. As expected, increasing either the carrier mobility, the number of carriers, the *dc* bias, or a combination of these results in an increase in the magnitude of the EM-pulse. However, the relationship between the various factors and the pulse magnitude is not linear. For example, saturation of the bias field by the propagating EM pulse results in a non-linear relationship between the *dc* bias field and the EM pulse magnitude [11,12].

3. PARALLEL EXCITATION OF SOURCES (2D ARRAYS)

Multiple EM sources can be created on a single LIPPES substrate by illuminating the substrate with multiple laser sources that are spatially separated on the wafer surface. The ability to generate multiple sources on a single substrate is possible because of the high resistivity ($>10^7 \Omega/\text{cm}$) provided by the semi-insulating GaAs and InP wafers. As a result, 2-dimensional LIPPES arrays can readily be created by splitting the optical pulse into multiple beams.

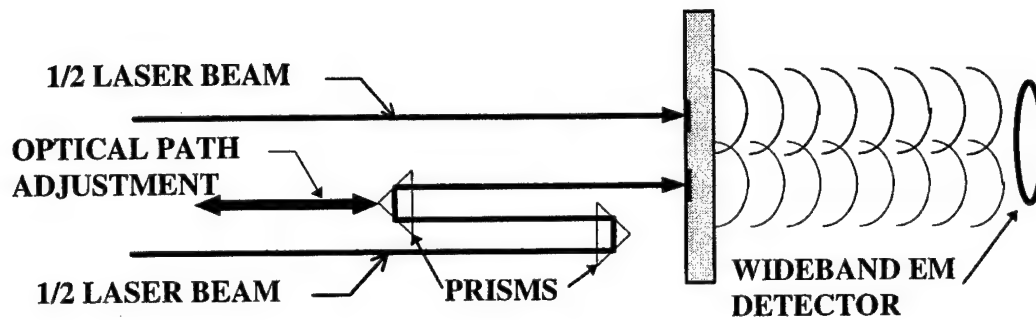


Figure 2. Experimental configuration for the parallel excitation of two separate areas of a single semiconductor EM source using a split laser beam.

Parallel excitation of a single substrate has been demonstrated by splitting the incoming laser pulses into two separate beams as illustrated in Fig. 2. An optical path adjustment is added to one of the two beam paths to allow the arrival time of the optical pulses to be varied. Each beam illuminates a spot on the substrate approximately 6 mm in diameter. The spots are separated by 3 cm. A broadband receiving antenna is mounted 1.5 m from the substrate on a rotatable arm centered on the specimen allowing measurements at various angles.

Figure 3 shows data for three separate setup conditions. The top two traces, Fig. 3, **a)** and **b)**, are taken with the receiving antenna aligned on the centerline of the optical pulses, and normal to the semiconductor substrate. In trace **a)** two distinct pulses appear. Each pulse corresponds to one of the two illuminated spots. The pulses are separated in time by approximately 400 ps, which corresponds to a 12 cm difference in the optical path length between the two optical beams. The slight variation in the two pulse heights results from

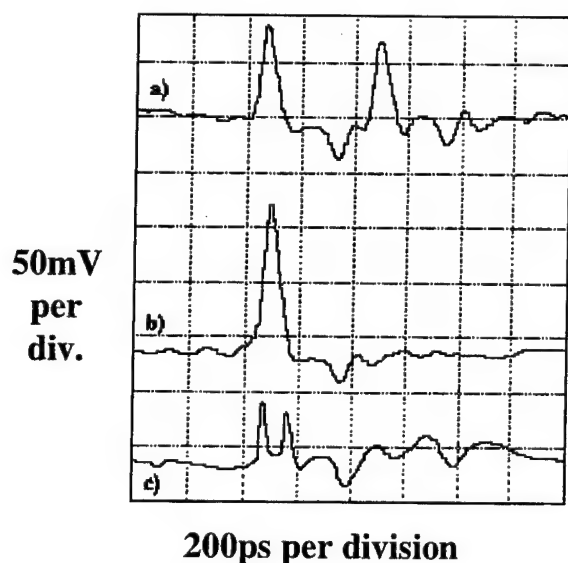


Figure 3. Response of microwave antenna for split laser beam excitation of two areas of a single semiconductor source (Figure 2) for: a) on the laser-antenna centerline, before optical path adjustment, b) on the centerline, with simultaneous arrival of the optical pulses c) at 90° to the centerline, with simultaneous arrival of the optical pulses.

different losses in the separate optical paths. Normalizing for the different optical fluences results in two pulses of equal amplitude.

In trace **b)** the optical path was adjusted so that the two optical pulses arrive at the substrate simultaneously. As a result, the two EM pulses are superimposed and a single EM pulse is recorded. The single EM pulse is the sum of the amplitudes of the two separate pulses seen in trace **a)**.

For trace **c)**, the receiving antenna was moved to a 90° with respect to the path of the laser beams. The rest of the system is set up as in trace **b)** where the optical pulses arrive simultaneously at the substrate. Again, the recorded EM pulses are separated in time. The separation of approximately 100 ps corresponds to the 3 cm separation between the two spots on the semiconductor substrate. It is

not clear whether the reduced amplitude of the pulses in trace c) is a measurement problem or is a result of the 'off-axis' nature of the measurement.

These measurements confirm that parallel excitation of a single substrate is possible and further, the EM pulse is a function of the observation angle. It is particularly exciting that the pulses can be generated on a single semiconductor substrate with a shared bias voltage thus simplifying the construction of the LIPPES array.

4. SERIES EXCITATION OF SOURCES

LIPPES pulse generators are dielectrics, and therefore allow microwave radiation to pass through with negligible absorption and reflection. This allows a novel antenna design where elements can be located not only in parallel on a single plane, but also in series with individual elements radiating through other elements of the array. The ability to build such a system has been evaluated and the results are presented here.

4.1 Dual Beam Excitation

The initial tests of series excitation were conducted using the setup shown in Fig. 4. As with parallel excitation, the laser beam is divided into two separate

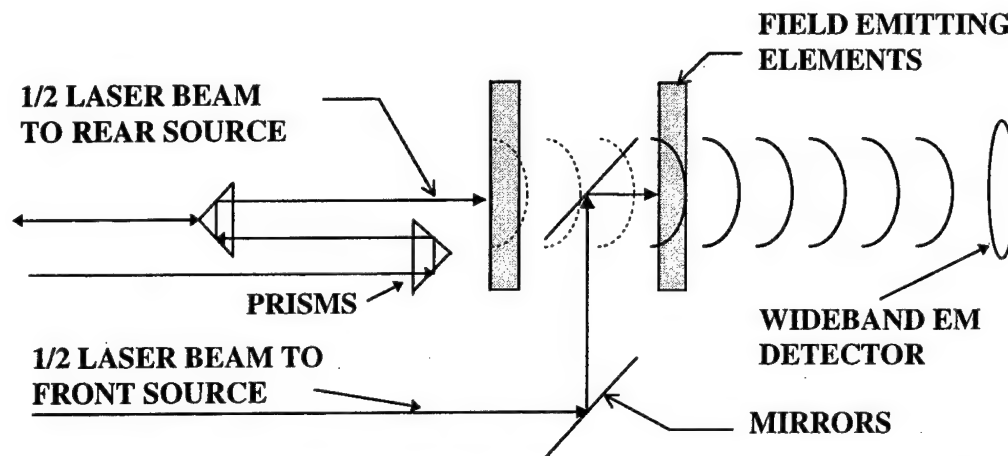


Figure 4. Experimental configuration for the serial excitation of two separate semiconductor EM sources excited by a split laser beam.

beams of nearly equal optical fluence. The first beam is used to excite the first or rear substrate. The second is routed, via mirrors, around the rear substrate to excite the second or front substrate. An optical delay line is added in the path of the first laser beam to allow for the optical path lengths of the two beams to be appropriately adjusted. For forward propagation of the beam, the optical delay length is set so that the optical pulse from the second laser beam and the EM pulse from the rear semiconductor substrate arrive at the front substrate simultaneously.

Figure 5 shows the results for dual beam, series excitation of two substrates. Trace **a)** shows the pulse generated when a *dc* bias is applied to the rear substrate only. Trace **b)** shows the pulse generated when a *dc* bias is applied to the front substrate only. The EM pulse generated from the rear source is measured as having approximately 60% the magnitude of the EM pulse from the

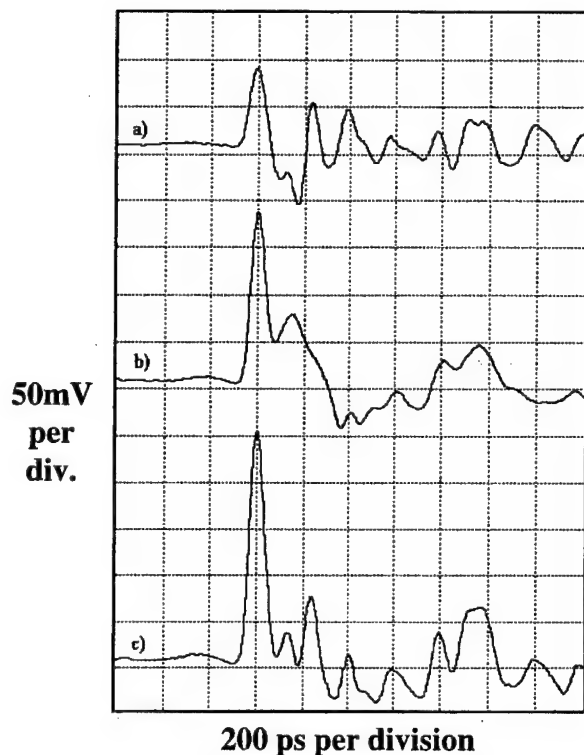


Figure 5. Response of microwave antenna to the split beam excitation of two separate semiconductor sources configured in series relative to the optical path (Figure 4) for: a) rear source only activated with applied *dc* field, b) front source only activated with applied *dc* field and c) both sources activated by *dc* fields.

front substrate. Lower optical fluence on the rear source can account for approximately a 10% reduction in the rear pulse. The remaining 30% reduction could be due to reflection and/or scattering off the forward substrate and the mounting structure. Trace c) shows the superposition of both pulses. As shown, the two pulsed add in the forward direction.

4.2 Single Beam Excitation

Another possibility utilizing LIPPES is series excitation utilizing a single beam. The basic setup for this type of system is shown in Fig. 6. Semiconductor substrates with different bandgaps are chosen. A dual color laser beam is chosen

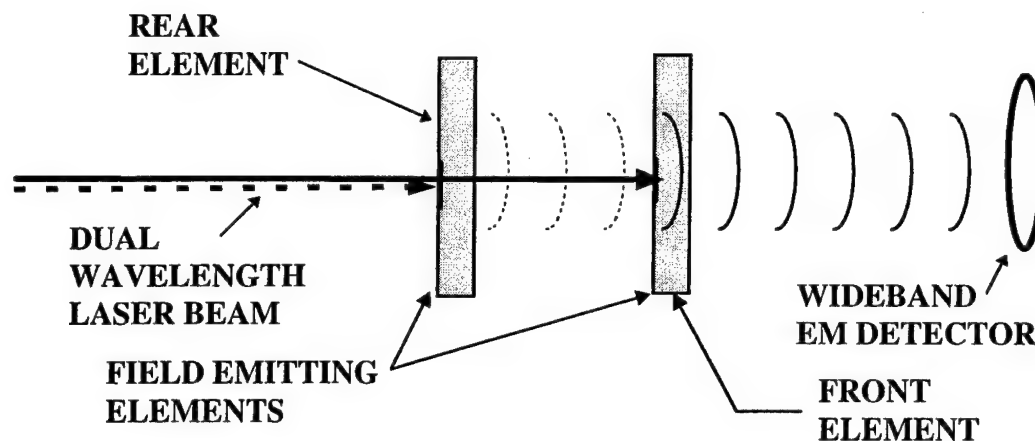


Figure 6. Experimental configuration for the serial excitation of two separate semiconductor EM sources excited by a single, two wavelength laser beam.

such that one color is absorbed by the rear substrate while the second color passes through the rear substrate and is absorbed by the front substrate. It is then possible to excite both substrates with the proper optical path lengths without the use of mirrors and prisms. This setup reduces the components involved in building the arrays, thus decreasing the complexity of a steerable array.

Initial tests have been performed using a combination of InP ($E_g = 1.26$ eV) for the front source and GaAs ($E_g = 1.43$ eV) for the rear source. Gallium arsenide strongly absorbs the 526 nm wavelength of the frequency doubled YLF laser, but is transparent to the undoubled 1052 nm fundamental component. Although the 1052 nm fundamental is not an ideal match, the InP

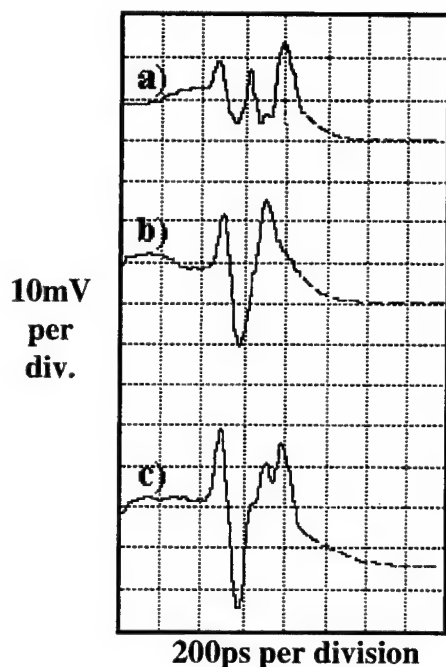


Figure 7: Response of microwave antenna to a single beam, two frequency excitation of two separate semiconductor sources configured in series relative to the optical path (Figure 6) for: a) rear source only with applied *dc* field, b) front source only with applied *dc* field and c) both sources activated by *dc* fields. (The reflective signals at the longer times have been removed for clarity)

responds reasonably to this wavelength allowing a proof of concept demonstration.

Figure 7 shows the measured data from the setup with InP as the front sample and GaAs as the rear sample and a single beam from the YLF illuminating both substrates. As with Fig. 5, trace **a)** shows the response from the rear substrate, trace **b)** shows the response from the front substrate, and trace **c)** shows the response from both substrates combined. Note that the laser wavelengths are not optimized for the substrate. However, the pulses clearly add in trace **c)** showing that the timing of the optical pulse and the microwave pulse are accurate.

5. DISCUSSION AND CURRENT RESEARCH

It has been shown that ultrawideband microwave pulses with frequency spectra from 1-20 GHz can be produced by laser induced pulsed picosecond sources. Utilizing LIPES, the ability to excite multiple sources on an individual substrate with a single bias voltage has been demonstrated. Potentially this allows a simple method for fabricating multiple sources in parallel. We have also demonstrated the ability to excite sources in series and combine the propagating EM pulses. Furthermore, a novel method for exciting the sources utilizing dual color laser beams with different semiconductor substrates has been demonstrated.

Current work focuses on improving the performance of individual elements by optimizing the optical pulse wavelength for the semiconductor substrate. Areas of future interest are aimed primarily at demonstrating the ability to steer and focus both 2- and 3- dimensional sources.

6. REFERENCES

- [1] G. Mourou, C.V. Stancampiano, A. Antonetti and A. Orszag, "Picosecond Microwave Pulses Generated with a Subpicosecond Laser-Driven Semiconductor Switch," *Appl. Phys. Lett.*, vol. 39(4), pp. 295-296, Aug. 1981.
- [2] D.H. Auston, K.P. Cheung, and P.R. Smith, "Picosecond Photoconducting Hertzian Dipoles," *Appl. Phys. Lett.*, vol. 45(3), pp. 284-286, Aug. 1984.

- [3] P.R. Smith, D.H. Auston, and M.C. Nuss, "Subpicosecond Photoconducting Dipole Antennas," *IEEE Journal of Quantum Electronics*, vol. 24(2), pp. 255-260, Feb. 1988.
- [4] Ch. Fattinger and D. Grischkowsky, "Point Source Terahertz Optics," *Appl. Phys. Lett.*, vol. 53(16), pp. 1480-1482, Oct. 1988.
- [5] Ch. Fattinger and D. Grischkowsky, "Terahertz Beams," *Appl. Phys. Lett.*, vol. 54(6), pp. 490-492, Feb. 1989.
- [6] N. Froberg, M. Mack, B.B. Hu, X.C. Zhang, and D.H. Auston, "500 GHz Electrically Steerable Photoconducting Antenna Array," *Appl. Phys. Lett.*, vol. 58(5), pp. 446-448, Feb. 1991.
- [7] X.C. Zhang, B.B. Hu, J.T. Darrow, and D.H. Auston, "Generation of Femtosecond Electromagnetic Pulses from Semiconductor Surfaces," *Appl. Phys. Lett.*, vol. 56(11), pp. 1011-1013, Mar. 1990.
- [8] B.B. Hu, J.T. Darrow, X.C. Zhang, D.H. Auston, and P.R. Smith, "Optically Steerable Photoconducting Antennas," *Appl. Phys. Lett.*, vol. 56(10), pp. 886-888, Mar. 1990.
- [9] X.C. Zhang and D.H. Auston, "Generation of Steerable submillimeter Waves from Semiconductory Surfaces by Spatial Light Modulators," *Appl. Phys. Lett.*, vol. 59(7), pp. 768-770, Aug. 1991.
- [10] D.W. Liu, J.B. Thaxter, and D.F. Bliss, "Gigahertz Planar Photoconducting Antenna Activated by Picosecond Optical Pulses," *Optics Letters*, vol. 20(14), pp. 1544-1546, July 1995.
- [11] D.W. Liu, P.H. Carr, and J.B. Thaxter, "Nonlinear Photoconductivity Characteristics of Antenna Activated by 80-Picosecond Optical Pulses," *IEEE Photonics Technology Letters*, vol. 8(6), pp. 815-817, June 1996.
- [12] J.T. Darrow, X-C. Zhang, D.H. Auston, and J.D. Morse, "Saturation of Large Aperture Photoconducting Antennas," *IEEE Journal of Quantum Electronics*, vol. 28(6), pp. 1607-1616, June 1992.
- [13] P.K. Benicewicz, J.P. Roberts, and A.J. Taylor, "Scaling of Terahertz Radiation from Large-Aperture Biased Photoconductors," *Journal of the Optical Society of America B*, vol. 11(12), pp. 2533-2546, Dec. 1994.

DEVELOPMENT OF MICROWAVE AND MMW INTEGRATED PHASED ARRAYS WITH SIMPLE CONTROL

Ernst F. Zaitsev
Anton B. Gouskov
Alexandr. S. Cherepanov
George A. Yufit
Michael R. Beltran
Yakov S. Khodorkovsky

BELTRAN, INC.
1133 East 35 Street
Brooklyn, NY 11210

Abstract

The active evolution of mm-wave techniques for civilian applications requires a significant reduction in the cost of the devices and components used at this band. One of the important problems is the creation of low cost antennas with electronic beam control. The integrated phased array (IPA) with ferrite control has a low cost (like patch antennas), simple control (like a single phase-shifter) and electrical scanning (like a conventional phased array). For the IPA the beam position control needs only one current for each plane. In addition, the IPA allows a beam to move continually through the scanning sector, which is beneficial in survey options. This paper presents the most recent achievements in the development of IPA with ferrite control. The general analysis given in previous works [1,4] was supplemented by an original method for the calculation of individual and mutual impedances using the radiation pattern diagram of a single dipole on the ferrite-dielectric-ferrite (FDF) structure. The obtained results were combined with equations that describe the wave process in the FDF-waveguide. Thus a system of equations was obtained to determine dipole currents. As a result the IPA pattern diagram and all antenna parameters can be calculated using a special software. Several antenna samples were made and tested. Depending on the antenna aperture the beamwidth can be from 5° to 1° , insertion loss 2-4 dB. In a simple case the scanning sector is $\pm 20^{\circ}$, the side lobe level -12° dB. It is possible to expand the scanning sector to $\pm 40^{\circ}$ or to reduce the side lobe level to below -20 dB. An active version of the antenna is also considered, which has higher performances.

1. Antenna Design and Operation

This paper describes a new class of antennas – integrated phased arrays with ferrite control [1-6], which can be used in the entire MMW band. The main advantages of these antennas are a low profile integrated design, very simple beam control and low cost.

Figures 1 and 2 show the design of a linear and planar antenna, respectively. The main antenna component is a three-layer waveguiding ferrite-dielectric-ferrite (FDF) structure. The bottom surface of the FDF-structure is metallized; radiating dipoles are disposed on the top surface. The dielectric layer, unlike the ferrite layers, is not solid, but is fabricated of one (Figure 1) or several (Figure 2) parallel rods. Wires for control winding are placed in the gaps between the rods. Rows of radiating dipoles are disposed precisely above the dielectric rods.

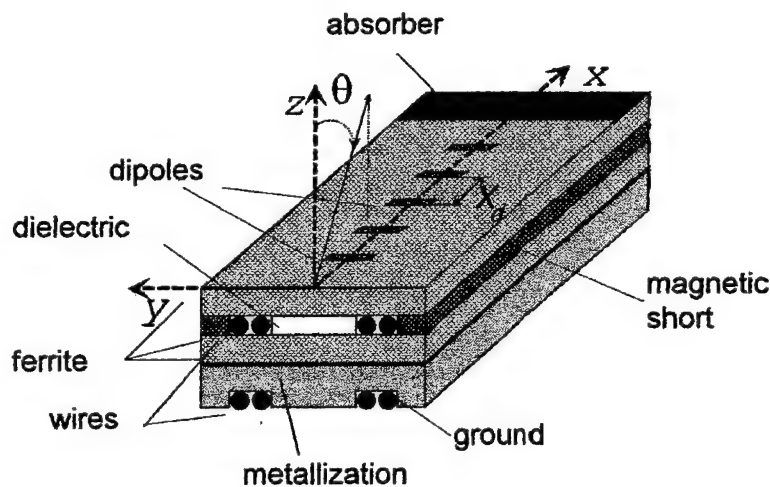


Figure 1. Linear IPA design.

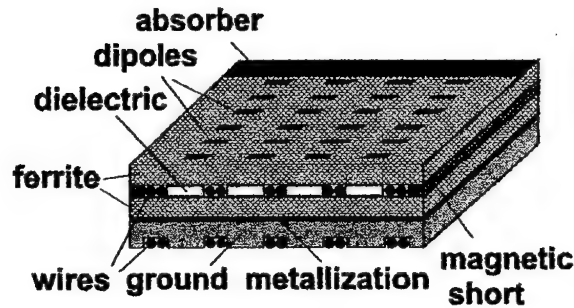


Figure 2. Planar IPA design.

Each dielectric rod together with the close-fitting areas of ferrite layers forms a waveguide. The wave propagating along this waveguide excites the currents in the dipoles which, in turn, radiate a space wave. The phase shift between currents in neighboring dipoles, and also the direction of maximum radiation, depend on the phase velocity v of the waveguide mode:

$$\sin\theta = q - n\lambda / d_x, \quad (1)$$

where θ – the angle between beam direction and normal (Figures 1, 2) in the XOZ plane (H -plane), $q = c/v$ – moderation factor of waveguide mode (c – velocity of light, v – waveguide mode velocity), n – an integer, λ – a wavelength, d_x – a distance between dipoles along the x axis. Usually $d_x / \lambda = 0.5 - 0.6$, q is about 4, so that $n=2$.

The current in the control winding magnetizes the ferrite layers in the opposite direction parallel to the y axis. Varying the magnetic induction in the ferrite layer changes the value q and leads to scanning of the beam in the H -plane, in accordance with (1). To scan in the transversal plane (E -plane) in the case of a planar antenna (Figure 2) it is necessary to control the phases of the waves excited at the FDF-waveguide inputs. This can be done in various ways, which will be discussed further on.

2. Various antenna configurations

The simplest version is the linear or planar antenna with 1D-scanning. Feeding of the linear antenna is provided by a standard rectangular waveguide; the planar antenna is fed by an E -horn. In both cases a dielectric matching transformer

is mounted at the input of each dielectric rod of the FDF-structure; the transformer is made of a dielectric with $\epsilon=5$ and it provides less than 1.5 VSWR in a wide frequency band. To minimize reflections an absorbing material is put on the dielectric rod at the opposite edge of the waveguiding structure.

The described version can be used in cases when the antenna does not have high requirements concerning side lobe level (which would be -12 dB in this case) and the main criterion is the cost of the antenna and the simplicity of beam control (1C-control). It is to be noted that the linear antenna can be used both independently and as a scanning radiator for a cylindrical-parabolic mirror.

It is always possible to achieve that the scanning sector be disposed almost symmetrically with respect to normal by means of the parameter choices involved in (1). In this case the 8 mm band antenna's scanning sector is ± 20 deg.; the scanning sector is the same for $\lambda > 8$ mm. The scanning sector is ± 10 deg. for $\lambda = 3-4$ mm.

Another choice is possible for the values q_{max} , q_{min} and d_x/λ , which provides that almost the whole scanning sector be disposed on one side from normal (Figure 3). If one input (output) of the antenna is now switched over to another FDF-structure edge, then the scanning sector travels to the other side from the normal. As a result the total sector redoubles.

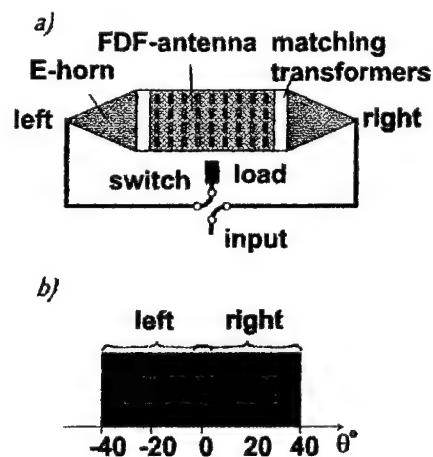


Figure 3. Antenna with expanded scanning sector:
a) schematic diagram, b) sector of scanning

An antenna with a low SLL is shown schematically in Figure 4. Both sides of the antenna are fed by the Y-joint, which can also be formed by an FDF-waveguide. The current distribution in the dipoles decreases on both sides from the center. One or two dipoles are absent near the center, which does not raise the SLL but further decreases it to -23 dB. This fact was first ascertained by calculations and was subsequently confirmed experimentally.

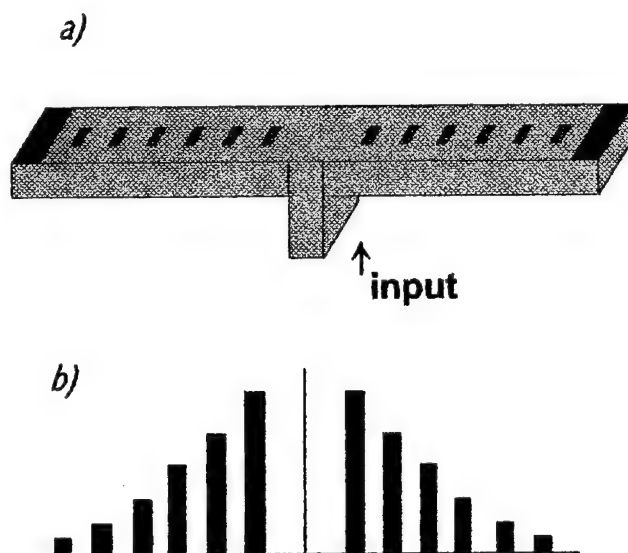


Figure 4. Antenna with lowered side lobe level:
a) antenna configuration, b) current amplitude distribution

It should be noted that the antenna in Figure 4 has a beam that is twice as narrow, with equal losses, in comparison with the simplest configuration.

A further reduction of SLL is possible when a special amplitude distribution of the currents in the dipoles is chosen, that is different from the exponential one. To achieve this the dipoles have to be of different lengths, making it possible to provide a given ratio of radiating power to the exciting wave power.

The next version (Figure 5) is a 2D - scanning antenna. It contains an electrically controlled power divider [2]. It has the same FDF-waveguide as the

antenna, but instead of radiating dipoles, the slot or dipole coupling elements with the waveguides of the antenna array are located on its side wall. The magnetizing current in the winding of this dividing waveguide changes the phases of the waves, exciting the waveguides of the antenna array and providing beam scanning in the *E*-plane. Thus, 2D-scanning is realized by only two control currents. But the extreme simplicity of beam control is achieved at the expense of 2-3 dB of additional losses.

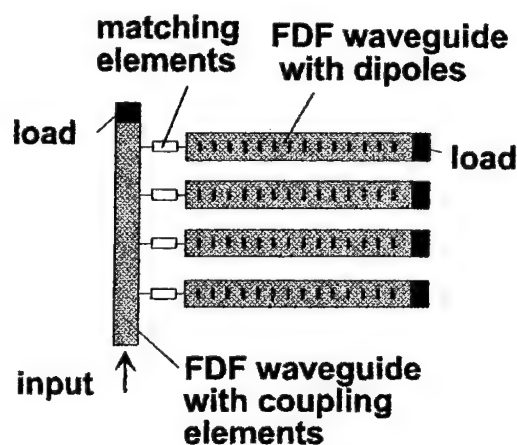


Figure 5. Configuration of 2D-scanning 2C-controlled antenna

It is to be noted that the same methods for performance improvement can be used that were described above: redoubling the scanning sector by switching waveguide ports, reducing SLL and decreasing losses (or further narrowing the beam) by having the antenna feed from the center.

A higher performance may be achieved by using an active antenna version [3]. In Figure 6 the schematic diagram of such an antenna and a possible practical realization are presented. The antenna consists of an electrically controlled FDF-power dividing unit with slot coupling elements, MMIC amplifiers and radiating patches. The coupling slots are etched in the metallization on the upper ferrite plate.

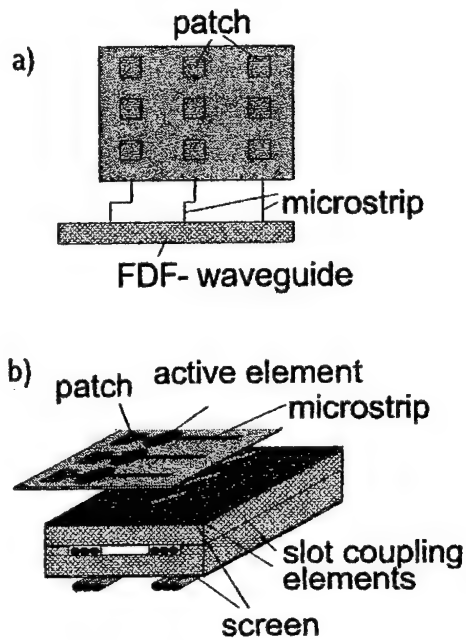


Figure 6 Active antenna: a)schematic diagram b) design

For this antenna the losses in the FDF-structure are not essential due to the amplifiers, if the amplifier gain factor is about 20 dB (or more). For example, in this case a receiving antenna has a G/T ratio (gain/temperature) close to D/T_a , where D is the directivity ratio, T_a – amplifier noise temperature; otherwise such an antenna is equivalent to a lossless antenna, having the same radiation pattern diagram.

The slotted connection between the FDF-waveguide and the microstrip line can be varied within a wide range of coupling factors by changing the parameters. Due to this, we can choose the coupling factor of the FDF-waveguide with each channel in such a way that the amplitude distribution to the edges and the low side lobe level are decreased. As a result, we attain a combination of high antenna performance and simple beam control, as well as low profile design. Planar 1D-scanning is cost effective, because the number of amplifiers is equal to the number of radiator rows, i.e., is relatively small. Such an antenna is convenient to use in short cm-waves.

3. Analysis and Calculation

In spite of its simple design the IPA is a complicated electrodynamic object, because the same integrated waveguiding and radiating structures unite a great number of various duties and have many different parameters. It is necessary to take into account the mutual influence of the radiating dipoles, the multimode operation of the FDF-waveguide and its nonreciprocity.

The general method of analysis that was presented in [1] is based on the presentation of the antenna as an equivalent UHF circuit. This circuit is described by a system of linear algebraic equations, the solution to which makes it possible to determine the complex amplitude of the currents in radiating dipoles. The coefficients of the system depend on the parameters of the equivalent circuit. These parameters are velocity and attenuation of each propagating waveguide mode, resistance of the coupling of the dipole with the waveguide modes, the distance between dipoles, the individual and mutual impedance of the dipoles with regard to their disposition on the nonreciprocal FDF-waveguide. To find these parameters only two basic problems need to be solved: an internal problem – about the propagating modes in homogeneous FDF-waveguides (without dipoles) taking into account the magnetization of the ferrite layers, and an external problem – about the diffraction of the plane wave that is incident on the FDF-structure. The solution of the second problem allows one to find the field radiated by the dipole disposed on the structure and the mutual impedance matrix. These and many other parameters of the equivalent circuit are found from the solutions of the basic problems with the help of the generalized reciprocity theorem [7].

The analytical method that is presented takes into account all the phenomena that occur while the antenna is operating. The accuracy of the calculations with this method depends on both the choice of FDF-structure model in each basic problem and the choice of the method for the analysis of this model. We can increase the accuracy of the calculations and simultaneously check their reliability by changing the simple models to more complicated ones and using more precise analytical methods.

Let us consider some of the new results.

Current distribution along dipole. In accordance with dipole antenna theory, the current distribution function $f(\xi) = I(\xi)/I(0)$ (ξ – coordinate along dipole) takes with satisfactory accuracy the form of a standing wave in the equivalent transmission line. In [1] this function is assumed to be equal to

$$f(\xi) = \cos \frac{\pi \xi}{l}, \quad |\xi| \leq l/2. \quad (2)$$

In reality, formula (2) is valid when the dipole length l is the resonant one: $l = \Lambda/2$, where Λ is the wavelength in the equivalent line. If l differs from $\Lambda/2$, then $f(\xi)$ takes another form. It is necessary to take into account that the dipole is excited by the EMF distributed along the dipole length and not lumped at the point $\xi=0$, as in the usual case. In our case the distributed EMF is equal to the tangent component of the electric field of the waveguide modes and the field of the other dipoles; this field varying only slightly along the dipole.

Thus, we obtain the following problem for finding the function $f(\xi)$: the effect of the almost constant external EMF $\bar{E}(\xi) \approx \text{const}$ is along the transmission line, line length is $l/2$, it is shorted in the section $\xi=0$ and is open at $\xi=l/2$. The solution of this problem has the following form:

$$f(\xi) = \frac{\cos \gamma \xi - \cos(\gamma l/2)}{1 - \cos(\gamma l/2)}, \quad (3)$$

where $\gamma = 2\pi/\Lambda$.

As is seen from (3), the shape of $f(\xi)$ varies but slightly even when the dipole length changes by 3-4 times (If the line is fed by a lumped EMF, then the shape of $f(\xi)$ has a significantly stronger dependency on the l/Λ ratio). Consequently, a correction of the $f(\xi)$ shape does not affect the dipole pattern diagram. Radiation resistance, coupling resistance with waveguide modes and mutual impedance can vary only over 2-3%. But individual reactivity is very sensitive to the $f(\xi)$ shape, as will be shown further on.

Far radiation field. First of all, the problem of the plane wave, which is incident at angles θ, φ on FDF-structure with magnetized ferrite, has to be solved.

We should find the field at the structure surface (in the place of the dipole disposition), which we mark

$$\mathbf{E}_{diff}(\theta, \varphi, \mathbf{e}_0)$$

where $\mathbf{e}_0 = \mathbf{e}_\theta$ or $\mathbf{e}_0 = \mathbf{e}_\varphi$ is the unit vector of incident wave polarization (amplitude of the wave is equal to unit).

This problem is solved for the plane layered FDF-structure by means of a matrix of surface impedance. This matrix is equal to a zero matrix at the lower screened surface. Then the consequent recalculation of the matrix from layer to layer right up to the top one is made. Recalculation formulas are obtained directly from the Maxwell equations; they are not given here because they are very cumbersome. A computer program for the recalculation procedure has been created; it allows one to obtain \mathbf{E}_{diff} for any given θ, φ .

Then using the generalized reciprocity theorem we can calculate the field radiated by the dipole in the far zone for $I(0)=1A$:

$$\mathbf{E}(\mathbf{r}) = \frac{ikwl}{4\pi r} e^{-ikr} \mathbf{F}(\theta, \varphi), \quad (4)$$

where

$$\mathbf{e}_0 \mathbf{F}(\theta, \varphi) = \int_{-l/2}^{l/2} f(\xi) e^{ik \sin \theta (x \cos \varphi + y \sin \varphi)} \mathbf{E}_{diff}(\theta, \varphi, \mathbf{e}_0) d\xi / l. \quad (5)$$

Here $\mathbf{F}(\theta, \varphi)$ is a complex pattern diagram having components F_θ and F_φ . To find them we must substitute in (5) correspondingly $\mathbf{e}_0 = \mathbf{e}_\theta$ and $\mathbf{e}_0 = \mathbf{e}_\varphi$. Other designations are $k=2\pi/\lambda$, $w=120\pi [\Omega]$.

Because the FDF-structure contains nonreciprocal media, field \mathbf{E}_{diff} in (5) must be calculated for transposed tensor $\hat{\mu}$, as the generalized reciprocity theorem demands.

The pattern diagram of the dipole in the H -plane calculated for different ferrite magnetization is shown in Figure 7. The calculation was made at a frequency of 37 GHz for the FDF-structure with a layer thickness of 0.7–0.3–0.7 mm and with dielectric permeability of 13–36–13 accordingly. The beam width of the dipole at the level -3 dB is up to 120 deg. This offers the possibility of

realizing a wide scanning sector for the IPA. If the ferrite is magnetized, then the pattern diagram of the dipole has a different steepness of slopes. As will be shown further, this leads to non-symmetry of the mutual impedance matrix.

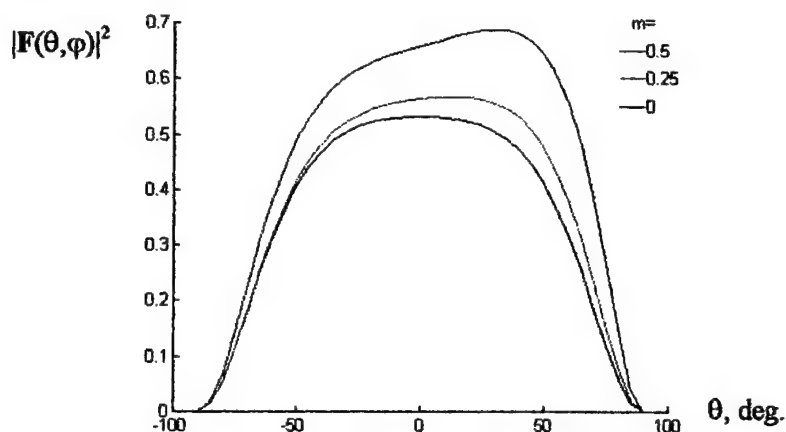


Figure 7. Pattern diagram of single dipole in *H*-plane.

Individual impedance of dipole. The equivalent UHF circuit for the antenna description contains a fictitious pair of poles in the middle of every dipole. The individual impedance $Z=R+iX$ is interpreted as the voltage to current ratio of the external source connected to a given dipole when the currents in all other dipoles are absent and the FDF-structure is matched at both ends.

In reality there are no poles and the dipole is excited by the distributed EMF (see above). Let a dipole be surrounded by enough distant surface S_1 and apply to the resulting volume the Pointing theorem

$$\int_V \mathbf{E} \cdot \mathbf{j}^* dV = \oint_{S_1} (\mathbf{E} \times \mathbf{H}^*) \cdot \mathbf{n} dS + i\omega \int_V (\mu_0 \mu |\mathbf{H}|^2 - \epsilon_0 \epsilon |\mathbf{E}|^2) dV. \quad (6)$$

The left side of the equation is a complex power S of external sources. In this case conductivity current \mathbf{j} flows only over the surface of the selected dipole. Integrating over the coordinates, which are transversal to the dipole axis, we obtain

$$S = P + iQ = \int_{-l/2}^{l/2} \bar{E}(\xi) I^*(\xi) d\xi = I^*(0) \int_{-l/2}^{l/2} \bar{E}(\xi) f(\xi) d\xi. \quad (7)$$

where P is active power, Q – reactive power, $\bar{E}(\xi)$ – tangent to dipole component of external field E_0 , averaged over the cross-section perimeter.

If the dipole has lumped poles, then it would be

$$S = UI^*(0).$$

Comparing this equation with (7), we can conclude that the following voltage should be taken at the fictitious pair of poles

$$U = \frac{S}{I^*(0)}$$

Accordingly, the individual impedance is determined as

$$Z = R + iX = S / |I(0)|^2. \quad (8)$$

The first integral on the right side of (6) has a real value at a large distance from the dipole. It is the sum of the power radiated in the space and the power brought away by all the propagating modes in the FDF-waveguide. We therefore have, in accordance with (8)

$$R = R_{rad} + \frac{1}{4} \sum_{m=1}^M (|k_m|^2 + |\dot{k}_m|^2). \quad (9)$$

Here

$$R_{rad} = w \left(\frac{l}{2\lambda} \right)^2 \int_0^{2\pi} d\varphi \int_0^{\pi/2} |\mathbf{F}(\theta, \varphi)|^2 \sin\theta d\theta \quad (10)$$

is the radiation resistance, which is determined from (4-5) by integrating $|\mathbf{E}(\mathbf{r})|^2 / w$ over the hemisphere area having radius r . The value $|k_m|^2 / 4$ is equal to the power of the m th mode excited by a dipole with $I(0)=1$. It was shown in [1] that

$$z_m = \int_{-l/2}^{l/2} f(\xi) \mathbf{E}^{(m)}(\xi) d\xi, \quad (11)$$

where $\mathbf{E}^{(m)}$ is a field of the m th mode, normalized to the unit power (value z_m is called the coupling resistance of the dipole with m th mode, the point above z_m means that the mode is propagating in the reverse direction).

The reactive component of individual impedance is determined by the second item on the right side of (6). The field located in the immediate vicinity of the dipole having predominantly the structure of a static field is the main contributor. So in order to calculate it we can use the dipole model as a transmission line segment. The reactive power in transmission line is equal to

$$Q = \omega \int_0^{l/2} (L|I(\xi)|^2 - C|U(\xi)|^2) d\xi = |I(0)|^2 X,$$

where L , and C are the standard parameters of the line. We should substitute here the current distribution function $f(\xi)$ from (3) and voltage

$$U(\xi) = -\frac{1}{i\omega C} \frac{dI}{d\xi} = -\frac{I(0)}{i\omega C} f'(\xi).$$

We obtain, after simple algebraic manipulation:

$$X = W_0 \frac{\gamma l (1 + \cos \gamma l) / 2 - \sin \gamma l}{2[1 - \cos(\gamma l / 2)]^2}, \quad (12)$$

where W_0 is the wave resistance of the line.

To calculate W_0 and the wavelength in line $\Lambda = 2\pi/\gamma$ we can use different transmission line models and various analytical methods. The simplest model: a dipole (strip having length l and width b) disposed at the air-ferrite boundary, the ferrite is an isotropic dielectric with permeability ϵ_f , its thickness is infinite. Then

$$\Lambda = l / \sqrt{\epsilon_e}, \quad W_0 = \frac{120}{\sqrt{\epsilon_e}} \left(\ln \frac{2l}{b} - 0.9 \right),$$

where

$$\epsilon_e = \frac{\epsilon_f + 1}{2}.$$

The formula for W_0 is approximate; its accuracy rises when the l/b ratio is greater.

More complicated models must take into account that the thickness of the ferrite layer is finite and that other layers and a metal screen are present. The model becomes more complicated when the ferrite is magnetized.

It is to be noted that the dependence of Z on dipole length differs radically from the dependence when the dipole is fed by a lumped EMF. The real part R increases monotonically when l increases. The plot of $X(l)$, in accordance with formula (12), is shown in Figure 8. The difference from the usual dipole antenna for $l/\lambda \leq 0.5$ is small, but it becomes essential for $l/\lambda > 0.5$. In particular, no second resonance is observed near $l=\lambda$ (inductive energy predominates). The next resonance occurs only near $l/\lambda=3/2$.

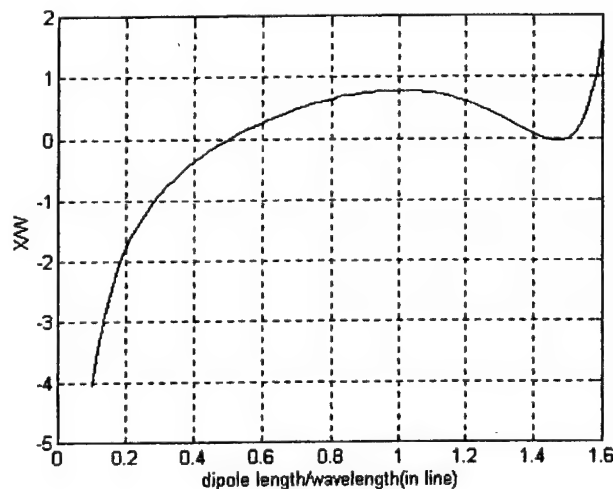


Figure 8.
Dependence of the reactive component $X(l)$
on dipole length.

Mutual impedance of dipole pair. This impedance $Z_{21}(\rho, \alpha)$ is a function of distance ρ and of polar angle α of the second dipole with respect to the first one. Using (4-5) we can obtain the asymptotic formula:

$$\tilde{Z}_{21}(\rho, \alpha) = \frac{wl_1 l_2}{8\pi\rho^2} e^{-ik\rho} \mathbf{B}_1(\alpha) \mathbf{B}_2^T(\alpha + \pi). \quad (13)$$

Here $\mathbf{B}(\alpha) = \partial \mathbf{F} / \partial \theta|_{\theta=\pi/2, \varphi=\alpha}$. The sign « ∂ » means that the function of directivity $\mathbf{F}(\theta, \varphi)$ is determined for the transposed tensor $\hat{\mu}$ that corresponds to the receiving regime.

Formula (13) is valid for a large ρ (in practice for $\rho > 2\lambda$). The diminution of \tilde{Z}_{21} as ρ^{-2} is determined by the fact that $\mathbf{F}(\pi/2, \varphi) = 0$ due to the existence of the screen.

Considering the power radiated by two arbitrary excited dipoles, we can obtain the following formula

$$\frac{1}{2} [Z_{12}(\rho, \alpha) + Z_{21}^*(\rho, \alpha)] = \frac{wk^2 l_1 l_2}{(4\pi)^2} \int_0^{2\pi} d\varphi \int_0^{\pi/2} \mathbf{F}_1^*(\theta, \varphi) \mathbf{F}_2(\theta, \varphi) e^{ik\rho \sin\theta \cos(\varphi - \alpha)} \sin\theta d\theta \quad (14)$$

It is valid for any ρ , but it determines only the Hermitian part of the mutual impedance matrix. If we form the function

$$Z_H(\rho, \alpha) = \frac{1}{2} [\tilde{Z}_{12}(\rho, \alpha) + \tilde{Z}_{21}^*(\rho, \alpha)]$$

from (13), then, as analysis shows, it passes through the same values as (14) does, but for slightly different values of ρ (when ρ is small). The behavior of the non Hermitian part of the impedance has the same character, because, together with Hermitian part, it has the same envelope. So the exact value of mutual impedance for all $\rho \geq \lambda/2$ is equal to

$$Z_{21}(\rho, \alpha) = \tilde{Z}_{21}(\rho + \Delta\rho, \alpha), \quad (15)$$

where $\Delta\rho$ – correction, which can be approximated by the expression

$$\Delta\rho = \frac{1}{C_1(\alpha)\rho + C_0(\alpha)}.$$

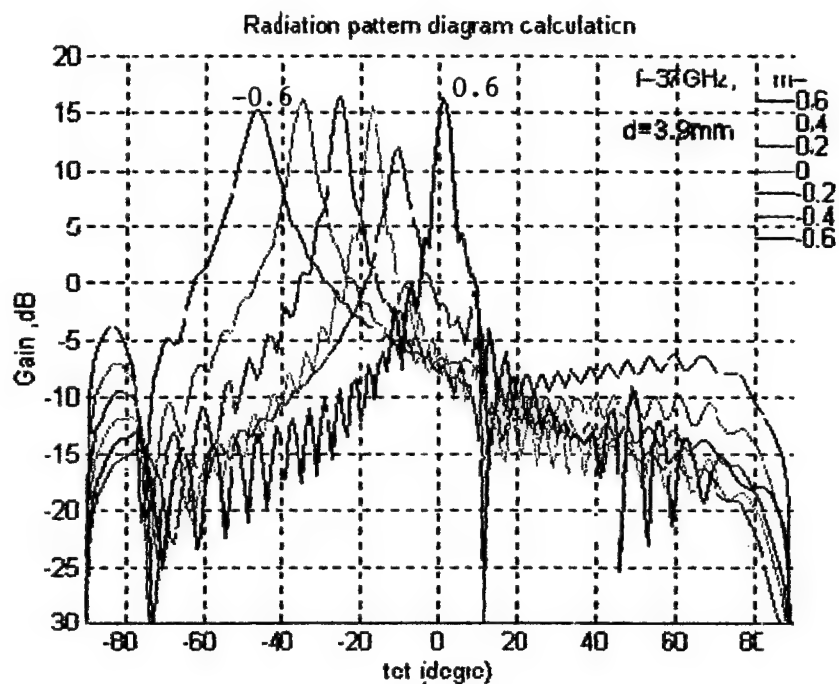
$C_1(\alpha)$ and $C_0(\alpha)$ are calculated by comparing (14) with $Z_H(\rho, \alpha)$ for small distances.

Software for antenna modeling has been developed. The input data are: thickness of dielectric and ferrite layers, dielectric permeability and loss tangent of each layer, magnetic permeability of ferrite layers and their magnetization. There is a separate program for the calculation of magnetization as a function of control current.

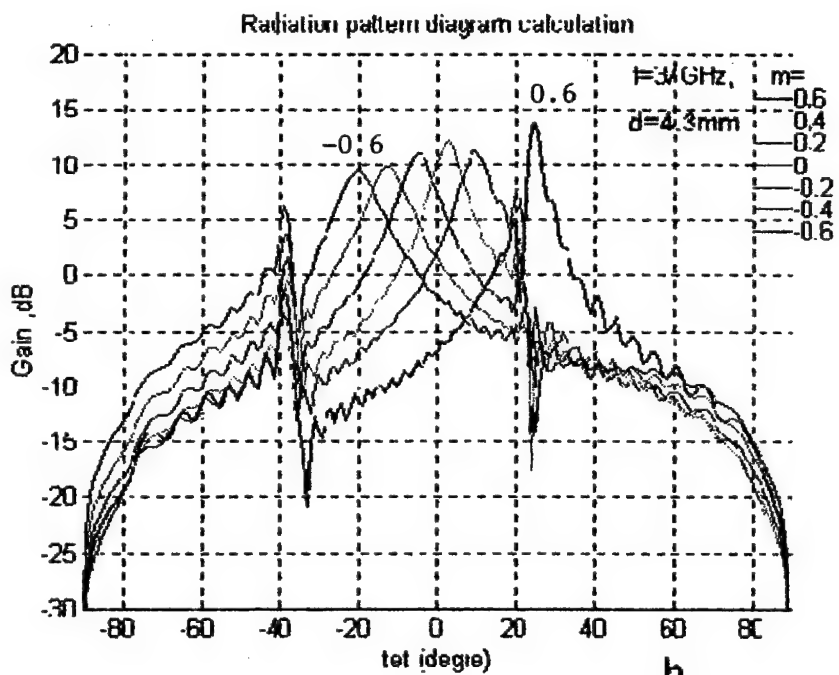
The program solves both internal and external problems and calculates the coefficients of the system of linear equations for the currents in the dipoles. After determining the currents, the pattern diagram of the antenna and its parameters (gain, efficiency, etc.) have been calculated.

The program allows the modeling of situations when the parasitic mode or the main (operating) mode are excited at the FDF-waveguide input and when reflections from the waveguide edge are present.

A set of pattern diagrams of a linear IPA is shown in Figures 9a and 9b. The antenna has 35 dipoles. The distance between dipoles is 3.9mm (Figure 9a) and 4.3 mm (Figure 9b). The pattern diagram in Figure 9b corresponds to the case when the antenna radiates at normal to the aperture, when the ferrite is demagnetized. As can be seen, this choice, at which the antenna radiates in a normal direction in a demagnetized state, causes a gain drop of 4-6 dB and side lobe level growth. The VSWR of the antenna also increases from 1.2-1.5 to 3-5 in the scanning sector. The reason is the in-phase addition of reflections of the reverse main mode. If radiation at normal to the antenna occurs with a magnetized state of ferrite, then this phenomenon is not observed.



a



b

Figure 9. Calculated pattern diagrams of the linear IPA.

4. Experimental Results

Various types of antenna samples have been worked out and fabricated.

A photo of a mm-wave 1D IPA is shown in Figure 10. The antenna contains about 60 dipoles. Total length is 250 mm. In this design the FDF-waveguide with dipoles is placed inside a horn, which serves as framework and forms the pattern diagram in the E -plane. Relative H -plane pattern diagrams of this antenna are shown in Figure 11. Its gain is about 20 dB, scanning sector width -43 deg. (H -plane).



Figure 10. Photo of mm-wave 1D IPA.

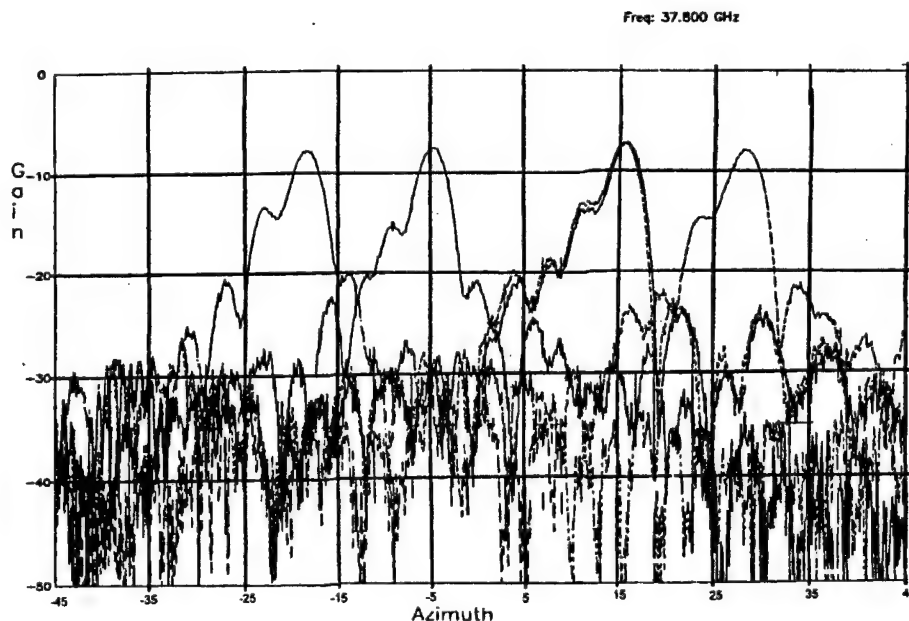


Figure 11. Relative pattern diagrams in H -plane.

The parameters of this antenna are given in Table 1.

Table 1. 1D IPA	
Wavelength range	8mm
Number of radiating elements	63
Gain	20 dB
Dimension	250 mm
Scanning sector in <i>H</i> -plane	43 deg.
Control current	± 700 mA
Beam width in <i>H</i> -plane	2.5deg
Beam width in <i>E</i> -plane	60 deg.

A photo of an 8 mm-wave 2D IPA, in which the principle of independent beam control in each plan by a single control current has been realized for the first time, is shown in Figure 12.

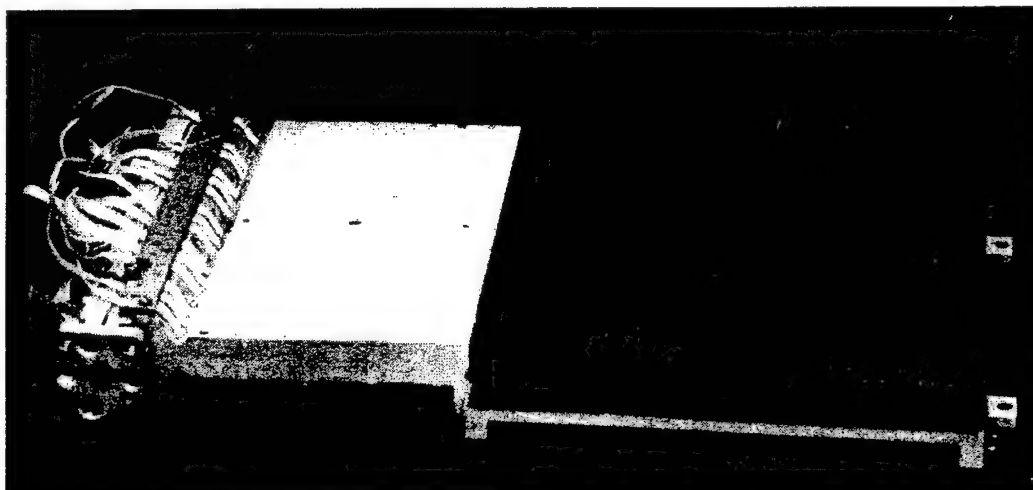


Figure 12. Photo of 8 mm-wave 2D IPA.

The antenna consists of a power distributor with controlled phase on the basis of the FDF-waveguide, phase correction unit and 2D radiating aperture. The dimensions of the radiating aperture are 110×110 mm and it contains about 500 dipoles. Pattern diagrams of the antenna in *E*- and *H*-planes are shown in Figures 13a and 13b.

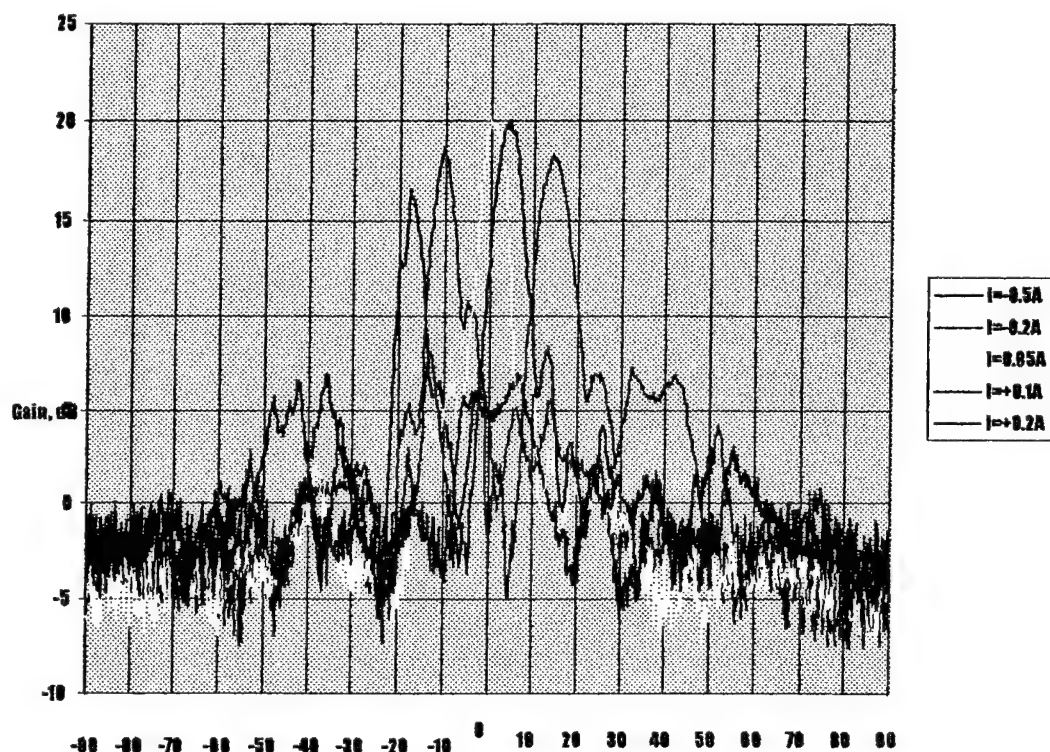


Figure 13a. *E*-plane pattern diagram.

Unfortunately, the poor quality of the materials and fabrication imperfections did not allow the obtaining of a high gain. It was about 20 dB. But this model successfully demonstrates the ability to realize the proposed principle of the antenna design and beam control. Its pattern diagram holds its shape in the whole scanning sector (from -17 to +17 deg. in the *E*-plane and from -10 to +33 deg. in the *H*-plane). Parameters are given in Table 2.

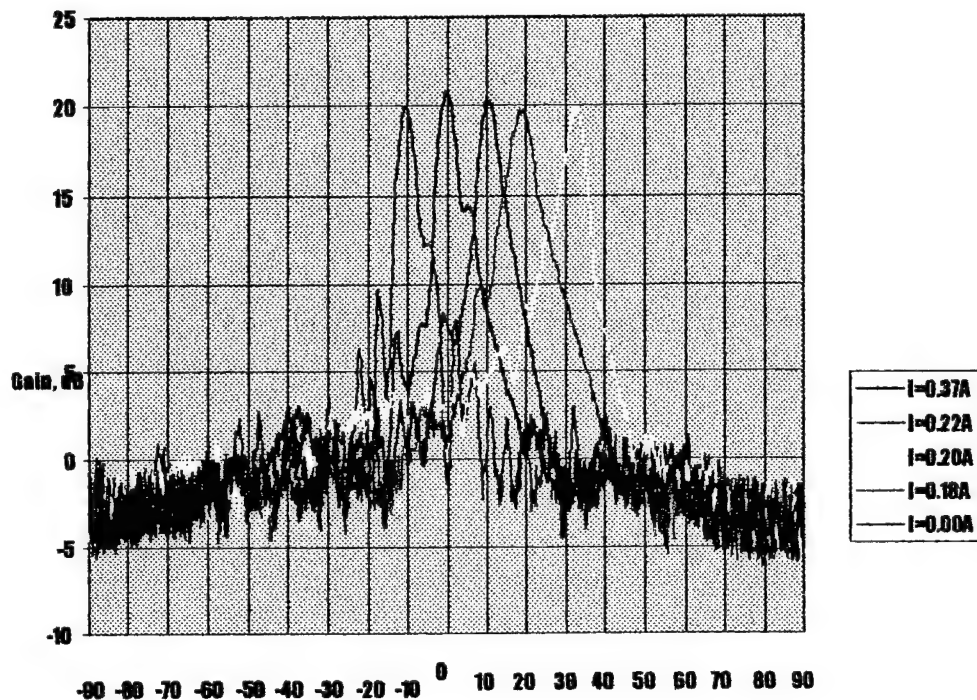


Figure 13b. H-plane pattern diagram.

Table 2. 2D IPA	
Wavelength range	8mm
Number of radiating elements	616
Gain	20 dB
Dimensions	110×110 mm
Scanning sector in <i>E</i> -plane	-17...+17 deg.
Scanning sector in <i>H</i> -plane	-10...+33 deg.
Control current	±1A
Beam width	5×5 deg.

5. Conclusions.

Integrated phased mm-wave arrays with ferrite control present a new class of antennas with specific features. These antennas have:

- a planar low-profile design;

- simple controls (the antenna has the ability to be driven by one current during 1D scanning or two currents during 2D scanning);
- low-cost in series and mass production.

Electrodynamic analysis and the developed software allow the prediction of the main characteristics of the different types of IPA: gain, pattern diagram, scanning sector. Experimental models of 1D and 2D IPA successfully demonstrate the ability to realize the proposed design and control principle. The use of ceramic with high quality $\sim 7000 - 10000$ will make it possible to obtain parameters as good as those of conventional arrays in the mm-wave band.

6. References

- [1] E. F. Zaitsev, et al., "MM-wave Integrated Phased Arrays with Ferrite Control", *IEEE Transaction on Antennas and Propagation*, vol. 42, No. 3, pp. 1262-1368, March, 1994.
- [2] E. F. Zaitsev, et al., "MM-wave Integrated Phased Arrays with One Current and Two Current Control", *Book of Proc. of Microwaves 1994 Conf.*, London, UK, October 25-27, 1994.
- [3] A. Cherepanov, A. Gouskov, et al., "Innovative integrated ferrite phased array technologies for EHF radar and communication applications", *IEEE Intl. Symp. on Phased Array Syst. and Technology*, Boston, October 1996.
- [4] E. F. Zaitsev, Yu. P. Yavon, G. A. Yufit, M. R. Beltran, J. S. Khodorkovsky, "Low Cost Microwave and MM-Wave Integrated Phased Arrays with Ferrite Control", *Proc. of 1996 Antenna Applics. Symp.*, Illinois, September 1996.
- [5] E. F. Zaitsev, Yu. A. Komarov, Yu. P. Yavon, "Analysis of Electrically Controlled FDF-Waveguide", *Proc. of the 15th International Symposium on Electromagnetic Theory*, St.Petersburg, Russia, 23-25 May, 1995.
- [6] E. F. Zaitsev, Yu. P. Yavon, G. A. Yufit, A. B. Gouskov, "Patch-MMIC-Ferrite Integration in Novel Phased Array Technology", *WRI International Symposium*, New York, September 11-13, 1996.
- [7] E. F. Zaitsev, V. N. Diky, A. I. Babenko, "Calculation of Nonreciprocal Receiving Antenna Characteristics", *Radiotekhnika i Elektronika*, Vol. 25, p. 639, March 3, 1980.

CEM CODE VALIDATION USING INFRARED IMAGING TECHNIQUES

Michael Seifert
Rome Laboratory/ERST
525 Brooks Road
Rome NY 13441-4505

Dr. John Norgard
University of Colorado
Colorado Springs, CO 80933

Abstract:

An infrared (IR) measurement technique is presented which has been developed to measure electromagnetic (EM) fields. This technique uses the thermal absorption properties of a thin, planar, and lossy IR detection screen to map the intensity of the EM energy over any two-dimensional region of interest. This measurement produces a two-dimensional IR thermal image of the electric or magnetic field being measured. This technique recently has been applied to determine near-field intensities and far-field antenna patterns, diffraction patterns of EM fields scattered from complicated metallic objects, intensities of EM fields coupled through apertures in shielded enclosures and modal distributions of EM fields excited inside cavities. This paper presents IR measurements of antenna patterns, EM energy scattered from an F-16 scale model aircraft and modal distributions of EM fields excited inside cavities. The results are compared to data predicted by numerical electromagnetic analysis codes. The purpose of this paper is to demonstrate the feasibility and illustrate the application of using IR measurements as an antenna diagnostic technique and as a means of validating computational electromagnetic tools.

1. Introduction

The Infrared (IR) measurement technique is a minimally perturbing measurement used to map EM fields and provide a visual representation of EM field distributions. This technique is based on the thermal heating which occurs

when EM energy is absorbed by a lossy dielectric or resistive detector material. The absorbed EM energy is converted into conducted and convected heat energy. The absorbed energy is then re-radiated as EM energy concentrated in the IR band. A sheet of carbon loaded Kapton is used as the IR detector material. It absorbs a small portion of the EM energy causing the surface temperature of the detector to rise above the ambient temperature. This temperature change is detected by an IR measurement system. For a thin, low-loss material, the fields in the material are approximated as constant; thus, the power absorbed per square meter is adequately described by:

$$P_{abs} = \frac{1}{2} \int_0^d [(\sigma' + j\omega\epsilon'')(E_t^2) + \omega\mu''(H_t^2)] d\hat{n} \quad (1)$$

where \hat{n} is a vector normal to the surface of the lossy material, d is the thickness of the lossy material, ω is the radian frequency, σ' is the real part of the material conductivity, ϵ'' is the imaginary part of the complex permittivity of the material, μ'' is the imaginary part of the complex permeability of the material, and the t subscripts on the field quantities imply the tangential components. The conductivity and the imaginary components of the permittivity and permeability cause the temperature of the detector to rise above the ambient temperature. The increase in temperature is proportional to the local electric and magnetic field intensity at every location on the detector. Thus, a two-dimensional map of the field intensity is produced. The absolute temperature across the IR detector is

recorded, digitized and stored using an Agema Thermovision infrared measurement system. This data can be used to directly obtain the relative field intensity.

2. Magnitude Measurements

Relative electromagnetic field intensity measurements can be used to validate CEM analysis tools. These measurements were performed in Rome Laboratory's anechoic chamber. The anechoic chamber is used to minimize unintentional EM fields and EM reflections from distorting the measurement results. It also provides a stable temperature environment. The measurement technique involves placing the IR detector in front of the EM radiating source. A standard gain horn was used to generate the EM field distribution. The physical dimensions of the horn were measured to allow the horn to be properly modeled for the CEM simulations. The IR detector is positioned directly in front of and at various distances from the face of the horn antenna. A long wave IR scanner with a spectral response of 8-12 microns and detects temperature changes as small as .08C. The IR scanner samples data at 136 lines per frame and 272 samples per line, the data is digitized and stored.

3. Scattering Experiments

For the scattering experiments, a brass cylinder is placed between the IR detector and the radiating source. The IR measurements begin by measuring the

background temperature over the IR detector without an EM field applied. The radiating source is then applied and the resulting scattered fields are then measured. The background temperature distribution is subtracted from the temperature distribution of the scattered fields, the result is the scattering effects cause by the radiating source. The CEM tool used during the scattering experiments was the General Electromagnetic Model for the Analysis of Complex System (GEMACS). GEMACS is a robust CEM tool that employs multiple solution techniques to determine various electromagnetic observables at high and low frequencies, interior and exterior to scattering objects. These observables include antenna patterns, field distributions, current distributions on structures, and EMI/EMC transfer functions [1]. GEMACS is used to predict the EM field distribution resulting from a horn antenna in free-space and in the presence of a cylindrical scatterer as previously described. IR Measured data and GEMACS simulations results are represented as gray scale images. The areas of high field levels and high temperatures are represented by white and the lowest field levels and temperatures are black. The IR measurement of the free-space field distribution of a Standard Gain horn is shown in Figure 1 and the GEMACS results are shown in Figure 2. The measured and simulation data compare very well, the number of rings is the same as is the relative field intensity.

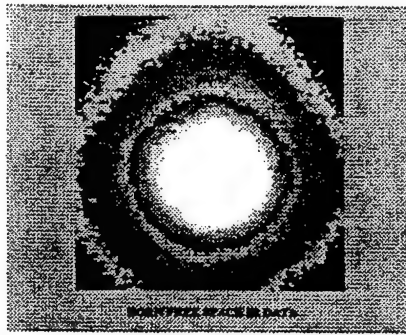


Figure 1- IR Measured Horn Pattern

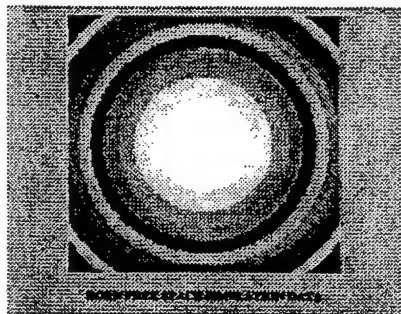


Figure 2- GEMACS Predicted Horn Pattern

Next a cylinder was placed in front of the Standard Gain Horn antenna to determine the scattered fields. The cylindrical obstruction, modeled by the Geometric Theory of Diffraction (GTD) capability in GEMACS. The IR measured data is shown Figure 3 and the GEMACS results are shown in Figure 4. Note that only half of the measurement plane is simulated to reduce computation time. Again the IR measured data compares favorably with the simulation data, the structure is similar with the simulation data being more defined. The hot spot on the side of the cylinder in the simulation data is due to discontinuities at the boundary of the cylinder. For a more complex object, Figure 5 shows the scattered fields from a scale model F-16 aircraft.

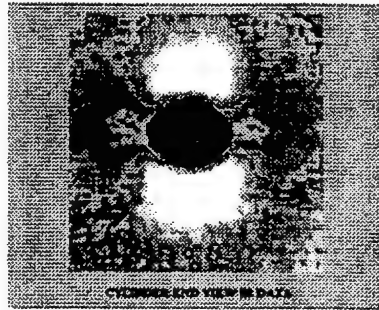


Figure 3- IR Measured Cylinder Scattered Fields

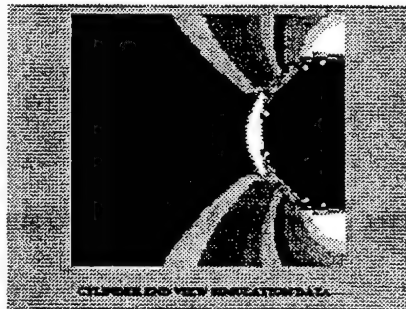


Figure 4- GEMACS Predicted Cylinder Scattered Fields



Figure 5- IR Measured Data F-16 Scattered Fields

4. Coupling Experiments

Miniaturization of electronic circuitry presents a major challenge in both the commercial and military worlds. The design of aircraft circuitry for the Air Force has additional challenges. The circuitry must operate under hostile electromagnetic environments. Since aircraft circuitry is housed within some type of equipment bay, it is important to accurately predict how the external electromagnetic energy is coupled within cavities. The FD-TD technique chosen consists of the standard Yee grid using second order accurate central difference expressions to approximate the spatial and temporal derivatives in Maxwell's two curl equations [2].

The Coupling Experiments were performed using a brass cylinder aligned parallel to the aperture of a standard gain horn antenna. One end of the cylinder is completely closed while the other end is covered with a fine wire mesh. This allows the IR camera to view the internal fields and modal distributions while representing a somewhat solid end at the frequencies used in this experiment. The horn is located 20 inches from the cylinder directly in front of the slot aperture. The cylinder is illuminated with an incident electric field polarized perpendicular to the cylinder axis. The detector is placed on styrofoam which fits tightly inside the cylinder. The IR measurement system records the thermal pattern at various

planes along the axis of the cylinder. The detector is allowed to heat for several minutes to obtain a steady state condition.

FD-TD simulations and IR measurements were conducted for various positions along the axis of the cylindrical cavity. Figure 6 shows the IR measured data of the internal mode structure just behind the aperture of the cylinder and Figure 7 shows the FD-TD simulation results for the same configuration.



**Figure 6- IR Measured Data of
Internal Mode Structure of Cylinder**



**Figure 7- FD-TD Simulation Results of
Internal Mode Structure of Cylinder**

5. Magnitude and Phase Measurements

To determine phase information to accurately determine the far field pattern of antennas, a plane to plane (PTP) phase retrieval technique was developed. A closely related phase retrieval algorithm has been successfully implemented by Yaccarino and Rahmat-Samii at the University of California at Los Angeles (UCLA) with a bi-polar planar hard-wired near-field measurement system using magnitude-only data measured over two planes separated by only 2.560λ [3]. Further modifications and improvements to this technique have been carried out by Rahmat-Samii, et al. [4] and Junkin et al. at the University of Sheffield, UK. [5,6,7]. The uniqueness of the solution obtained from a plane-to-plane phase retrieval algorithm has been addressed by several authors, most notably Isernia, Leone, and Pierri [8,9].

Various variables and constants are defined and an estimate of the magnitude and phase of the aperture field is made. This estimate is then propagated to measurement plane 1 by Fourier transformation. A convergence error is then calculated,

$$\xi = \frac{\sum |A - M|^2}{\sum M^2} \quad (2)$$

where M is the measured magnitude data and $|A|$ is the calculated magnitude data at each pixel location in the plane of interest. The calculated magnitude is then

replaced with the measured magnitude with the calculated phase retained. These complex data are then propagated by Fourier techniques back to the original aperture plane. All data outside the antenna aperture are then truncated, and the truncated data are propagated to the second measurement plane. Again the convergence error is calculated and the calculated magnitude data replaced with the measured magnitude at plane 2 with the calculated phase retained, and these data are then propagated back to the aperture plane. At this point in the process, the change in the convergence error from the previous iteration is checked, and if the change in convergence error is less than a set tolerance, the iterations are halted. If, however, the change in convergence error is still sufficiently large, the iteration is repeated, starting with a truncation of data outside the antenna aperture.

A 36 element patch array operating at 4 GHz was selected as the test antenna and the two measurement planes were at a distance of 32.4 cm and 45.0 cm. Since the array operates at a frequency of 4 GHz, these distances were approximately 4.3λ and 6λ . The measurement planes were chosen to be well outside the reactive near-field and having a plane separation of greater than one wavelength, but not so far apart as to result in a large difference in peak thermal paper temperatures.

To verify the PTP technique, a number of simulations was performed before processing the thermally measured data. First, the array antenna was measured by the National Institute of Standards and Technology (NIST) on their near-field antenna test range. The near-field to far-field FFT processing method discussed above was then used to compute the magnitude and phase of the fields of the array at the two measurement planes selected for the IR thermal measurements (32.4 cm and 45.0 cm). The magnitudes of these data were then used as an initial simulation of the capabilities of the PTP algorithm.

Figure 8 is an overlay of the far-field pattern of the array as determined by the PTP algorithm (dashed *) and from the original NIST complex data (solid +). As the figure illustrates, the agreement between the PTP determined far-field pattern and the real far-field pattern of the array is excellent. The PTP algorithm was then

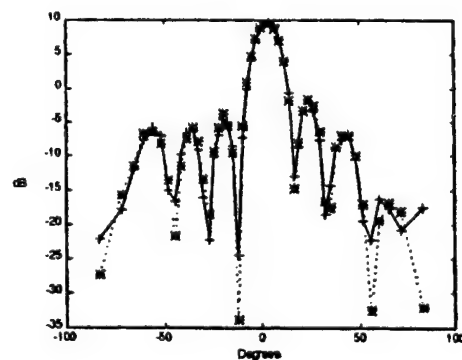


Figure 8- PTP Generated Far-Field
from NIST Magnitude Data

rerun with the NIST magnitude data truncated at amplitudes below 20 dB down from the peak as an estimate of the effects of very low dynamic range magnitude data. The result of this simulation is shown in Figure 9.

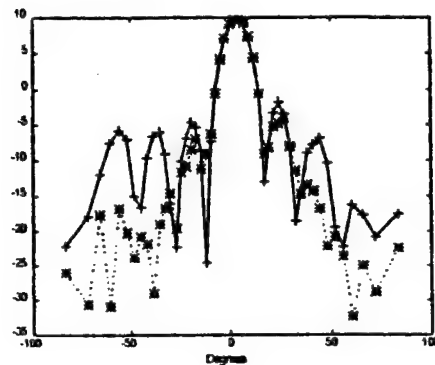


Figure 9- PTP Results Using NIST
Magnitude Data Truncated to 20 dB Dynamic Range

As illustrated in this figure, the PTP algorithm was able to only reconstruct the antenna main-lobe and provide an indication of the location of the first two side-lobes (but not the correct amplitudes for the side-lobes). Obviously, the results from the simulations of 20 dB dynamic range are only marginally useful.

Actual IR thermograms were then taken over these same measurement planes using the current AGEMA 900 thermal camera at Rome Laboratory. Direct comparison of the field magnitudes from the thermograms to the expected values based on the NIST measured data indicated that the thermal measurements produced about a 25 dB RF magnitude dynamic range. The result of the PTP

algorithm on these data are shown in Figure 10 and provides good agreement with the simulation results.

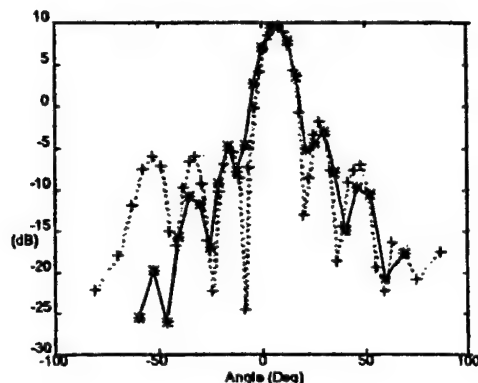


Figure 10- PTP Results Using Thermograms from IR Camera

In summary, the PTP iteration algorithm is very well suited to the reconstruction of the far-field pattern from thermographic measurements on 2 near-field planes.

6. Conclusions

IR measurements were used to map the electromagnetic field distributions generated by a standard gain horn and the fields scattered by and coupled into a metal cylinder. Each measurement scenario was directly modeled and simulated using CEM tools to provide a comparison with the measured results. The measured IR data compared favorably to the simulation data, the general shape and relative levels of the radiation patterns are in close agreement. The IR measurement technique provides a quick and accurate representation of antenna patterns and electromagnetic scattering and coupling effects. The IR

measurement technique can also be used to identify potential problems in the development of antenna models and simulation techniques. This paper has demonstrated the feasibility of using IR measurements. This validation technique can provide insight in the area of model development, model enhancement, and simulation techniques which can improve the performance of CEM tools. It also shows promise as an antenna diagnostic technique for phased array antennas, eliminating the problems associated with mechanical positioning of near-field measurements.

7. References

- [1] E.L. Coffey, N.W. Coffey and D.L. Kadlec 1988. "GEMACS Source Book." Technical Report RADC-TR-88-102. Rome Air Development Center/RBCT, Griffiss Air Force Base, NY.
- [2] A. Taflove, Computational Electrodynamics: The Finite-Difference Time-Domain Method, Artech House, Boston, MA.
- [3] R.G. Yaccarino and Y. Rahmat-Samii, "Phaseless Near-Field Measurements Using the UCLA Bi-Polar Planar Near-Field Measurement System," *16th Annual Antenna Measurement Techniques Association Symposium*, pp. 255-260, October 1994.
- [4] R.G. Yaccarino and Y. Rahmat-Samii, "Phaseless Bi-polar Near-field Measurements: A Squared Amplitude Interpolation/Iterative Fourier Algorithm,"

1995 Antenna Measurements Techniques Association 17th Meeting and Symposium, Williamsburg, pp. 195-200, Nov 13-17, 1995.

[5] C.A.E. Rizzo, G. Junkin, and A.P. Anderson, "Near-field/Far-field Phase Retrieval Measurements of a Prototype of the AMSU-B Space-Borne Radiometer Antenna at 94 GHz," *1995 Antenna Measurements Techniques Association 17th Meeting and Symposium*, Williamsburg, pp. 385-389, Nov 13-17, 1995.

[6] G.Junkin, A.P.Anderson, C.A.E.Rizzo, W.J.Hall, C.J.Prior, and C.Parini, "Near-field/Far-field Phase Retrieval Measurement of a Prototype of the Microwave Sounding Unit Antenna AMSU-B at 94 GHz," *ESTEC Conference on Millimeter Wave Technology and Applications*, Noordwijk, Netherlands, 1995.

[7] G.Trueba, G.Junkin, "A Numerical Beam Alignment Procedure for Planar Near-field Phase Retrieval," *Electronics Letters*, 1995.

[8] T.Isernia, G.Leone, R.Pierri, "Phaseless Near-field Techniques: Uniqueness Conditions and Attainment of the Solution," *Journal of Electromagnetic Waves and Applications*, Vol. 8, No. 7, pp. 889-908, 1994.

[9] R.Barakat and G.Newsam, "Algorithms for Reconstruction of Partially Known, Band-limited Fourier-transform Pairs from Noisy Data," *Journal of the Optical Society of America*, Vol. 2, No. 11, pp. 2027-2039, 1985.

LIGHTWEIGHT PHASED ARRAY ANTENNA

Leo Diaz, P. Keith Kelly
Ball Corporation
Telecommunication Products Division
P.O. Box 1538
Broomfield, Colorado 80038-1538

ABSTRACT: A unique phased array antenna concept is presented, which lends itself to lightweight applications. The array consists of pillbox-fed line source elements arrayed in one dimension, each producing multiple beams in the other dimension for 2-D scan. The pillbox elements consist of array-fed parabolic reflectors constrained in parallel-plate regions, fed with a multi-element feed array. The design is capable of low-sidelobe operation and can be made deployable. The pillbox elements produce linear polarization that can be rotated by a twist polarizer or converted with an active lens.

1. INTRODUCTION

The lightweight phased array antenna consists of an approximately 5 m horizontal array of 333 vertical line sources 1.6 m tall. The line sources (subarrays) are fed by constrained parallel-plate (parabolic pillbox) reflectors with multi-element feeds.

Figure 1 shows the antenna concept. Rear, front, and side views are shown. The lightweight "boxkite" structure of the array gives it the necessary rigidity while keeping the weight low (at about 1000 lb for the x-band 10 KW version). The

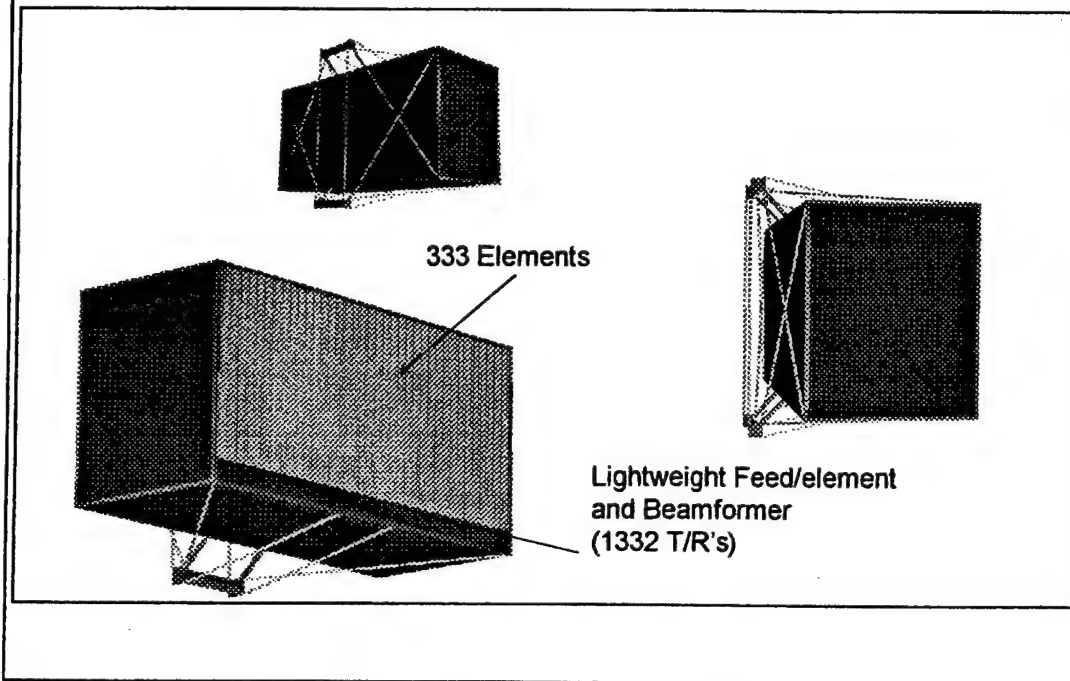
pillboxes have metallized composite walls held tight by tensioning cables and a rigid kingpost external composite structure. The array operates at 10 GHz.

Each subarray forms multiple beams in elevation. A number of subarray units have been built and tested during development to validate the design concept. The 16-beam version scans ± 7.5 deg in elevation with better than 1.0 dB crossover loss. The subarrays are phased in azimuth for ± 60 deg scan. On receive, sum and difference elevation patterns are produced with low-sidelobe elevation and azimuth tapers. On transmit, a uniform azimuth taper is used for maximum radiated power.

The design concept of the subarray is similar to [1], and uses a parallel-plate version of the scan concept of [2], made practical with a proprietary Ball feed.

The pillbox elements are operated in parallel-plate mode, so small variations in the pillbox walls due to physical loads do not disrupt the aperture phase distribution and only affect the amplitude distribution a small amount. For low sidelobe operation, an array of probes is used to monitor the aperture fields for electronic compensation. This can take place in combination with thermal and mechanical monitors that record any temperature or structural changes for adaptive.

Figure 1: Lightweight Array Concept



The antenna operates in horizontal polarization, but vertical polarization can be achieved with a twist polarizer at the aperture. **Table 1** shows the performance characteristics of the design. The 10 KW peak transmit power is produced by 1332 10 W amplifiers or Microwave Power Modules, 4 on each pillbox.

The efficiency of the array is 3 dB with about .8 dB being dissipated in the polarizer. The transmit efficiency budget is shown in **table 2**. It includes everything from the High-Power Amplifiers to the outside of the aperture. There is a circulator at each feed array element to separate the transmit and receive manifolds at that point.

Table 1; Expected Array Performance

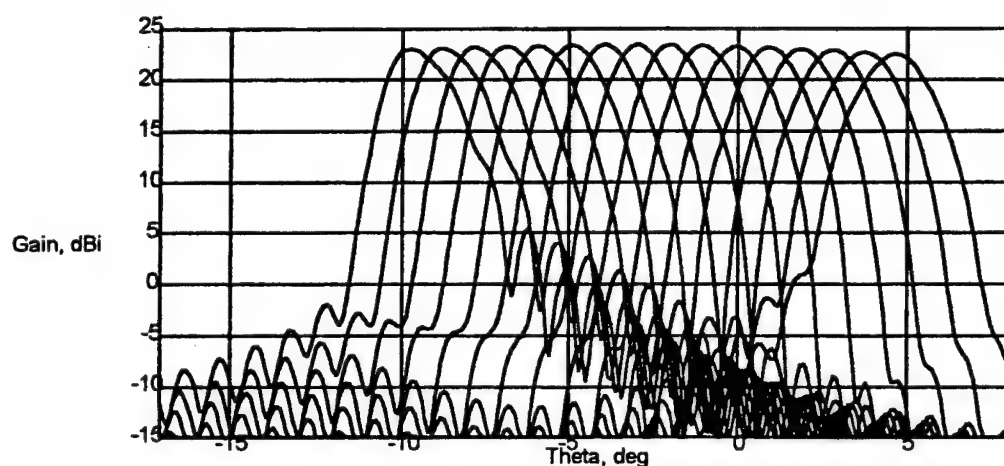
Parameter	Expected Performance
Aperture, m	1.6 by 5
Net Radiated Power, Watts peak	10000 (20 % duty cycle)
Transmit AZ beamwidth, deg.	.35
Transmit EL beamwidth, deg.	1.3
Receive AZ beamwidth, deg.	.50
Receive EL beamwidth, deg.	1.4
AZ Scan Range, deg.	+/- 60
EL Scan Range, deg.	+/- 7.5
EL Beam crossover loss, dB	1.0 max
EL Beam scan loss, dB	1.0 at 7.5 deg.
Polarization	vertical linear (with polarizer)

Table 2; Transmit Efficiency Budget

Parameter	Loss (dB)
3-bit transmit phase shifter	.3
circulator	.4
switch	.5
transition and feed board	.1
feed element efficiency	.2
spillover loss	.3
loss in pillbox walls	.2
aperture and polarizer mismatch loss	.2
polarizer loss	.8
net loss	3.0

The predicted elevation patterns of the multi-beam design are shown in **figure 2**. The reflector is illuminated with a 10 dB edge taper for all the beams for optimal gain performance.

Figure 2: Predicted Multi-Beam Elevation Scan Performance



In transmit, the azimuth taper is uniform to maximize the power on target. The elevation taper, however, is determined by the requirement of meeting the plus-or-minus 7.5 deg scan range with 16 beams with 1 dB or better crossover losses, resulting in individual beams that are broader than with a uniform illumination. The weight budget of the array components are listed in **table 3**. The structure is the most significant component but its weight has been carefully estimated.

Table3; Weight Budget, XSAR Concept

Component	Quantity	Weight, lb.
Feed arrays	333	10
circulators	19(333) = 6327	18
high power switches	4(333) = 1332	29
power amplifiers	4(333) = 1332	147
power phase shifters	4(333) = 1332	75
transmit EL manifold	333	10
LNA's	22(333) = 7326	30
receive EL manifold	333	10
calibration system	1	90
transmit AZ manifold	1	30
receive AZ manifold	1	20
power distribution	1	120
control distribution	1	70
feed housing	1	22
reflector panel	1	43
pillbox sheets	334	107
structural components	-	175
polarizer	1	16
total		1022

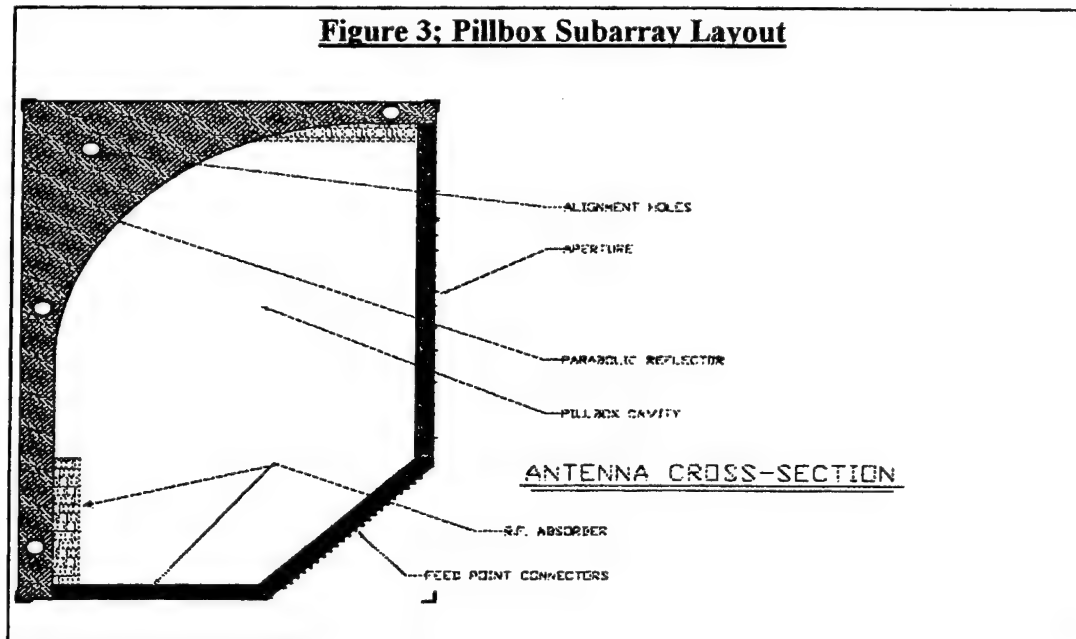
The power amplifiers and the reflector panel are the next most significant contributors. The overall weight is estimated at 1022 pounds, which is significantly less than the weight estimated for a conventional phased array using the same basis of estimate (the phased array is estimated to weigh at least 500 pounds more).

The composite pillbox walls are metallized with 30 KAngstroms (greater than 3 skin depths) of aluminum coating.

2. PILLBOX SUBARRAY DESIGN

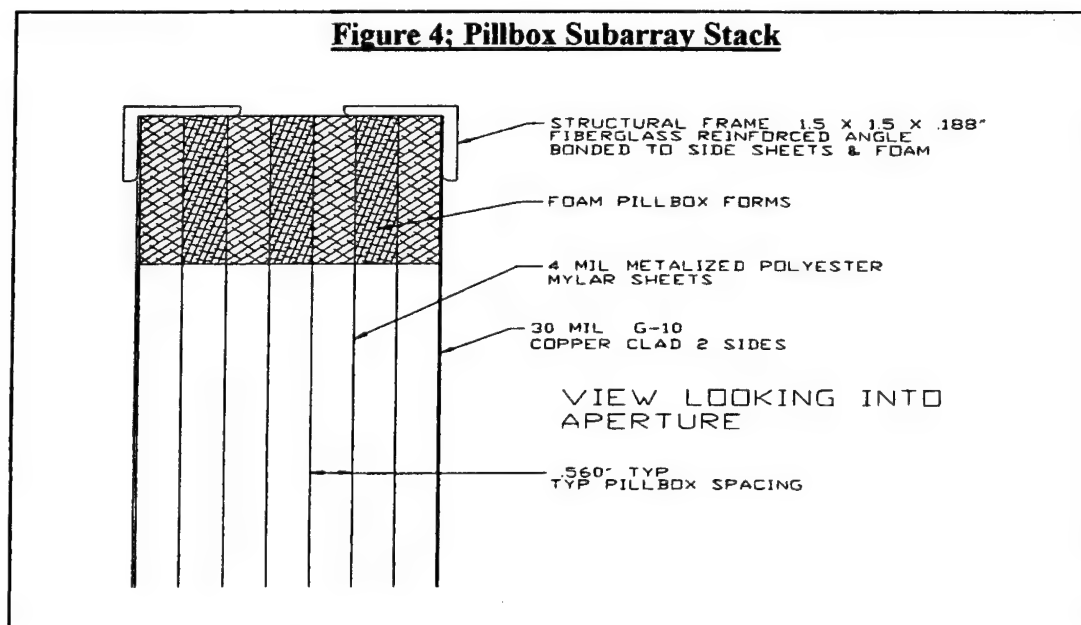
The layout of the pillbox subarray is shown in **Figure 3** . Two metallized composite sheets on either side of the assembly comprise the pillbox walls. Perimeter tensioning eliminates the need for internal supports which can increase sidelobes.

The aperture contains a half-wave lightweight foam radome. A multi-element feed



array is also shown in the figure. The fields in the pillbox region are parallel-plate fields with the electric field normal to the walls (out of the page in **figure 3**). The feed elements are currently coaxial-fed end-fire microstrip radiators.

The reflector itself is made of lightweight foam lined with a metallic surface at the front (to implement the precision reflective surface). The radome, feed, and reflector are all structural components of the integrated structure. A stack of pillboxes is shown in **figure 4**, which illustrates the stacked structure concept. The reflector foam sandwich has significant mechanical strength and low weight.



3. PROTOTYPE MODEL

A proof-of-concept 1.0-m array-fed pillbox demo element was built with Ball Lightweight Antenna Technology, although it did not incorporate the final ultra-low weight materials and processes proposed for the final design. A risk-reduction prototype model is currently being assembled as a follow-on effort and will include the final material and process developments. The 1.0 m subarray prototype was designed to scan ± 12 deg with 16 beams.

Since the parabolic reflector is constrained in a parallel plate environment, the feed elements must be matched in that environment [3]. Several candidate architectures were investigated to find the best design, culminating in an end-launched element (fed through the back wall with microstrip lines) compatible with azimuth array stacking.

Once the feed elements were tuned, the radiation properties in the array environment were characterized. Representative patterns are shown in **figure 5**. The return loss of all the elements are shown in **figure 6**.

Figure 7 shows the measured multi-beam patterns of the prototype reflector. They were measured at the Ball 75-ft indoor tapered chamber. The results show very good crossover-loss performance. Compensating for the 75-ft range effects, the measured patterns correspond fairly well to the predicted ones [4]. The measured and predicted patterns of the center feed element (# 10) are shown in **figure 8**.

Figure 5; Typical Pattern from Ball Feed at 10 GHz

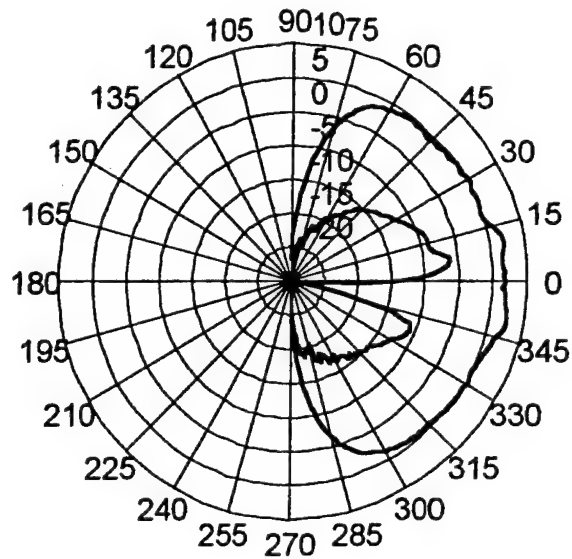
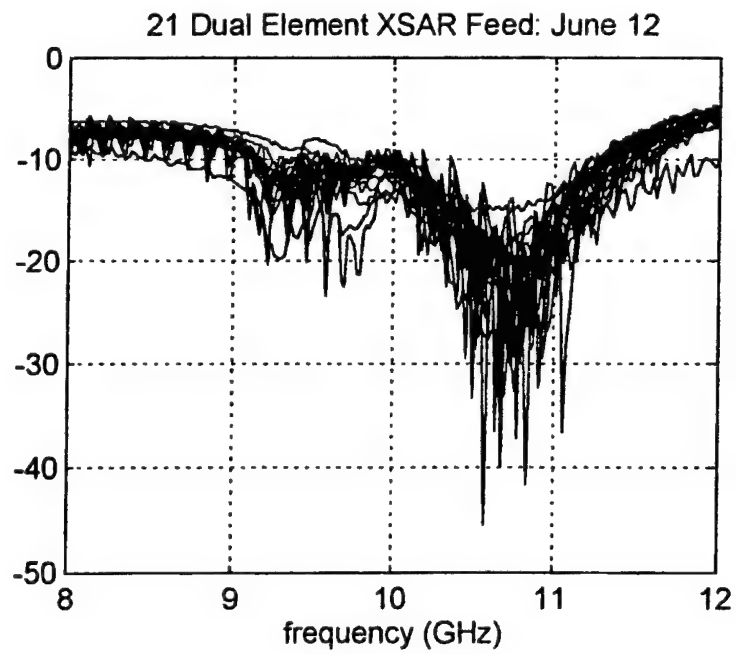


Figure 6; S11 Measurements for Dual Element Feed Array



Because of the uncertainty of the precise phase center location of the feed elements, some distortion is apparent in the beams shown in **figure 7**. This will be corrected in future versions by offsetting the feed array.

The scan loss and crossover loss are shown in **figure 9**. Less than 1 dB scan loss and good crossover performance were achieved.

Figure 7; Measured 1.0 m Pillbox Reflector Patterns

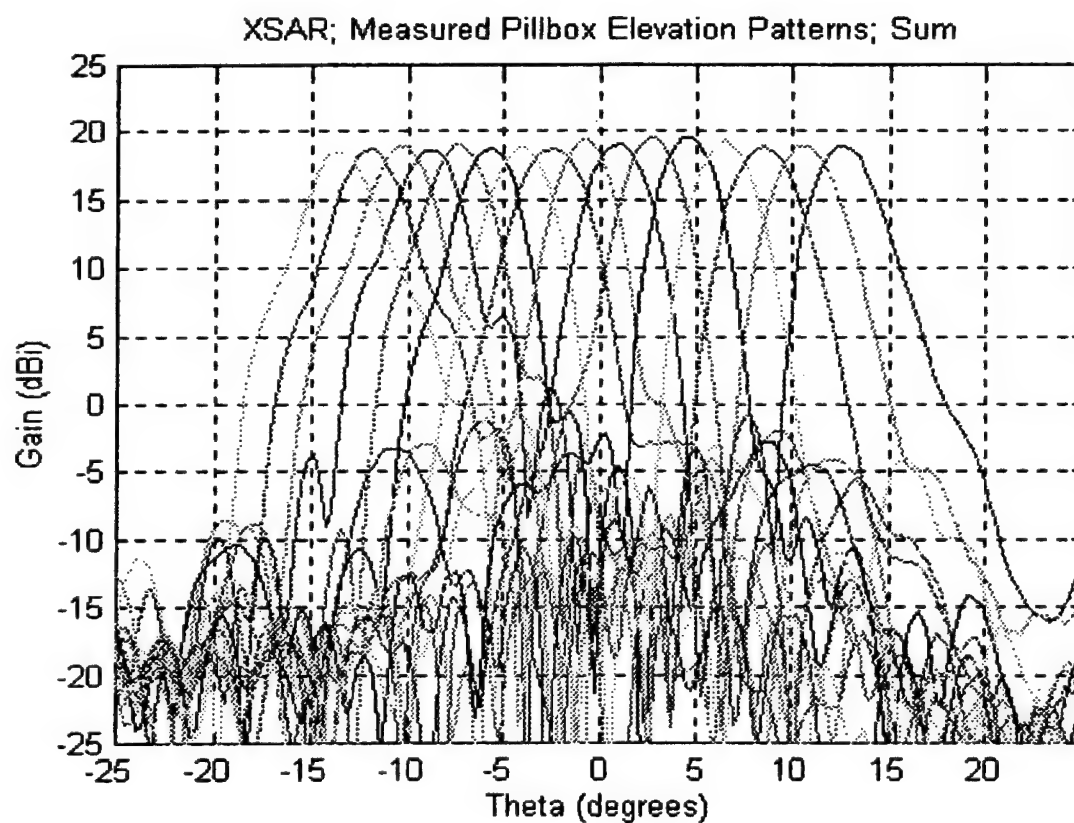


Figure 8; Measured and Predicted Patterns, Prototype Pillbox Subarray

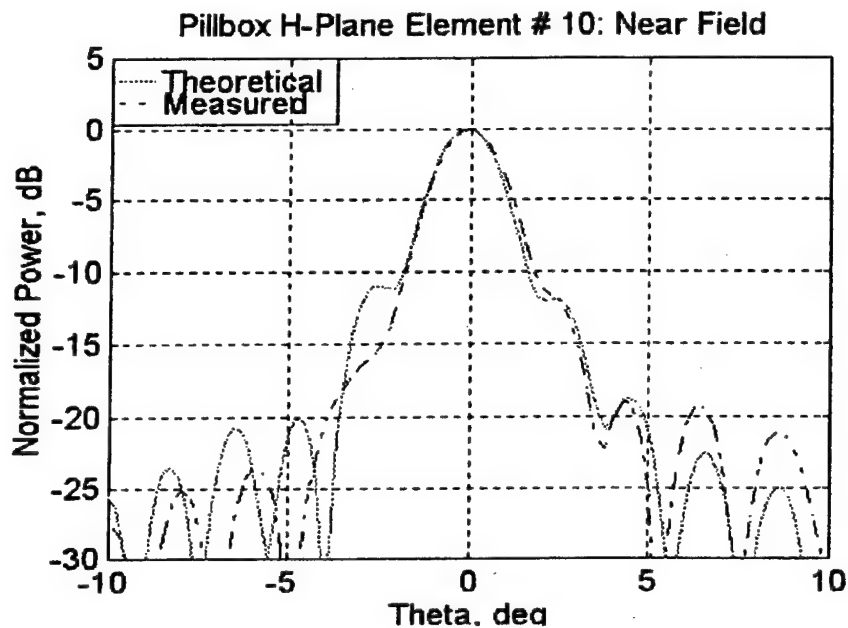
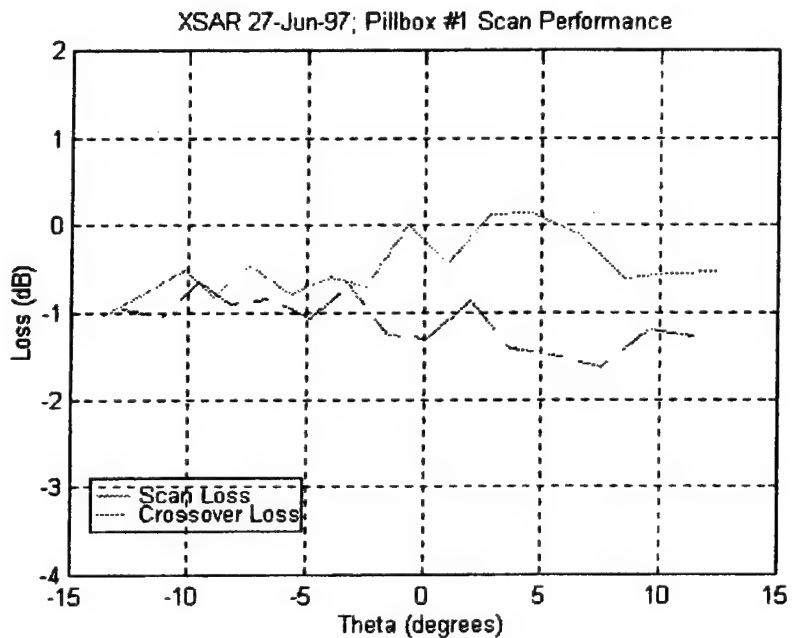


Figure 9; Scan and Crossover Loss: Measured



Since the prototype pillbox did not have the external frame-and-cable structure to hold the pillbox walls in parallel, the pillbox walls were held in place with an external frame, shown in **figure 10**. This structure also served the purpose of a range fixture. The prototype unit is shown in **figure 11**, painted and unpainted.

Figure 10; External Fiberglass Brackets Support the Prototype Pillbox

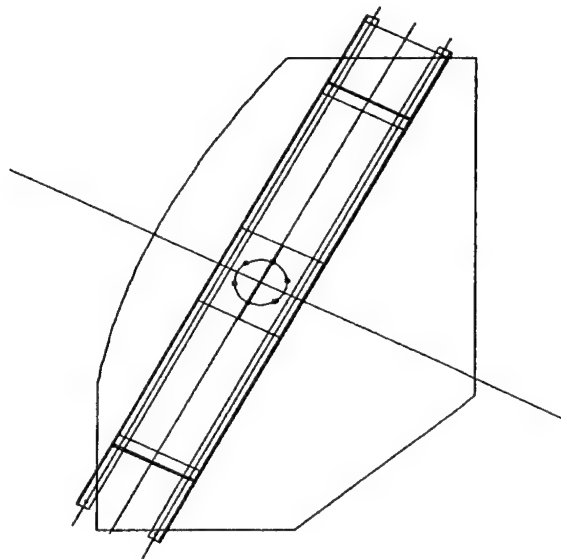
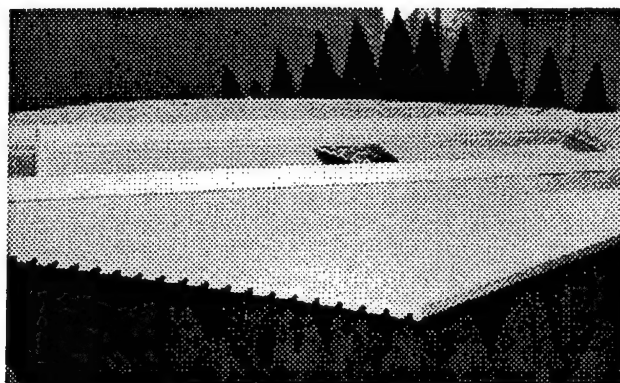
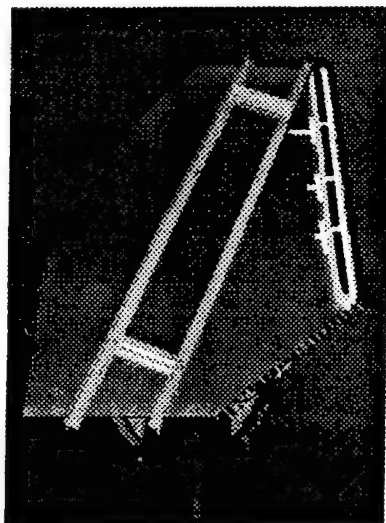


Figure 11; Prototype 1.0 m Subarray Pillbox



4. REFERENCES

- [1] Donald Archer, Sherwood McOwen, Robert Prickett; "Parabolic Horn Antenna with Microstrip Feed". Patent 4051476, Sept 27, 1977.
- [2] Coleman Miller; "Array-Fed Reflector Antenna for Transmitting and Receiving Multiple Beams". Patent 5202700, April 13, 1993

[3] R. C. Rudduck, L. L. Tsai, "Aperture Reflection Coefficient of TEM and TE_{01} Mode Parallel-Plate Waveguides," IEEE Trans. Antennas and Propagation, vol. AP-16, pp. 83-89, January 1968.

[4] L. Diaz and Tom Milligan, *Antenna Engineering Using Physical Optics*, Boston: Artech House, 1996

Miniature UHF SATCOM Antenna for Airborne Platforms

Will McKinzie

Atlantic Aerospace Electronics Corporation
6404 Ivy Lane, Suite 300, Greenbelt, MD 20770
(301) 982-5271

Abstract

The Department of Defense has long needed a small, low profile antenna that can provide adequate gain over the SATCOM band for tactical aircraft such as the F-14 or F/A-18. Traditional designs, such as the conformal cavity-backed annular slot or the protruding "bat wing", are not compatible with these high-performance aircraft because of the large volume required in the former and aerodynamic limitations of the latter. Here we present a unique implementation of a patent pending Tunable Patch Antenna (TPA) mounted in a conformally installed cavity. This electrically-small (8.25"x8.25"x2.4") and efficient prototype antenna offers circularly polarized coverage over the FLTSATCOM band (240-320 MHz). This is accomplished by electronically tuning a narrow band resonance (3 - 4 MHz) over the 80 MHz operational bandwidth at tuning speeds sufficient to accommodate DAMA (Demand Assigned Multiple Access) operation. Performance data are presented for tuning states, efficiency, and gain patterns.

System Description

The conformal antenna presented here is a circularly-polarized, UHF SATCOM antenna system designed for tactical aircraft applications where weight, and especially size, are significant design constraints. The system (see Figure 1) is comprised of an Antenna Control Unit (ACU) and a Tunable Patch Antenna (TPA). The microcontroller-based ACU reads serial data commands from a DAMA compatible modem, such as the ViaSat MD-1324/U, then processes these commands, and extracts frequency information for tuning purposes. Analog control signals are output from the ACU to actuate electronic switches in the TPA. All of the RF circuits and components are contained within the TPA.

A breadboard ACU was fabricated and tested in system demonstrations. This UHF SATCOM antenna system is DAMA compatible since the specified minimum DAMA switching time is 875 μsec , and the typical propagation delay through the ACU is less than 400 μsec . This delay includes the 211 μsec necessary to receive the one byte serial character needed to switch between channels. Transmit-to-receive or receive-to-transmit tuning changes within the same DAMA channel can be accomplished in about 50 μsec . In the system demonstrations to date, frequency information for tuning has been obtained by tapping into the serial data bus from the modem. Alternatively, the ACU may read frequency information directly from the AN/ARC-210, or any other radio with available tuning information.

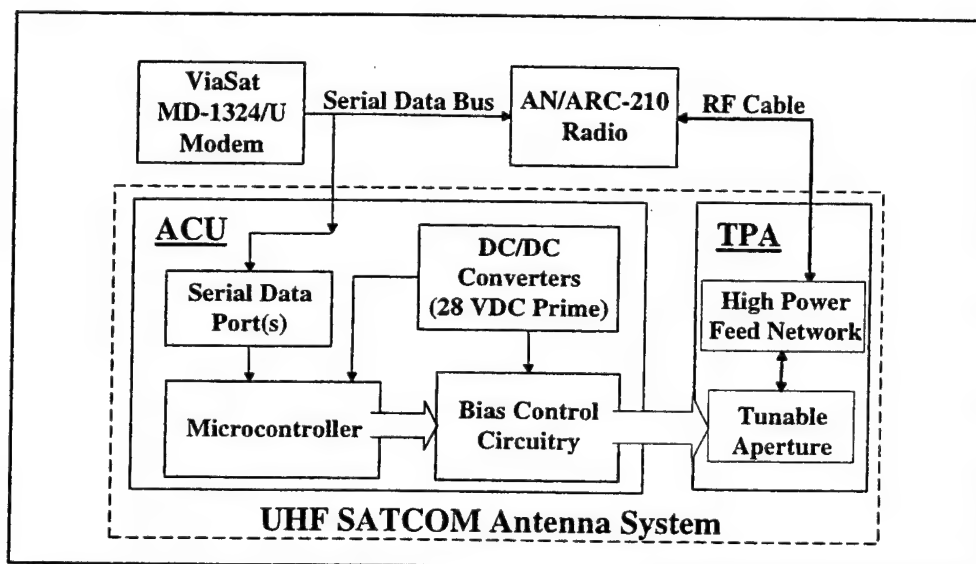


Figure 1. Block diagram of the tunable UHF SATCOM antenna system.

Tunable Patch Antenna (TPA)

This conformal aperture has been designed for optimum gain in a small volume. Extensive computer simulations have parametrically characterized all material losses, both conductor and dielectric, as a function of antenna size. The trade study of efficiency vs. aperture size led to the development of a 17 lb. prototype TPA with an 8"x8" aperture. Photographs are shown in Figures 2 and 3. Not shown in these photos is a planar dielectric radome which bolts to the flange.

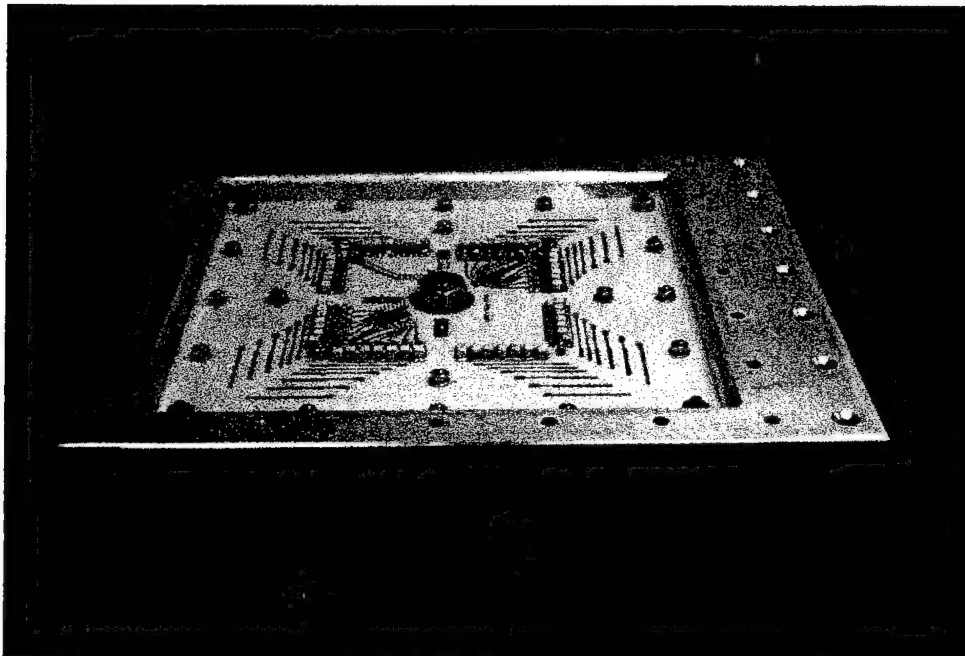


Figure 2. Top side view of a miniature (8"x8" aperture) UHF SATCOM antenna with its dielectric radome removed.

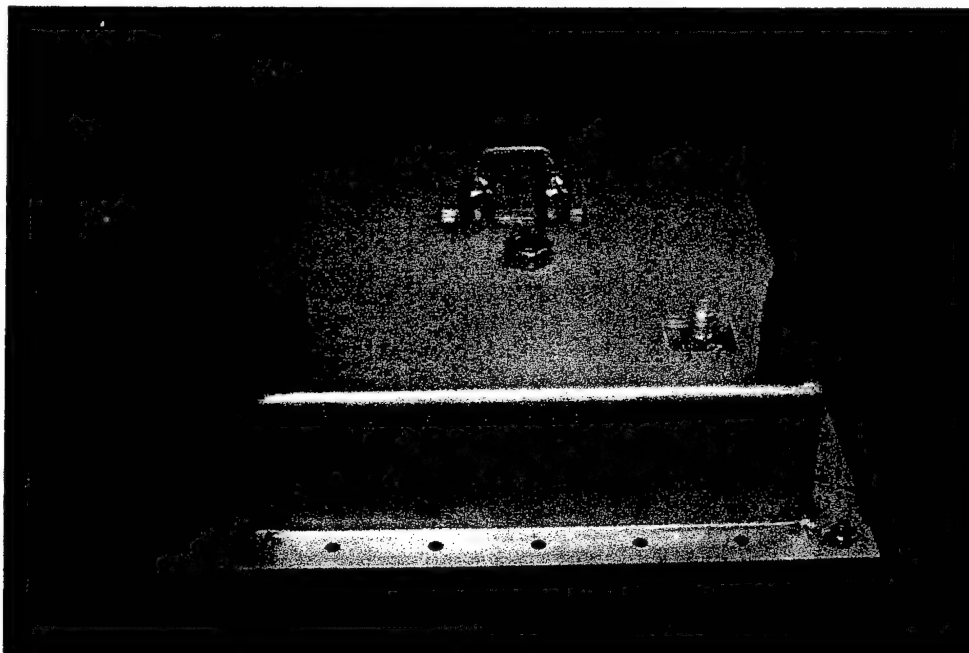


Figure 3. Bottom side view of the prototype UHF SATCOM antenna.

The cavity of the TPA has a volume of 8.25" x 8.25" x 2.4", whereas its flange measures 10" x 11" overall. The purpose of the asymmetric flange was to provide space for the attachment of a future miniaturized ACU. The estimated weight of an integrated ACU and TPA is approximately 20 lb.

The TPA includes an integral feed network within the aperture housing as shown schematically in Figure 4. This high power, 150 Watt, feed network provides to the two feed probes equal amplitude signals in phase quadrature as needed for circular polarization. An external RF jumper, connecting ports 2 and 3, is removable to facilitate measurements of tuning states and radiation efficiency.

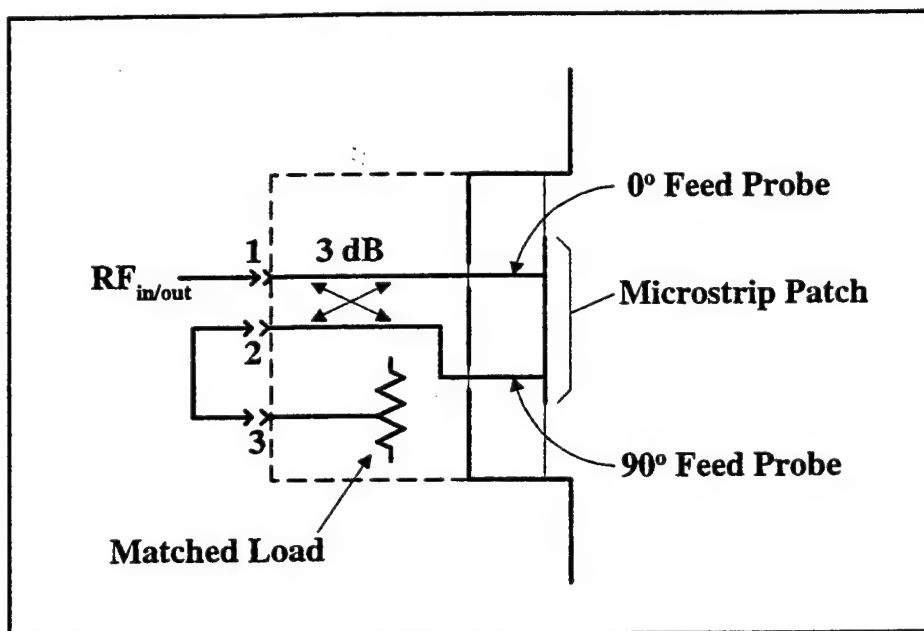


Figure 4. Schematic of the TPA's integrated feed network.

The basic tuning concept is illustrated in Figure 5 where the antenna type is a cavity-backed microstrip patch. The resonant frequency is determined by factors such as the substrate height, h , the substrate dielectric constant, ϵ_r , and the patch dimension d . Tuning is accomplished with solid state switches which are used to connect peripheral tuning bars to the central patch. In this manner, the effective electrical size and, hence, the operating frequency of the patch antenna, are discretely adjusted over a large frequency band. A tuning state is a specific combination of aperture switch settings which yield a given resonant frequency. The lowest frequency tuning state is achieved when all tuning bars are connected

to the central patch, and the highest frequency tuning state is achieved when all tuning bars are disconnected.

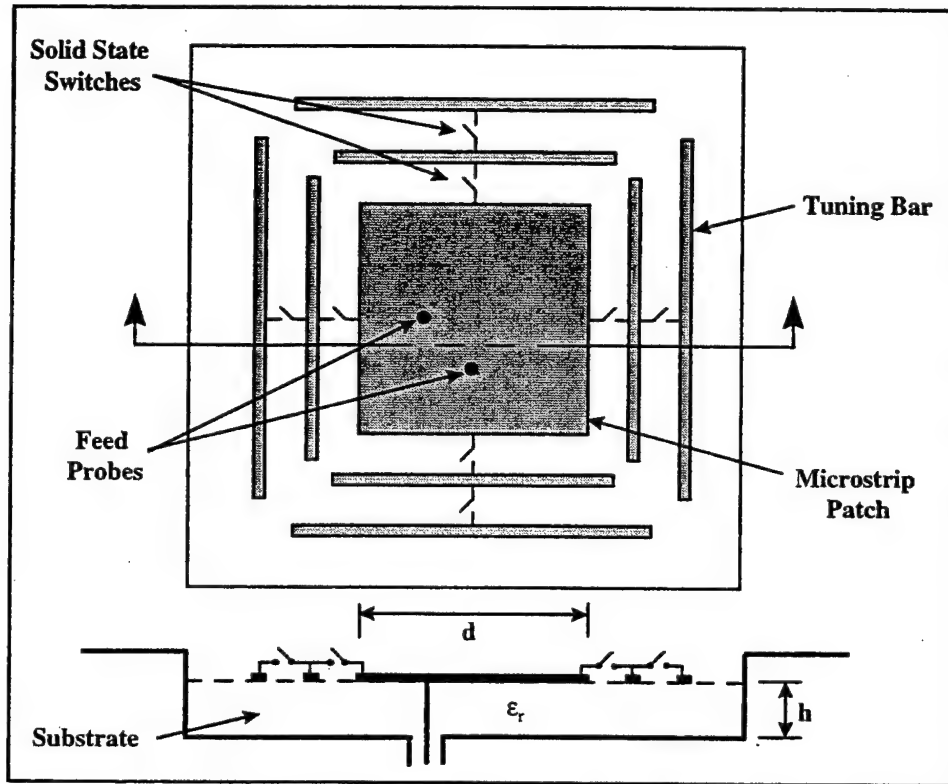


Figure 5. The fundamental tuning concept is to electronically adjust the effective electrical size of a patch antenna with switched tuning bars.

Measured Results

Tuning states are measured by examining a swept S_{12} response as defined by the RF ports in Figure 4. Each feed probe in the aperture presents a narrow band, matched resonance at the tuned frequency. Off-resonance, the probes are poorly matched. When viewed through the hybrid feed network, an S_{12} measurement reveals a null at the resonant frequency. Away from resonance, the incident power is primarily reflected from the feed probes and into the integrated matched load. Figure 6 shows 45 of the available tuning states in which aperture resonant frequencies range from about 242 to 317 MHz.

The antenna's input return loss, plotted in Figure 7, is measured with the RF jumper installed so as to provide a matched load for the hybrid feed network.

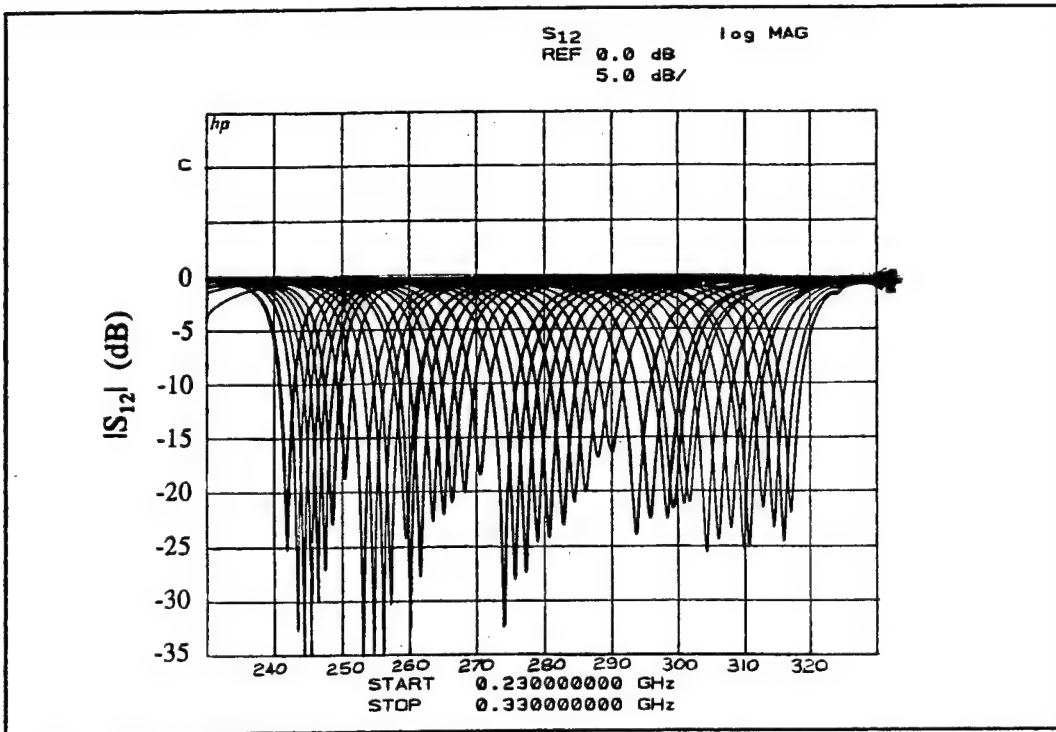


Figure 6. Measured tuning states for of the prototype TPA.

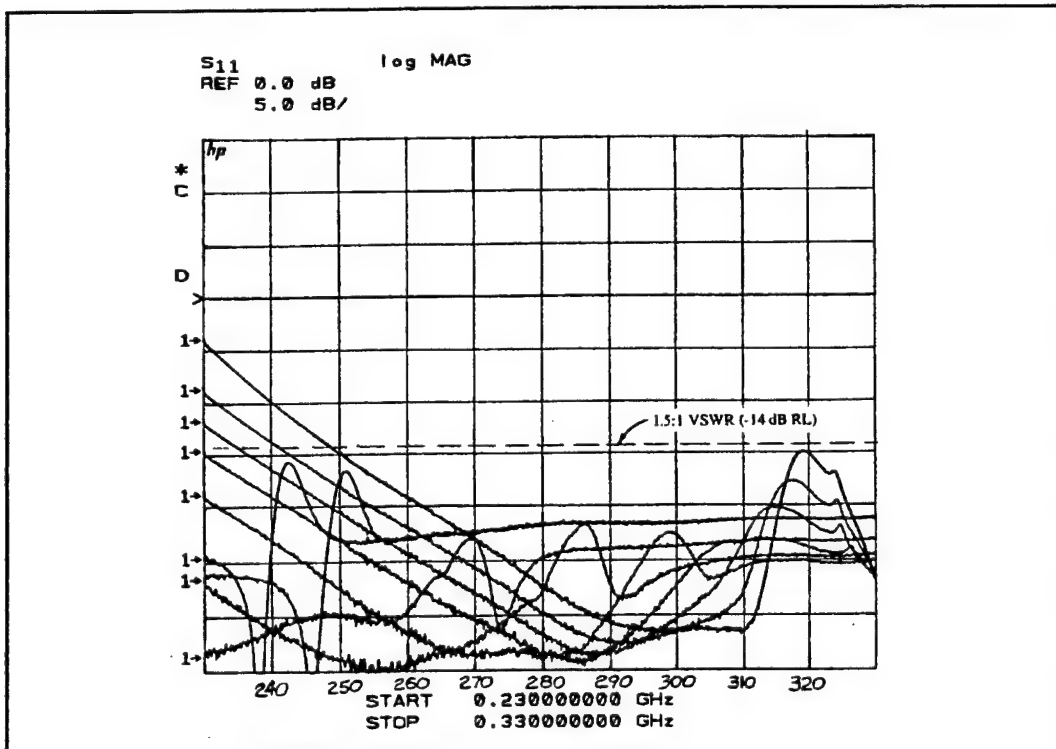


Figure 7. Return loss for various tuning states with the RF jumper installed.

The return loss displayed in Figure 7 is plotted for nine different tuning states with resonant frequencies centered at 242.2, 250.5, 270.4, 286.1, 300.6, 307.9, 311.2, 314.4, and 317 MHz. Measured S_{11} is below -14 dB (1.5:1 VSWR) from 250 to 320 MHz. Below 250 MHz, only some of the high frequency transmit band (290-320 MHz) tuning states exceed this -14 dB level. So the TPA is well matched at a 1.5:1 or better VSWR within at least 50 MHz of the intended frequency of operation.

Gain measurements were performed on an outdoor range at NAWCAD with the TPA installed in the center of a flat, 4 foot diameter, aluminum ground plane. Figure 8 shows circularly-polarized principal-plane elevation patterns with peak gains (at zenith, normal to the ground plane) of +4 to +5 dBic.

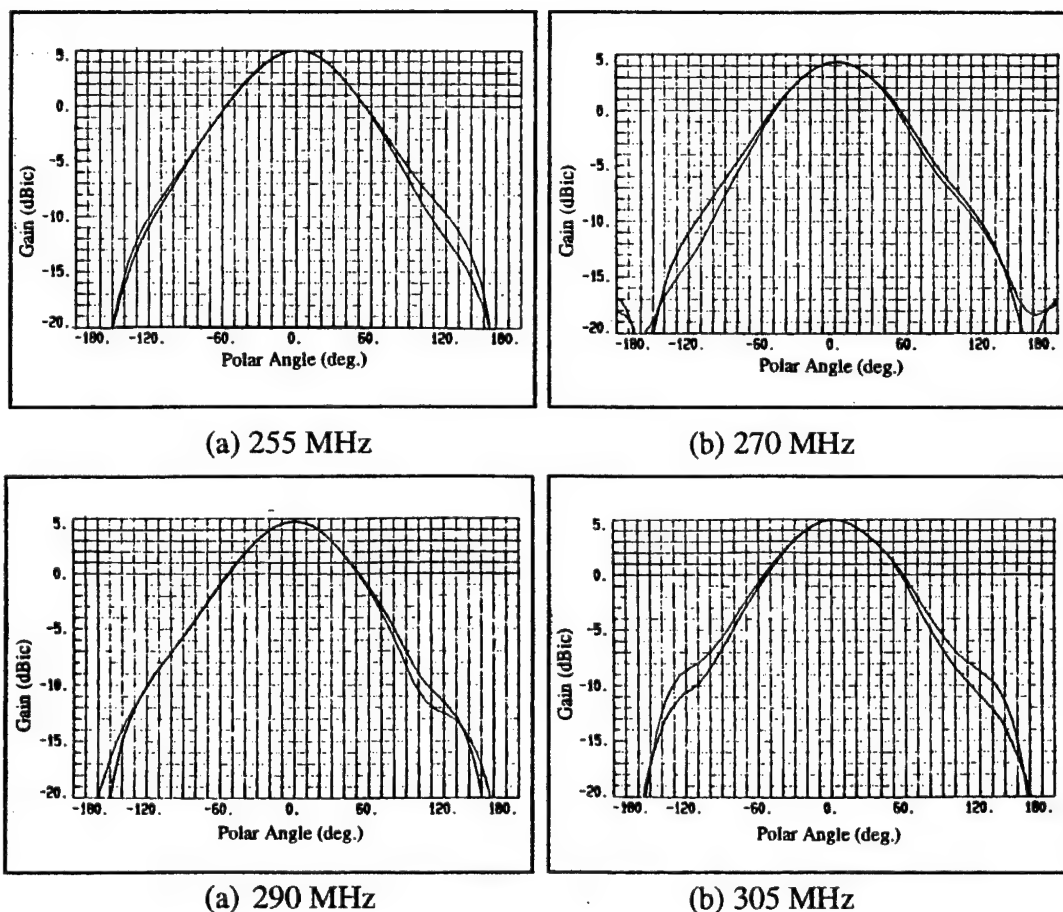


Figure 8. Circularly-polarized principal-plane elevation patterns as measured on a 4 foot dia. ground plane: (a) 255 MHz, (b) 270 MHz, (c) 290 MHz, (d) 305 MHz.

Swept gain measurements at boresight were performed to determine the gain bandwidth of individual tuning states. Peak gain is found, as expected, at the center of the TPA's resonant frequency. The two frequencies associated with gain levels that are 0.5 dB down from this peak define the half-dB gain bandwidth. Using this measure, the gain bandwidth for the lowest frequency tuning state (242 MHz) is about 2.5 MHz. This half-dB gain bandwidth increases monotonically to about 4 MHz for the highest frequency tuning state (317 MHz). The 1 dB gain bandwidth varies from 4 to about 6 MHz over this same frequency range.

Radiation efficiency was measured using a modified Wheeler cap technique [1]. The efficiencies of selected tuning states whose center frequencies span 242 to 317 MHz are plotted in Figure 9. It can be seen that the radiation efficiency exceeds -2 dB from 242 to about 312 MHz. The roll-off at the high end of the transmit band can be mitigated with further design modifications.

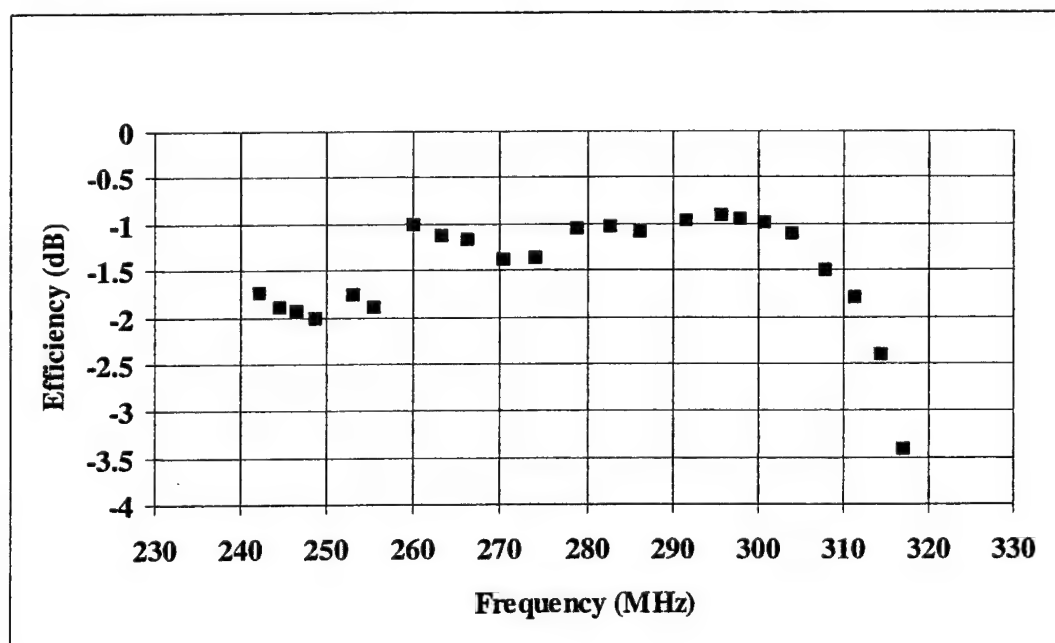


Figure 9. Measured radiation efficiency of the prototype TPA.

Preliminary high power testing has been performed at 300 MHz. The TPA has handled CW power levels of up to 150 Watts for 2 minutes when tested at ambient laboratory conditions. Thermal design improvements are being evaluated to extend the time for which 150 Watts can be transmitted.

Conclusions

This paper documents the development of a prototype tunable UHF SATCOM antenna system which is comprised of an Antenna Control Unit (ACU) and a Tunable Patch Antenna (TPA). This system tunes contiguously from 240 to 320 MHz with center frequencies spanning 242 to 317 MHz. It has been demonstrated to be hardware compatible with ViaSat's MD-1324/U DAMA SATCOM modem. The prototype TPA has a measured efficiency which exceeds -2 dB over 242 to 312 MHz. Gain patterns measured on a four foot circular ground plane demonstrate a boresight gain of +4 to +5 dBic. Half-dB gain bandwidths for individual tuning states vary from 2.5 MHz in the receive band up to 4 MHz in the transmit band. Short term (< 2 minute) power handling capability of 150 Watts CW has been demonstrated. This 17 lb. prototype TPA has an 8" square aperture ($\lambda/6$ sq. at 242 MHz), and it is believed to represent the state-of-the-art in miniature airborne conformal SATCOM antennas.

Acknowledgment

The work reported here was funded by a Phase II SBIR contract, no. N00019-96-C-2026, with sponsorship from the Naval Air Systems Command and the Naval Air Warfare Center Aircraft Division, located at Patuxent River, MD. Project sponsors and government points of contact are Dennis DeCarlo, (301)342-9152, and Andrew Miller, (301)342-9103.

References

1. W. E. McKinzie III, "A Modified Wheeler Cap Method for Measuring Antenna Efficiency," *1997 IEEE Antennas and Propagation Society International Symposium Digest*, Montreal, Canada, July 13-18, 1997, Vol. 1, pp. 542-545.

TWIST POLARIZER DESIGN

P. Keith Kelly, Leo Diaz, and Andrew Shroyer
Ball Aerospace & Technologies Corporation
Telecommunication Products Division
P.O. Box 1538
Broomfield, Colorado 80038-1538

Abstract: A simple numerical model to analyze a twist polarizer is presented. The twist polarizer is a layered structure with each layer made up of an array of conductive strips. The analysis is based on cascading the (4x4) transfer matrices of each layer making up the polarizer. The transfer matrices are derived from the scattering parameters of a planar array of conductive strips. This scattering matrix can be derived from measurement or theory. Arbitrary angle of incidence and polarization of the incident plane wave is handled by decomposing it into parallel and perpendicular components. The parallel and perpendicular waves are weighted by the scattering matrix of the polarizer and recombined to give the transmitted and reflected fields for the incident wave. The model is validated by measurement of a 5 layer 90 degree twist polarizer with a design frequency of 10 GHz.

1. INTRODUCTION

A twist polarizer is used to rotate the polarization of a linearly polarized wave, e.g. from horizontal to vertical. The polarizer is a layered design with each layer consisting of a thin dielectric substrate with metallic strips etched on one side. Typical dielectric substrates used are fiberglass epoxy, Mylar, and Duroid. The layers are separated (usually a quarter wavelength) using roacell foam [1,2,5]. Figure 1 shows a 90 degree twist polarizer made up of five sections. Performance

usually improves with addition of layers, i.e. finer rotation angles to achieve the same total rotation.

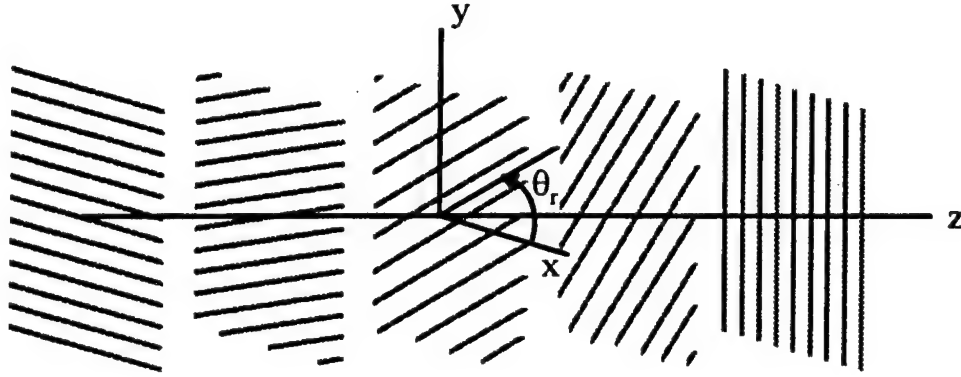


Figure 1 5 layer 90 degree twist polarizer

The following sections describe the details of the analytical methodology and validation. The idea is to characterize the polarizer by cascading the transfer matrix of each layer. The transfer matrix for the polarizer is then converted to a scattering matrix which can be used to determine the reflection and transmission coefficients for the device.

2. INCIDENT WAVE

The polarizer lies in the xy plane of the coordinate system (see figure 2). The incident wave of arbitrary polarization has wavenumber \vec{k} with the wavenumber in the xy plane defined by $\hat{k}_{xy} = \frac{\vec{k} - \vec{k} \cdot \hat{z}}{k_0}$. This unit vector crossed with the normal

from the polarizer gives the unit normal to the plane of incidence (1). The incident electric field is decomposed into a component perpendicular to the plane of incidence (this component has x and y components only) and a component parallel to the plane of incidence (the magnetic density has x and y components only). For the parallel electric field, only the x and y components interact with the polarizing structure. The component normal to the polarizer is assumed to transmit through uninterrupted. The equations for decomposition are shown in (2) - (4).

$$\hat{n}_{poi} = \hat{k}_{xy} \times \hat{z} \quad (1)$$

$$\vec{E}_{per}^i = (\vec{E}^{inc} \cdot \hat{n}_{poi}) \hat{n}_{poi} \quad (2)$$

$$\vec{H}_{par}^i = \frac{(\hat{k} \times (\vec{E} - \vec{E}_{per}^i))}{Z_0} \quad (3)$$

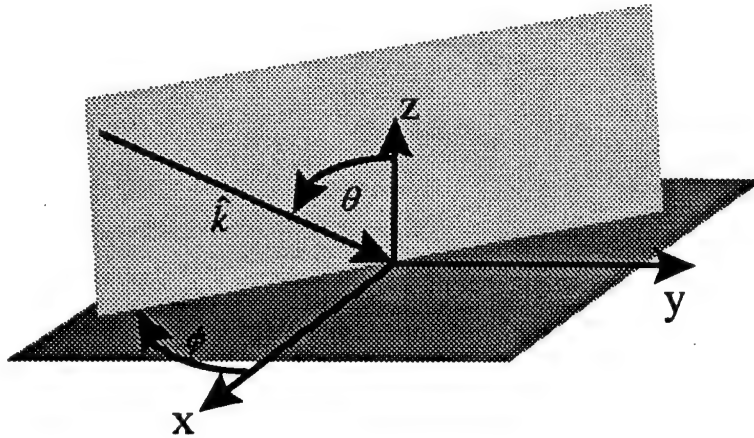


Figure 2 Plane wave incidence geometry

$$\vec{E}_{par}^i = Z_0 \cdot (\hat{z} \times \vec{H}_{par}^i) \quad (4)$$

By converting the incident wave into the perpendicular and parallel components, the polarizer can be modeled for each case separately. Once the transmitted waves for each case are obtained, the electric fields are recombined to provide the reflected and transmitted fields for the original incident wave.

3. GRATING EQUATIONS

Once the incident field has been simplified to two orthogonal incident plane waves, the scattering matrix can be constructed. As shown in figure 3, an input electric field is incident from the left and the right on the material. For the general case, the input electric fields (E_{x1} , E_{y1} , E_{x3} , and E_{y3}) are both transmitted and reflected. The material thickness is typically $\ll \lambda$. The scattering matrix for the electric fields describing the relation between the inputs and outputs is given in (5), [3].

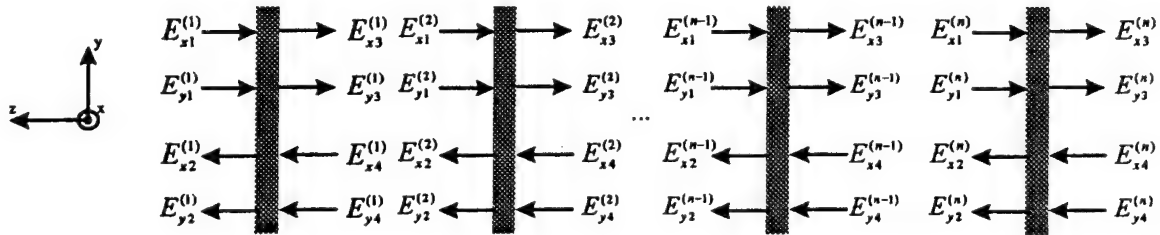


Figure 3 Incident and Reflected Fields transverse to individual grating layers

$$\begin{bmatrix} E_{x2} \\ E_{y2} \\ E_{x3} \\ E_{y3} \end{bmatrix} = \begin{bmatrix} R_{11} & R_{12} & T_{11} & T_{12} \\ R_{21} & R_{22} & T_{21} & T_{22} \\ T_{11} & T_{12} & R_{11} & R_{12} \\ T_{21} & T_{22} & R_{21} & R_{22} \end{bmatrix} \cdot \begin{bmatrix} E_{x1} \\ E_{y1} \\ E_{x4} \\ E_{y4} \end{bmatrix} \quad (5)$$

The scattering matrix for a polarizer with the gratings parallel to the x-axis is given by (6). (The polarizer is assumed to be reciprocal.) However, as the grating is inclined with respect to the x-axis by angle θ_r , the incident fields must be rotated to a coordinate system in alignment with the grating for (6) to hold. To get the components in the original coordinate system, the result is then rotated back by angle θ_r . This matrix operation is given by (7).

$$\begin{bmatrix} R_{11} & R_{12} & T_{11} & T_{12} \\ R_{21} & R_{22} & T_{21} & T_{22} \\ T_{11} & T_{12} & R_{11} & R_{12} \\ T_{21} & T_{22} & R_{21} & R_{22} \end{bmatrix} = \begin{bmatrix} R_{//} & 0 & T_{//} & 0 \\ 0 & R_{\perp} & 0 & T_{\perp} \\ T_{//} & 0 & R_{//} & 0 \\ 0 & T_{\perp} & 0 & R_{\perp} \end{bmatrix} \quad (6)$$

$$\begin{bmatrix} \cos \theta_r & -\sin \theta_r & 0 & 0 \\ \sin \theta_r & \cos \theta_r & 0 & 0 \\ 0 & 0 & \cos \theta_r & -\sin \theta_r \\ 0 & 0 & \sin \theta_r & \cos \theta_r \end{bmatrix} \cdot \begin{bmatrix} R_{//} & 0 & T_{//} & 0 \\ 0 & R_{\perp} & 0 & T_{\perp} \\ T_{//} & 0 & R_{//} & 0 \\ 0 & T_{\perp} & 0 & R_{\perp} \end{bmatrix} \cdot \begin{bmatrix} \cos \theta_r & \sin \theta_r & 0 & 0 \\ -\sin \theta_r & \cos \theta_r & 0 & 0 \\ 0 & 0 & \cos \theta_r & \sin \theta_r \\ 0 & 0 & -\sin \theta_r & \cos \theta_r \end{bmatrix} \quad (7)$$

For an inclined grating with rotation angle θ_r , the variables in (6) are given by the expressions in (8). These are the result of carrying out the matrix multiplication in (7) and simplifying the result.

$$\begin{aligned} T_{11} &= T_{//} \cos^2 \theta_r + T_{\perp} \sin^2 \theta_r, & T_{12} &= T_{21} = \frac{1}{2}(T_{//} - T_{\perp}) \sin 2\theta_r, \\ T_{22} &= T_{\perp} \cos^2 \theta_r + T_{//} \sin^2 \theta_r, & R_{11} &= R_{//} \cos^2 \theta_r + R_{\perp} \sin^2 \theta_r, \\ R_{12} &= R_{21} = \frac{1}{2}(R_{//} - R_{\perp}) \sin 2\theta_r, & R_{22} &= R_{\perp} \cos^2 \theta_r + R_{//} \sin^2 \theta_r, \end{aligned} \quad (8)$$

Now that the scattering matrix has been defined, the transfer matrix must be determined. The transfer matrix form allows the individual polarizer layer matrices to be cascaded. This operation is necessary in order to characterize the performance of the entire polarizer rather than a single layer. The cascade matrix equation is given in (9) with the transfer matrix [A] being defined by (10) and (11). Care must be taken since the determinant of the T matrix (transmission matrix defined above) approaches zero as the polarizer approaches the ideal performance, i.e. $T_{//}=0$, $T_{\perp}=1$.

$$\begin{bmatrix} E_{x3} \\ E_{y3} \\ E_{x4} \\ E_{y4} \end{bmatrix} = [A] \begin{bmatrix} E_{x1} \\ E_{y1} \\ E_{x2} \\ E_{y2} \end{bmatrix} \quad (9)$$

$$\begin{aligned} A_{11} &= T_{11} \det(T) + R_{11}(T_{12}R_{21} - T_{22}R_{11}) + R_{12}(T_{21}R_{11} - T_{11}R_{21}) \\ A_{12} &= T_{12} \det(T) + R_{11}(T_{12}R_{22} - T_{22}R_{12}) + R_{12}(T_{21}R_{12} - T_{11}R_{22}) \\ A_{13} &= (T_{22}R_{11} - T_{21}R_{12}) \quad A_{14} = (T_{11}R_{12} - T_{12}R_{11}) \\ A_{21} &= T_{21} \det(T) + R_{21}(T_{12}R_{21} - T_{22}R_{11}) + R_{22}(T_{21}R_{11} - T_{11}R_{21}) \\ A_{22} &= T_{22} \det(T) + R_{21}(T_{12}R_{22} - T_{22}R_{12}) + R_{22}(T_{21}R_{12} - T_{11}R_{22}) \\ A_{23} &= (T_{22}R_{21} - T_{21}R_{22}) \quad A_{24} = (T_{11}R_{22} - T_{12}R_{21}) \\ A_{31} &= (T_{12}R_{21} - T_{22}R_{11}) \quad A_{32} = (T_{12}R_{22} - T_{22}R_{12}) \\ A_{33} &= T_{22} \quad A_{34} = -T_{12} \quad A_{41} = (T_{21}R_{11} - T_{11}R_{21}) \\ A_{42} &= (T_{21}R_{12} - T_{11}R_{22}) \quad A_{43} = -T_{12}; A_{44} = T_{11} \end{aligned} \quad (10)$$

$$[A] = \frac{[A]}{(\det(T))} \quad (11)$$

A foam spacer is typically used to separate the layers by about a quarter wavelength. This can be accomplished by including the transfer matrix for a uniform nonconducting material given by (12). Using (11) and (12), a polarizer can be analyzed by cascading the matrices. Equation (13) gives the transfer matrix for an n-layer polarizer.

$$\phi = \begin{bmatrix} e^{-j\frac{2\pi}{\lambda}d} & 0 & 0 & 0 \\ 0 & e^{-j\frac{2\pi}{\lambda}d} & 0 & 0 \\ 0 & 0 & e^{j\frac{2\pi}{\lambda}d} & 0 \\ 0 & 0 & 0 & e^{j\frac{2\pi}{\lambda}d} \end{bmatrix} \quad (12)$$

$$T_r = A_n \phi_{n-1,n} A_{n-1} \dots \phi_{12} A_1 \quad (13)$$

T_r represents the transfer matrix of the entire polarizer. To characterize the reflection and transmission coefficients, the transfer matrix must be converted back to a scattering matrix, [4]. The equations for the conversion are given in (14) and (15). The final form of the analysis is given in (16). By supplying the two input waves (left side non-zero, right side is set to 0), and weighting by the scattering matrix of the system, the reflection coefficient and transmission coefficients can be determined.

$$\begin{aligned}
B_{11} &= (A_{41}A_{34} - A_{31}A_{44}) & B_{12} &= (A_{42}A_{34} - A_{32}A_{44}) \\
B_{13} &= A_{44}; B_{14} = -A_{34} \\
B_{21} &= (A_{43}A_{31} - A_{33}A_{41}) & B_{22} &= (A_{43}A_{32} - A_{33}A_{42}) \\
B_{23} &= -A_{43} & B_{24} &= A_{33} \\
B_{31} &= A_{11}(A_{44}A_{33} - A_{43}A_{34}) + (A_{13}B_{11} + A_{14}B_{21}) \\
B_{32} &= A_{12}(A_{44}A_{33} - A_{43}A_{34}) + (A_{13}B_{12} + A_{14}B_{22}) \\
B_{33} &= (A_{13}B_{13} - A_{14}B_{23}) & B_{34} &= (A_{13}B_{14} - A_{14}B_{24}) \\
B_{41} &= A_{21}(A_{44}A_{33} - A_{43}A_{34}) + (A_{23}B_{11} + A_{24}B_{21}) \\
B_{42} &= A_{22}(A_{44}A_{33} - A_{43}A_{34}) + (A_{23}B_{12} + A_{24}B_{22}) \\
B_{43} &= (A_{23}B_{13} + A_{24}B_{23}) & B_{44} &= (A_{23}B_{14} + A_{24}B_{24})
\end{aligned} \tag{14}$$

$$[B] = \frac{[B]}{(A_{44}A_{33} - A_{43}A_{34})} \tag{15}$$

$$\begin{bmatrix} E_{x2} \\ E_{y2} \\ E_{x3} \\ E_{y3} \end{bmatrix} = [B] \cdot \begin{bmatrix} E_{x1} \\ E_{y1} \\ E_{x4} \\ E_{y4} \end{bmatrix} \tag{16}$$

4. REFLECTION AND TRANSMISSION COEFFICIENTS

Given the transmitted and reflected electric field densities, the transmission and reflection coefficients can be found. First, the transmitted electric field is determined for the parallel and perpendicular cases using the output electric fields from (16), which must be calculated for both parallel and perpendicular cases.

(17) shows how the transmitted electric fields for both cases is reconstructed. The z component of the parallel case is simply the z component of the incident field and the z component of the perpendicular case is zero since the incident field is zero. Using (18), the transmitted electric field through the polarizer for the incident electric field of arbitrary polarization and angle of incidence can be determined. Finally, the transmission coefficient is found by taking the ratio of the transmitted to incident power, (19).

$$\vec{E}_{par}^t = \begin{bmatrix} E_{x3\ par} \\ E_{y3\ par} \\ \vec{E}_{par}^i \cdot \hat{z} \end{bmatrix} \quad \vec{E}_{per}^t = \begin{bmatrix} E_{x3\ per} \\ E_{y3\ per} \\ 0 \end{bmatrix} \quad (17)$$

$$\vec{H}_{par}^t = -\frac{(\hat{k} \times \vec{E}_{par}^t)}{Z_0} \quad \vec{E}^t = \vec{E}_{per}^t + \vec{E}_{par}^t \quad (18)$$

$$T = 10 \log_{10} \left(\frac{\vec{E}^t \cdot \vec{E}^{t*}}{\vec{E}^i \cdot \vec{E}^{i*}} \right) \quad (19)$$

The same procedure is followed to obtain the reflection coefficient (20-22). However, the z component of the parallel electric field is assumed to be zero since the incident z component is transmitted without interruption.

$$\vec{E}_{par}^r = \begin{bmatrix} E_{x2\ par}^r \\ E_{y2\ par}^r \\ 0 \end{bmatrix} \quad \vec{E}_{per}^r = \begin{bmatrix} E_{x2\ per}^r \\ E_{y2\ per}^r \\ 0 \end{bmatrix} \quad (20)$$

$$\vec{H}_{par}^r = -\frac{(\hat{k} \times \vec{E}_{par}^r)}{Z_0} \quad \vec{E}^r = \vec{E}_{per}^r + \vec{E}_{par}^r \quad (21)$$

$$R = 10 \log_{10} \left(\frac{\vec{E}^r \cdot \vec{E}^{r*}}{\vec{E}^i \cdot \vec{E}^{i*}} \right) \quad (22)$$

5. Polarizer Design Results

A five layer polarizer was designed to rotate a linearly polarized incident wave 90 degrees. The spacing, s , between the gratings was chosen to be $\lambda/20$ at 10 GHz with the wire width equal to $s/4$. In order to predict the performance of the twist polarizer, a periodic moment method code was used to characterize the scattering parameters of a single grating. Plots of the transmission and reflection coefficients are given in Figures 4 and 5 for the xz plane scan case. The parallel component is along the y axis and the perpendicular component is along the x axis using the coordinate system shown in Figure 2. In this case, the grating is parallel to the y axis. The cross polarized components of the scattering parameters were all found

to be below -80 dB. Predictions for two different planes of scan are given in Figure 6 for the transmission coefficient of the twist polarizer.

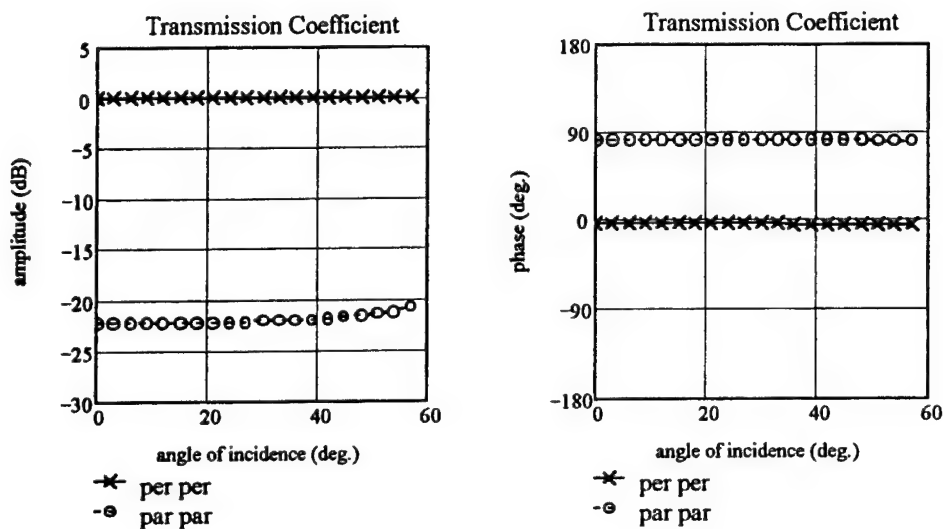


Figure 4 Transmission Coefficients for Single Grating: $\phi=0$

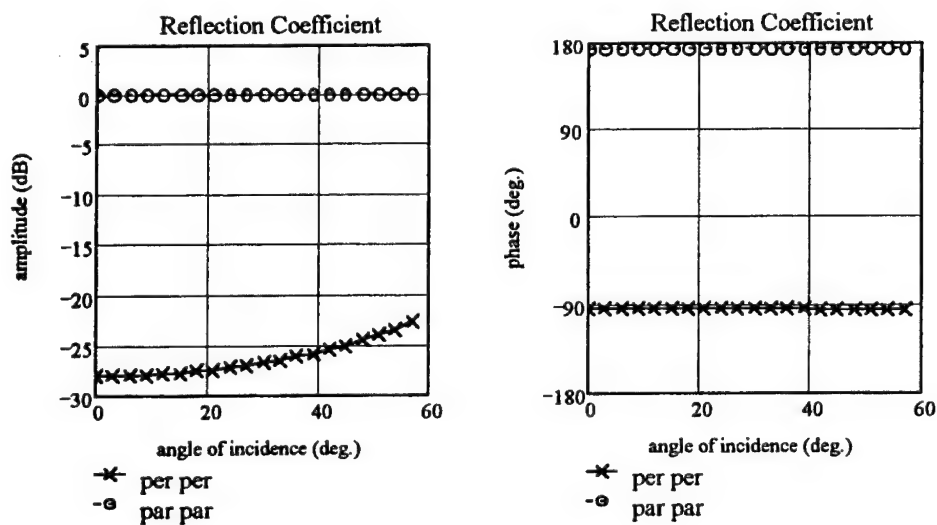


Figure 5 Reflection Coefficients for Single Grating: $\phi=0$

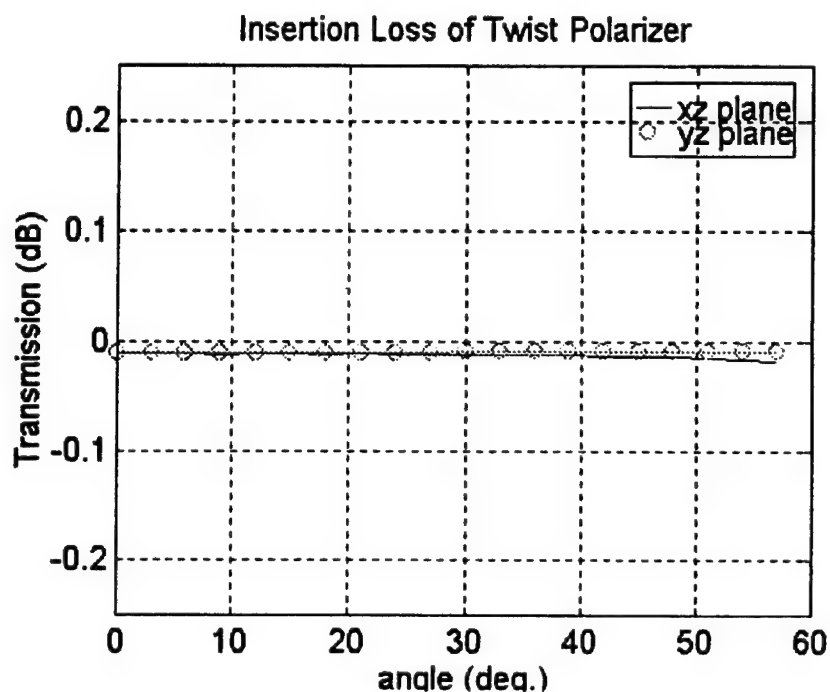


Figure 6 Predicted Insertion Loss of 5 layer twist polarizer

In an effort to validate the model, a twist polarizer was constructed and several techniques were used to measure its performance. The gratings were etched on 5 mil G10 (fiberglass) and the separation between layers was approximately $\lambda/4$. This separation was accomplished with 2 layers of 1/8 inch foam and 1 layer of 1/16 inch foam. The first measurement technique attempted involved an arch setup inside of an absorber lined box with two horns placed on a circle surrounding the object under test. Since the horns had dual linear capability it was possible to measure the insertion loss of the twist polarizer. However, a means for accurately calibrating the setup was not found since the traditional "thru" measurement could

not be obtained due to the difference in performance of the vertical to horizontal reception without the polarizer (close to zero reception). Also, the vertical to vertical thru signal without the polarizer was found to be unacceptable as well.

The second measurement technique involved measuring the gain of a linear antenna both with and without a polarizer and comparing the co-pol to the cross-pol of the two measurements. The polarizer was placed directly in front of the apertures of two different antennas. The first antenna measured was an 8.2 GHz standard gain horn and the second antenna measured was an open ended waveguide probe. Both the E and H plane patterns were characterized. Figures 7-10 give the measured patterns and the difference in the patterns (deduced polarizer insertion loss). As can be seen in the data, the comparison of the patterns is quite good; however, at the pattern minimas larger insertion losses (sometimes gain) is observed in the measurement leading to an unrealistic ripple throughout the deduced polarizer insertion loss. Figures 9 and 10 give results which are more consistent with a passive structure; however, a 1 dB peak to peak ripple is present.

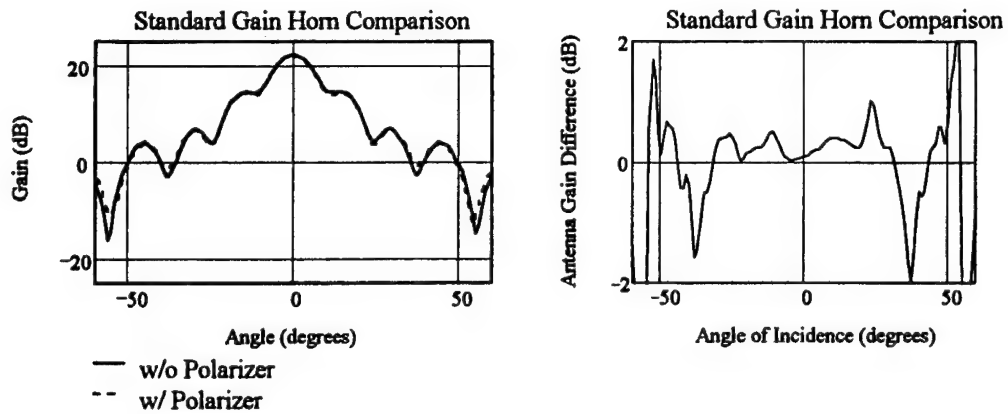


Figure 7 H-Plane Standard Gain Horn Patterns and Deduced Polarizer Loss: HH without and VH with Polarizer

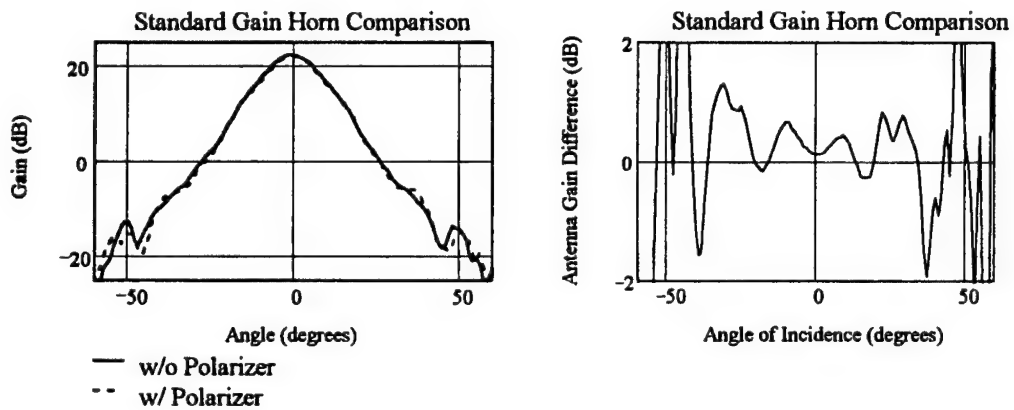


Figure 8 E-Plane Standard Gain Horn Patterns and Deduced Polarizer Loss: VV without and HV with Polarizer

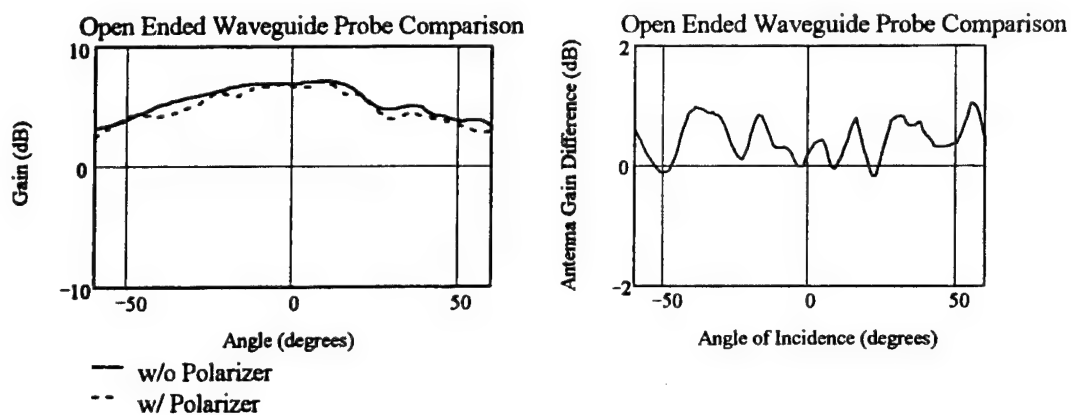


Figure 9 H-Plane Open Ended Waveguide Probe Patterns and Deduced Polarizer Loss: VV without and HV with Polarizer

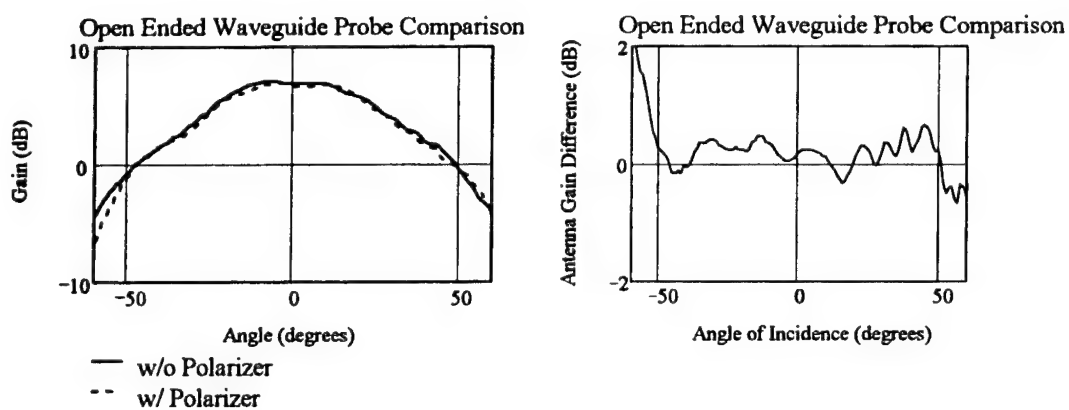


Figure 10 E-Plane Open Ended Waveguide Probe Patterns and Deduced Polarizer Loss: HH without and VH with Polarizer

Although the accuracy of the measured data on the twist polarizer presented in this paper was not sufficient to validate the modeling results, the envelope of the measured data was consistent with the model. In hind sight, a better approach to

validating the model would have been to analyze a design which did not perform as well, i.e. more insertion loss, as the current polarizer design.

7. REFERENCES

- [1] A. A. M. Saleh, "An adjustable quasi-optical bandpass filter-Part I: Theory and design formulas," IEEE Trans. Microwave Theory Tech., vol. MTT-22, no. 7, pp., 728-734, July 1974.
- [2] A. A. M. Saleh, "An Adjustable Quasi-Optical Bandpass Filter-Part II: Practical Considerations," IEEE Trans. Microwave Theory Tech., vol. MTT-22, no. 7, pp., 734-739, July 1974.
- [3] N. Hill, S. Cornbleet, "Microwave transmission through a series of inclined gratings," Proc. Inst. Elec. Eng., vol. 120, pp. 407-412, Apr. 1973.
- [4] C. G. Montgomery, R. H. Dicke, and E. M. Purcell, *Principles of Microwave Circuits* (Mass. Inst. Technol. Radiation. Lab. Series), vol. 8. New York: McGraw-Hill, 1948, pp. 150-151.
- [5] N. Amitay, and A. A. M. Saleh, "Broad-Band Wide-Angle Quasi-Optical Polarization Rotators," IEEE Trans. Ant. Propag., vol. AP-31, no. 1, Jan. 1983.

A Characterization of The Sinuous Antenna Implemented In A Polarimeter

Timothy R. Holzheimer

Raytheon E-Systems
Airborne Systems Division
Greenville Operation
Greenville, Texas 75403

Polarimeters are used to determine the polarization state of an emanating signal. Most polarimeters designed use dual polarization or multiples of single polarization horns for the polarimeter elements. Large amounts of measured data exist for polarimeters using linear polarized horns, but limited data are available using other element types. This paper investigates the use of the dual polarized sinuous antenna as a polarimeter element. In the case of this element, sparse data exist on phase and polarization versus angle and frequency. The method used to determine the polarization is limited by available measurement data. Again, a large amount of additional measured data was acquired in order to evaluate the potential for the use of the sinuous element in a polarimeter.

New data acquired includes amplitude and phase variations versus angle and frequency over the 2 to 18 GHz frequency range. A basic set of measured data was successfully verified against a particular co-polarization set of data from the sinuous antenna vendor. The new measured data were then evaluated for use in a polarimeter. The data and analysis were then compared to a standard dual linear polarization polarimeter element.

The analysis of the measured data on the sinuous element provided both insight and some surprises when trying to use this element in a polarimeter. Two interesting characteristics were that the polarization of the element wanders slightly over angle and the phase versus angle is not linear over the entire measured frequency range. This does not preclude the use of the sinuous element in a polarimeter, but it does complicate the method of calibration to be invoked.

A comparison is then made between using the sinuous element

versus the standard dual linear polarization element in a classic linear polarization ratio polarimeter. Additional insight is provided in the use of the sinuous element and limited comments are discussed as to how a system calibration can be made when using this element in a polarimeter. The presented measured data, analysis and conclusions apply to all forms of generic polarimeters.

Introduction:

Polarization information of a antenna is described as linear, circular, or elliptical polarized based on the orientation of the electric field vector. This information has to be measured and when this information is obtained it describes the properties of the particular antenna for use in a polarimeter system. There are several methods of measuring the polarization of the antenna under test which include linear polarization ratio, circular polarization ratio, amplitude or Stokes Vector, radiation pattern response with spinning linear source, and six field response components.[1-5] These measurement methods can generally be described as spinning linear, six components, and a single pair of orthogonal components.

These measurement methods rely on the definitions listed in the appendix which are also described in great detail in the above mentioned references. The three overall measurement methods are summarized with additional details available in the cited references.

The spinning linear source method requires measuring the amplitude response of the antenna under test (AUT) to a spinning dipole as the AUT is rotated about its field of view. The measured amplitude is plotted versus dipole rotation angle. This provides direct measurement of the tilt angle. The resultant radiation pattern produced is described as the polarization ellipse, but it will not yield a determination of all polarizations. The problem that arises is the determination of right or left hand elliptical polarization (could be right hand or left hand circular polarization RH/LHCP) even though axial ratio and tilt angle are measurable quantities. The solution is to use a different dual polarized antenna and make a second identical set of measurements.

The six component method requires AUT amplitude responses from horizontal, vertical, slant + 45 degrees, slant -45 degrees, LHCP and RHCP source antennas. Then by calculating the stokes vector parameters the polarization sense of the antenna is determined without having to measure the phase responses.

The single orthogonal polarization pair measurement can be performed using dual linear, dual slant or dual circular polarization antennas. Generally these measurements are described as polarization ratio measurements. The

amplitudes and phase of each antenna port are measured. The polarization ratio is computed from the amplitudes and the phase angle is measured between the orthogonal antenna ports.

The linear polarization ratio (LPR) measurement was the approach implemented using dual polarized sinuous antennas. This is the easiest method that can be implemented in hardware using in phase and quadrature phase detectors along with the amplitude information.

The antenna elements used in the polarimeter system are the key to any of the measurement methods implemented. This paper investigated the use of the dual polarized sinuous antenna for implementation in a broadband 2 to 18 GHz polarimeter.

Collected Sinuous Polarization Data:

The data was collected for use in a linear polarization ratio polarimeter using a sinuous antenna element. The LPR method requires a amplitude ratio calculation and a phase delta. The basic equation is as follows:

$$\text{LPR} = ((\text{E-vertical})/(\text{E-horizontal})) * (\text{phase angle electric field})$$

where: Polarization Ratio (PR) = E-vertical/E-horizontal

The vertical and horizontal components could be LHCP and RHCP or slant +45 and slant -45 as long as they are an orthogonal pair. It is equally important that with LPR polarizations that are nearly linear (PR very large or very small) axial ratio is almost irrelevant while tilt angle is important. With polarizations close to circular, tilt angle is of less importance except for sign of the angle while the polarization or axial ratio is the important information.

The theoretical PR and phase angle are shown below in table I.

Table I. Theoretical Values for Six Polarization States

Polarization	Polarization Ratio	Phase Angle	Comments
Horizontal	0	irrelevant	vertical(V) = 0
Vertical	infinite	irrelevant	horizontal(H) = 0
LHCP	1	90	H = V
RHCP	1	-90	H = V
Slant +45	1	0	H = V
Slant -45	1	180	H = V

Manufacturers data was compared for generation of a starting basis and calibration of the measurement system. The phase data provided was delta phase co-polarized to port 1 minus co-polarized to port 2 which is close to response from a circular polarized source. The data was verified to an

accuracy of within plus or minus 2 degrees. The delta phase data used for a calibration check is shown in figure 1.

Two dual linear polarized antenna elements were measured. Two elements were measured in order to determine how well two different elements tracked with respect to gain, delta amplitude and delta phase. Delta amplitude and delta phase are defined at the two linearly polarized output ports of the sinuous antenna. The measured boresight antenna gain is shown in figures 2 and 3. The antenna gains track within 0.5 dB with minor deviations of approximately 1 dB at 2 GHz.

The cross polarization response of the sinuous antenna elements was better than expected. The measured data is shown in figure 4 and 5 where each element port is co-polarized to the source. The cross polarized isolation is 15 to 20 dB over the 2 to 18 GHz measurement band of interest with one frequency where it drops to 12 dB. However a second set of sinuous elements that were measured exhibited a cross-polarized isolation of only 10 to 15 dB.

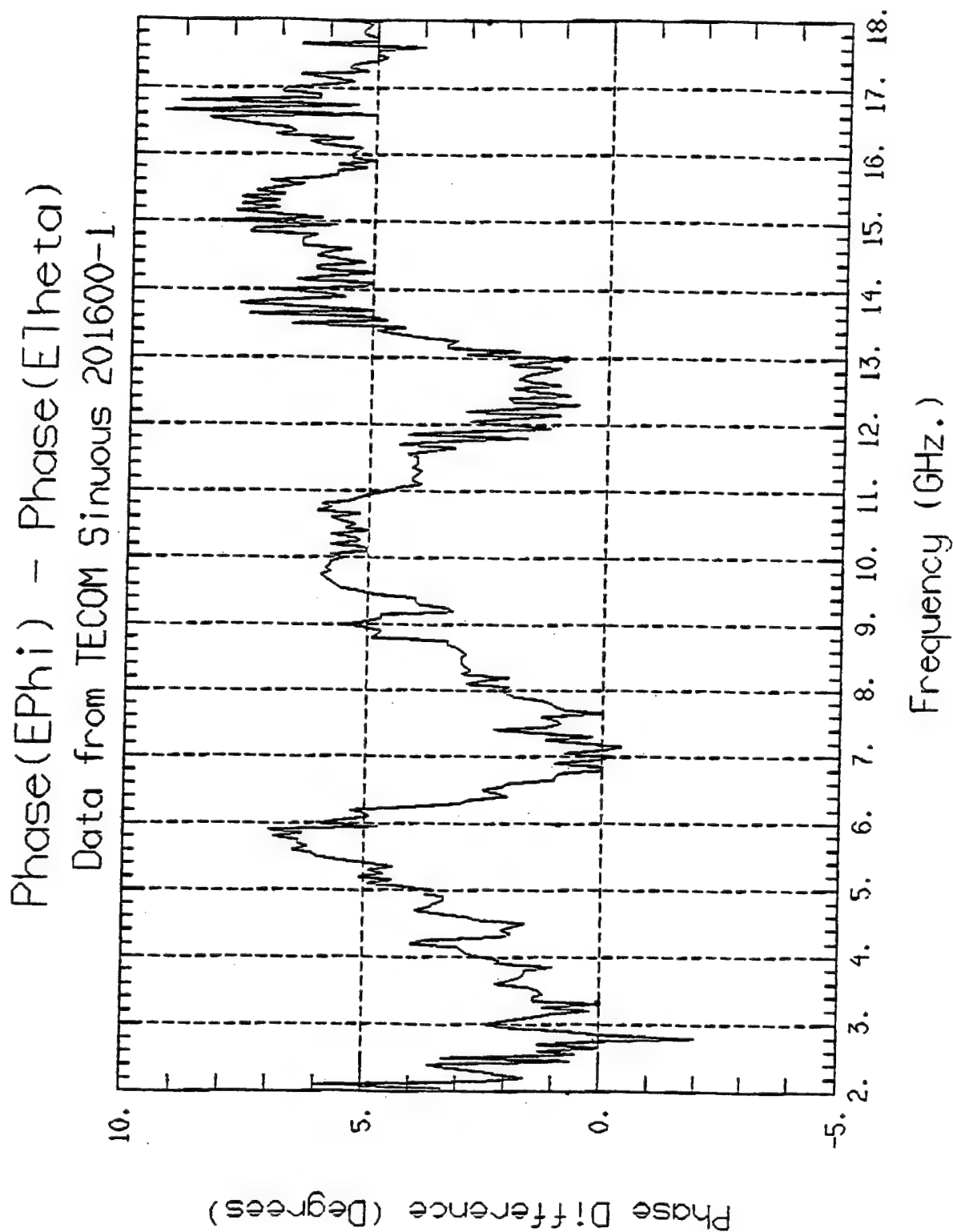


Figure 1. Delta Phase (Co-pol. to Co-pol.) Versus Frequency
From Tecom.

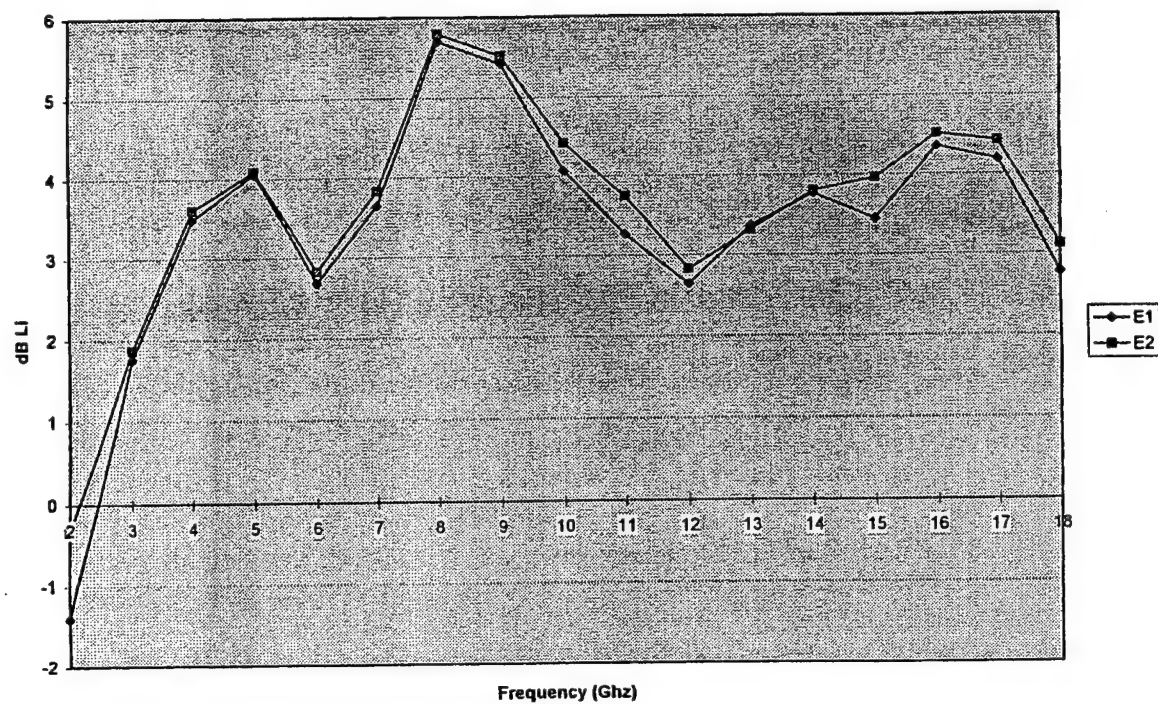


Figure 2. Gain (dBli) Versus Frequency for Sinuous SN-117 at Boresight.

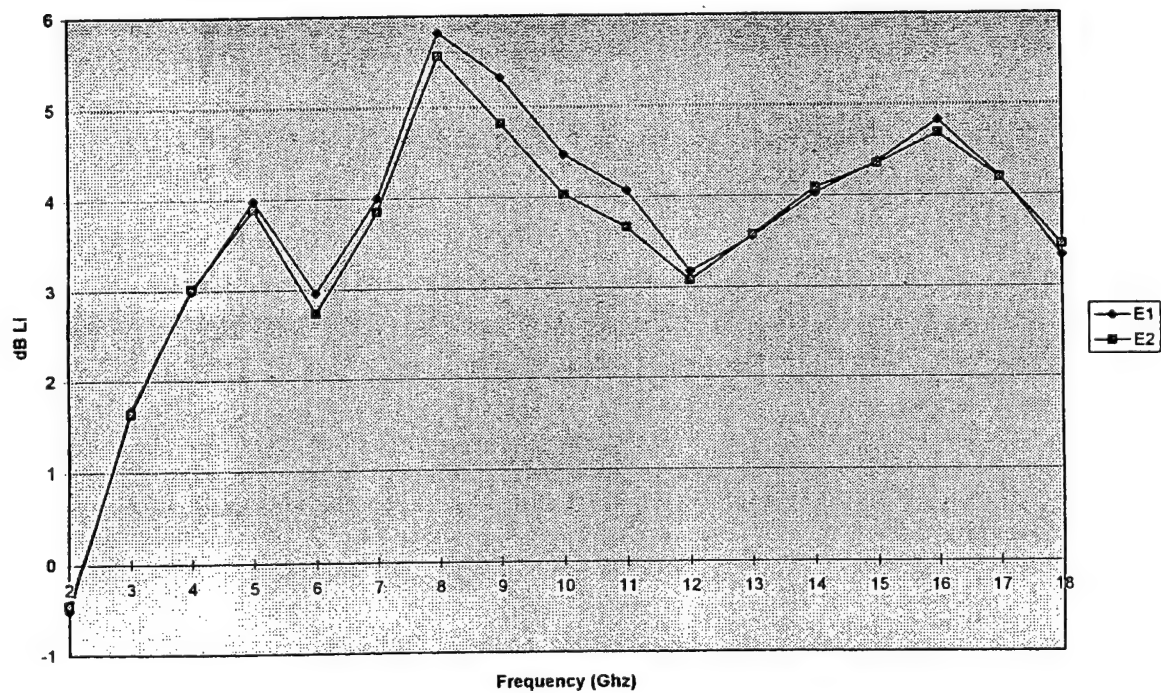


Figure 3 Gain (dBli) Versus Frequency for Sinuous SN-118 at Boresight.

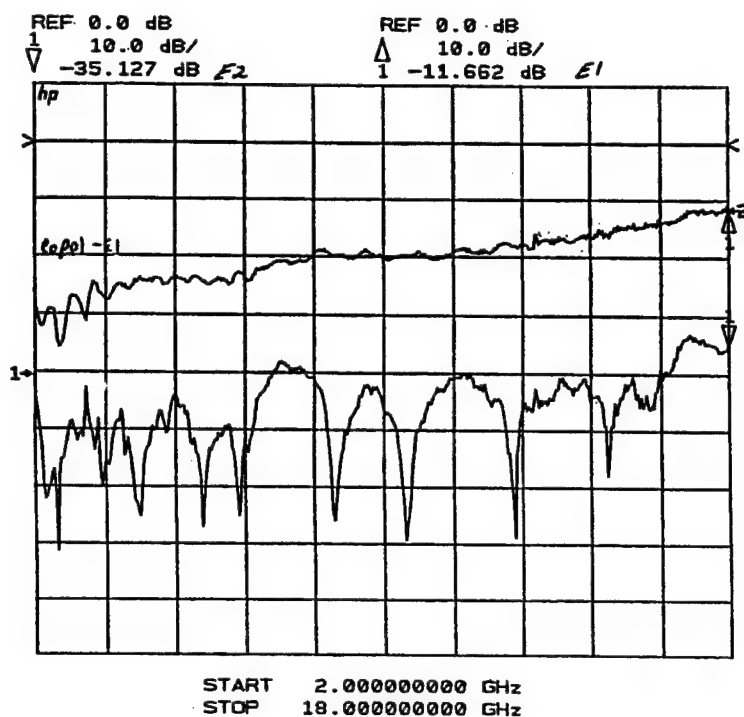


Figure 4. Cross-polarization Isolation Versus Frequency for Co-polarized Horizontal Source.

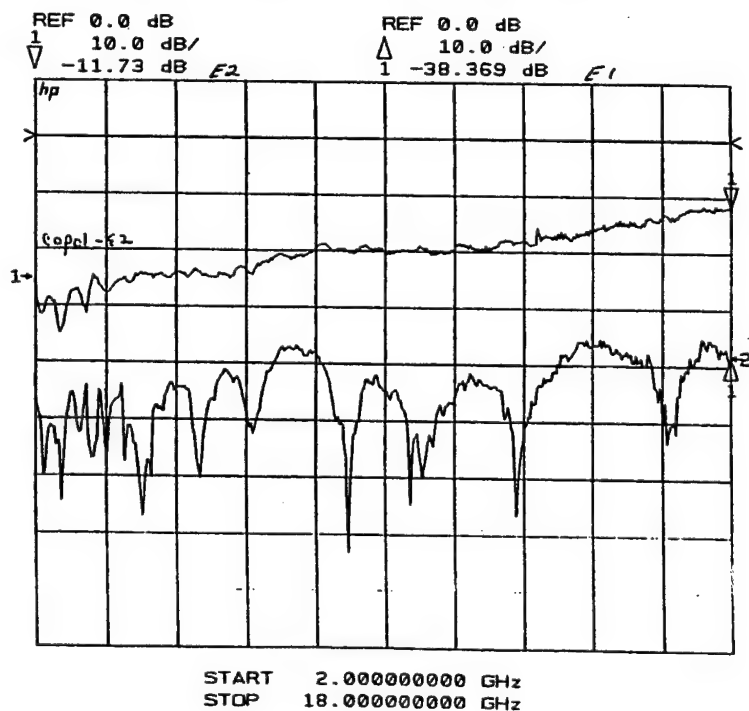


Figure 5 Cross-polarization Isolation Versus Frequency for Co-polarized Vertical Source.

The delta phase and delta amplitude data discussed next was collected with a dual slant 45 degree orthogonal pair using the sinuous antenna element over the 2 to 18 GHz frequency range.

The measured delta phase when one port of the AUT is co-polarized is shown in figure 6. The phase information is unusable, but the amplitude from the co-polarized port determines the sense of polarization. This provides a valuable insight into how actual hardware could be implemented.

The next set of data shows the variation in delta phase when the AUT is mounted in the dual slant 45 degree configuration. The delta phase data is shown for a vertical source at azimuthal angles of 0, 15, 45 and 60 degrees from boresight. They are shown in figures 7 through 10. The data shows delta phase of plus or minus 10 degrees for 0 degrees azimuth, but as the azimuth angle increases to 15 degrees the delta phase changes very little and may even become a little more stable. However, when the azimuth angle is 45 degrees the delta phase starts to grow to at least plus or minus 12.5 degrees while at 60 degrees in azimuth the delta phase increases to plus or minus 15 degrees. It is expected that as the azimuthal angle of the AUT increases from boresight that the delta phase will increase. The plus or minus numbers stated are an average that can be refined by looking at the figures over the frequency ranges of particular interest.

The change in delta phase was then measured over azimuth angle at several frequencies. The data shown in figures 11 through 13 are at 2, 10 and 18 GHz over an azimuth angle from 0 to 40 degrees. The data shows the increase in delta phase that occurs both in larger azimuth angle, but also as the frequency approaches 18 GHz. The delta phase variation is 2.5 degrees at 2 GHz, 5 degrees at 10 GHz and 7 degrees at 18 GHz.

Delta amplitude was also investigated and is shown for three different polarizations which are vertical, slant +45 and RHCP. Figures 14 and 15 are delta amplitude at 0 and 30 degrees in azimuth. This data shows a 5 dB variation over frequency. Figures 16 and 17 are delta amplitude for slant +45 degrees at 0 and 30 degrees in azimuth. This data shows the case of co-polarized with one port and cross-polarized with the other port where the delta amplitude is averaging approximately -25 dB for both 0 and 30 degrees in azimuthal

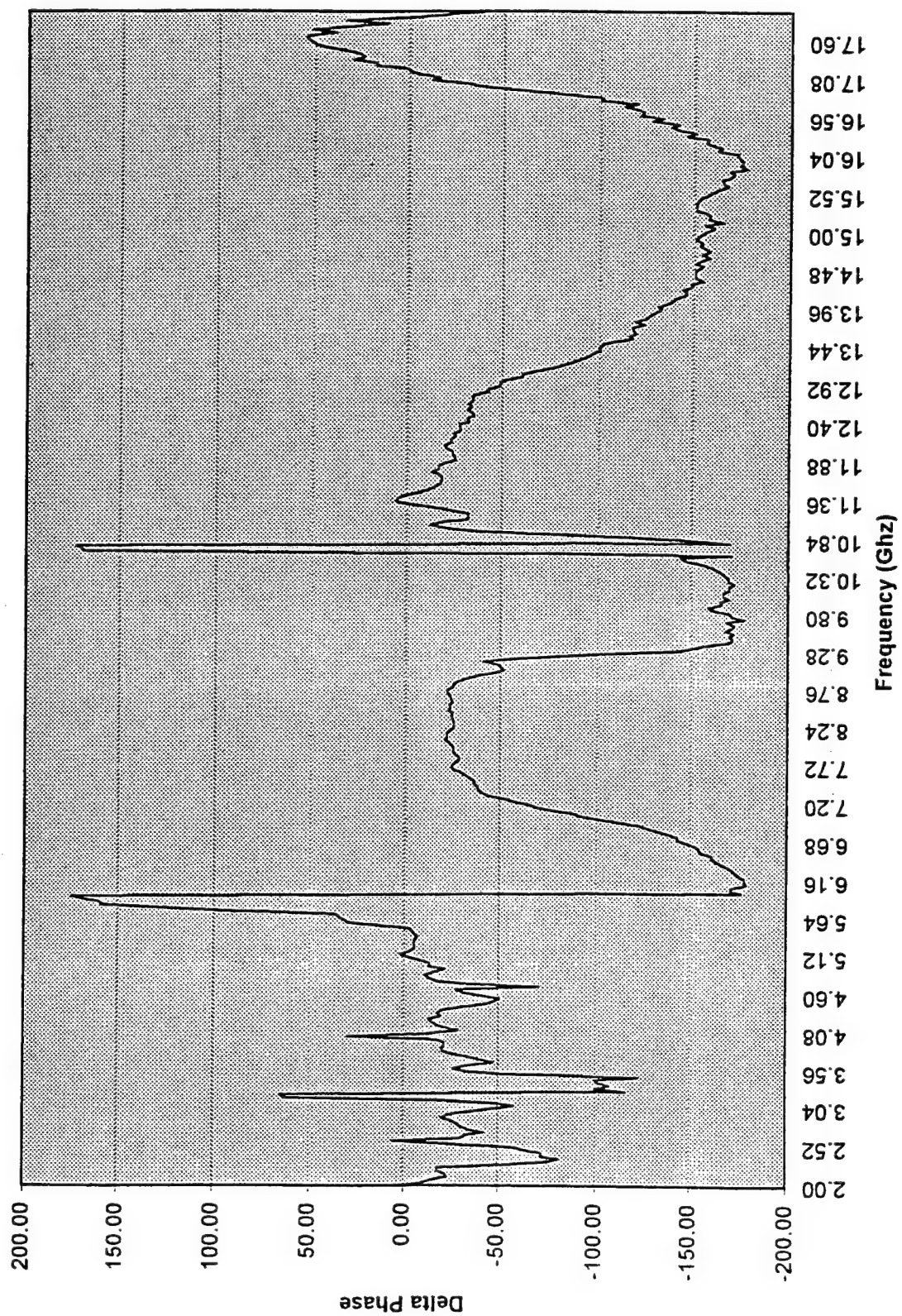


Figure 6. Delta Phase (Co-pol. to Cross-pol.) Versus Frequency.

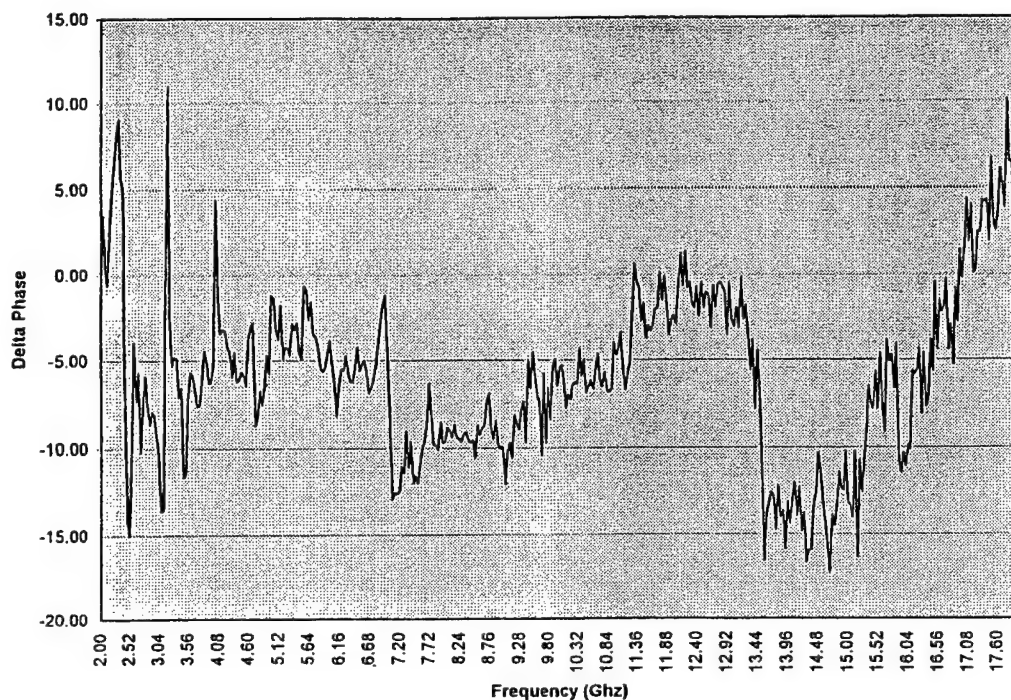


Figure 7. Delta Phase Versus Frequency for AUT at slant 45, Azimuth = 0 Degrees, Vertical Source.

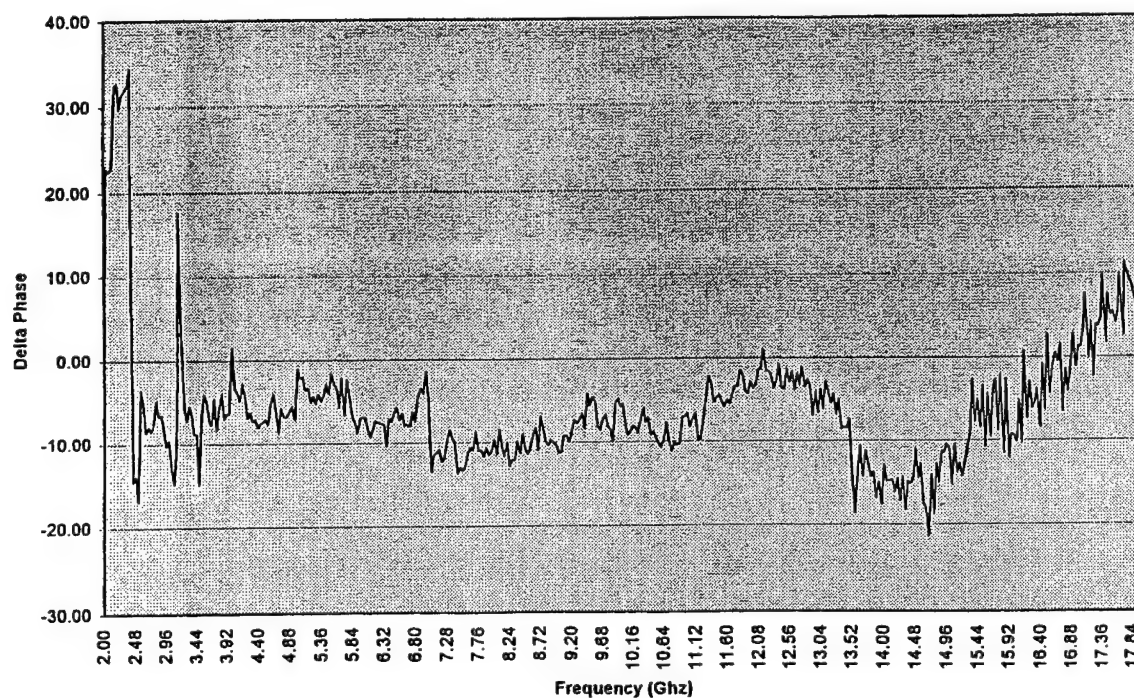


Figure 8 Delta Phase Versus Frequency for AUT at slant 45, Azimuth = 15 Degrees, Vertical Source.

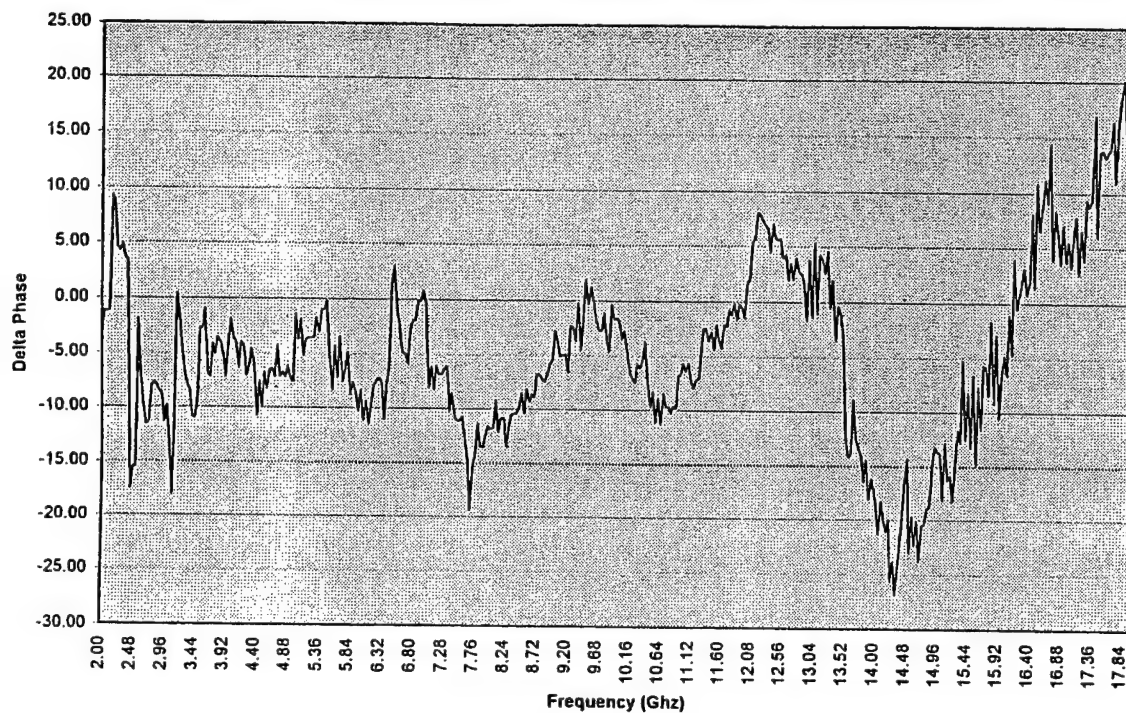


Figure 9. Delta Phase Versus Frequency for AUT at slant 45, Azimuth = 45 Degrees, Vertical Source.

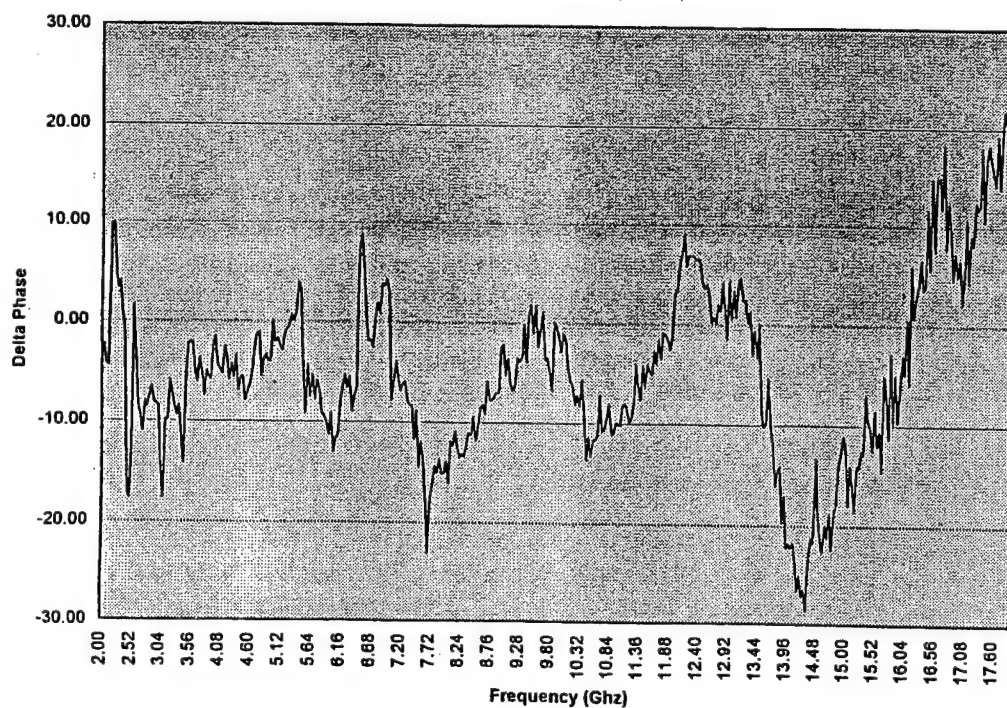


Figure 10 Delta Phase Versus Frequency for AUT at slant 45, Azimuth = 60 Degrees, Vertical Source.

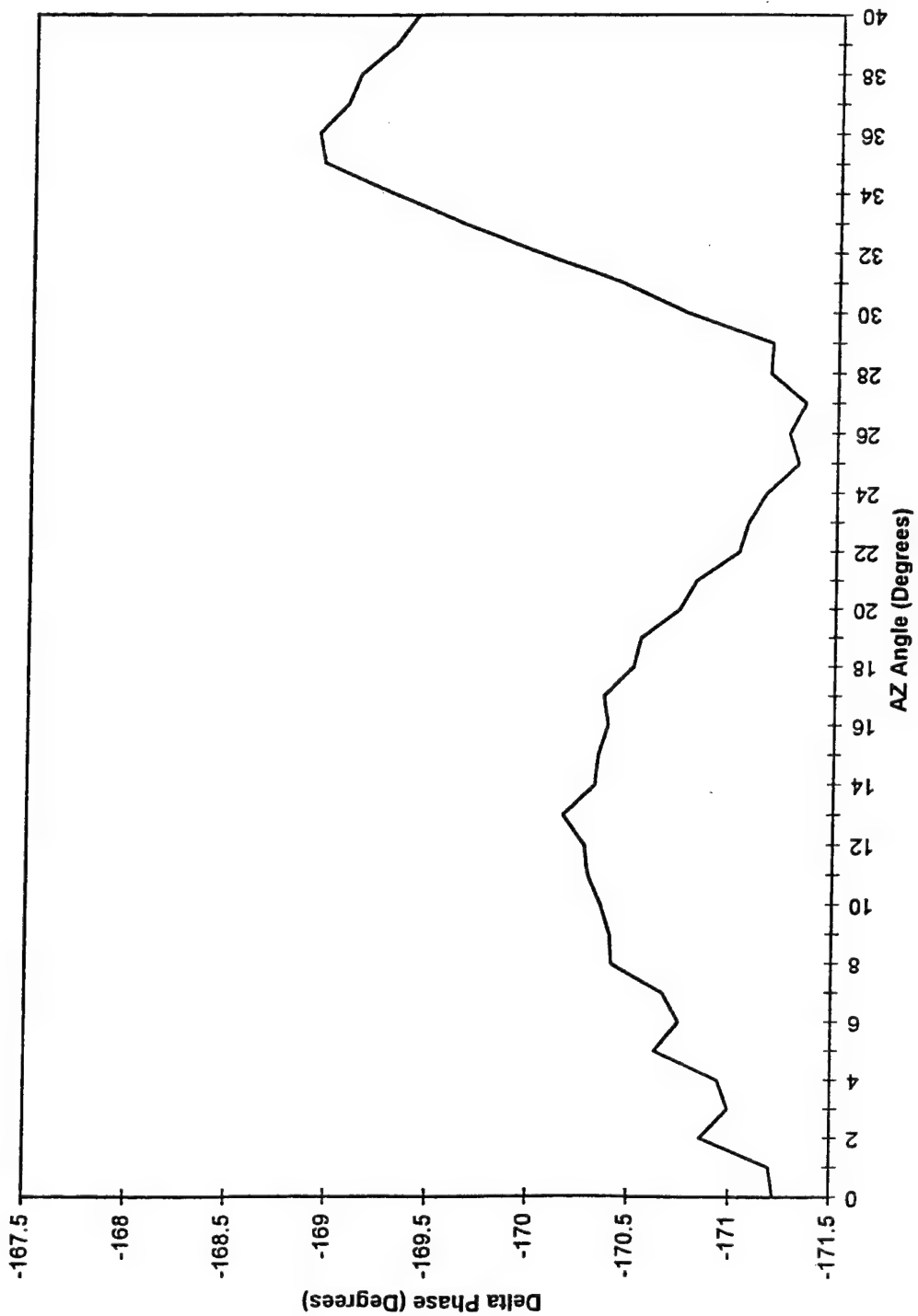


Figure 11. Delta Phase Versus Azimuth Angle, AUT at slant 45 with Vertical Source, at 2 GHz.

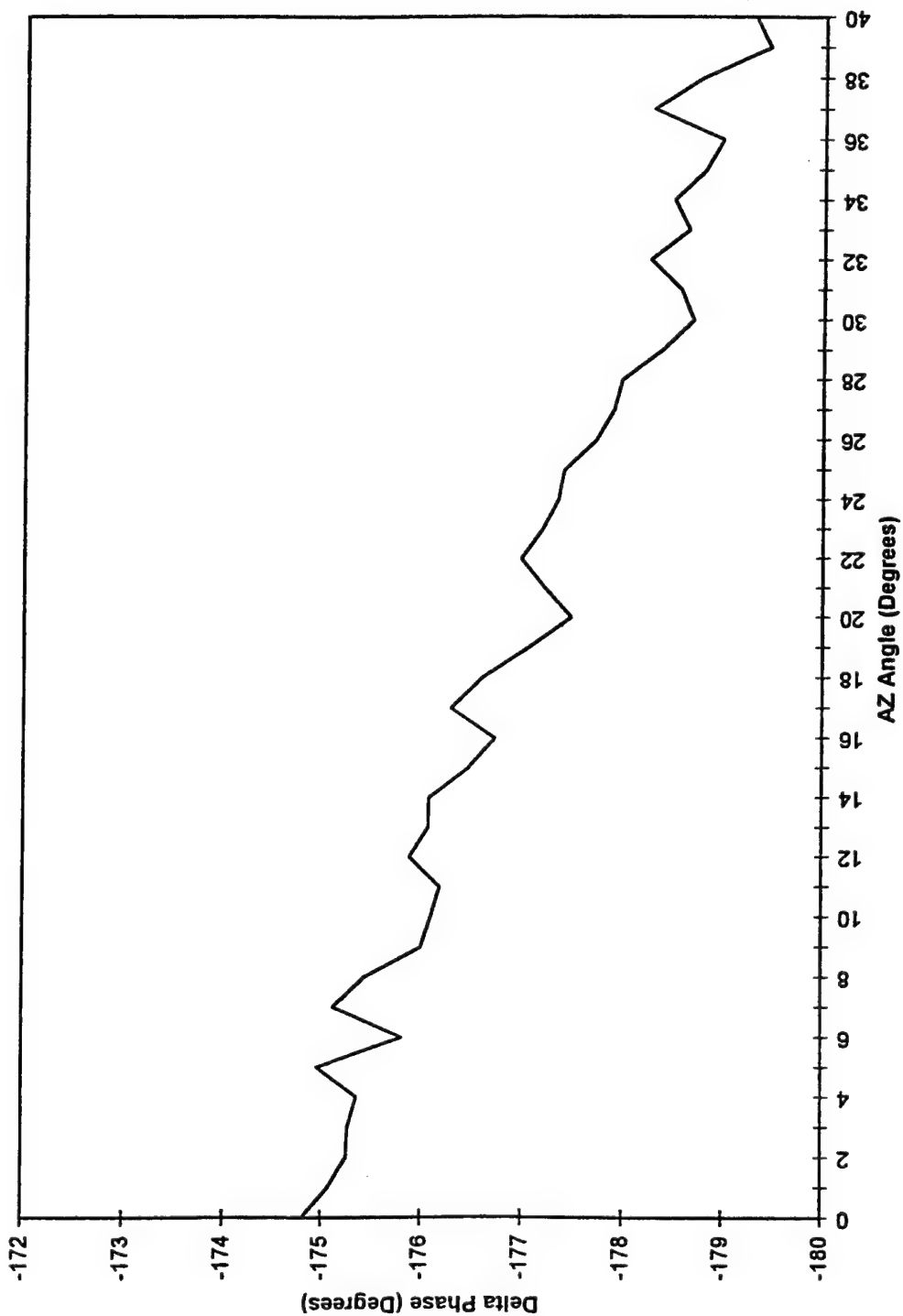


Figure 12. Delta Phase Versus Azimuth Angle, AUT at slant 45 with Vertical Source, at 10 GHz.

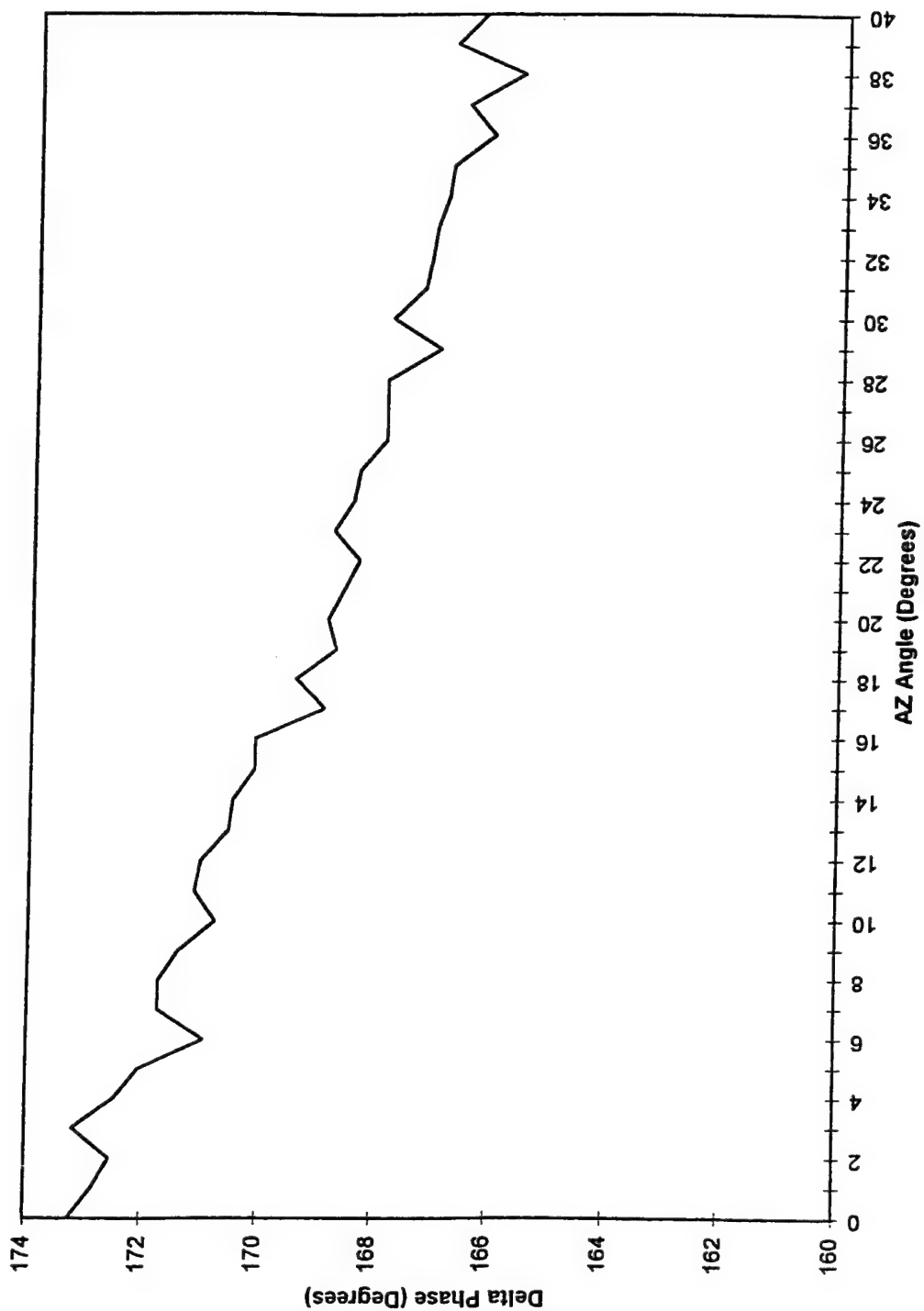


Figure 13. Delta Phase Versus Azimuth Angle, AUT at slant 45 with Vertical Source, at 18 GHz.

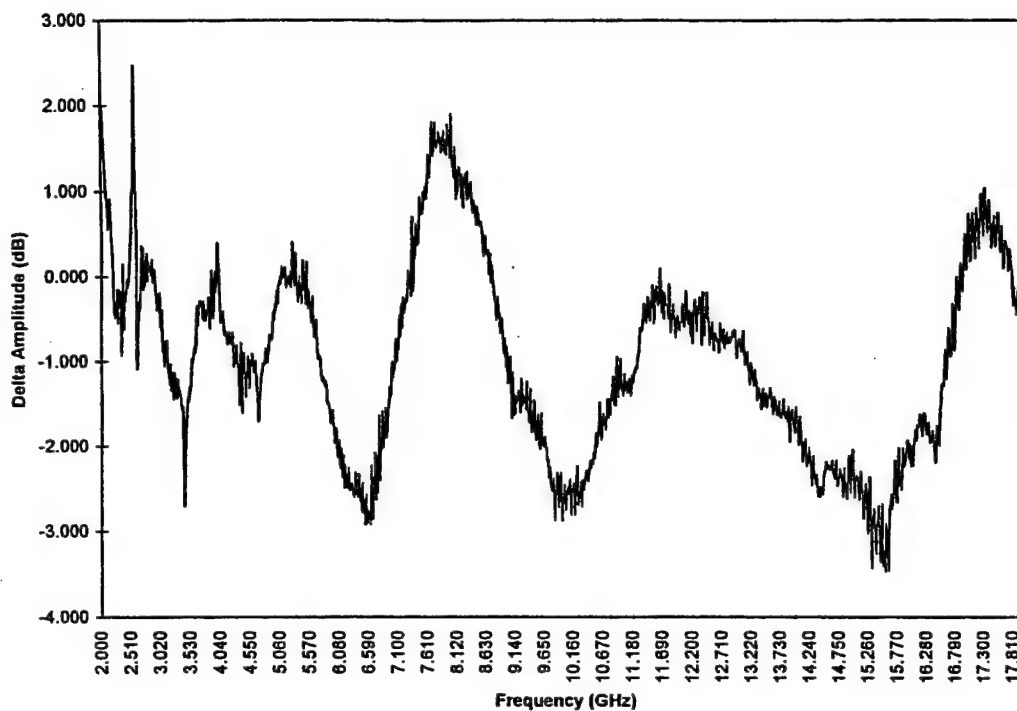


Figure 14. Delta Amplitude Versus Frequency for AUT at slant 45, Boresight, Vertical Source.

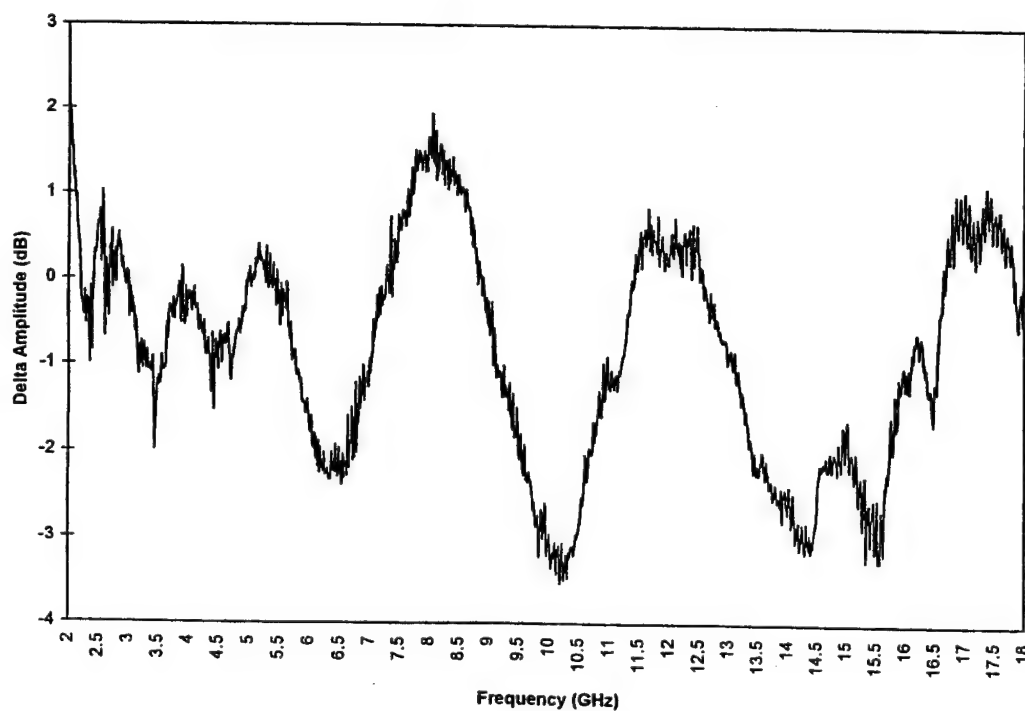


Figure 15 Delta Amplitude Versus Frequency for AUT at slant 45, 30 Degrees Azimuth, Vertical Source.

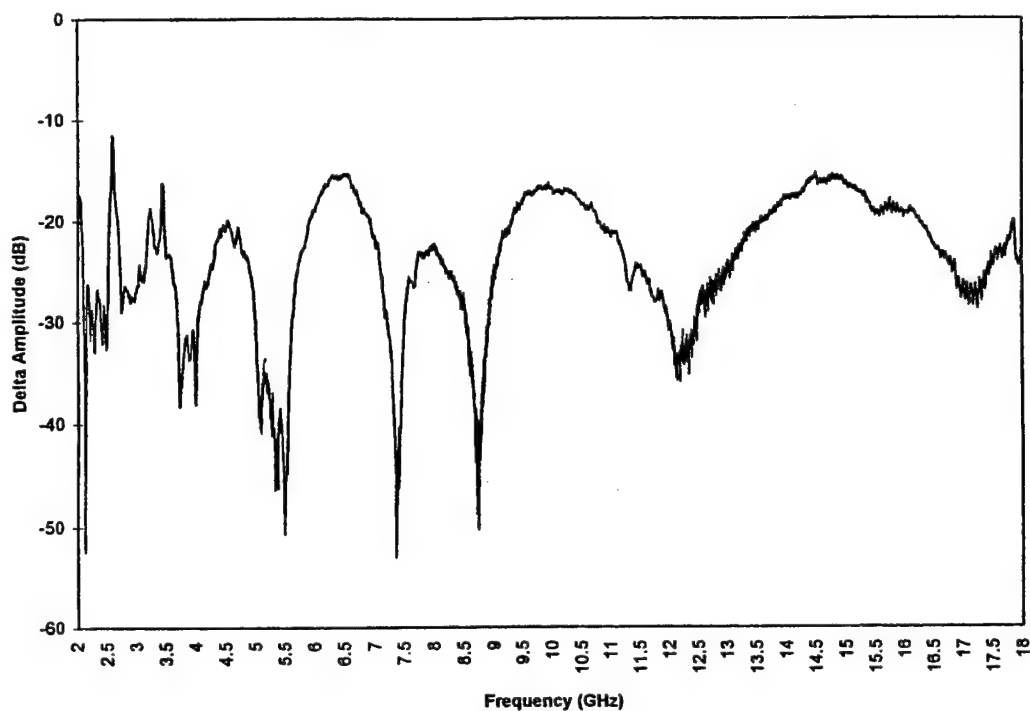


Figure 16. Delta Amplitude Versus Frequency for AUT at slant 45, Boresight, Slant 45 Source.

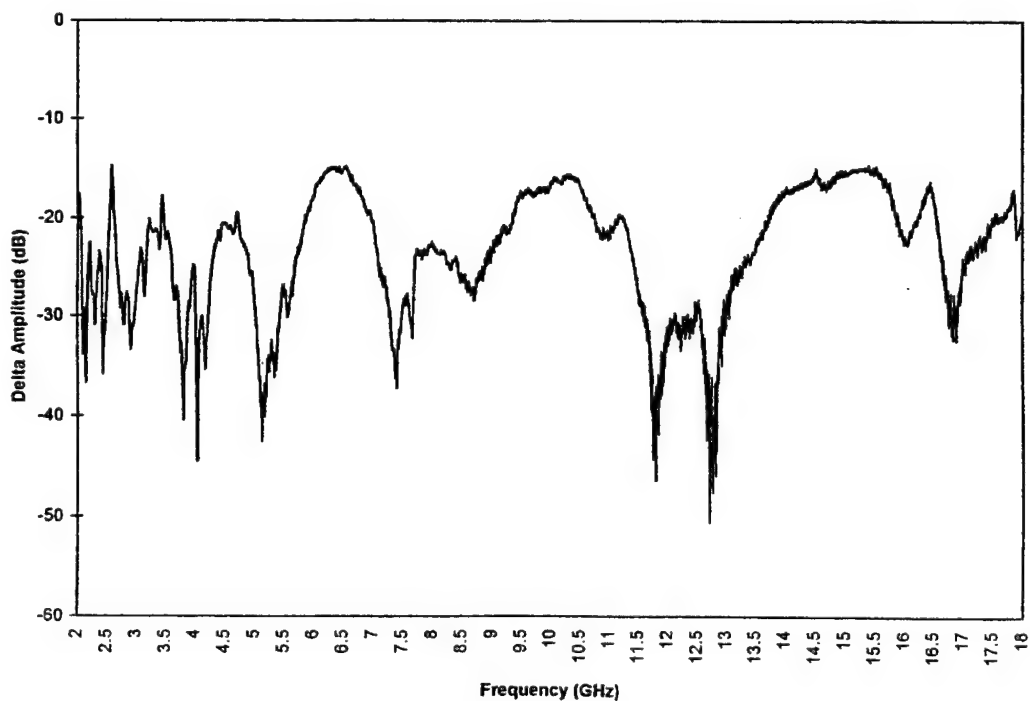


Figure 17 Delta Amplitude Versus Frequency for AUT at slant 45, 30 Degrees Azimuth, Slant 45 Source.

angle. Figures 18 and 19 are delta amplitude for a RHCP source at 0 and 30 degrees in azimuth. At 0 degrees in azimuth the variation averages approximately 2 dB while at 30 degrees it averages approximately 2.5 dB.

Delta amplitude was measured versus 0 to 40 degrees in azimuth at 2, 10 and 18 GHz for a vertical source. The data is shown in figures 20 through 22. The change in delta amplitude is expected to be small and is indeed the case with 0.3 dB change at 2 GHz, 0.65 dB at 10 GHz and 0.4 dB at 18 GHz.

The next set of data is for a quad ridged dual linear polarized horn antenna which is typically used in polarimeters. The antenna measured covered the 12 to 18 GHz frequency band using a vertical source. Figures 23 through 28 show both delta phase and delta amplitude over a plus or minus 60 degrees azimuth angle for the frequencies of 12, 15, and 18 GHz. This horn has a measured cross-polarization isolation of 25 to 30 dB. There is a little skew in the data due to the application for which the horn was designed. No modifications were made to correct this in the horn. The variations in delta amplitude and delta phase exhibit smooth curves except for 18 GHz where the horn was not optimized and the radiation pattern has high sidelobes affecting the measurements. The variation in delta amplitude was 3 dB except at 18 GHz where it was close to 6 dB. The delta phase was worst at 12 GHz with 49 degrees of variation, 29 degrees of variation at 15 GHz and 25 degrees of variation at 18 GHz.

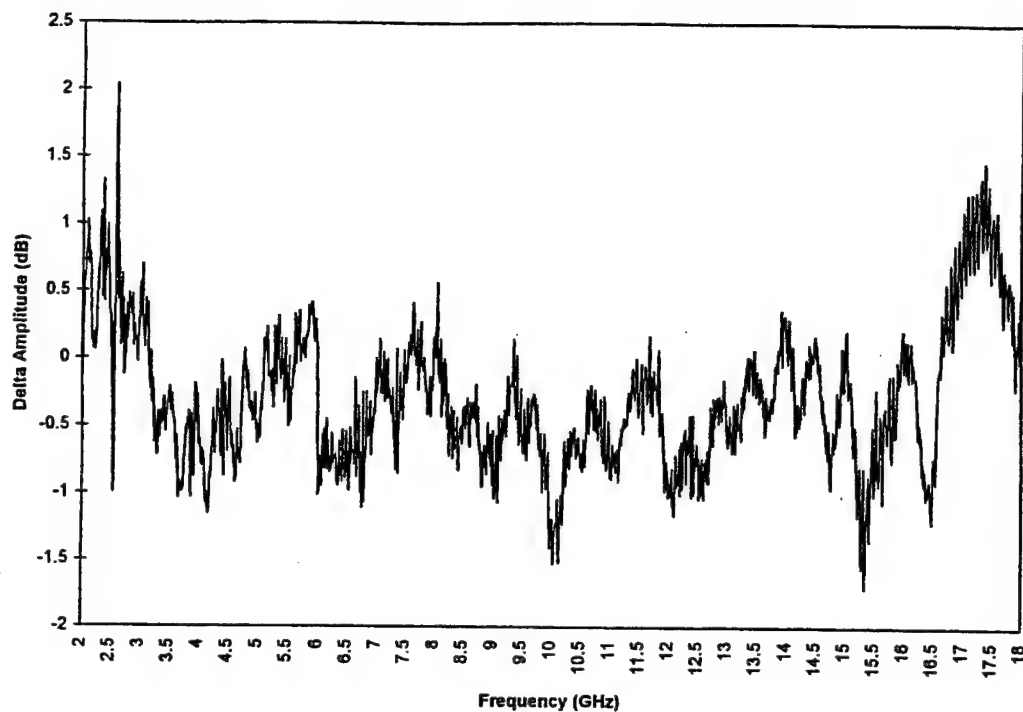


Figure 18. Delta Amplitude Versus Frequency for AUT at slant 45, Boresight, RHCP Source.

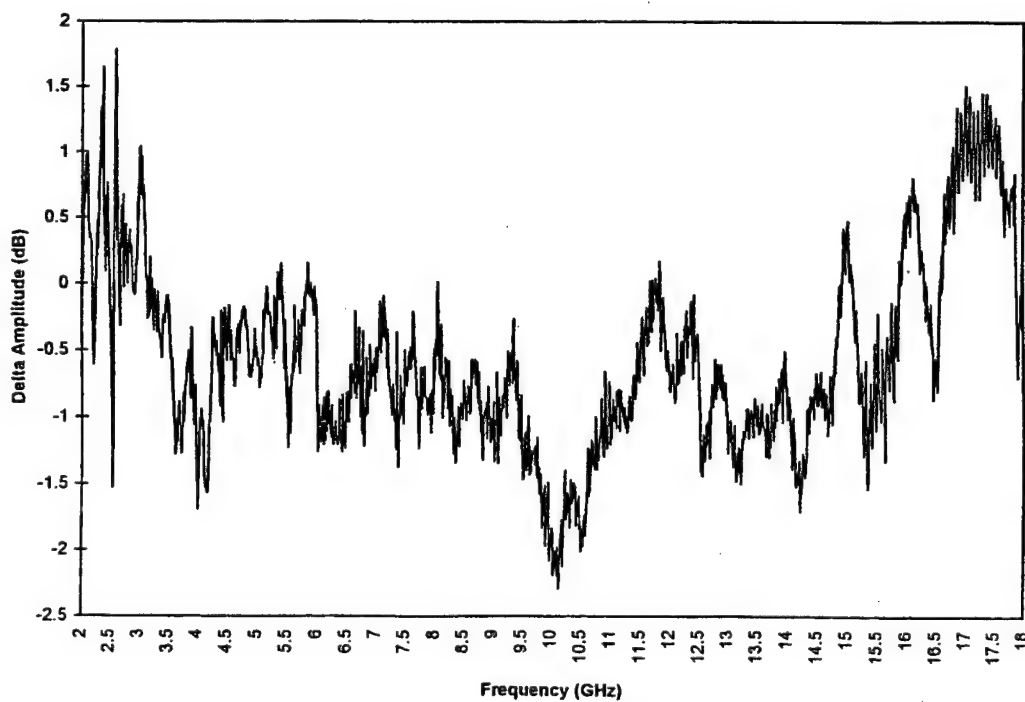


Figure 19 Delta Amplitude Versus Frequency for AUT at slant 45, 30 Degrees Azimuth, RHCP Source.

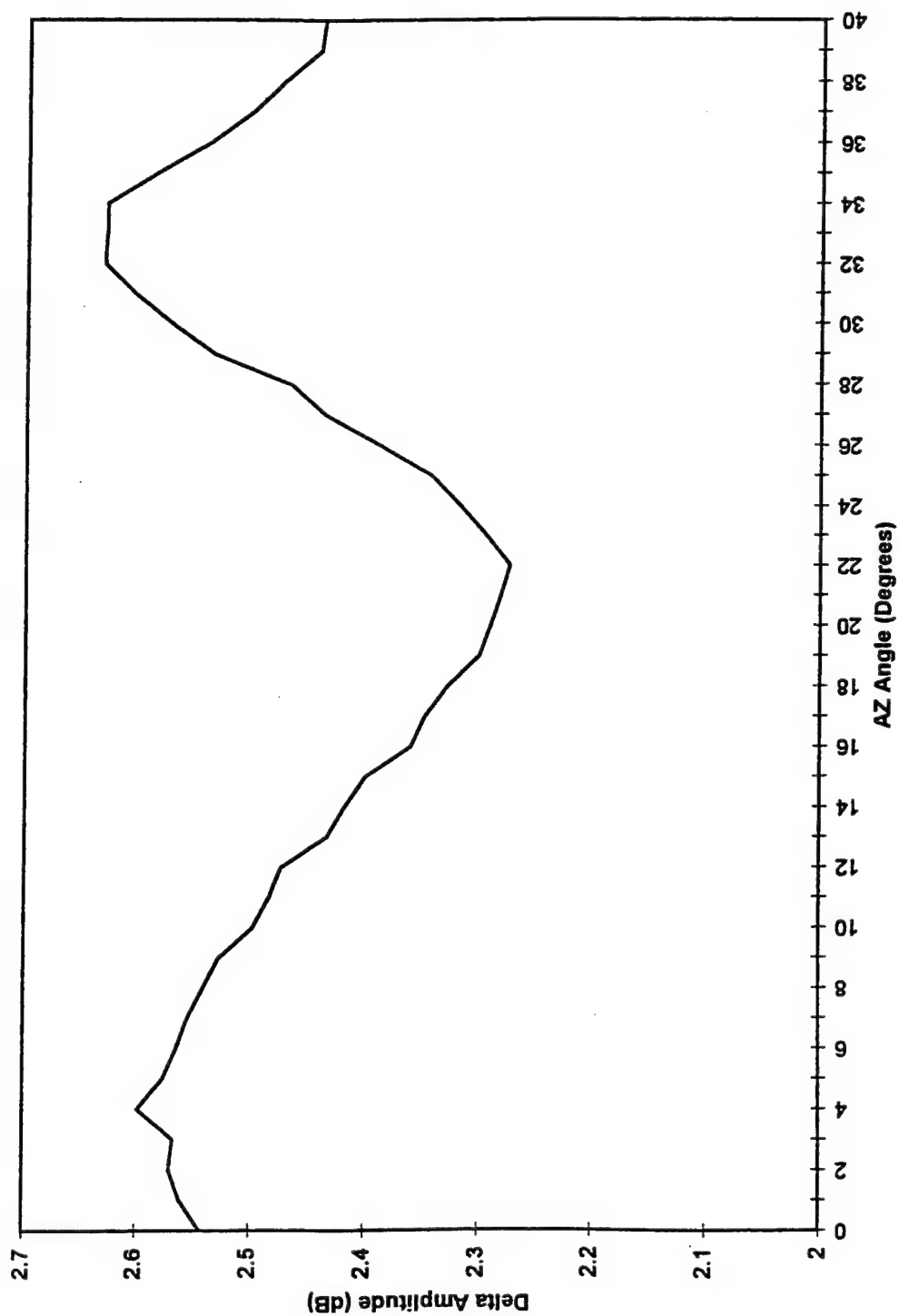


Figure 20. Delta Amplitude Versus Azimuth Angle, AUT at slant 45 with Vertical Source, at 2 GHz.

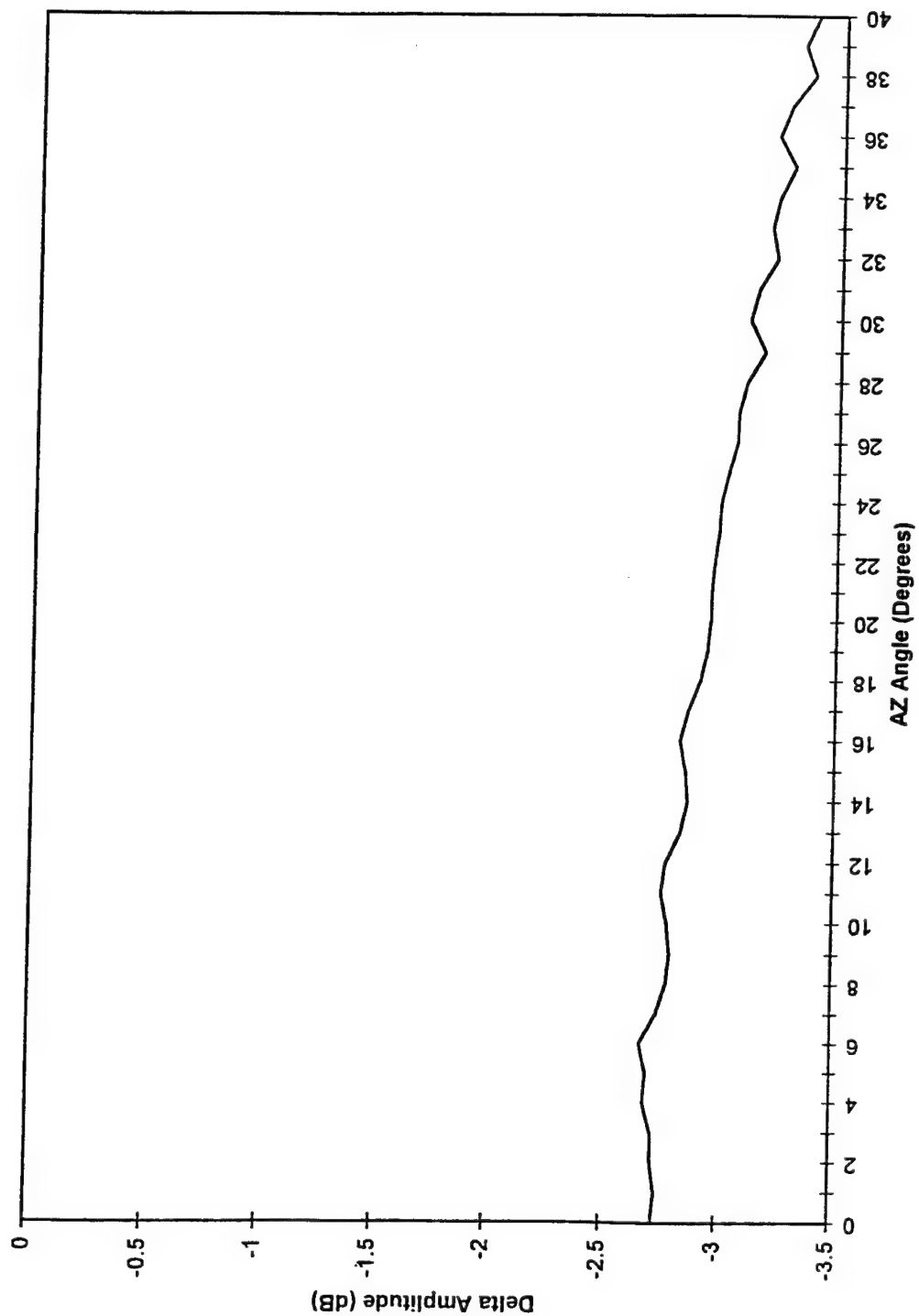


Figure 21. Delta Amplitude Versus Azimuth Angle, AUT at slant 45 with Vertical Source, at 10 GHz.

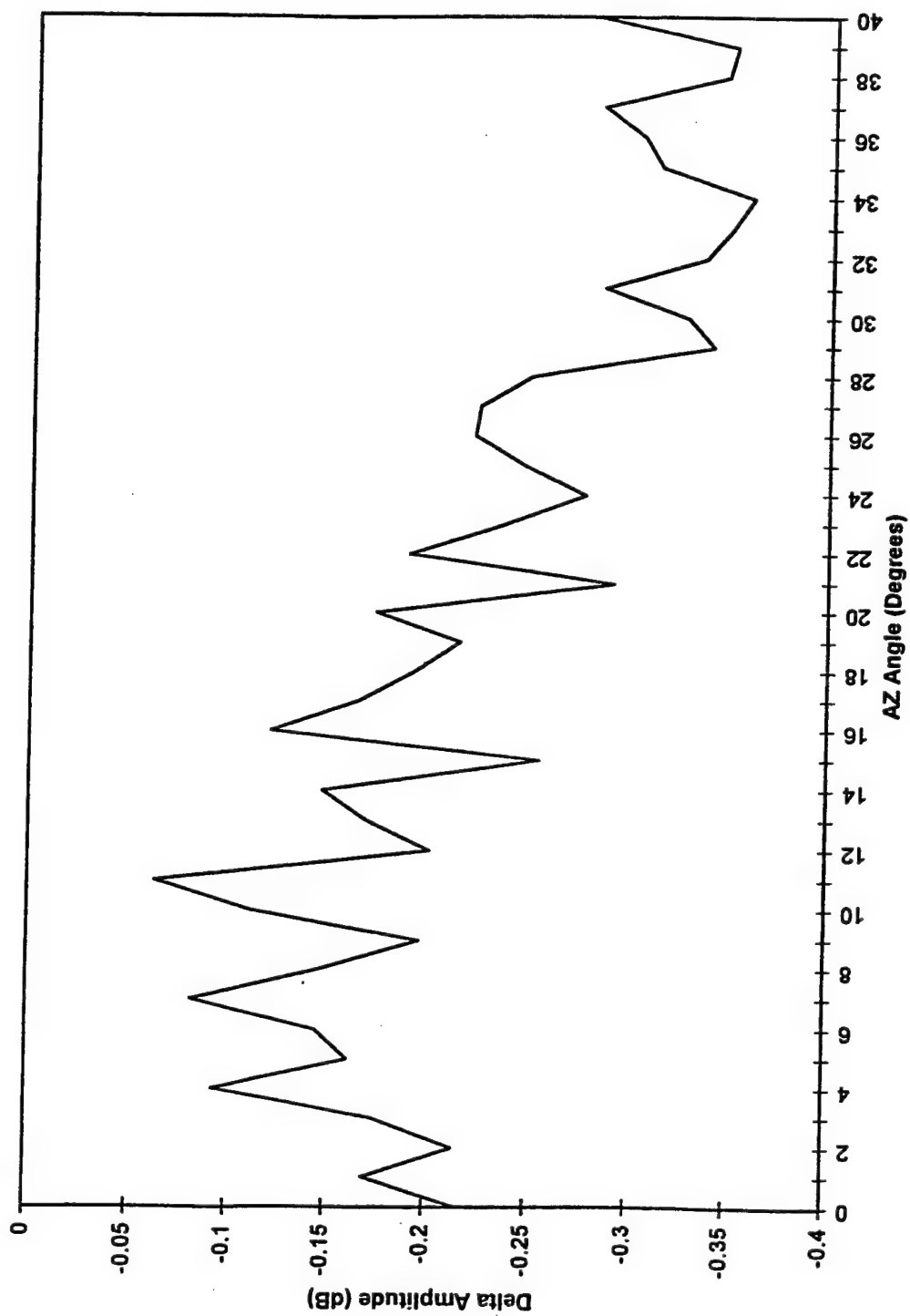


Figure 22. Delta Amplitude Versus Azimuth Angle, AUT at slant 45 with Vertical Source, at 18 GHz.

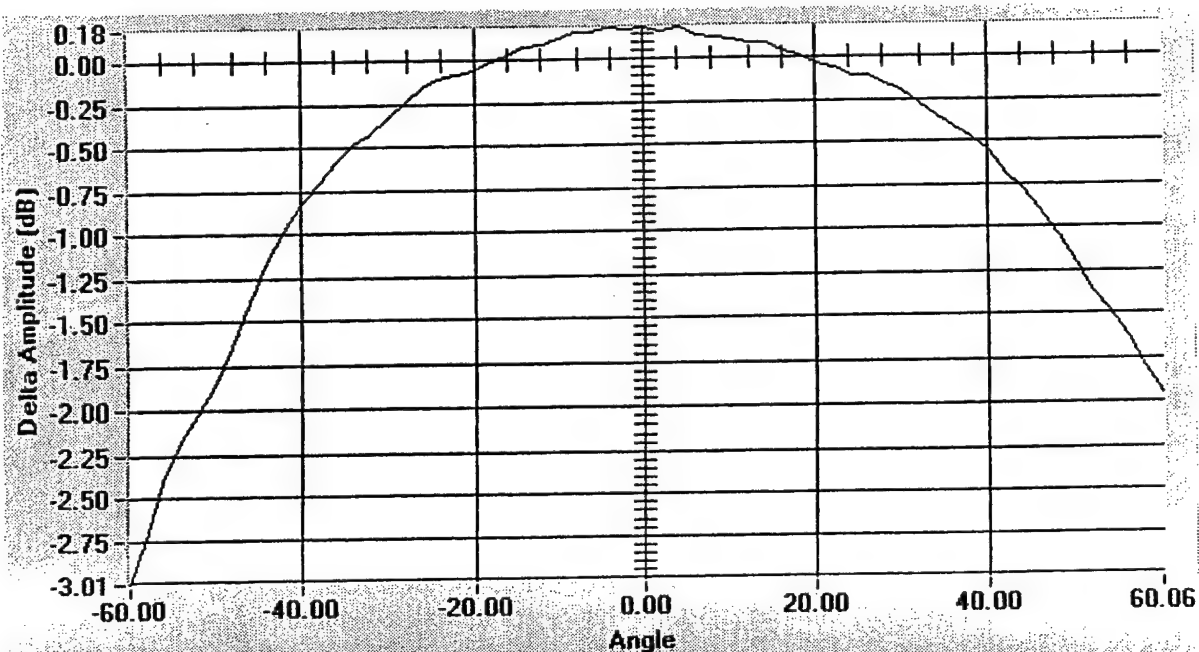


Figure 23. Delta Amplitude Versus Azimuth Angle, for Dual polarized Quad Ridged Horn, Vertical Source at 12 GHz.

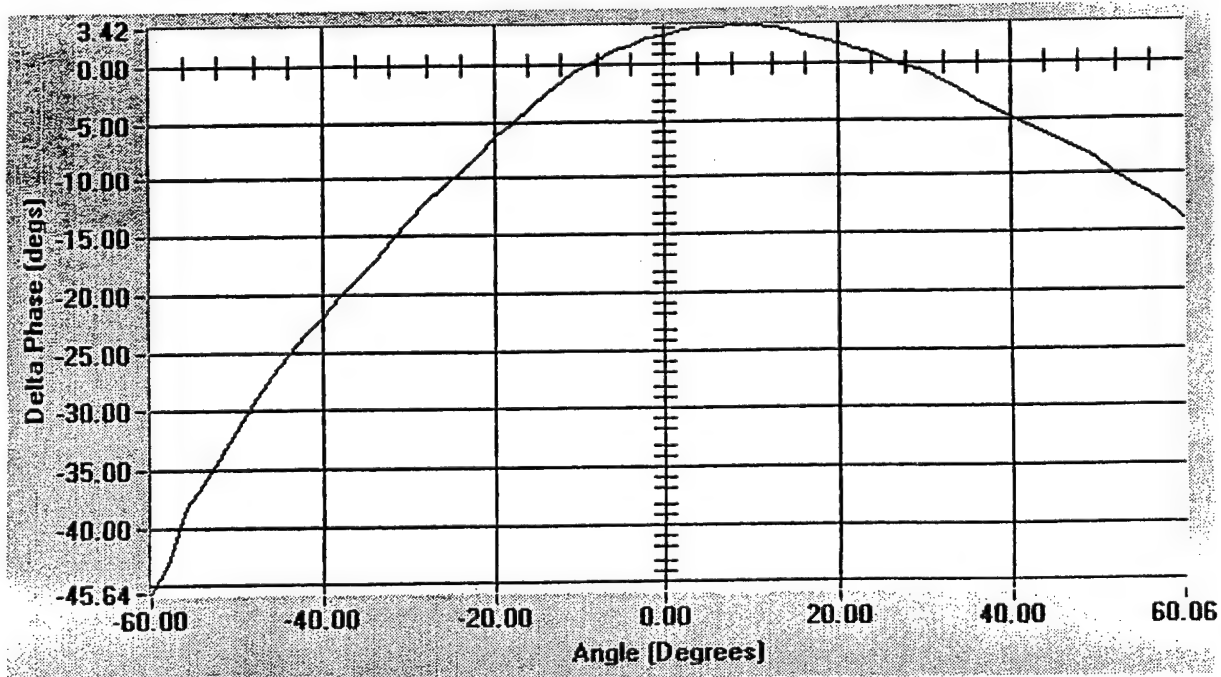


Figure 24 Delta Phase Versus Azimuth Angle, for Dual polarized Quad Ridged Horn, Vertical Source at 12 GHz.

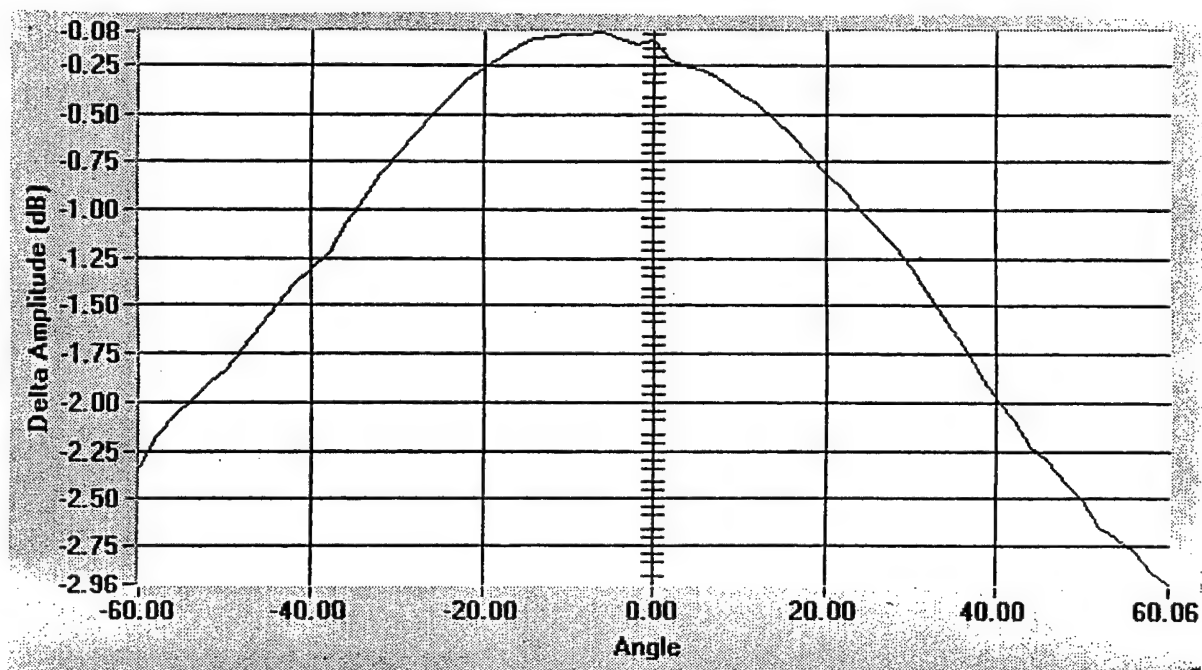


Figure 25. Delta Amplitude Versus Azimuth Angle, for Dual polarized Quad Ridged Horn, Vertical Source at 15 GHz.

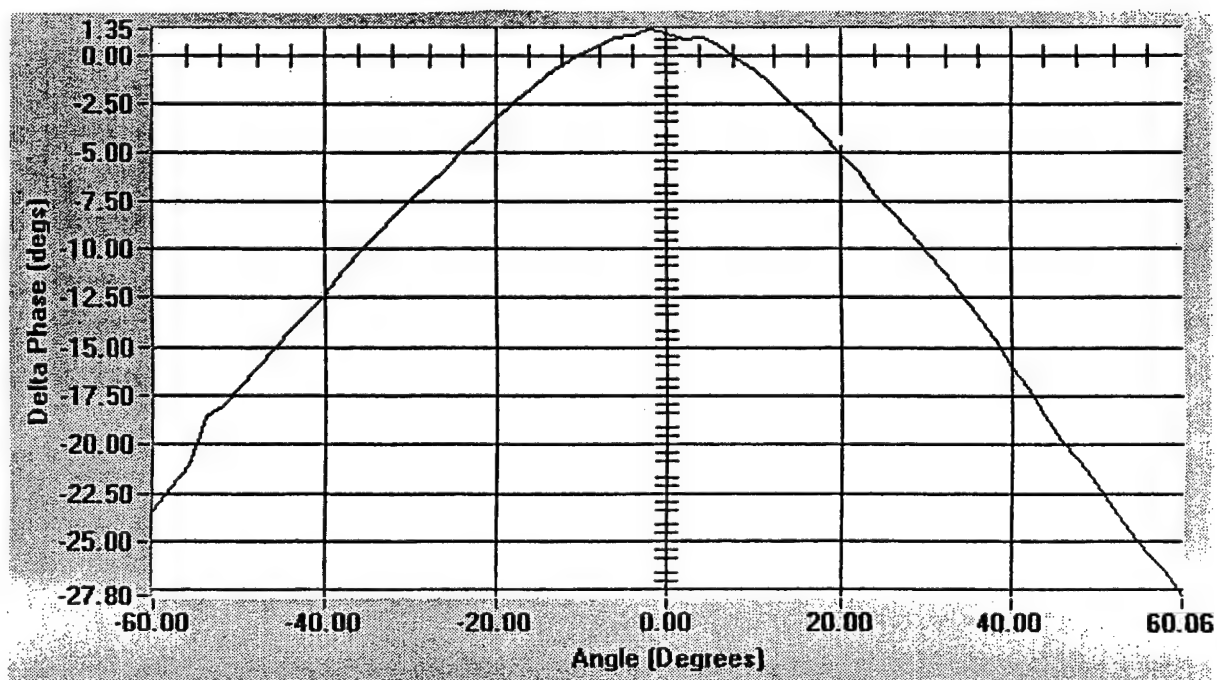


Figure 26 Delta Phase Versus Azimuth Angle, for Dual polarized Quad Ridged Horn, Vertical Source at 15 GHz.

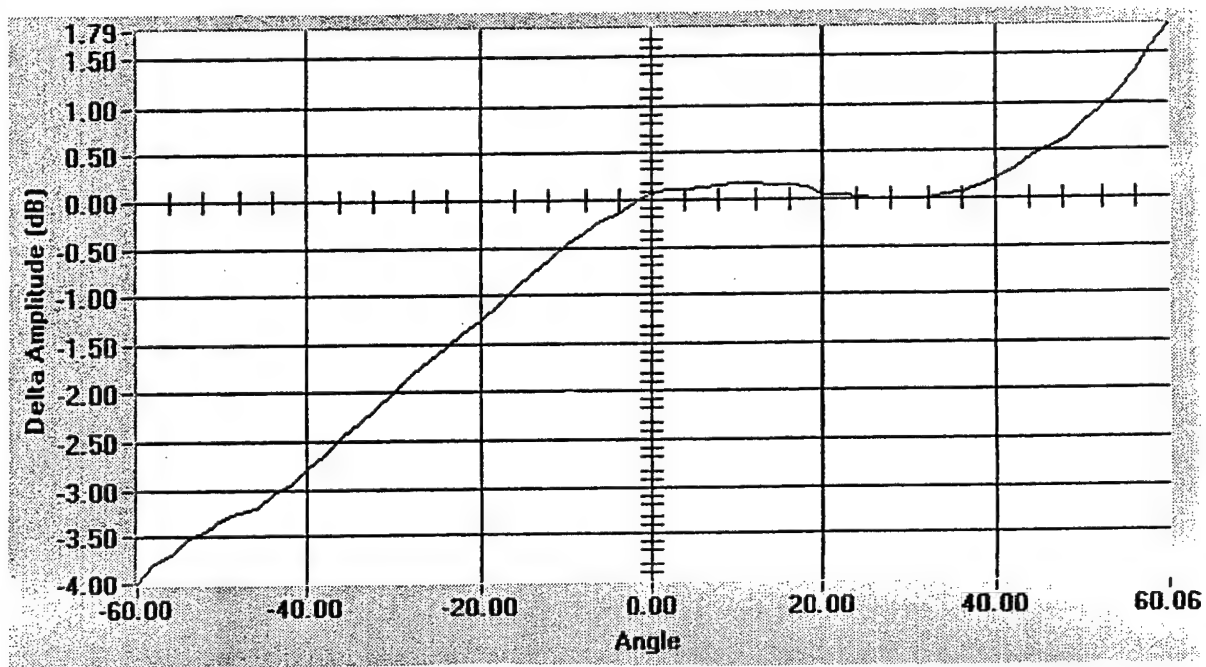


Figure 27. Delta Amplitude Versus Azimuth Angle, for Dual polarized Quad Ridged Horn, Vertical Source at 18 GHz.

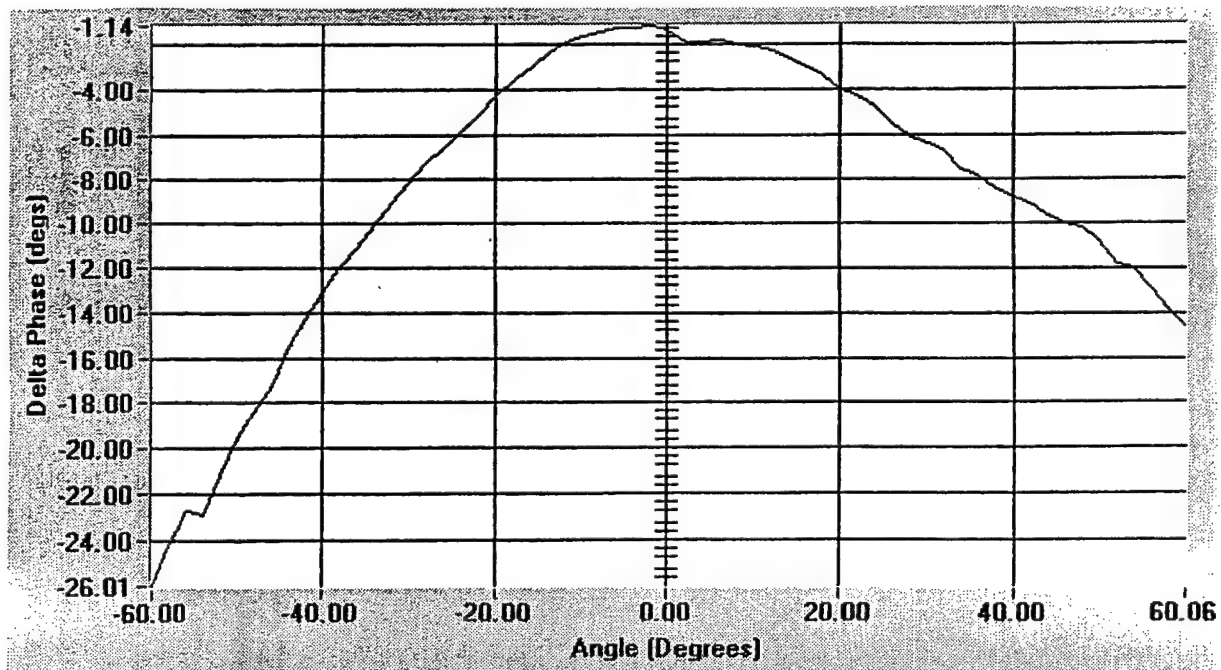


Figure 28 Delta Phase Versus Azimuth Angle, for Dual polarized Quad Ridged Horn, Vertical Source at 18 GHz.

Discussion:

The sinuous antenna element exhibits some interesting characteristics in both amplitude and phase. The delta amplitude can exhibit variations over frequency and azimuthal angle which are not linear and must be bounded if simple calibration is to be implemented. However, delta phase requires linearization with modulo-360 variations taken out and 180 degree phase jumps accounted for. The variation in delta phase requires an extensive calibration table for the polarimeter to identify the polarization correctly. As the figures show, an extensive set of phase measurements of the sinuous antenna has now been done and it is not linear in phase as well as amplitude. This places the added requirement, of any polarimeter system it is installed into, of extensive calibration. The cross-polarization isolation is not large enough as compared to the horn antenna. Measured data on multiple sinuous elements shows large variations in the cross-polarization isolation from antenna to antenna.

Other antennas were looked at, in particular the quad ridged dual polarized horn. The horn antenna exhibited excellent cross-polarization isolation and both delta amplitude and delta phase were fairly well behaved as compared to the sinuous. A simple calibration would suffice for the horn antenna in a polarimeter.

The sinuous antenna does exhibit a slight polarization wandering and this coupled with the smaller amount of cross-polarization isolation can account for the variation in delta amplitude and delta phase. This was not seen in the horn antenna which exhibited close to a 30 dB cross-polarization isolation across its operational bandwidth.

A single 2 to 18 GHz horn antenna will exhibit a narrowing of the field of view as the frequency approaches 18 GHz. The solution for this problem is to use several horns over smaller portions of the 2 to 18 GHz frequency band. This allows the horn to still provide the 30 dB cross-polarization isolation and still be fairly easy to calibrate.

Conclusion:

This is the first set of sinuous 2 to 18 GHz data detailing some of the problems in using it for a polarimeter element. The element can be used as a polarimeter element but it will require extensive calibration and look up tables in order for it to work in a system. This may prove uneconomical due to the massive amount of calibration data required. Other installation issues will still need to be addressed such as installing the element in a radome. The two largest problems discovered are the nonlinear delta amplitude variations and the necessity of modulo-360 reduction in the delta phase which still requires extensive linearization. The use of the horn antenna is a better choice based on obtainable cross-polarization isolation and the well behaved delta phase and delta amplitude. The horn exhibits the potential for less extensive calibration. However, in order to function over the 2 to 18 GHz frequency band, multiple horns will have to be used so that decreasing field of view does not effect the delta amplitude and delta phase.

Acknowledgment:

I wish to thank Vito Minerva of Tecom for the data he provided on the sinuous elements used for comparison. I wish to thank Danny Bennett for help in the measurements and data reduction. I wish to thank Hank Burnett for providing the dual polarized quad ridged horn data.

References:

1. Stutzman, W. L., Polarization in Electromagnetic Systems, Artech House, Norwood, MA, 1993.
2. Mott, H., Polarization in Antennas and Radar, John Wiley & Sons, New York, 1986.
3. IEEE Standard Test Procedures for Antennas, IEEE Std. 149-1979, IEEE through Wiley-Interscience, 1979.
4. Kraus, J. D., Electromagnetics, Fourth Edition, McGraw-Hill, Inc., New York, 1992.
5. Hawthorne, D. L., Polarization Measurement: Part 1, Watkins-Johnson Tech-notes, Vol. 14, No. 6, Palo Alto, CA, November/December, 1987.

Appendix:

Polarization Ratio: (PR) the ratio of V to H

Tilt Angle: In the cartesian plane it is the orientation of the major polarization axis with respect to the reference coordinate. β is the angle to the horizontal axis when using H and V. β range is from -90 to 90 degrees for H and V. $\beta = \arctan (V/H)$

Axial Ratio (AR): The ratio of the magnitude of the polarization ellipse major axis to the minor axis. If $AR = 0$ the ellipse is linear and if it is 1 the ellipse is circular and for LHCP the $AR = +1$ and for RHCP $AR = -1$.

Ellipticity Angle: α is the angular expression for the polarization ellipse ellipticity. $\alpha = \arccot (AR)$ $\alpha = 0$ degrees for linear and 45 degrees for circular.

Phase Angle: Delta phase (ϕ) between the V and H components from -180 to 180 degrees.

Poincare' Sphere: Spherical representation of polarization. Linear polarization is on the equator with H = 0 degrees and V = 180 degrees. LHCP is at the top pole and RHCP is at the bottom pole. Longitude is twice the tilt angle (2β) and latitude is twice the ellipticity angle times the sign of the phase angle ($2\alpha * \text{sign} (\phi)$).

Stokes Vectors:
$$AR = \tan(1/2(2PR\sin(\varphi)/1-(PR)^2 + 4PR\cos^2(\varphi))$$

$$\beta = 1/2(\tan^{-1}(2\sqrt{PR}\cos(\varphi)/(1-PR))$$

$$CP = 2 H'V'\sin(\varphi) = Z$$

$$LP = H'^2 - V'^2 = Y$$

$$SP = 2H'V'\cos(\varphi) = X$$

Where: H' or V' are normalized,
 CP is degree of circular polarization,
 LP is degree of linear polarization,
 SP is degree of slant linear
 polarization.

OPTIMIZED DESIGN METHODOLOGY OF CAVITY-BACKED MICROSTRIP ANTENNAS WITH DIELECTRIC OVERLAYS

Douglas J. Hermes Peter J. Collins

August 12, 1997

Abstract

Microstrip antennas are renowned for poor pattern directivity. In this paper, we investigate the ability of dielectric overlays applied to cavity-backed microstrip antennas to tailor the radiation pattern. Of primary interest is our application of designed experiments methodology, traditionally reserved for industrial engineering applications, to the electromagnetic design problem. By combining the techniques of Response Surface Methodology (RSM), designed experiments, and cavity-backed antenna analysis based on a hybrid Finite Element Method (FEM) code, we develop an optimized design procedure to quickly and efficiently determine required antenna parameters for a desired performance. The optimized design procedure implements a concise, empirical model to describe an antenna's performance based on systematic FEM code calculations, thereby reducing a lengthy and computationally intensive analysis step. The accuracy of the empirical model is verified numerically with predicted FEM data highlighting the usefulness of these industrial techniques to the electromagnetics design arena.

1 Introduction

Designed experiments have found a permanent home in the area of industrial engineering since they provide insight concerning the variance of nondeterministic systems. Recently, the electromagnetics community began utilizing designed experiments to study the effects of varying design parameters in such areas as antenna radiation patterns and input impedance [3]. This paper applies the concepts of designed experiments, system empirical modeling, and Response

Surface Methodology (RSM) to a cavity-backed microstrip antenna with dielectric overlays demonstrating the utility of their combined design methodology.

1.1 Problem

A cavity-backed microstrip antenna is a difficult boundary value problem to consider, especially when adding layers of dielectric superstrate material to an antenna design. Modern hybrid integral equation/Finite Element Method (FEM) electromagnetic analysis codes can provide accurate solutions for antenna gain and radiation patterns but typically require too much CPU time for efficient design exploration. The problem at hand is two-fold. First, an efficient and accurate design methodology that produces an optimized antenna design in seconds rather than hours or days is required. Second, to create an optimized design methodology, a precise antenna empirical model that determines gain values over a specified angular region is necessary. The empirical model must closely emulate the antenna properties under all conditions such as varying dielectric permittivities and thicknesses along with an adjustable antenna frequency. In addition, the empirical model must provide reasonably accurate antenna gain values that coincide well with predicted values of the FEM code used in the data collection process.

1.2 Problem Constraints

The initial step towards creating an optimized antenna design methodology is the selection of antenna parameters. Table 1 lists the fixed and variable antenna

Fixed parameters	Cavity dimensions Patch dimensions Patch location in cavity Feed location Substrate permittivity Substrate thickness Number of dielectric superstrates Net thickness of superstrates
Variable parameters	Frequency Superstrate permittivities Superstrate thicknesses

Table 1: Antenna Design Parameters.

parameters selected for the empirical model. By fixing certain parameters, the scope of the experiment is kept reasonable and the effects from a small, controllable group of variable parameters can be studied.

The constant parameters of the antenna design came from a scaled version of an existing operational antenna (Figure 1). The cavity dimensions in length, width, and height are $11.75\text{cm} \times 11.75\text{cm} \times 2.37\text{cm}$. The radiating patch located approximately 0.711cm above the cavity's base, is centered in the cavity and is rectangular with dimensions of $6.53\text{cm} \times 6.53\text{cm}$. The patch feed point is located approximately 0.33mm off center in both \hat{x} and \hat{y} dimensions. The substrate has a relative permittivity of 4.0 and is 0.948cm thick, just covering the radiating patch. Of the fixed antenna parameters, the dielectric superstrates are the only design parameters not borrowed from the original antenna design. In this antenna design procedure, we consider two dielectric superstrate layers. To maintain constant cavity dimensions, the total thickness of the two dielectric superstrates is maintained at 1.422cm .

The variable parameters of the antenna design are shown in Figure 1. Since

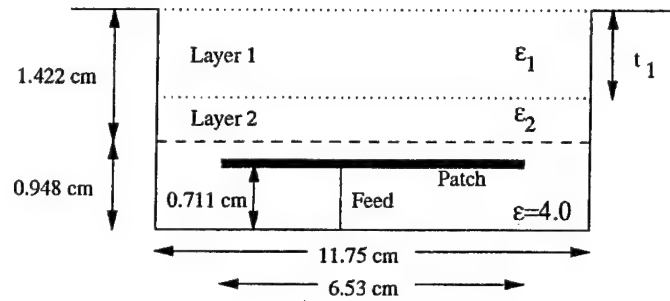


Figure 1: Cavity-Backed Microstrip Antenna with Dielectric Overlays.

two layers of dielectric superstrates are being considered, a total of four input parameters are available for adjustment and study. The permittivities of both superstrate layers 1 and 2 are adjustable to any value in the range of 1.0 to 8.0. Since the net thickness of the superstrate layers remains constant, the thickness of only one layer, the top layer, is adjusted to provide a third input variable. The thickness of superstrate layer 2 is dependent upon the thickness of layer 1 and the net total superstrate thickness. The antenna frequency provides the fourth variable, being adjustable to any frequency value between 0.9 GHz and 1.3 GHz.

2 Designed Experiments

According to Montgomery [2], designed experiments holds a critical place in both the industrial and the engineering worlds. Application of experimental design techniques early in process and product development stages results in several advantages over cumbersome trial and error methods.

1. Improved process yields.

2. Reduced variability and closer conformance to nominal or target requirements.
3. Reduced development time.
4. Reduced overall costs.
5. Efficient evaluation and comparison of basic design configurations.
6. Efficient evaluation of material alternatives.
7. Precise selection of design parameters so that the product will work well under a wide variety of field conditions.
8. Accurate determination of key product design parameters that impact product performance.

Many of these advantages are directly applicable to the antenna design problem.

2.1 Full Factorial Designed Experiments

The most common type of experimental design is the full factorial design experiment. Full factorial experiments are detail oriented and provide an accurate and orderly method of performing experimental measurements that contain well behaved system conditions as well as system transitions and discontinuities. Furthermore, full factorial experimental designs are applicable for any number of input variables, constrained only by the cost of additional measurements and data collection time. All possible combinations of variable levels are investigated in the full factorial design. For example, if four variables are tested at five levels each, a total of 5^4 (625) experimental configurations of the proposed antenna design are available. Each possible combination of the antenna configuration must be examined to ensure all possible test conditions and parameter influences are encountered for the construction of a complete experimental data

Variable	Level 1	Level 2	Level 3	Level 4	Level 5
Frequency (GHz)	0.9	1.0	1.1	1.2	1.3
Permittivity Layer 1	1	2	4	6	8
Permittivity Layer 2	1	2	4	6	8
Thickness (cm) Layer 1	0.237	0.474	0.711	0.948	1.185

Table 2: Variables and Corresponding Levels.

set. In this case 625 total experimental runs of the FEM code are necessary to complete the full factorial experiment. Montgomery [2] lists several advantages of full factorial experimental designs over all other forms of experimental designs including the Central Composite design and the Latin Squares design. The full factorial experiment design:

1. Is more efficient than one factor at a time experiment.
2. Is necessary when variable interactions are present to avoid misleading conclusions.
3. Allows the effects of a factor to be estimated at several levels of the other factors, yielding conclusions valid over a range of conditions.
4. Allows multitudes of comparisons to be performed and so facilitate model creation and criticism.
5. Provides highly efficient estimates of constants whose variances are small.
6. Leads to simple empirical models using linear regression or cubic splines.

Table 2 lists the levels of each variable used in this experiment, and Table 3 lists the corresponding full factorial design.

3 Cubic Splines

Having determined an appropriate experimental design, the next step in the design methodology is to build an appropriate empirical model. To construct

Test Number	Layer 1 Thickness (cm)	Layer 1 Permittivity	Layer 2 Permittivity	Frequency (GHz)	Antenna Gain
1	0.237	1	1	0.9	y_1
2	0.237	1	1	1.0	y_2
3	0.237	1	1	1.1	y_3
4	0.237	1	1	1.2	y_4
5	0.237	1	1	1.3	y_5
6	0.237	1	2	0.9	y_6
\vdots	\vdots	\vdots	\vdots	\vdots	\vdots
625	1.185	8	8	1.3	y_{625}

Table 3: Four Factor, Five Level, Full Factorial Design.

an empirical model of the measured antenna gain responses, the cubic spline technique was selected over linear regression for two reasons. First, the development of the cubic spline algorithm accounts for the slopes and curvatures of data points while constructing smooth splines between data points. Of course, a higher order polynomial used in linear regression would also closely model measured data with four input variables, but linear regression does not consider slopes or curvatures. Second, cubic splines are adaptable to a query format with any number of independent variables [4]. Cubic splines continuously recalculate appropriate variable coefficients as the query progresses towards a final system response taking into account all input variable parameters. In the case of linear regression, variable coefficients are determined prior to performing queries. Therefore, linear regression is less likely to maintain close accuracy while predicting system performance. In short, cubic splines closely model transitioning data, and in the case of discontinuities, if an adequate amount of data points are measured cubic splines will provide a fairly reasonable estimate of the system response.

The fundamental cubic spline equation is a third order polynomial of the form

$$y = a_i(x - x_i)^3 + b_i(x - x_i)^2 + c_i(x - x_i) + d_i \quad (1)$$

where i indicates the i th interval between test point locations in the variable x dimension. The coefficients and variables with the i subscripts are relevant only to the i th interval. New coefficients are determined for each data interval and variable dimension.

4 Response Surface Methodology

Following the data acquisition phase from the full factorial experimental design and the model generation phase from cubic splines, the selection of an optimum antenna configuration with respect to variable parameters is the next step to accomplish. Response Surface Methodology (RSM) is fundamentally a method of applying a gradient search routine to a data model with the goal of locating either a maximum or a minimum data response [2]. RSM uses a steepest ascent approach to locate maximum system responses and likewise uses a steepest descent approach for minimum system responses. In the case of non-deterministic problems like process yields from an assembly line, RSM continually fits new, higher-order data models to locations of maximum process response. Unfortunately, this generation of new data models near optimum locations calls for repeated data collection in the vicinity of optimum responses. The process of data collection and model fitting continues until an optimum response of

acceptable accuracy is achieved. In the case of deterministic processes where system responses are exactly equal for repeated identical input parameters, the repeated data collection and model building steps are not required. For example, in the case of an FEM code used in antenna gain predictions, the FEM code will determine the antenna gain values to be exactly the same for repeated calculations dependent only upon antenna model input parameters. Therefore, an accurate model created using a relatively large number of test points to adequately describe the system response under all test conditions is sufficient without additional data collection phases and model building. The application of an optimization software routine to a coded cubic spline algorithm is a form of the RSM technique. The optimization routine may be used to determine the exact variable combination providing the optimum system response, like antenna gain in the region of interest, thereby fulfilling the functions of RSM.

5 Optimized Design Methodology

In the development of an optimized design methodology for a cavity-backed microstrip antenna with dielectric overlays, the full factorial designed experiment, a five dimensional cubic splines empirical model, and an adapted form of RSM were used. The intention of the design methodology is to provide an accurate, reliable, fast algorithm to determine antenna gain and manipulate the antenna pattern for the antenna design under consideration. In that vein, an optimal antenna design that produces a minimum average gain value in the angular

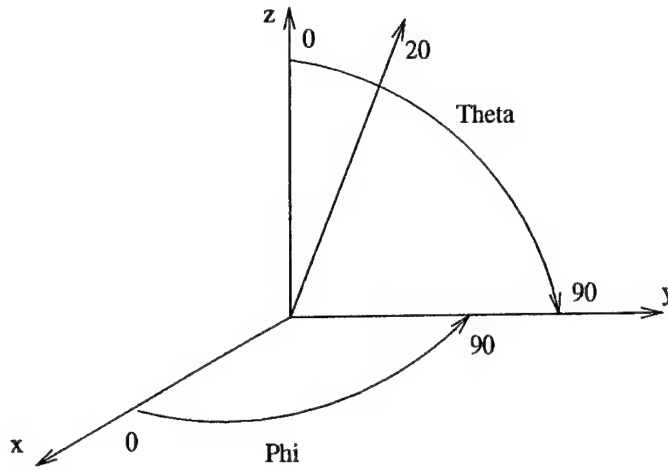


Figure 2: Region of Interest.

region,

$$0^\circ \leq \theta \leq 20^\circ \quad (2)$$

$$0^\circ \leq \phi \leq 360^\circ \quad (3)$$

as depicted in Figure 2 was selected as the desired antenna response. Ultimately, a null in the radiation pattern on boresight created by the combined effects of antenna resonant frequency, permittivity choices of layers 1 and 2, and layer 1 thickness is the desired response.

5.1 Application of Designed Experiments

The full factorial design example in Section 2.1 was implemented where a total of 625 test cases were performed using an FEM code to determine resulting antenna gain. Gain values were calculated for each angular location in the region given in Equations (2) and (3) in 5° steps. Average gain values were

determined according to Equation (4)

$$averagegain = 20 \log \left(\frac{10^{\left(\frac{gain_{00}}{20}\right)} + 10^{\left(\frac{gain_{80}}{20}\right)} + \dots + 10^{\left(\frac{gain_{200}}{20}\right)}}{5} \right) \quad (4)$$

to be used later in the cubic spline routine. The full factorial design consisting of the 625 test cases took approximately 12 hours to complete using a Silicon Graphics Origin 200 with four R10000 processors running simultaneously (elapsed time). On average, each test case took approximately five minutes of processing time.

5.2 Application of Cubic Splines

To implement an accurate empirical model to describe the performance of the FEM code based on the full factorial design, the cubic spline technique mentioned earlier was implemented. This empirical model gives the average antenna gain as defined in Equation (4) as a function of the four variable parameters. Since cubic splines are created for only one variable at a time, a special query technique was used to locate gain solutions in five dimensional space. The query technique devised by Wilson [4] is as follows:

1. Using the initial 625 (5^4) test configurations and their corresponding gain values, create cubic splines in the direction of the frequency input variable at all possible level combinations of the remaining three input variables.
2. Set the frequency variable to its desired input value.
3. Determine gain values in terms of the remaining three input variables and their five levels at the desired frequency value for a total of 125 (5^3)

calculations.

4. Using the resulting 125 possible test configurations and their corresponding gain values, create cubic splines in the direction of the next input variable, the permittivity of layer 1, at all possible level combinations of the remaining two input variables.
5. Set the permittivity of layer 1 to its desired input value.
6. Determine gain values in terms of the remaining two input variables and their five levels at the desired input values of both frequency and permittivity of layer 1 for a total of 25 (5^2) calculations.
7. Using the resulting 25 possible test configurations and their corresponding gain values, create cubic splines in the direction of the next input variable, the permittivity of layer 2, at all possible level combinations of the remaining input variable.
8. Set the permittivity of layer 2 to its desired input value.
9. Determine gain values in terms of the remaining input variable, the thickness of layer 1, and its corresponding five levels at the desired input values of frequency, permittivity of layer 1, and permittivity of layer 2 for a total of five calculations.
10. Using the resulting five possible test configurations and their corresponding gain values, create cubic splines in the direction of the final input variable, the thickness of layer 1.

11. Set the thickness of layer 1 to its desired input level and calculate the final gain value that now is in terms of the desired levels of all input variables.

Obviously from this description of the query process, cubic spline coefficients were created on the fly and do not require a huge set of interpolated data points for estimates of gain values. Gain values for precise input variable levels were quickly found using this technique and are easily extended for larger experiments involving more than four variables. Ultimately, the final answer to the cubic spline query is located with respect to the levels of all four input variables. The basic cubic spline coded algorithm used in this methodology was obtained from Gerald [1].

5.3 Application of RSM and Optimization

The application of RSM to the five dimensional cubic spline algorithm is a straightforward application of a software optimization routine designed to locate minimum function responses due to varying input values. Implementing the FORTRAN optimization routine, SUBPLX.F, to determine an optimized minimum average gain value in the 0 to 20 degree range of theta required less than one minute to process on a Silicon Graphics Indy machine equipped with a single R5000 processor. This processing time represents approximately 180 calls to the cubic spline model, for an average of 0.3 seconds per call. Obviously, in a particular region of interest having an empirical model that accurately describes the region and an appropriate optimization routine drastically reduces the computational time and effort required to arrive at an optimal design.

Frequency	1.3 GHz
Layer 1 permittivity	6.0
Layer 2 permittivity	8.0
Layer 1 thickness	0.337 cm
Average gain (spline)	-5.853 dB
Average gain (FEM)	-6.206 dB

Table 4: Optimum Antenna Design.

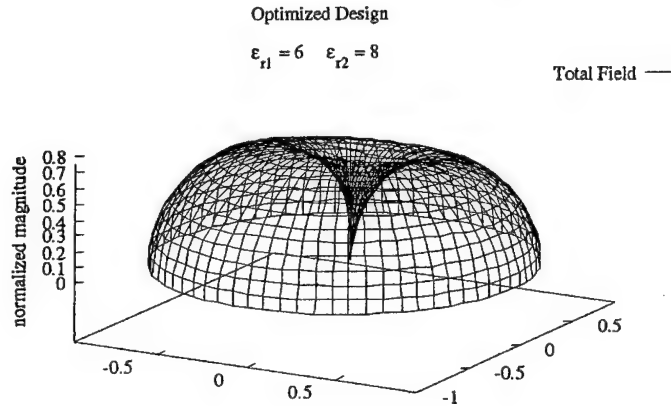


Figure 3: Optimum Gain Configuration.

6 Results

Using the design methodology developed above, an optimized antenna design was reached based on the cubic spline model and verified using the FEM code. The final design and gain values from both the design methodology and the FEM code are provided in Table 4 and the resulting antenna pattern is given in Figure 3. The final design using the cubic spline results deviated in field values approximately 4.2 percent from the FEM results. A 4.2 percent error in values is well within acceptable limits for the design methodology since an FEM code or moment method code could always be used to verify final optimized designs. Coincidentally, the optimized design of Figure 3 is extremely similar to one of

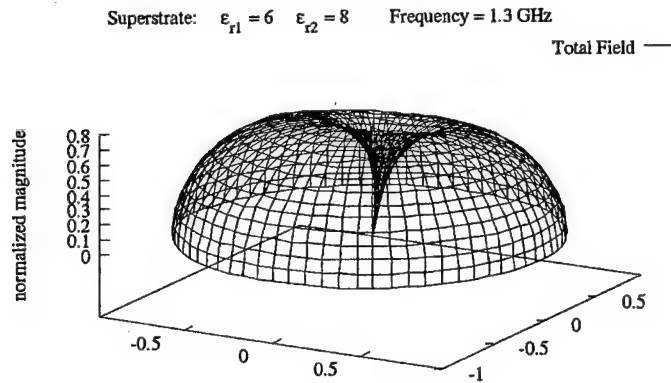


Figure 4: Approximate Optimal Setting.

Frequency	1.3 GHz
Layer 1 permittivity	6.0
Layer 2 permittivity	8.0
Layer 1 thickness	0.237 cm
Average gain (boresight)	-5.779 dB

Table 5: Approximate Optimum Test Case.

the initial test cases used in the full factorial data acquisition phase, Figure 4, with the antenna specifics for the test case provided in Table 5. Comparing the resulting performances of the optimized antenna configuration, the test setup of Table 5, and an additional configuration in Table 6, the optimized design is superior. According to Figure 5, the optimized antenna design produced lower gain values throughout the angular region.

This example illustrates the ability of the optimized design methodology to

Frequency	0.9 GHz
Layer 1 permittivity	1.0
Layer 2 permittivity	1.0
Layer 1 thickness	0.237 cm
Average gain (boresight)	3.375 dB

Table 6: Additional Test Case.

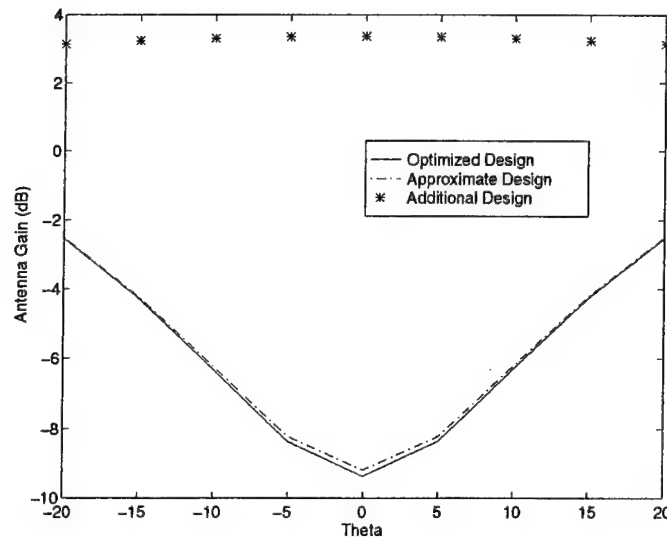


Figure 5: Pattern Comparison.

find an optimized minimum gain antenna configuration in any angular region of the far field antenna radiation pattern. The antenna design methodology used here to design an optimized cavity-backed microstrip antenna with dielectric overlays is applicable to other antenna design configurations. The steps used in the optimized design methodology include:

1. Select an appropriate experimental design procedure and the pertinent input variables along with their levels.
2. Select an appropriate data collection technique such as FEM, moment method codes, or antenna measurements from existing antennas.
3. Select an appropriate empirical model to accurately describe the results obtained using the data collection technique.

4. Create an appropriate confirmation test set of different data points not included in the original experimental design but within the limits of the experiment for verification of the empirical model.
5. Implement an adapted form of RSM to optimize the antenna design for input parameters under consideration.

Besides comparable gain results, the most startling measure of usefulness of this design methodology is the measure of time needed to converge to an optimal antenna design. This optimized design methodology required only 55 seconds to converge to the optimized design in Figure 3. If accomplished manually, the optimized configuration would have possibly have taken days to complete. To determine gain values for the optimized design of Figure 3, the Fortran coded cubic spline routine required less than 1 second while the FEM code needed 3 hours, 6 minutes, and 7 seconds to converge upon the final gain value. Certainly, this antenna configuration was more difficult than the initial test configurations used in the full factorial design experiment. In the optimized design, the FEM code solved for 201,650 total unknowns and completed 1513 iterations. In the initial data collection phase, the FEM code completed 200 iterations and solved for 2000 unknowns in an average time span of 5 to 10 minutes for each test combination.

7 Conclusion

The subject, optimized design methodology, based upon designed experiments, accurate modeling, and RSM techniques offers fast, accurate, and reliable results. In this experiment, the design methodology located an optimized design within a single minute of elapsed time and determined its minimum average gain within 4.2 percent of the calculated value from an FEM code. Comparisons with other antenna configurations demonstrate that the optimized configuration provides the best match to the desired antenna gain pattern.

References

- [1] Curtis F. Gerald and Patrick O. Wheatley. *Applied Numerical Analysis*. Addison Wesley Publishing Company, Massachusetts, third edition, 1984.
- [2] Douglas C. Montgomery. *Design and Analysis of Experiments*. John Wiley and Sons, New York, 1991.
- [3] Peter J. Moosbrugger, Zane Lo, Lynn A. Carpenter, and Russell R. Barton. Experimental design of a two layer electromagnetically coupled rectangular patch with a global response surface modeling technique. In *IEEE Transactions on Antennas and Propagation*, volume 45, pages 781–787, May 1997.
- [4] Kelce Wilson. Interview, June 1997. Query technique for cubic splines.

A GENETIC ANTENNA DESIGN FOR IMPROVED RADIATION OVER EARTH

Brian S. Sandlin
Andrew J. Terzuoli
Air Force Institute of Technology

Abstract

A wire antenna is designed for optimal gain at low elevation angles in the presence of a real earth. A genetic algorithm (GA) is implemented using real-valued chromosomes to determine the geometry which exhibits the largest gain at low elevation angles. The performance of the design is analyzed using Numerical Electromagnetics Code (NEC) Version 4.1. The resulting GA design provides a slight improvement in gain over a $\lambda/4$ monopole.

1 Introduction

1.1 Problem

Monopole antennas, despite their simplicity, continue to have applications in many communications and remote sensing systems. A system that typically employs monopoles is the Remote Intrusion Monitoring System (RIMS). These systems are frequently commercial and are deployed to observe and report on activity within a distant region. A typical implementation of a RIMS is shown in Figure 1 and contains the following components:

- **Unattended Sensors:** These units are placed in the region to be observed. Sensors are most often buried, leaving only the antennas above ground. The sensors can be customized to provide magnetic, seismic, passive infrared, or acoustic data.
- **Optical Sensor:** This unit is similar to the unattended sensor with the exception that it provides visual information, requiring the need for an attached camera unit.
- **Field Processor:** This unit receives the information from the multitude of sensors and formats the data as an input to data analysis software, located in the Field Analysis Unit and the Analysis Unit.
- **Field Analysis Unit:** This unit is a laptop personal computer that can be connected directly to the Field Processor. Data analysis software operates for human interpretation of the sensor data.
- **Analysis Unit:** This unit is a personal computer that receives data from the Field Processor via satellite.
- **Repeater:** This unit receives and retransmits signals from the sensors, allowing for greater distances between the unattended sensors and the field processor.

The primary components in most RIMS relay signals via monopole antennas. The monopole antennas are designed for the center frequency of the band designated by the Federal Communications Commission (FCC) for unattended ground sensors. This band ranges from 138–153 MHz. At the center frequency, the monopole is 0.25 wavelengths (λ) long. This is a common design and comes from the idea that if the antenna exists on an infinite, perfectly conducting ground plane, image theory applies and the system can be treated as a center-fed $\lambda/2$ dipole radiating in free space. The

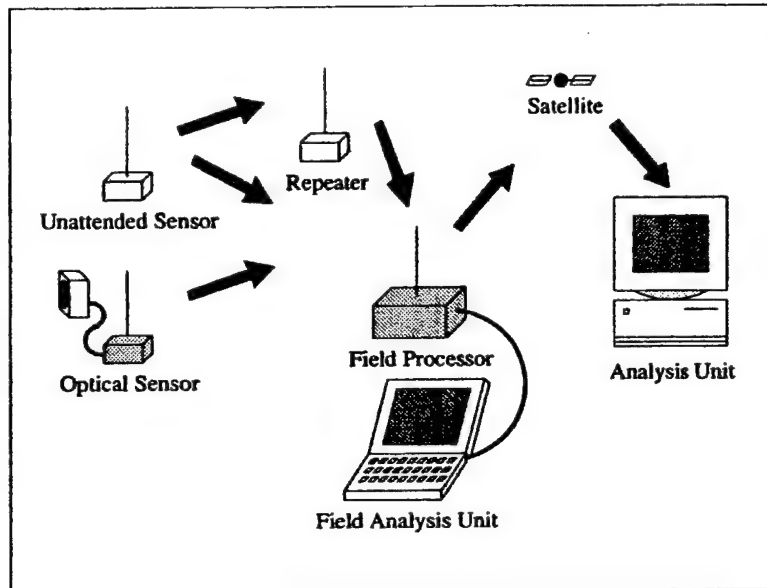


Figure 1: Typical Components of a Remote Intrusion Monitoring System (RIMS)

performance of a $\lambda/2$ dipole is well known and popular because—for small wire radii—its input impedance has a resistance near 50Ω with a very small reactive component [1]. The main problem with using the monopole for a RIMS is that the antenna does not reside on a perfect ground plane. A more rigorous design approach must be used.

1.2 Problem Constraints

All users of RIMS desire the systems to be reliable. In general, the unattended sensors, optical sensors and field processor are located in a non-supportive environment. Any design solution must fit within this context. That is, the greatest possible performance is desired while keeping the physical structure of the antenna as inconspicuous as possible. The steadfast nature of this requirement leads to numerous considerations:

- The physical dimensions of the antennas in the system need not be easily visible with the naked eye. Current implementations of RIMS meet this requirement by

using a thin, wire monopole antenna.

- The unattended sensors and field unit are often located in foliage. An electromagnetic wave's ability to penetrate foliage increases when its frequency decreases, leading to an important design trade-off. For successful communications at lower frequencies, larger antennas are required. For this reason, VHF is common.
- The amount of power used by the sensors for transmitting a message to the field analysis unit must be sufficient for VHF line-of-sight communications, but the size of the power supply cannot force the physical dimensions of the sensors to unreasonable levels.
- The voltage source driving the antenna should be located very close to or on the ground. A bulky transmission line to feed the antenna at some point above the ground cannot be used.
- The fields produced by the antenna should not vary greatly with azimuth. Because of the non-supporting environment, antenna orientation cannot be guaranteed.
- For a RIMS, little or no opportunity for maintenance exists. Often, users consider the unattended sensors to be expendable. Therefore, the design should incorporate dependability and zero requirement for maintenance, as well as a reasonably low cost.

2 Approach

2.1 Modeling a RIMS Monopole

The $\lambda/4$ monopole designed for the center frequency of the unattended ground sensor band is a 51.51 cm long wire with a radius of approximately 0.04 cm. A common

device used to drive a RIMS antenna is the Motorola MHW607-1 VHF Power Amplifier. According to the specifications provided by Motorola on this device, it provides 7.0 Watts of power at 9.0 Volts. A worst-case scenario is chosen for the research, so the model is driven by a 6 Volt source. The same source used in the model is used to drive the GA designed antennas. This is an important consideration for considering antenna performance as a function of geometry.

Usually, a matching network is introduced between the output of the power amplifier and the antenna. The exact impedance value of this network is unavailable, but the network is modeled by a fixed reactive load with a value of -27.2384Ω . This network helps match the source to the antenna, making the input impedance of the model $50.1907 + j0.0001 \Omega$.

The model experiences a well known result. The linearly-polarized field is severely attenuated at low elevation angles, a drastic change over the expected pattern of a $\lambda/2$ dipole radiating in free space. The only component of the field that is seen in the far field is θ -directed, and its pattern is shown in Figure 2.

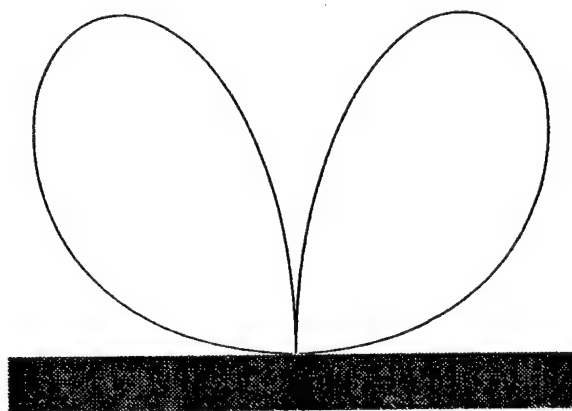


Figure 2: Normalized E_θ of a RIMS Monopole in the Presence of a Ground with $\sigma = 0.002 \text{ U/m}$ and $\epsilon_r = 10$.

The figure of merit of the most interest in this application will be the average power gain over the surface of the earth, a calculation performed by NEC4.1. Over the surface of the earth (computed at elevations of 0.2° , 0.3° , 0.4° and 0.5° and azimuth angles of -45.0° , 0° , and 45° , while observed at a radial distance of 500 m) the model has an average gain of 1.15487×10^{-3} dB. This result will be compared directly to that of the GA design.

2.2 Background on Genetic Algorithms

The genetic algorithm is a stochastic optimization method which is patterned after the biological occurrences of natural selection, mating and mutation. A GA is part of the broader class of global optimization methods. The best way to understand the GA is to progress through examples. A good introduction and several electromagnetic examples are found in [3].

2.3 Implementation

2.3.1 Implementation Constraints

Certain requirements are imposed to make computation time reasonable and to enforce the design context described previously. In a manner similar to that found in [4], the wires of the design are confined to a particular space. For this problem, the space is chosen to be a rectangular box above the x - y plane, bounded by $0 < z \leq 2.0$ meters, $-0.5 \leq x, y \leq 0.5$ meters. The lossy earth is defined by $z \leq 0$ and was given constant values comparable to that of poorly conducting jungle, a relative dielectric constant of $\epsilon_r = 10$ and a conductivity of $\sigma = 0.002$ mS/m [5].

Other requirements are imposed related to the connection of the straight wires. With an applied E-field voltage source positioned at the origin, the first wire is connected to that source. The fact that the source lies in the ground plane is an important

characteristic of the actual antenna. Each additional wire is connected in series to the previously defined wire.

Since the desired solution would have a nearly constant gain in the azimuth plane, symmetry is imposed on the design. In generating the symmetric design, the first wire was created in the octant described by $x, y, z > 0$. After a wire is generated in this region, it is copied three more times, the copies rotated about the z -axis and spaced evenly in the azimuth direction.

2.3.2 Genes

The decision to use real-valued chromosomes is made to avoid the possibility that an ideal location for a wire endpoint would lie somewhere between two values represented with binary code. Another advantage to this decision is that it makes implementation simpler and execution faster, as there is no requirement for encoding and decoding schemes. Each gene is simply the value for the endpoint of the associated wire in Cartesian coordinates. That is,

$$g_m = (x_m, y_m, z_m) \quad (1)$$

describes the rectangular coordinates of the m^{th} wire endpoints. The wire's other endpoint is defined by $(0, 0, 0)$ in the case of the first wire and by $(x_{m-1}, y_{m-1}, z_{m-1})$ in the case of the other wires.

2.3.3 Chromosomes

The chromosomes are defined by the number of wires in a particular design. The chromosome will have M genes, where M is the number of wires. The somewhat

arbitrary choice for this research is $M = 4$. For this choice, the n^{th} chromosome is then

$$c_n = g_1, g_2, \dots, g_M \quad (2)$$

$$c_n = (x_1, y_1, z_1), (x_2, y_2, z_2), (x_3, y_3, z_3), (x_4, y_4, z_4) \quad (3)$$

An initial population of 100 is generated selecting the wire endpoints with a uniform random variable generator.

2.3.4 Cost Function

The cost function assigned to each chromosome is simply the average gain value of the twelve positions described previously. No convergence criteria is set. The GA was allowed to create a tenth generation design. The chromosome (design) with the best cost function after the creation of the tenth generation is analyzed further.

2.3.5 Parent Selection

After the cost of each chromosome is evaluated, the gene pool is sorted with the antenna design with the greatest average gain at the top. Then, the top two chromosomes are chosen to be the first set of parents. The third and fourth ranking chromosomes become the next set, and so on until the top 40% of the gene pool has been selected. The task of the parent chromosomes is to repopulate the bottom 60% of the gene pool.

2.3.6 Mating

The mating scheme is simple. By not replacing the entire gene pool with children, the possibility that a reasonably good set of parents could produce poor children is

accounted for. Keeping the parents in the gene pool assures that a good design is not replaced with a poor design.

Each pair of parents creates three children. Each gene in the first child was generated by using the midpoint of the line between the corresponding genes (wire endpoints) in the parents. The second and third child's genes are generated by finding the two points along the line between the parents and the previously acquired midpoint. For example, if the first parent is defined as

Parent A: (7.0, 1.0, 9.0), (2.0, 3.0, 8.0), (6.0, 4.0, 5.0)

and the second parent is

Parent B: (1.0, 3.0, 9.0), (4.0, 8.0, 2.0), (5.0, 6.0, 7.0)

Then, the children produced from these parents are

Child 1: (4.0, 2.0, 9.0), (3.0, 5.5, 3.5), (5.5, 5.0, 6.0) ,

Child 2: (2.5, 1.5, 9.0), (2.5, 4.25, 6.5), (5.25, 4.5, 5.5) ,

and

Child 3: (5.5, 2.5, 9.0), (3.5, 6.75, 5.0), (5.75, 5.5, 6.5) .

2.3.7 Mutation

Mutation allows the genetic algorithm to find a global optima. The GA for this problem implements mutation for each of the child chromosomes. Mutation is implemented in each child chromosome by assigning one new coordinate value to single wire endpoint

in each design. Since each design was described by four wires the mutation rate is 8.3%.

2.3.8 Interfacing With NEC4.1

The key to interfacing with NEC4.1 is what to do when the NEC code finds an error with the geometry. With the random nature of the iterations in the genetic algorithm, a fatal error such a crossed wires would cause the code to stop [2]. The NEC code is modified to prevent such abort conditions from occurring, and the corresponding chromosomes cost was set to zero. This helped the GA to converge to designs which would be computable by the NEC code. For the sake of computational speed, no attempt is made to modify problem designs. The potential in correcting problem designs is that the code could iterate indefinitely while trying to fix a bad design.

3 Preliminary Results

After ten generations of computing, the resulting antenna design is created and shown in Figure 3. The design includes 16 wires. The first four wires are defined by the following coordinates:

wire #1: (0.000, 0.000, 0.000) to (0.000, 0.140, 1.618)

wire #2: (0.000, 0.140, 1.618) to (0.214, 0.484, 1.025)

wire #3: (0.214, 0.484, 1.025) to (0.046, 0.327, 0.430)

wire #4: (0.046, 0.327, 0.430) to (0.390, 0.171, 1.805)

The rest of the antenna geometry is generated from the above four wires being copied and rotated as described previously.

The design achieved by the genetic algorithm is a very modest improvement over

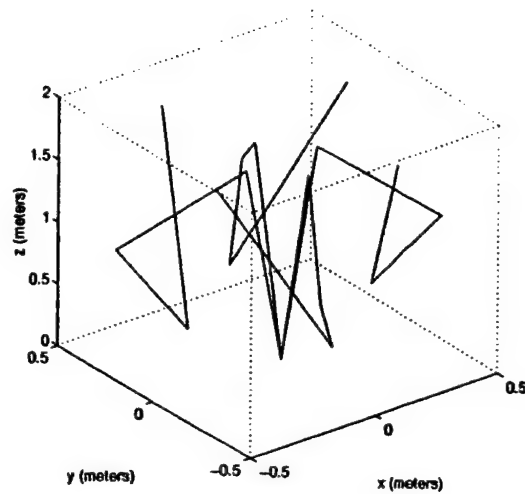


Figure 3: Tenth Generation Design Shown Inside the Space Allowed for Wire Placement

the $\lambda/4$ feed-loaded monopole commonly used. The average power gain over the angles of interest was computed by NEC4.1 to be 3.49258×10^{-3} dB. With no consideration for input impedance, this is only a 2.3377×10^{-3} dB improvement over the $\lambda/4$ monopole, certainly not enough to make a significant impact. Input impedance is a very important consideration. The input impedance for an unloaded GA design is $576.490 - j68.9716 \Omega$.

The GA design meets the criteria necessary for use in a RIMS. The imposed design symmetry was useful to produce an azimuth plot shown in Figure 4.

The main interest is not in the azimuth cuts of the antenna pattern but the elevation cut, where the GA design outperforms the monopole, as can be seen in Figures 5 and 6. Looking at the θ -directed field component and comparing it to the monopole, one sees that GA design has improved field levels at lower elevations.

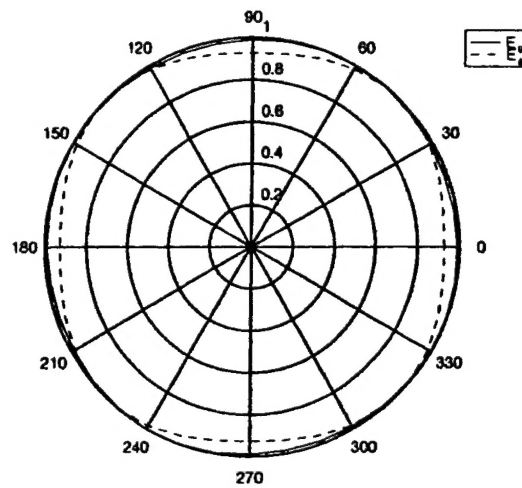


Figure 4: Azimuth Cut of Normalized Fields Taken at $\theta = 89^\circ$

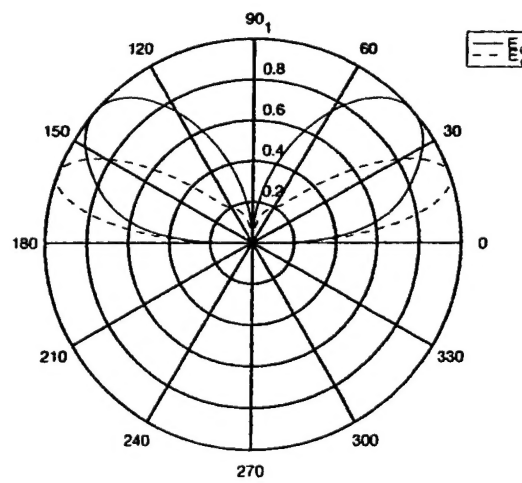


Figure 5: Elevation Cut of Normalized Fields Taken at $\phi = 0^\circ$

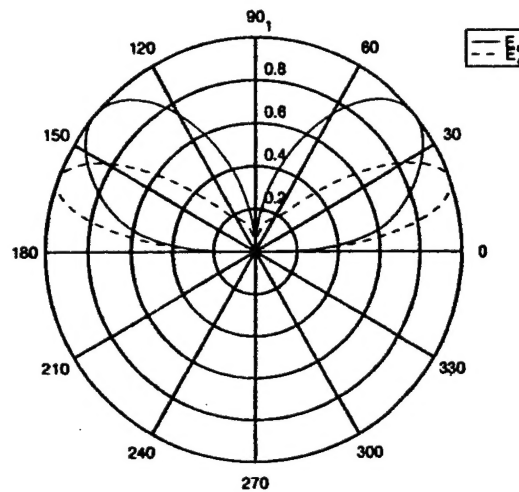


Figure 6: Elevation Cut of Normalized Fields Taken at $\phi = 45^\circ$

4 Further Research

For future research, other design parameters will be incorporated into the genetic algorithm. For instance, instead of requiring the wires to be series connected, the possibility that the antenna can have any number of junctions is interesting.

The current genetic algorithm requires a fixed number of wires as an input parameter. As an extension to this, the code can be slightly modified to allow for a range of different numbers of wires. Of interest is the direct comparison of designs consisting of a variety of straight wires.

Acknowledgments

The authors gratefully acknowledge the following people for their help and advise:

The Air Force Technical Applications Center

Ed Altshuler,

Jeff Berrie,

Peter Collins,

Errol English,

Ben Munk,

Ed Newman,

Gary Thiele,

Eric Walton.

References

- [1] Constantine A. Balanis. *Antenna Theory*. John Wiley and Sons, Inc., second edition, 1997.
- [2] Gerald J. Burke. *Numerical Electromagnetics Code-NEC-4, Method of Moments, Part I: Users Manual*. Lawrence Livermore National Laboratory, 1992.
- [3] Randy L. Haupt. "An Introduction to Genetic Algorithms for Electromagnetics". *IEEE Antennas and Propagation Magazine*, 37(2):7-15, April 1995.
- [4] Derek S. Linden and Edward E. Altshuler. "Automating Wire Antenna Design Using Genetic Algorithms". *Microwave Journal*, pages 74-86, March 1996.
- [5] J.W. Rockway and J.C. Logan. *MININEC Broadcast Professional for Windows*. EM Scientific, Inc., 1996.

***MISSION
OF
AFRL/INFORMATION DIRECTORATE (IF)***

The advancement and application of information systems science and technology for aerospace command and control and its transition to air, space, and ground systems to meet customer needs in the areas of Global Awareness, Dynamic Planning and Execution, and Global Information Exchange is the focus of this AFRL organization. The directorate's areas of investigation include a broad spectrum of information and fusion, communication, collaborative environment and modeling and simulation, defensive information warfare, and intelligent information systems technologies.